T2R2 東京工業大学リサーチリポジトリ
Tokyo Tech Research Repository

# 論文 / 著書情報
# Article / Book Information

| | |
|---|---|
| 題目(和文) | |
| Title(English) | GaInAsP/InP Membrane Integrated Lasers for On-chip Optical Interconnection |
| 著者(和文) | 井上大輔 |
| Author(English) | Daisuke Inoue |
| 出典(和文) | 学位:博士(工学),<br>学位授与機関:東京工業大学,<br>報告番号:甲第10639号,<br>授与年月日:2017年9月20日,<br>学位の種別:課程博士,<br>審査員:荒井 滋久,水本 哲弥,宮本 恭幸,西山 伸彦,庄司 雄哉,碓塚 孝明 |
| Citation(English) | Degree:Doctor (Engineering),<br>Conferring organization: Tokyo Institute of Technology,<br>Report number:甲第10639号,<br>Conferred date:2017/9/20,<br>Degree Type:Course doctor,<br>Examiner:,,,,, |
| 学位種別(和文) | 博士論文 |
| Category(English) | Doctoral Thesis |
| 種別(和文) | 要約 |
| Type(English) | Outline |

Powered by T2R2 (Tokyo Institute Research Repository)

# GaInAsP/InP Membrane Integrated Lasers for On-chip Optical Interconnection

**by**

**Daisuke Inoue**

Department of Electrical and Electronic Engineering
Graduate School of Science and Engineering
Tokyo Institute of Technology

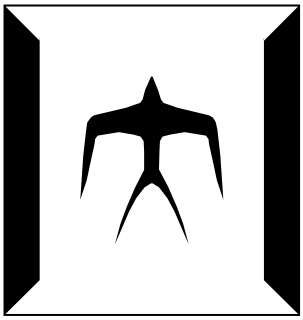

A DOCTRAL DISSERTATION

Directed by Professor Shigehisa ARAI
Associate Professor Nobuhiko NISHIYAMA

2-12-1-S9 O-okayama, Meguro-ku, Tokyo, 152-8552, Japan
Quantum Nanoelectrornics Research Core
Tokyo Institute of Technology

# GaInAsP/InP Membrane Integrated Lasers for On-chip Optical Interconnection

# Table of Contents


## Chapter 1
## Introduction

1.1 Introduction 1
1.2 Energy dissipation in CMOS LSIs 3
1.2.1 Performance improvement of microprocessors 3
1.2.2 Energy reduction technique 10
1.2.3 Energy dissipation in a wiring 16
1.3 Novel on-chip interconnection technology 20
1.3.1 Electrical interconnection 20
1.3.2 Optical interconnection 26
1.3.3 Comparison between optical and electrical interconnection 31
1.4 Performance requirements for on chip-optical interconnection 35
1.4.1 Optical devices in fiber optics communication 37
1.4.2 Devices for on-chip optical interconnection 42
1.5 Semiconductor lasers for optical interconnection 46
1.5.1 Types of semiconductor laser cavity 46
1.5.2 Integration methods on silicon 56
1.6 Semiconductor membrane structure 61
1.6.1 Features of membrane structure 61
1.6.2 Research history of membrane lasers 64
1.7 Objective and outline of this thesis 73
References

## Chapter 2
## Theoretical analysis of membrane devices for on-chip optical interconnection

2.1 Introduction 88
2.2 Effect of link loss on required optical power 91
2.3 Analysis on membrane DFB laser performance 96
2.3.1 Threshold current characteristics of DFB structure 100
2.3.2 High modulation efficiency characteristics 106
2.4 Conclusion 115
References

## Chapter 3
## Design and fabrication of membrane butt-jointed built-in structure


3.1 Introduction 118
3.2 Method of monolithic photonic integration 119
3.3 Butt-jointed built-in (BJB) structure 126
3.3.1 Selective area regrowth 126
3.3.2 BJB structure in photonic integration 128
3.4 Calculation of membrane BJB structure 133
3.4.1 Calculation method for BJB coupling 133
3.4.2 Analysis on coupling efficiency and back reflection 137
3.5 Process investigation of membrane BJB structure 145
3.5.1 Growth process 145
3.5.2 Dependence on regrowth mask shape 152
3.5.3 Dependence on island fabrication process 159
3.5.4 Evaluation of regrown layer by photoluminescence 164
3.6 Conclusion 170
References


## Chapter 4
## Lasing characteristics of membrane DFB lasers


4.1 Introduction 175
4.2 Structure and design of membrane DFB laser 177
4.2.1 Device structure 177
4.2.2 Grating design 180
4.3 Fabrication process 183
4.3.1 Equipment 183
4.3.2 BCB (benzocyclobutene) wafer bonding 188
4.3.3 Grating formation method 194
4.3.4 Fabrication procedure 200
4.4 Static characteristics of membrane DFB laser 207
4.4.1 Uniform grating device 207
4.4.2 $\lambda/4$-shifted grating device 213
4.4.3 Reliability of membrane DFB lasers 217
4.5 Dynamic characteristics of membrane DFB laser 225

4.5.1 Relative intensity noise (RIN) measurement 225
4.5.2 Small signal modulation 230
4.5.3 Eye diagrams and bit-error-rate (BER) measurement 240
4.6 Conclusion 246
References

## Chapter 5
## Integration of membrane DFB laser and p-i-n photodiode

5.1 Introduction 255
5.2 Device structure and fabrication 257
5.2.1 Device structure 257
5.2.2 Fabrication process 259
5.3 Electrical isolation between the integrated devices 262
5.3.1 Isolation process 264
5.3.2 Measurement of isolation resistance 266
5.3.3 Isolation effect on the photocurrent characteristics 270
5.4 Integrated membrane DFB laser and p-i-n photodiode with isolated structure 272
5.4.1 Lasing characteristics of integrated laser 275
5.4.2 Static optical transmission characteristics 277
5.4.3 Dynamic optical transmission characteristics 281
5.5 Conclusion 289
References

## Chapter 6
## Future prospects of membrane optical link

6.1 Introduction 290
6.2 Integration of low-loss waveguide 291
6.2.1 Properties of membrane rib-waveguide 292
6.2.2 Preliminary experimental results 294
6.3 Integration of membrane distributed-reflector laser 297
6.4 Conclusion 302
References

# Chapter 1 Introduction

1.1 Introduction 1
1.2 Energy dissipation in CMOS LSIs 3
1.2.1 Performance improvement of microprocessors 3
1.2.2 Energy reduction technique 10
1.2.3 Energy dissipation in a wiring 16
1.3 Novel on-chip interconnection technology 20
1.3.1 Electrical interconnection 20
1.3.2 Optical interconnection 26
1.3.3 Comparison between optical and electrical interconnection 31
1.4 Performance requirements for on chip-optical interconnection 35
1.4.1 Optical devices in fiber optics communication 37
1.4.2 Devices for on-chip optical interconnection 42
1.5 Semiconductor lasers for optical interconnection 46
1.5.1 Types of semiconductor laser cavity 46
1.5.2 Integration methods on silicon 56
1.6 Semiconductor membrane structure 61
1.6.1 Features of membrane structure 61
1.6.2 Research history of membrane lasers 64
1.7 Objective and outline of this thesis 73
References

## 1.1 Introduction

As performance improvements of microprocessors have been drastically accelerated, the power dissipation for interconnection became serious problem. For the limitation of thermal design of microprocessors, the allowable power consumption is restricted to be 100–200 W. There is no more available power consumption to use for the switching logic devices. The proportion of the power consumed in the wiring is not trivial amount

compared with the logic device. Consequently, newly interconnect technology is strongly demanded so as to reduce the power dissipation in wiring. Many electrical interconnect methods have been proposed for on-chip wiring. Unlike the extension of previous electrical wiring technology, the interconnection using an optical communication is thought as one of the potential candidate for on-chip wiring. However, conventional optical devices for fiber communication are energy inefficient to use in ultra-short distance communication such as on-chip interconnection. Recently, remarkable advances in the field of low-power consumption semiconductor lasers are reported for on-chip optical interconnection. In this thesis, I investigate semiconductor lasers using semiconductor membrane and distributed-feedback (DFB) structure for the purpose of low-power consumption laser for on-chip interconnection.

In this chapter, the motivation for the on-chip optical interconnection and membrane DFB laser will be described. A brief overview of progress in integrated circuits, an energy saving technique and energy dissipation in wiring will be given in the section 1.2. A comparison between the electrical and optical interconnection approaches will be explained in section 1.3. Performance requirement of a semiconductor laser for on-chip application compared with the lasers for optical fiber communications will be explained in section 1.4. A types of semiconductor laser cavity and an integration method of the lasers on a Si substrate is shown in section 1.5. The features of membrane DFB structure and summarize of our research history is given in section 1.6. Finally, in section 1.7 the problems of previous works will be pointed and objectives of this thesis will be described.

## 1.2 Energy dissipation in CMOS LSIs

### 1.2.1 Performance improvement of microprocessors

A large-scale integrated circuits (LSIs) have essential rolls in today's information processing. This is a result of continued growth of integrated circuit complexity annually 53% in the past 50 years boosted by transistor miniaturization and maturing of manufacturing process. First, the development of LSIs and microprocessors technologies is overviewed. And, that the history of development of electronics to reduce of power consumption for higher performance computing will be confirmed

In the early 20th century, programmable digital computers used electron tubes. British cryptanalyzer Colossus, which started operation in 1944, used vacuum tubes and thyratrons for a computing [1]. This computer consisted of 2,400 of electron tubes and consumed 15kW of power for an operation. Computers using electron tubes had concerns for a large size, a large power consumption and a low reliability. The point contact type germanium transistors were first invented by J. Bardeen, W. Brattain and W. Shockley at Bell Labs in 1947. Figure 1.1 shows a photograph and a schematic of the first transistor. After 10 years from first invention of transistor, J. Kirby in Texas instruments noticed the possibility of miniaturizing the computer by integrating the many transistors

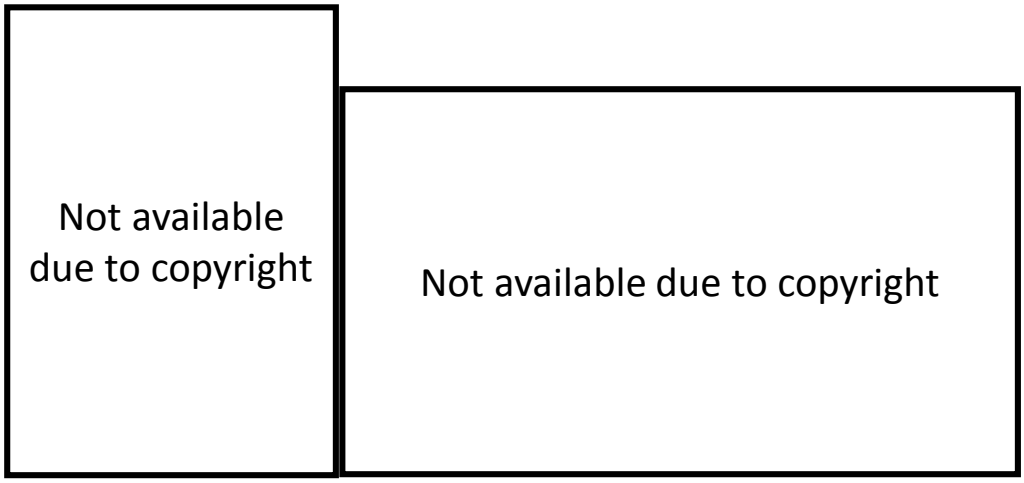


**Figure 1.1** The first point contact transistor [2].


**Figure 1.2** Early IC using planar Si process manufactured by Fairchild[2].

on a single chip. First patent of integrated circuits (ICs) was applied in 1959 by Kirby. However, an idea of the today's planer type ICs shown in Figure 1.2 was developed by F. Noyce at Fairchild Semiconductor. After the invention of the point contact transistors, Bell Laboratories developed a bipolar type transistor. The bipolar transistor exhibited a higher reliability, higher power efficiency and lower noise property than those of point contact transistors. This is the reason why bipolar transistors were used in early integrated circuits. Whereas the base current continue to flow when the circuits in not in operation, static power consumption restrict the maximum number of transistors integrating in a single chip. In 1960s, a mass production of metal-oxide-semiconductor field effect transistor (MOSFET) has begun. The idea of MOSFET was proposed in a patent by J. Lilienfeld at Leipzig University in 1925. The similar structure proposed by O. Heil at University of Cambridge in 1935 was not operated owing to the problem in a material. In 1964, the first paper on logic gates using MOSFETs was published by F. Wanlass at Fairchild [3]. Because this logic gate used both n-channel and p-channel MOS transistors, it became called complementary metal oxide semiconductor (CMOS). Although the circuit consisted of discrete transistors, it operated with nW power consumption which was the order of $10^{-6}$ lower than the corresponding circuit consisting of bipolar transistors. Boosted by a development of Si planar process, it became important to reduce the cost by fabricating the transistors smaller and simpler in the manufacturing process of CMOS

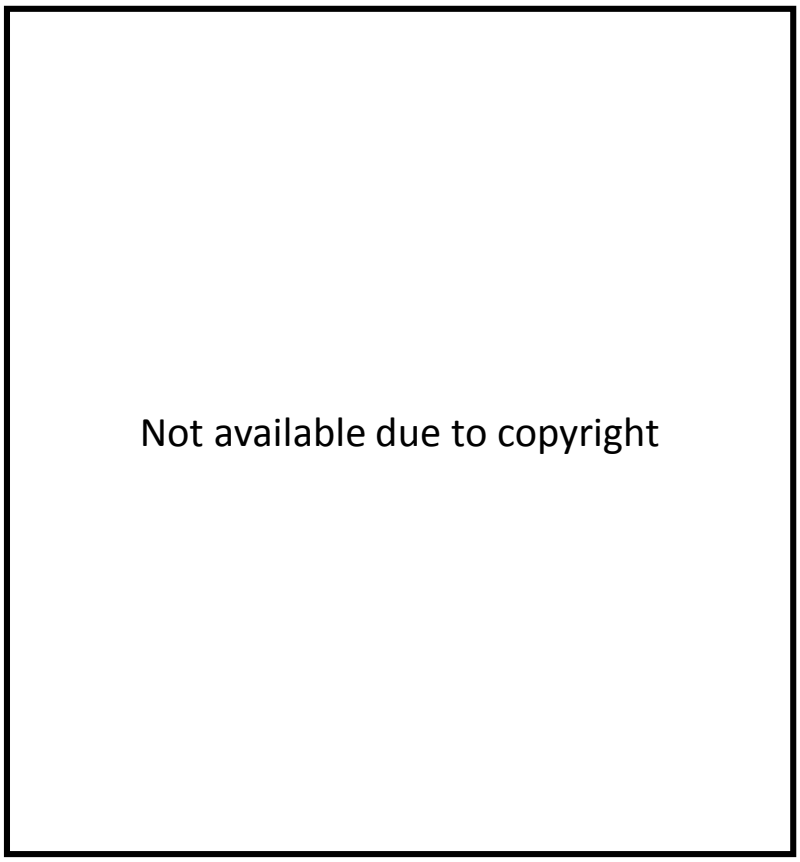


**Figure 1.3** A history of Intel's microprocessors [4].

integrated circuits. While p-MOS transistors were used in early commercial IC chips, the performance, yield a reliability had problems. *n*-MOS transistors were preferred to use in 1970. While the n-MOS logic took advantage over manufacturing cost compared with CMOS logic, it consumed power in static state. The CMOS logic consumed negligible power without switching, and firstly application of CMOS logic was circuit in a watch [5]. As millions of transistors integrated in a chip in the 1980's, power consumption became an important issue and CMOS logic was used to struggle for the increased power. As a result until the now, *n*-MOS and bipolar logics were replaced with CMOS logic in the field of digital logic circuits.

In 1965, the performance of ICs was predicted by Moore's law which forecast that the number of transistors in a dense integrated circuit doubles approximately every two years [6]. Figure 1.3 shows a brief history of Intel's central-processor-units (CPUs). As technology scale becomes miniaturized, the number of transistors integrated into CPUs

**Table 1.1** Number of transistors of Intel's microprocessors [4].

| microprocessor | year | Number of transistors |
|---|---|---|
| Intel 4004 | 1971 | 2,300 |
| Intel 8086 | 1978 | 29,000 |
| Intel 286 | 1982 | 134,000 |
| Intel 486 | 1989 | 1,200,000 |
| Intel Pentium II | 1997 | 7,500,000 |
| Intel Pentium 4 | 2000 | 42,000,000 |
| Intel Itanium 2 | 2002 | 220,000,000 |
| Dual-Core Intel Itanium 2 | 2006 | 1,720,000,000 |

is exponentially increased and also operating clock frequency was increased. As shown in Table 1.1, the number transistors in Intel microprocessor has doubled at every 26 months since the Intel 4004. Although, integrated circuits were classified according to its number of integrating gates, since 1980, all ICs became called a large-scale-integrated circuit (LSI) or a very-large-scale-integrated-circuit (VLSI). As a support of this fact, a scaling law of MOSFET was formulated by R. H. Dennard at IBM in 1974 [7]. The Dennard scaling law describes design rule in miniaturization that scale down the parameters of the MOSFET on the same factor and simultaneously reduces the applied voltage. Miniaturization of MOSFET based on this scaling rule provides following profit (1) increment of transistor number per unit area (2) improvement of total performance by increased operating speed for single transistor (3) reduction of power consumption by lowing supply voltage. However, the increment in clock frequency boosted by scaling became slow down around 2004. The trend of increasing clock frequency was stopped up to around 3 GHz because of available power limitation so-called "power wall" as shown in Figure 1.4. The total chip power is obtained by the product of capacitive load, square of voltage and switching frequency. In other word, there are no more energy to switching

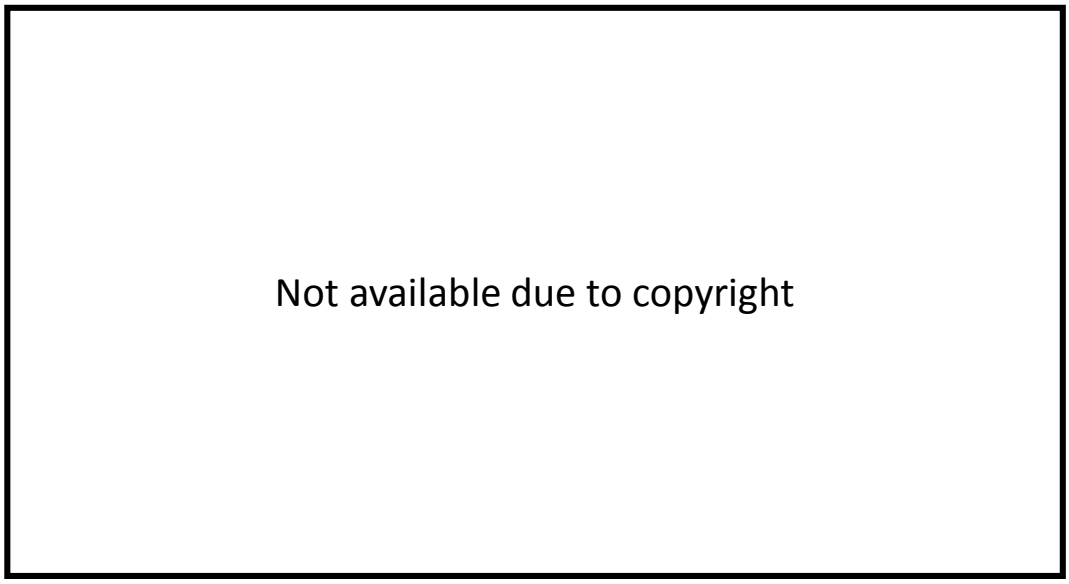


**Figure 1.4** Clock frequency and power for Intel microprocessors [8].

the devices. It was pointed out that the power consumption in microprocessors continues to increase exponentially. However, as this trend continues, the power density of high performance microprocessors was considered to reach the nuclear reactor level (200 $W/cm^2$) by 2005. This estimation indicated that it was difficult to expect a further improvement of the microprocessor performance with the conventional approaches explained in previous sentences. The power consumption of the microprocessor is limited to approximately 150–200 W from the viewpoint of thermal design. Therefore, power reduction techniques are strongly demanded to improve the performance with a limited available power.

Performance improvement using single core is prevented by limitation of heating and clock frequency. Typically, the total performance of computers is measured by execution time for application. It should be noted that the performance improvement is achieved by another factor than clock frequency. As the integration density of transistors increased, wiring for interconnections between the gates need innovations. In the past, two or three interconnect layers were standard design, however the appearance of chemical-mechanical-polishing (CMP) enabled us to process the seven or more layers interconnection [9]. Aluminum (resistivity: $\rho = 2.65$ μΩcm) was adopted as wiring metal


**Figure 1.5** Cross-section of multi-layer interconnection in LSI [10].

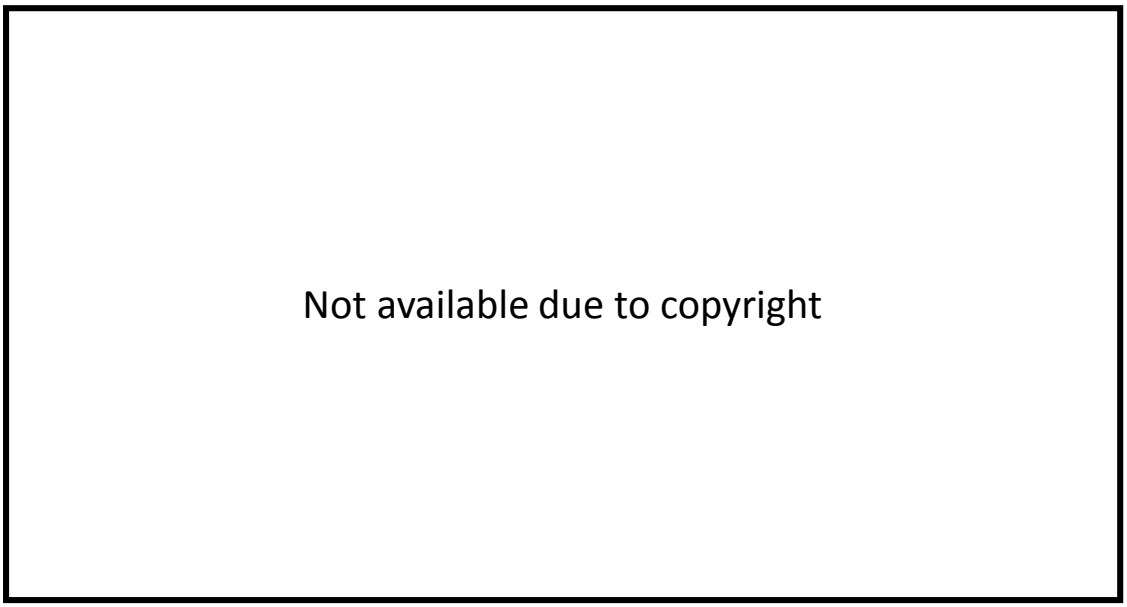


**Figure 1.6** A die photograph of multi-core processor chip [11].

for long decades. In the process of sub-$\mu$ m scale, copper (resistivity : $\rho$ = 1.68 μΩcm) has come to be used due to lower resistivity than that of aluminum [12]. To reduce the resistance and capacitance of wires, copper wiring and low-k interlayer insulation material are used in current process. Figure 1.5 shows cross section of IBM microprocessors manufactured in 90 nm process. The number of metal layers are 11 layers.

The most bottom layer is tungsten local wire which connect the each transistor gate. The top layer has thick and wide design because it is usually used as power supply or clock distribution.

The idea of multi-core CPU is the introduction of parallelism into the CPU. The multi-core CPU has several processor core on a single chip. Figure 1.6 shows a photograph of multi-core CPU die manufactured by Intel. The die size of multi-core CPU increases proportional to the number of core. The large segmented thread can be divided into small thread, and executed in parallel by each core. But, there are processes that cannot be processed and executed in parallel. The cores, cache and memory are interconnected by high speed bus lines to communicate each other in distance. If the number of cores grow, a demand for high speed and long-distance buss wiring rises.

According to the above overview, when the number of integrated CMOS transistors on a chip reaches several million or billion, the problem for power consumption appears even in CMOS logic LSI. In 1990, when CPU reached the power wall, the engineers began to reduce the supply voltage for decreasing the dynamic energy by abandoning the 5 V of supply voltage used in long term. The approach of reduction of supply voltage forced LSI to decrease the threshold voltage of MOSFET until sub-threshold leakage becomes inevitable issue. The gate leakage became problem as the thickness of gate insulator approaching atomic scale. In addition, as the supply voltage became close to 1 V, there was no room to save more power consumption in LSIs.

### 1.2.2 Energy reduction technique

Although the early LSIs have been restricted its function by their chip size, the performance of current LSI limited by the power consumption. Recently, it is said that the power limitation produces the dark silicon, which refer to a device that need to be shut down in order to avoid overheating of the chip. The power reduction by decreasing a supply voltage based on the scaling law seems to reach a saturation point. Here, a brief theoretical explanation for energy consumption in LSIs and power reduction techniques used in recent LSIs are reviewed.

The factors of an energy consumption in LSIs are roughly classified into dynamic power and static power. Dynamic power is dissipated by switching of the logics. Static power include energy consumption caused by gate leakage current and subthreshold leakage, which are happened without switching. The dynamic power can be represented as following equation;

$$P_{switching} = \alpha C V_{DD}^2 f \quad (1.1)$$

where $\alpha$ is activity factor, $C$ is load capacitance, $V_{DD}$ is supply voltage and $f$ is clock frequency. The activity factor means transition probability from 0 to 1 state. The higher clock frequency induces more power consumption. The squared supply voltage has strong effect on power consumption. The static power can be expressed as following;

$$P_{static} = (I_{sub} + I_{gate} + etc.)V_{DD} \quad (1.2)$$

where $I_{sub}$ is substhreshold leakage current and $I_{gate}$ is gate leakage current. The other factors contributing static power are omitted in this equation. We will look at the technology for reducing these power consumption by the approach from circuit design and process development.

## Circuit design approaches

## Clock gating

Clock gating controls the clock distribution to the unnecessary circuits by inserting AND logic of clock signal and enable signal (Figure 1.7) [13]. The activity factor of clock signal is 1, and others have lower activity factor than that of clock in equation (1.1). When

blocking a large logic circuits block, the clock can be prevented at the base of the clock distribution network. Because a part of the clock distribution network can also be blocked, stopping of the clock signal which has the activity factor of 1 has a large contribution for the power reduction.

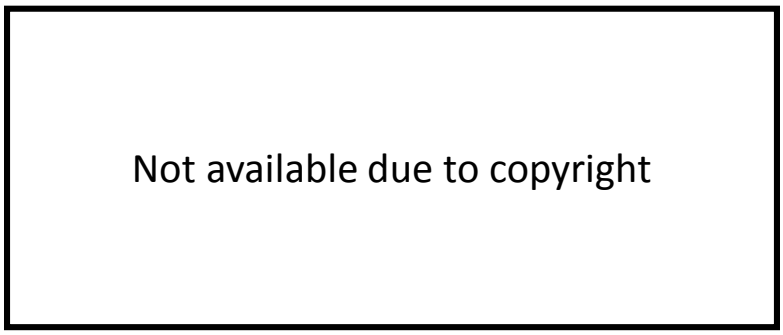


**Figure 1.7** Clock gating circuit (a) typical latch element (b) a latch element with clock gating signal [13].

## Power gating

Power gating cut off power supply to un-operated circuit blocks to suppress the leakage currents (Figure 1.8) [14]. In this case, power supply is provided for each processor core. The transition from the operating state to the sleep state requires a transition time and energy. This is because the power wiring has the decoupling capacitance of several 100 nF, and results in large transition time and energy. Therefore, power gating is effective when the sleep time of the circuit block is sufficiently long.


**Figure 1.8** Power gating circuit. [14]

## Voltage domain

By using voltage domain, the circuits block in a chip can be divided into several blocks which are suppled different optimum power voltages as shown in Figure 1.9. For example, high voltage is supplied for memory region to guarantee cell stability and low voltage is supplied I/O region which operate relatively low speed. The problem is the voltage conversion of the signal line which cross over the different voltage domains. A typical solution is to insert a level converter between the different voltage domain [15].


**Figure 1.9 V**oltage domain in SPARC multi-core processor. [16]

## Dynamic Voltage and frequency scaling

In different systems, performance requirements for signal processing are different depending on processing data. In a Dynamic voltage/frequency scaling (DVFS), clock frequency is decreased within a processing can be completed on time. Simultaneously, supply voltage is also decreased to a certain voltage that circuit can be operated the clock frequency. According to the equation (1.1), the power consumption is significantly reduced by frequency and voltage decreasing. As shown in Figure 1.10, at supply voltage of 1.2 V, operating speed and power consumption are 915 MHz and 737 mW, respectively. Then, reducing the supply voltage to 0.8 V, although the operating speed drop down to 500 MHz, the power consumption is significantly reduced to 174 mW.


**Figure 1.10** Operating frequency and power consumption of microprocessor as a function of supply voltage supply voltage [17].

## Process development approaches

### High *k* dielectric

By using a high dielectric constant (high-*k*) material as the gate insulator, the gate leakage current induced by carrier passing through the insulator in the ON state can be suppressed. $SiO_2$ has been used as a gate insulator material in conventional MOSFETs. However, the leakage current has been increased owing to follow the scaling law which scale down the gate insulator thickness close to atomic scale to maintain constant electrical field density. Thickness of gate insulator can be increased by using a material which has higher dielectric constant than the $SiO_2$ dielectric constant of $k = 3.9$. The high-*k* material was first used for mass production of Intel's 45 nm process in 2007 and $HfO_2$ $k = 20$ was introduced[18].

### Silicon-on-insulator (SOI)

SOI substrate consists of Si substrate, buried oxide layer and thin top Si laser. MOSFETs are formed on an SOI substrate in which Si layer is formed on an insulating material. Figure 1.11 shows a schematic structure of SOI substrate provided by Soitec. By

using SOI substrate, capacitance between the source/drain and body can be removed. Addition to that, sub-threshold slope becomes steep slope (SS) and the leakage is suppresed [19]. As another application other than electronics, SOI substrate is often adopted as platform of photonic integrated circuit, well known as silicon photonics.


**Figure 1.11** Fully-depleted SOI substrate from Soitec [20].

## Porous low-*k*/air gap

Using a low dielectric constant (low-*k*) material as the interlayer dielectrics filling the interconnection, the reduction of the interconnect capacitance enable to reduce delay, noise, and power consumption [21]. However, low-*k* materials are difficult to instigate to Si or metals for the reason of softness and low adhesion. SiOF, which is added the F to $SiO_2$, has dielectric constant *k* of 3.6 and adopted in 130 nm process. SiCOH which is added C element has dielectric constant *k* of 2.8–3 used in 90nm, 65nm generation process. The porous polymer material possesses lower dielectric constant. The porous silicon-based polymer SiLK has $k = 2.6$. The ultimately low dielectric material is the air which has dielectric constant *k* of 1.00059. IBM actually manufactured a microprocessor with interconnection using air gap structure (Figure 1.12).


**Figure 1.12** Interconnection with an air gap [22].

## Fin-FET

The Fin-FET is a MOSFET with a gate surrounded in three dimentional planes (Figure 1.13). The name of Fin-FET is originated from that the shape of the channel looks like the fin of the fishes. Since the charge generated in the channel can be more strongly controlled planar gate structure, it is possible to suppress the sub-threshold leakage current and also to increase the on-state current. The original idea of three-dimensional channel FET was invented by D. Hisamoto at Hitachi [23]. Intel first introduced the fin structure in 22 nm process.

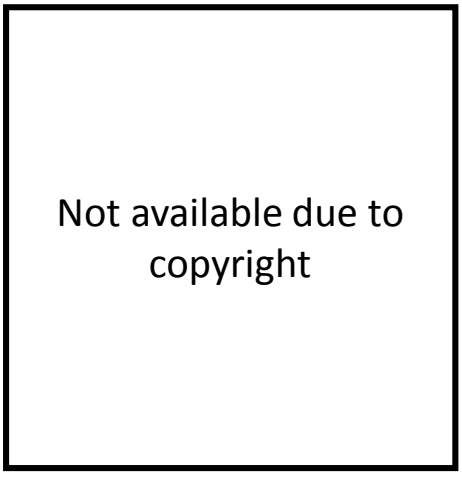


**Figure 1.13** SEM image of cross section of PMOS trigate with SiGe source/drain [24].

### 1.2.3 Energy dissipation and delay in a wiring

In the previous subsection, we introduced the circuit design technologies and the fabrication process technologies proposed to improve the performance of the microprocessor including power consumption. In a LSI, many number of devices are interconnected by high density wiring distributed with a three dimensional crossing. Therefore, the capacity and delay of the wiring have a large influence on the performance because a large number of thin and highly resistant wirings are integrated. Next, we will look at the roll of the wiring in LSIs.

When the MOSFETs are down sized following by the scaling law, the wiring should be also miniaturized to interconnect the scaled MOSFETs. Wiring in LSIs is roughly classified into three categories. (1) Local wiring connecting the logic devices in lowest metal level block with minimum wiring pitch (2) Semi-global wiring routing in metal revels above local wiring with larger cross sectional dimension that the minimum feature size (3) global wiring routing data bus lines or acting as a clock distribution and power supply. In the local wiring, the delay remains constant value as scaling. This is because although the capacitance per unit length and the resistance increase, the wiring length is also scaled. As for the semi-global wiring, the delay also remains nearly constant for the same reason as local wiring. However, the delay in global wiring is not constant as scaling progresses, even if appropriate repeater buffers are inserted. In contrast to the MOSFETs and other wirings, the global wiring has the worse delay. The interconnect distance in global level is depended on not a size of MOSFET but the die size. Figure 1.14 shows schematic of wire structure with indication of feature sizes and circuit parameters expressed with scaling factors. The scaling factor $S$ means the device scaling factor in Dennard scaling. The $S_c$ represents chip scaling factor. The main feature size of wires in LSIs can be described by thickness h, width of $W$, pitch of $d$ and length of $L$. The size of the local wire is scaled by a factor of the device scaling factor $s$ because it is designed to have the minimum pitch in the process node. Therefore, the $RC$ constant remains constant in spite of increased resistance. On the other hands, the length of global wiring is not


**Figure 1.14** Rough estimation of RC constant at local wire and global wire [25].

scaled by the device scaling factor *S*. As a consequence, the resistance and the capacitance of global wiring are $SS_c$ and $S_c$ times larger than that of local wiring. Finally, the *RC* delay constant cannot remain the constant value for global wiring. The wiring capacitance per unit length is given by the aspect ratio and it is not determined by the wire size. Therefore, it is difficult to improve power consumption and delay determined by the capacitance of global wiring by design effort. By inserting a repeater buffer shown in Figure 1.15, the increment of delay for wire length becomes slowing down. The interconnection with length of *L* has an *RC* delay proportional to $L^2$. After dividing the interconnection into number of *N* segment, inverters which called as repeaters are inserted to drive each divided wiring. Each new interconnection have RC delay of $(L/N)^2$. The total delay of *N* number wiring becomes $L^2$/N. If the segment number increases as the interconnect length, the delay finally is linearly proportional to the length of *L*. However, a large amount of repeaters leads to increment in power consumption and waste of chip area occupied by repeaters. Therefore, available repeater number is limited due to the power consumption. The repeater buffer can alleviate the increment of the delay but not a solution for problems happened in long global wiring.

The global wiring has a fewer number than a local and semi-global, but it has a large influence on signal processing. Intel analyzed the interconnect length distribution in a microprocessors designed in 0.13 μm technology [26]. According to Figure 1.16, the local

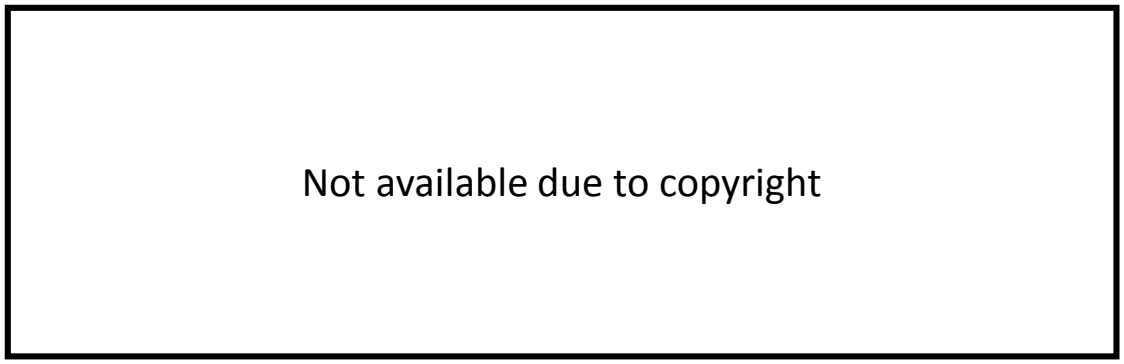


**Figure 1.15** Circuit model of repeated RC interconnection [27].

wiring distribution concentrates around short length region. On the other hand, the global wiring has a distribution over longer length region. It is notable that there exits some distribution in global wiring up to few cm length. These long global wiring cannot be negligible effect in the total power consumption whereas the number is very small. Figure 1.17 shows total dynamic power consumption in microprocessor manufactured by 0.13 μm process divided into local and global wiring portion. We can see the global wiring affect significantly to the total dynamic power consumption in spite of its small number of nets. For the reasons of interconnect scaling characteristics and wiring distribution, unique interconnect methodologies are required to improve the performance especially in long wiring such as global net.


**Figure 1.16** Length distribution of local nets and global nets [26].


**Figure 1.17** Total dynamic power in microprocessor broken into local and global wiring [26].

## 1.3 Novel on-chip interconnection technology

It has been revealed that the performance of the interconnect wiring cannot be improved by the design of the dimension different from that of the MOSFET. In this section, novel interconnection technologies proposed for low delay and energy consumption local and global wiring are described. I categorize these into two groups.

[1] Electrical interconnection

[2] Optical interconnection

In the electrical interconnection, novel wiring material, a differential transmission line and new driving methods have been proposed. On the other hand, optical interconnection is an extraordinary innovative method that replacing the electrical wiring by the optical communication link, and quite different characteristics from the electrical wiring are expected [28].

### 1.3.1 Electrical interconnection

#### Single-walled (SW) or multi-walled (MW) carbon nanotubes (CNT)

Carbon nanotubes (CNT) are a carbon with a cylindrical structure binding by $sp^2$ bonding state first invented in 1991[29]. Figure 1.18 shows a SEM image of CNTs and


**Figure 1.18** SEM image of CNTs (upper). Graphene, SWCNT and MWCNT (lower) [30].

microscopic structures for various carbon-based materials. Multi-wall CNTs have all metallic property. On the other hands, single wall CNT can be either semiconducting (66%) or metallic (33%) depending on the chirality of the tube. Metallic multi-wall and single wall CNTs are expected to be used as new interconnection material because of their superior high mechanical, thermal stability and electrical properties. A metallic CNT has theoretical conductivity of 1 Ωcm. Multi-wall CNT, however, is difficult to achieve ballistic transport over long lengths [31]. Single-wall CNT is preferred to be used as interconnection [30, 32, 33]. The CNT interconnections have a potential for as a local wiring rather than semi-global or global interconnection due to its significant tolerance for high current density. The first CMOS circuits interconnected by multi-wall CNT was demonstrated in 2008 [34].

## Inductive coupling

As a solution for no-chip wiring problems, 3D-stacked chip was proposed, which communicate between the proximity contacting tacked dies. Inductive coupling links are wireless communication method utilizing near-field coupling between on-chip coils. Figure 1.19 shows a photograph and schematic of 3D-stacked chips communicating with inductive-coupling coils. The link distance is intrinsically limited to short region such as between the proximity contacted chips. The data-transmission at 1.1 Gbit/s with energy consumption of 10 fJ/bit was achieved over the 22-μm-distance [35].


**Figure 1.19** 3D-stacked chips each communicate with inductive-coupling links [36].

## Low voltage-swing differential signaling (LVDS)

High-speed and low power interconnection can be expected by transmission line even at long interconnection. However, single ended transmission lines, such as microstrip lines and co-planar lines, require a large ground plane. Therefore these are difficult to use as on-chip wiring. The differential transmission line (DTL) consists of pair transmission line which does not require a ground plane (Figure 1.20). The DTL can be driven by low-voltage differential signaling (LVDS) thanks to the strong tolerance for a common-mode noise. LVDS was originally used for high speed copper cable to connect electronics productions. Energy reduction of on-chip interconnection by this technique is based on the relation between dynamic energy and voltage swing as described in equation (1.1). The amount of charging and discharging of the interconnect capacitance is reduced due to low voltage swing produced by a level converter. As a negative side of low swing, noise immunity of signal is weaken due to reduction of signal voltage. The use of DTL can improve this noise immunity of signal due to its high common mode noise rejection property. As a report for a low-energy operation, a 10 Gbit/s transmission through 5-mm-long DTL was demonstrated with energy consumption per bit of 270 fJ/bit [37].


**Figure 1.20** Differential transmission line and driver/receiver circuit [38].

## Current-mode logic (CML)

The current-mode logic (CML) circuits consists of CML driver and current sensing circuits. This circuit configuration takes a reduced RC time constant, thus has an

advantage for high-speed operation. However, typical CML driver circuits requires continuous current flowing which results in large static power consumption. For on-chip interconnection, CML showed worse energy efficiency than that of voltage-mode circuits. By adopting significantly small voltage swing of 60 mV, a 3 Gbit/s signal transmission with energy consumption of 95 fJ/bit was demonstrated for an interconnect length of 10 mm [39].


**Figure 1.21** Current-mode-logic driver circuit [39].

## Capacitively driven interconnect

In capacitive driving scheme, a long interconnection of capacitance is driven through in-line coupling capacitor. Figure 1.22 shows comparisons of wire driving schemes. Differing


**Figure 1.22** Schematic comparisons of (a) conventional scheme; (b) current-mode logic scheme; (c) capacitive transmitter scheme [40].

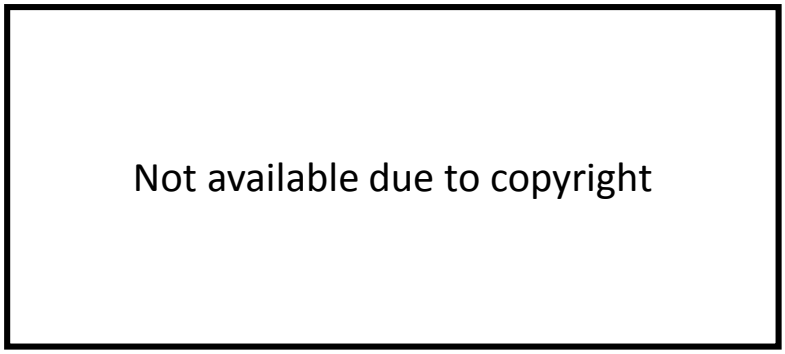


**Figure 1.23** Schematic of coupling capacitor with pitch-folk structure [41].

from conventional and current mode logic scheme, the capacitive transmitter drives only the load of coupling capacitor. The coupling capacitor as shown in Figure 1.23 is design to have lower capacitance than total capacitance of wiring. The driver circuit sees the coupling capacitor as a load, thus low-voltage and low-energy signaling is achieved. Typically long wires show low-pass frequency response due to its RC components. The coupling capacitor acts as a short in high frequency region and enhance the high frequency response. Therefore, the 3dB-bandwidth of wire is increased by pre-emphasis effect of the capacitance. A 2 Gbit/s signal transmission with energy consumption of 28 fJ/bit/mm was reported for 1-cm-long capacitively driven wire fabricated in 90 nm CMOS process [40]. As for report utilizing 28 nm CMOS process, a 10 Gbit/s signal transmission with energy consumption of 19.4 fJ/bit/mm was demonstrated for 7-mm-long wire [42].

Figure 1.24 shows comparisons of energy consumption per bit for 4-mm-long wire as a function of operating frequency. A conventional full-swing interconnection (FSI) is capable of most high speed operation, but the energy consumption is also high. Multi-supply interconnection (MSI) which is equal to LVDS method outperforms the FSI in the view point of energy consumption. Since the wiring number of this is twice, the maximum frequency is degraded by the available cross sectional area. The CDI can simultaneously achieve the low energy consumption and high speed operation thanks to pre-emphasis effect of the capacitance.


**Figure 1.24** Energy consumption per bit as a function of operating frequency for different interconnect architectures over a distance of 4 mm where FSI is full-swing interconnection, MSI is multi-supply interconnection including LVDS and CDI is capacitively driven interconnect [43].

Finally, Table 1.2 summarizes the performance comparison of the electrical on-chip wiring explained in this section.

**Table 1.2** Performance comparison of the electrical on-chip wiring.

| | **Inductive-coupling** | **LVDS** | **CML** | **CD** |
|---|---|---|---|---|
| Distance | 0.022 mm | 5 mm | 10 mm | 7 mm |
| Energy | 10 fJ/bit | 270 fJ/bit (54 fJ/bit/mm) | 95 fJ/bit (9.5 fJ/bit/mm) | 136 fJ/bit (19.4 fJ/bit/mm) |
| Data-rate | 1.1 Gbit/s | 10 Gbit/s | 3 Gbit/s | 10 Gbit/s |
| Ref. | [35] | [37] | [39] | [42] |

### 1.3.2 Optical interconnection

The introduction of optical communication into intra-chip interconnection is getting much attention as an alternative technology for the conventional electrical interconnection. As in fiber optic communications, the basic components of on-chip optical interconnection light sources or modulators, passive waveguides, and detectors. The arrangement of light source position significantly varies the configuration of optical interconnection. There are two approaches to implement on-chip optical links. Optical links using on-chip light sources or an external light sources with on-chip modulators will be explained.

#### Off-chip laser optical interconnection

One of the promising candidates for on-chip optical interconnection is Si based photonic integrated circuits so called “silicon photonics”. Si waveguides are fabricated with the dimension of 400 nm-wide and 220 nm-thick core in a typical design. This very small size waveguide is made possible by the large refractive index difference between the Si core and $SiO_2$ or air cladding layer. The application of silicon for integrated optical circuit has been first demonstrated by R. Soref in 1986 [44]. Along with the invention of silicon-on-insulator substrate, the research field in silicon photonics explosively grown since early 2000’s. The technological maturity of silicon-based optical devices soon get to a practical level. Various optical components based on silicon to construct many functional integrated circuits were demonstrated such as wire waveguides [45-48], high-speed electro-optical modulators [49], and Ge photodetectors [50, 51]. The biggest challenge in silicon photonics is the realization of on-silicon light sources because silicon has an indirect transition type band diagram. Although there are reports on silicon based lasers [52, 53], the use of laser based on III-V materials is practical to signaling in silicon photonics circuits.

Based on a silicon photonics technology, on-chip optical links have been demonstrated with an external laser and ring modulators [54-58]. Figure 1.25 shows an integrated optical link fabricated on silicon photonics platform [54]. This optical link utilized the ring

modulator with only 12 μm diameter. The total energy cost of the link for 3 Gbit/s transmission was 120 fJ/bit which including energy of tuning bias current for ring but excluding external laser. The energy consumption of the modulator itself was estimated to be 86 fJ/bit. Afterword this report, higher performance optical links using this device configuration are reported [55]. Recently, electric and photonic convergence circuits using silicon photonics


**Figure 1.25** Integrated silicon photonics optical link consists of electro-optical ring modulator, waveguide and germanium MSM detector [54].


**Figure 1.26** Microprocessor using optical link for communication.[58]

optical link as a wiring were demonstrated and successful signal transmission was achieved [57, 58]. The first microprocessor that communicate using optical wring is shown in Figure 1.26. Although silicon ring modulators can operate at high-speed and with low-energy consumption in principle, they require heater tuning to change their operation wavelength match to that of the external laser [58], because the operation wavelength of the ring modulator is easily affected by temperature changes and fabrication tolerances. Even though the energy consumption of the ring modulator is itself very small due to small capacitance (several fJ/bit [59]), that of micro-heaters is much higher than that, and has been reported to be as high as 192 fJ/bit [58]. As an example for using other type external modulators, an optical link implemented on a III-V/silicon-on-insulator (III-V/SOI) platform using an electro-absorption modulator achieved high-speed operation with a 3-dB bandwidth of 13 GHz [60].

## On-chip laser optical interconnection

The use of on-chip light source is reasonable idea because no alignment between an external light and a coupler on a chip is required. By employing a directly modulated on-


**Figure 1.27** Optical microscope image and cross section of the microdisk laser-based optical link [61].

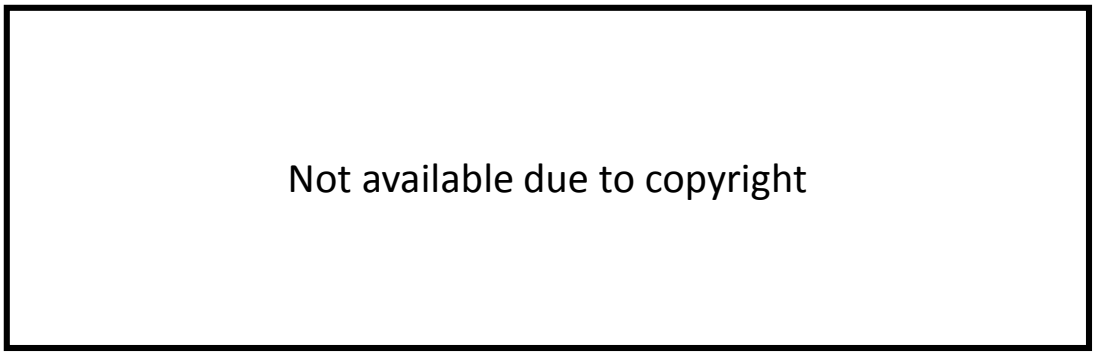


**Figure 1.28** Schematics of III-V/SOI optical link with ring laser and photodiode [62].

chip light source, a reduction of the laser current results in a reduction in the total consumed link energy. A key challenge concerning on-chip light source is to obtain ultra-low energy consumption semiconductor lasers [63]. The design and cavity type of the laser strongly have an impact on the performance of an optical link. The integrated optical links using microdisk laser fabricated on III-V/SOI platform are demonstrated (Figure 1.27) [61, 64]. The microdisk laser is evanescently coupled to a bus silicon waveguide. The in-line waveguide type photodiode is also coupled to the same bus silicon and detects the transmitted optical signal from the laser. The microdisk laser showed threshold current of 0.45 mA which indicate potential for low energy consumption operation. The maximum 3dB bandwidth of the full-optical link was 7.6 GHz at a laser bias current of 3.4 mA and a photodiode bias voltage of -1 V. Although the bandwidth was sufficient for high speed transmission, the waveform of 10 Gbit/s large signal transmitted through the link was noisy and distorted due to the low optical power or reflection problem. An optical link using GaAs-based ring laser on III-V/SOI platform is reported (Figure 1.28) [62]. The ring laser has a diameter of 80 μm and evanescently coupled to a silicon waveguide as also previously explained one. The integrated photodiode is made from GaInAs/GaAs MQWs. As a high speed performance, 12.5 Gbit/s large signal was transmitted through the optical link and clear eye opening was obtained. To achieve low energy operation, the threshold current of 10 mA and the bias current for modulation should be reduced. Even though these two optical links on III-V/SOI platform are capable of low-threshold and high-speeds, the evanescent coupling between the laser and the passive silicon waveguide

prevents an efficient light coupling. As a notable example of the optical link using ultra-low threshold laser, photonic crystal-based optical link in monolithically integrated in an InP showed impressive performance. The photonic crystal lasers exhibited 4.8-μA threshold operation [65], and optical links using photonic crystal waveguides and p-i-n photodiodes (PDs) have been demonstrated [66, 67]. Figure 1.29 shows SEM images of the photonic crystal devices and an optical microscope image of the overall picture of photonic crystal-based optical link. The ultra-low energy of 28.5 fJ/bit signal transmission was reported for data rate of 4 Gbit/s. The transmitted signal of this optical link structure (laser and PD integration) was not evaluated in terms of bit-error-rate characteristics, because of the small output power of the photonic crystal laser resulting in noisy transmitted waveform. This is because not only low output power of photonic crystal laser and also difficulty in extracting the output power from photonic crystal cavity.

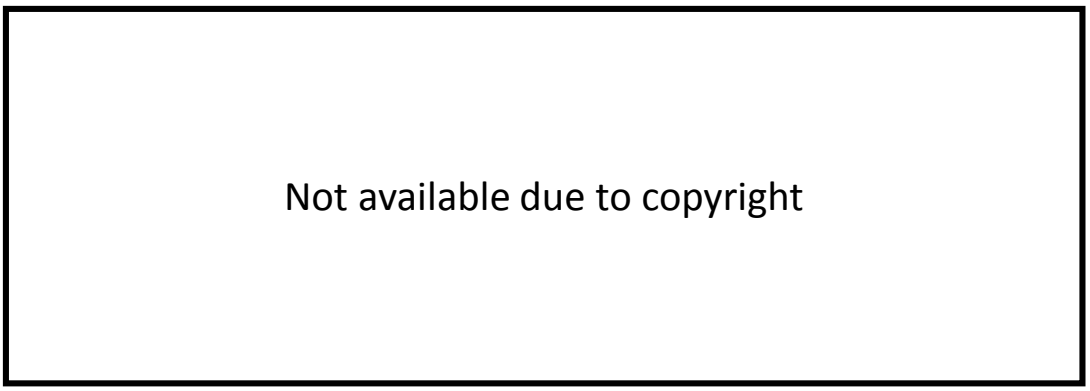


**Figure 1.29** SEM images of the laser and photodiode. Optical microscope image of the photonic crystal-based optical link [66].

### 1.3.3 Comparison between optical and electrical interconnection

As mentioned above, we have seen the approaches based-on the electrical wire and the optical link. However, because the wirings constructed by both approaches have significantly different characteristics, it is necessary and valuable to investigate the applicable areas that each wiring can take advantage of its characteristics. In this sub section, by investigating the performance of electrical wiring and optical wiring from the viewpoint of delay and energy consumption, we will state the application area of on-chip optical interconnection which is the final target of this thesis.

A comparison of optical wiring and some electrical wiring was done by K. C. Saraswat et al. in Stanford University [68]. They assumed copper wiring in 22-nm technology,


**Figure 1.30** Comparison of latency for Cu, CNT, optical interconnect in 22-nm technology node. $l_0$ represents mean free path, $C_{det}$ represents the detector capacitance [68].


Figure 1.31 Comparison of energy consumption per bit for Cu, CNT, optical interconnect in 22-

nm technology node [68]. SWCNT bundle with packing density (PD) 33% and optical interconnects consists of III-V MQWs modulator, silicon waveguides, a Ge detector and an external laser. As for the optical interconnection, the optical devices are driven by a CMOS circuit and a transimpedance-amplifier (TIA). The delay occurs when driving the capacitance of the CMOS gate and the modulator. Energy consumption is the sum of the modulator and receiver. Here, off-chip laser is assumed, however the fundamental conclusion to be derived later can be applicable for the optical interconnect using directly modulated on-chip laser. Figure 1.30 shows comparison of latency for different wiring schemes as a function of wiring length. The plots for CNTs are showed the case where the mean free paths $l_0$ are 0.9 μm and 2.8 μm. The plots for optical interconnects are showed for the case where the detector capacitances $C_{det}$ are 10 fF and 50 fF. In Cu and CNTs, the delay increases linearly due to the insertion of repeater buffer. The reason for CNTs have smaller delay than that of Cu is effect of low resistivity of CNT. The delay in optical interconnection during the propagation is approximately 10 ps/mm assuming that the equivalent refractive index in the waveguide is 3. That is why the delays in modulator

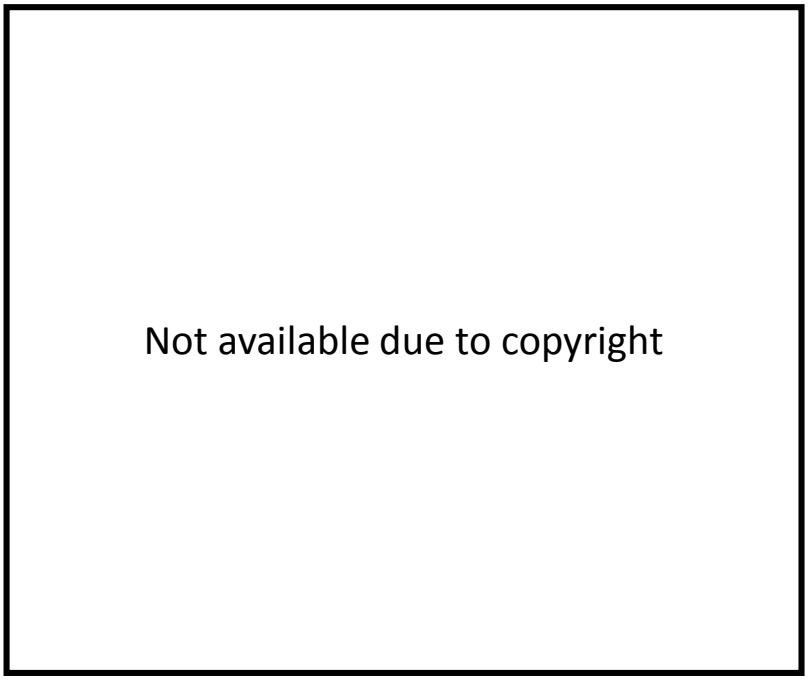


**Figure 1.32** Energy per bit versus bandwidth of wire with fixed wiring length of 10 mm for various interconnect schemes for the 22-nm technology. [68].

and receiver are dominant for optical interconnection. The optical interconnects outperform the other electrical wiring over a wide wiring length. Especially in wiring length more than several mm, the optical interconnects which have negligible delay depending on wiring length are exhibited the best performance. Figure 1.31 shows comparison of energy consumption per bit for different wiring schemes as a function of wiring length. Because the reduction in wiring resistance of CNTs does not affect the capacitance, the energy consumption of CNTs wiring is almost the same as copper wiring. While the copper and CNT consume the dynamic switching energy proportional to $CV^2$ as shown in equation (1.1), the optical interconnect consume the static energy consumption at the transceiver which amount is independent of wiring length. Moreover, the smaller detector capacitance leads to the lower energy consumption. According to these facts, in the global wiring region having a length of several mm or cm, the optical wiring exceed the electrical wiring in terms of delay and energy consumption.

Figure 1.32 shows energy per bit as a function of bandwidth of wire characteristics with fixed wiring length of 10 mm for capacitively driven CNT and copper wires with repeaters, conventional CNT and copper wires and optical interconnect with detector capacitance $C_{\mathrm{det}}$ of 10 fF. The width of electrical wire was assumed to be four times the minimum wire half pitch. Capacitively driven wiring exhibits the lowest energy consumption up to operation speed of 5 Gbit/s. At above the 5Gbit/s, the energy rapidly increase as the wire bandwidth. This is because of performance limitation of the transceiver circuits for capacitive driving. In the case of optical interconnection, very low energy consumption of approximately 100 fJ/bit can be obtained even at high speed operation exceeding 10 Gbit/s and outperform the other wirings except for low operating speed below 5 Gbit/s. Even if directly modulated on-chip laser is used, this energy consumption is possible with an ultra-low energy consumption laser.

When operating speed and wiring length are chosen as a parameter, the electrical and optical wiring shows significantly different performance. From the discussion in this subsection, the most promising application field of optical interconnection as an on-chip wiring is considered to as follows;

---

1) **Semi-global and global wiring having several mm length**
2) **High speed bus lines operating more than Gbit/s speed**

---

In the next section, we describe the requirements for optical devices to realize such low power consumption optical interconnection.

## 1.4 Performance requirements for on-chip optical interconnection

As mentioned in the previous section, ultra-low energy consumption, high speed and high efficiency laser is a key component for the efficient on-chip optical interconnection surpassing the electrical wiring. For low energy operation, semiconductor lasers are posed to significantly different performance compared with lasers for fiber optic communication. In order to get an insight for low energy consumption laser, the relations ruling the fundamental laser characteristics such as the threshold current and efficiency will be explained. Subsequently, the semiconductor lasers used in current fiber optic communication systems are to be reviewed. By referring to the laser performance trends in commercial optical systems, the requirement for the laser in an on-chip optical interconnection will be mentioned.

The rate equations account for particle numbers of carries and photon in a cavity. Based on analysis on the rate equation, a simple expression for the threshold current of semiconductor laser can be derived as follows; [69]

$$I_{th} = \frac{eV_a N_{th}}{\tau_s} \tag{1.3}$$

$$= \frac{eV_a B_{eff}}{\eta_i}\left( N_g + \frac{1}{\xi \frac{dg}{dN}}(\alpha_{WG} + \alpha_m) \right)^2 \tag{1.4}$$

where, $I_{\mathrm{th}}$ is the threshold current, $e$ is the electron charge, $V_{\mathrm{a}}$ is the active medium volume, $N_{\mathrm{th}}$ is the threshold carrier density, $\tau_{\mathrm{s}}$ is the carrier lifetime, $B_{eff}$ is the effective recombination coefficient, $N_{\mathrm{g}}$ is the transparent carrier density, $\eta_{\mathrm{i}}$ is the internal quantum efficiency, $\xi$ is the optical confiment factor to the active layer, d$g$/d$N$ is the differential gain, $\alpha_{\mathrm{WG}}$ is the waveguide loss and $\alpha_{\mathrm{m}}$ is the mirror loss. The most important point to achieve the low threshold current of the semiconductor laser is to reduce the active layer volume $V_{\mathrm{a}}$ that can take a wide range of values by cavity design. Reduction of mirror loss $\alpha_{\mathrm{m}}$ can also reduce the threshold current, however it is closely related to an external

differential quantum efficiency $\eta_d$ as expressed by the following equation

$$\eta_d = \eta_i \frac{\alpha_m}{\alpha_m + \alpha_{WG}} \tag{1.5}$$

If the mirror loss is decreased and the optical power is strongly confined in the resonator, the light in a cavity becomes difficult to emit and result in low external differential quantum efficiency. Therefore, even if the threshold current is decreased small mirror loss, the required power to obtain certain optical output power will increase. For this reason, it is essential to design a mirror loss considering the tradeoff between a low threshold current and external differential quantum efficiency. In addition to the design consideration about static characteristics, the design of the laser in terms of modulation characteristics is also important. The threshold current density determines the carrier lifetime in the active layer and affects the relaxation oscillation frequency and the rise and fall time under large signal modulation. The origin of high speed capability of the semiconductor laser on the GHz order is rapid carrier recombination induced by stimulated emission. The resonance frequency of stimulated emission and carrier recombination is called the relaxation oscillation frequency and is an important feature of the modulation bandwidth of the semiconductor laser. The relaxation oscillation frequency $f_r$ is expressed as following equation;

$$f_r = \frac{1}{2\pi} \sqrt{\frac{\xi \frac{dg}{dN} v_g \eta_i}{eV_a}} \sqrt{I_b - I_{th}} \tag{1.6}$$

where, $v_g$ is the group velocity, and $I_b$ is the bias current. We can find that the small active volume and the strong optical confinement factor can enhance the relaxation oscillation frequency at same bias current density condition. It should be noted, however, the maximum output power of the semiconductor laser is determined by heat generation and Auger recombination. Since the small active layer volume results in high current density at low total injection current, the increment of Auger recombination occurs with small bias current and limit the maximum output power. Consequently, using too small active layer volume sacrifices the maximum light output power. The designs for cavity and

waveguide structure can control the many aspects of laser characteristics. In next subsection, I will explain what type of laser is developed and implemented in fiber optic commutation systems.

### 1.4.1 Optical devices in fiber optics communication

The first room-temperature continuous wave operation of the semiconductor laser was achieved in 1970 [70, 71]. The device consisted of GaAs/AlGaAs double hetero structure with the lasing wavelength of 0.8 μm. At the same time, studies of the reduction of propagation loss of the optical fiber started because the milestone of propagation loss of 20 dB/km at wavelength of 0.63 μm reported by Kapron *et al*. from Corning Inc.[72]. In the late 1970s, the studies for lasers emitting over 1 μm was started, which was stimulated by the prediction that the lowest propagation loss should be obtained at a longer wavelength [73]. As the prediction, the significant loss reduction for propagation losses of 0.47 dB/km [74] and 0.2 dB/km [75] were achieved at wavelengths of 1.3 μm and 1.55 μm, respectively. GaInAsP/InP semiconductor lasers which operate at a wavelength of 1.3 μm [76, 77] or 1.55 μm [78, 79] were realized in the end of 1970s. Not only the realization of long wavelengths semiconductor lasers, numerous key technologies have been developed during the decades, such as distributed-feedback (DFB) lasers[80-82], Vertical cavity surface emitting lasers(VCSELs)[83-85], quantum well (QW) lasers[86], strained quantum well[87-90], AlGaInAs/InP system[91, 92], Bragg wavelength detuning[93] and modulation doping[94, 95].

Today's actually implemented direct modulation laser performance in a fiber communication will be explained. In current communication systems, digital coherent optical transmission system using high-order phase modulation are used for transpacific. And on-off keying (OOK)-transmission system using electro-absorption modulator integrated DFB laser are used for core and metro network. Directly modulated laser has large wavelength chirping under modulation, and waveform distortion is large in long distance propagation due to wavelength dispersion. Therefore, the main application is

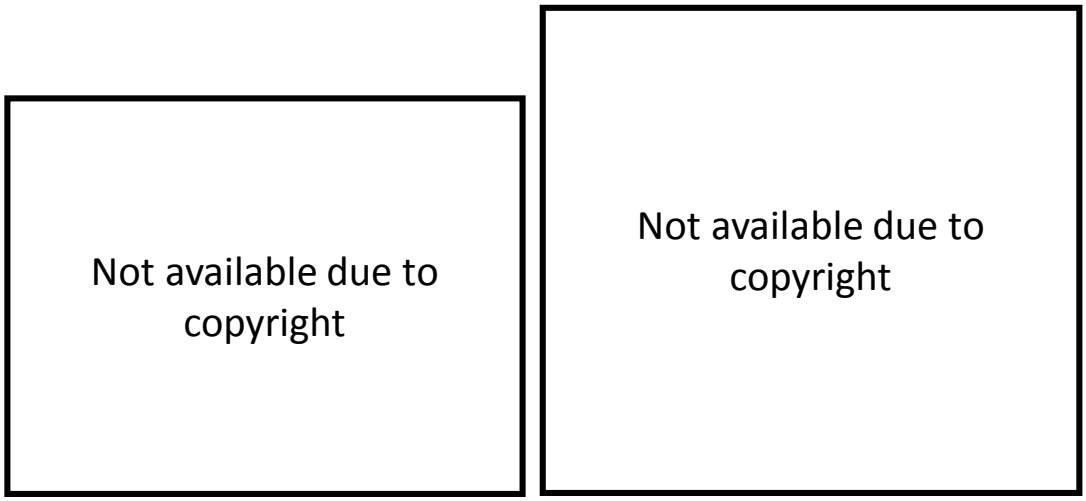


**Figure 1.33** Ridge waveguide 1.3 μm AlGaInAs-MQW DFB laser [96].


**Figure 1.34** 120°C 25.8Gbit/s operation of 1.3 μm AlGaInAs MQW DFB laser[97].

short reach communication in metro or datacom. For the application of 100-giabit Ethernet (100GbE), many DFB lasers operating at 25.8–28 Gbit/s have been reported. Figure 1.33 shows an AlGaInAs-based MQW DFB laser with a ridge waveguide structure [96]. The threshold current at 25°C is 8.4 mA. 25.8 Gbit/s direct modulation is obtained for 25°C and 85°C environments with a bias current of 37 mA and 56 mA, respectively. Recently, 25.8 G/bit operation under temperature of 120°C is obtained with a bias current of 70 mA, and shows good transmission characteristics (Figure 1.34) [97]. For the 400GbE

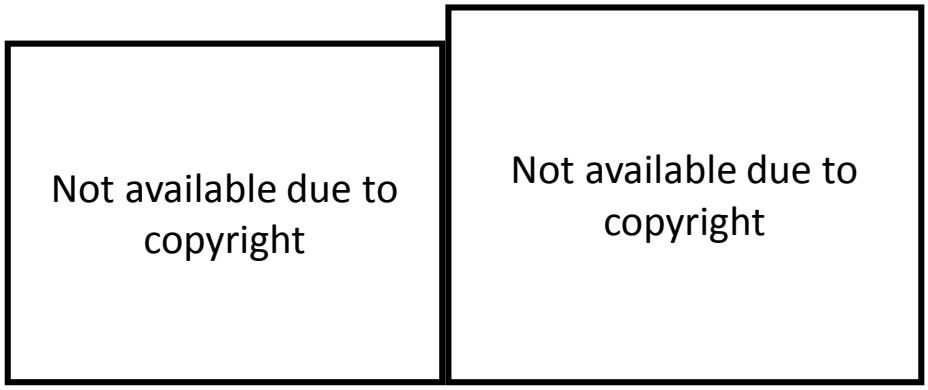


**Figure 1.35** Ridge waveguide MQW DFB laser operating 50 Gbit/s [98].


**Figure 1.36** Schematic image and light output characteristics of double intra cavity 1060 nm VCSEL [99].

consists of 50 Gbit/s ×8λ, 50 Gbit/s direct modulation of DFB lasers are reported. Figure 1.35 shows the structure of the ridge waveguide 1.3 μm AlGaInAs MQW DFB laser

operated at 50 Gbit/s reported by NTT [98]。 The threshold currents for the device with cavity length of 100, 150 and 200 μm were 6.2, 6.6 and 7.8 mA, respectively. By adopting short cavity length of 100 μm, 50 Gbit/s transmission is obtained over 20, 40 and 60 km single mode fiber using bias current of 60 mA at 25°C. In recent year, VCSELs have received an attention as a low cost and low power consumption light source inside the supercomputers and data centers. The strong cavity confiment by a pair of DBR enable the VCSELs to operate at low threshold current lower than 1 mA. Since VCSELs require small current swing to direct modulation, a low cost SiGe drivers using BiCMOS process can be available [100, 101]. There are many reports on a direct modulation of VCSELs with energy consumption. The Furukawa Electric. demonstrated low power dissipation 1060 nm VCSEL with double intra cavity structure [99]. The double intra cavity contact avoid the current path through the DBR region which has high resistivity. The threshold current was 0.4 mA. 10.3125 Gbit/s operation was achieved with energy consumption of 180 fJ/bit. Finisar corp. developed VCSEL based interconnects for data-centers [102]. The VCSEL has emission diameter of 7 μm. the threshold current was 0.65 mA at 25°C. As a transceiver characteristics, 28 Gbit/s transmission was demonstrated

**Table 1.3** Comparison of the energy consumption of the directly modulated lasers at 25**°C**.

| **Laser type** | **Threshold current [mA]** | **Data rate [ Gb/s ]** | **Energy cost [ fJ/bit ]** | **application** | **Ref.** |
|---|---|---|---|---|---|
| DFB | 8.4 | 25.8 | 1700 | Core and metro | [96] |
| DFB | 7 | 25.8 | 1860 | Core and metro | [97] |
| DFB | 6.2 | 50 | 1440 | Core and metro | [98] |
| VCSEL | 0.4 | 10 | 180 | Data-center | [99] |
| VCSEL | 0.65 | 28 | 590 | Data-center | [103] |

with energy consumption of approximately 590 fJ/bit. This energy was calculated using operating current and voltage given in the paper.

Table 1.3 summarizes the energy consumption of the directly modulated lasers. DFB lasers, which for a core and metro network application with communication distance up to 40 km, have threshold current of several mA range. And the values of energy consumption are more than 1000 fJ/bit. This is because a few 10 mW optical output power is required to DFB laser and relatively large active volume is used. In contrast, VCSELs for data-center exhibited threshold current of below 1 mA. Typical energy consumption was the order of 100 fJ/bit. However, even for state-of-the-are VCSEL, the maximum optical output power is several mW. Generally, lasers with low energy consumption operating and a low threshold is required for a shorter communication distance even at the expense of output power. Now, we consider what performance is required for on-chip optical interconnection that communicates in cm distance.

### 1.4.2 Devices for on-chip optical interconnection

As we can see from the energy consumption of the lasers in a fiber optics communication, significantly lower energy consumption is required as the communication distance becomes shorter. It can be imagine that smaller energy consumption is required for on-chip optical interconnection. The International Technology Roadmap for Semiconductors (ITRS) roadmap 2007 has said that the power dissipation in chips was saturated at around 200 W, and a large portion of the power is consumed at the interconnects and the repeater amplifiers. Therefore, the requirement for lower energy consumption of interconnect is also consistent from the viewpoint of electric circuits. In order to introduce on-chip optical interconnection into LSI, it is necessary to exceed the performance with electrical wiring as for energy consumption and delay. The semiconductor lasers used as light source is required to operate ultra-low power consumption and high efficiency .The roadmap of optical devices for the on-chip optical interconnection was wrote down by D. A. B. Miller at Stanford University in 2009 [63].

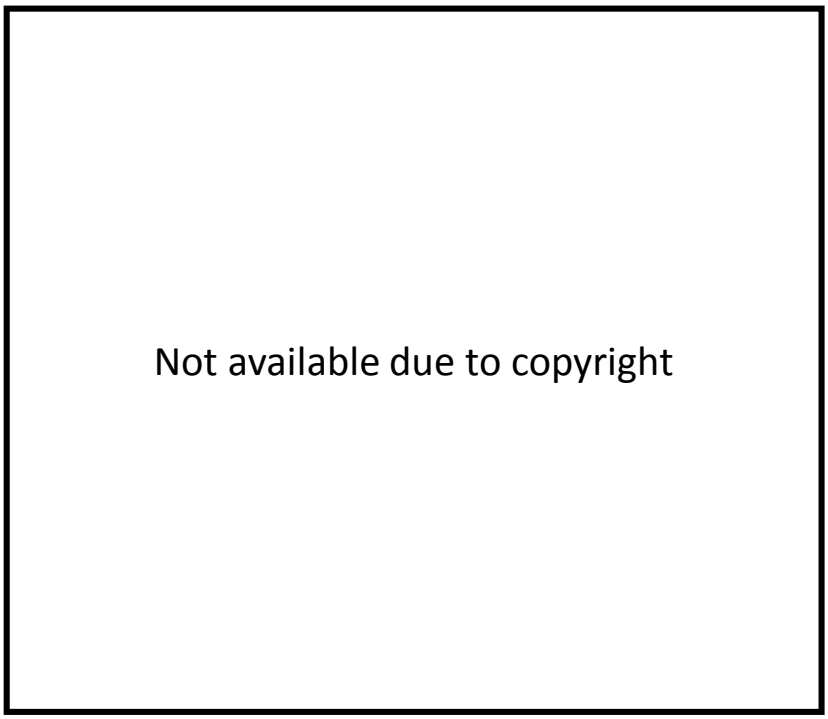


**Figure 1.37** The trend of available energies per bit for off-chip system, off-chip devices and on-chip devices [63].

This roadmap is based on the technology node parameters, on-chip and off-chip clock frequencies and signal I/O pins of the ITRS 2007. Figure 1.37 shows the trend and prediction of the available energy consumption per bit for the off-chip and on-chip interconnection. It was assumed that 20% of the total chip power including the interconnection including clock distribution and logic circuits was allocated for the off-

**Table 1.4** Light output power requirement for on-chip optical interconnection.

| | | |
|---|---|---|
| Requirement from the roadmap | Minimum received power | 0.05 mW (-13dBm) |
| Our assumption | Coupling loss between LD and waveguide | -1.5dB |
| | Propagation loss for 2 cm-long waveguide | -2dB (-1dB/cm) |
| | Coupling loss between LD and waveguide | -1.5dB |
| **Calculated value** | **Required light output power of LD** | **0.16 mW (-8dBm)** |

**Table 1.5** An example of the performance of the laser for on-chip interconnection.

| | |
|---|---|
| Output power | 0.16 mW |
| Bias current | 1 mA |
| Operating voltage | 1 V |
| 3dB bandwidth | 7.7 GHz |
| Threshold current | 0.1 mA< |
| External differential quantum efficiency | 23%> |
| Differential resistance | 200 Ω< |

chip interconnection. Additionally, 20% of the energy of the off-chip interconnection was allocated for that of the on-chip interconnection. In other words, the middle line for off-chip also shows not only the energy of the off-chip devices but also including the on-chip system energy. Therefore, the total chip energy should be less than 100 fJ/bit from 2015 onward. For the on-chip devices, the energy is expected to be less than 10 fJ/bit by 2020. This prediction says that the available energy cost of the one directly modulated laser must be less than at least 100 fJ/bit. Recently, demand for over 10 Gbit/s high-speed bus line between the cores rise due to the trend of multi-core processor. Therefore, although the data-rate of 10 Gbit/s is chosen as target operating speed, higher speed such as 20 Gbit/s is also feasible. To fulfill above energy requirement, the laser should operate at 10 Gbit/s with bias current and voltage of 1 mA and 1 V, respectively. Here, consider a system including a laser, an optical waveguide, and a photodetector. Assuming the detector sensitivity, coupling efficiency, and a waveguide loss as shown in Table 1.4, the output power required for the laser is estimated. First, the minimum average received power at which the bit error rate of less than $10^{-9}$ for the 10 Gbit/s signals is of the photodiode is set to -13 dBm (0.05 mW). This corresponds to the case where a signal with SNR of 28dB is received by a system with a bandwidth of 5 GHz for 10 Gbit/s and an impedance of 50 Ω and is amplified by an amplifier having noise figure of 6dB. The total link loss is assumed to be 5 dB, including the coupling loss between the waveguide and the active devices (1.5 dB×2) and the propagation loss in the waveguide over a length of 2 cm (2 dB). As a results, the required optical output power is estimated to be -8 dBm (0.16 mW) for 10 Gbit/s data-transmission. A 3dB bandwidth of 7.7GHz is needed for 10 Gbit/s operation because the achievable bit-rate for the non-return-to-zero (NRZ) signals is 1.3 times higher than the $f_{3dB}$ in a directly modulated laser [104]. Table 1.5 shows an example of the laser performance which satisfies the requirement for application of on-chip optical interconnection. Most remarkable point is that the threshold current significantly lower than 1 mA is required. Not only low threshold current but also external differential quantum efficiency higher than 23% is necessary for this case. Aforementioned directly modulated lasers used in fiber communications have threshold current of several mA for

a DFB laser and 0.5 mA–1mA for VCSELs. In the next section, we consider what kind of lasers is suitable to achieve the performance requirement for on-chip optical interconnection.

## 1.5 Semiconductor lasers for optical interconnection

### 1.5.1 Types of semiconductor laser cavity

For the on-chip application, the semiconductor lasers are posed to strict low-energy consumption requirement. From the first operation of semiconductor laser at room-temperature, there are a number of reports for the lasers which have various cavity structure. The performances and characteristics of the lasers strongly depend on the structure of their cavities. Some representative cavity structure that can operate low-threshold below 1mA regime will be introduced in this section.

#### Vertical cavity surface emitting lasers (VCSELs)

VCSELs have a laser cavity structure consists of an active layer sandwiched by upper and bottom high reflectivity mirrors. In contrast to conventional edge-emitting lasers, VCSEL's light output emit from top or bottom surface. The first concept was proposed by Iga at Tokyo Institute of Technology in 1977 shown in Figure 1.38. Under liquid nitrogen temperature (77K), the first VCSEL using GaInAsP/InP material system was operated at threshold current of 0.9 A with pulsed driving current in 1979 [83]. The first RT-CW operation of VCSEL was achieved by using 0.89 μm wavelength AlGaAs/GaAs system in 1988 [84]. In order to increase the reflectivity of mirrors, a bottom Au/$SiO_2$/$TiO_2$/ $SiO_2$ mirror and a top $SiO_2$/$TiO_2$ multilayer DBR were used. The threshold current of 32 mA and single-mode operation was achieved. After that, significant reduction of threshold current was accomplished by oxidize current and optical confiment structure[105], multi-oxidized DBR structure [106]and buried-hetero structure[107]. The VCSEL specialized to attain a low-threshold current showed a record threshold current of 8.7 μA among the VCSELs[108].

In recent years, the low-power consumption and surface emitting characteristics which enables wafer scale testing for low-cost of VCSEL get much attention for short reach optical communication such as in data-centers and supercomputers. A low energy


**Figure 1.38** Sketch of first concept of VCSEL [109].

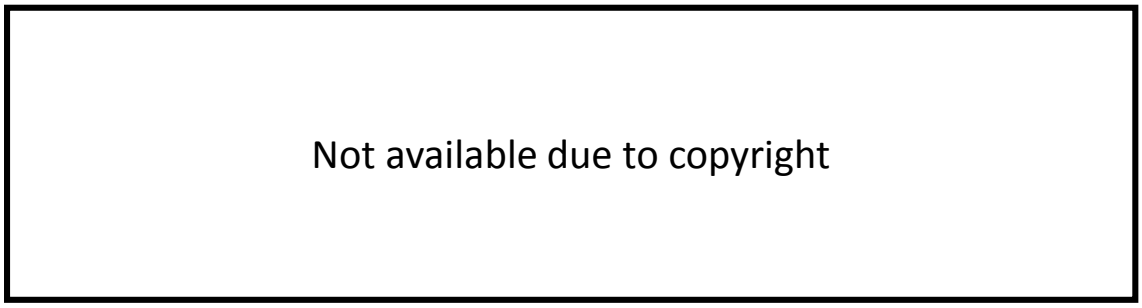


**Figure 1.39 C**ross-sectional view of VCSEL-based optical interconnects using the polymer vertical splitter on a silicon substrate [110].

cost operation less than 100 fJ/bit was demonstrated 81 fJ/bit in 2011 [111] and 56 fJ/bit in 2012 [112] by P. Moser at TU Berlin. However, VCSEL structure is suitable only for vertical fiber coupling (rather than horizontal integration) and requires a 45° total reflection mirror (Figure 1.39) to make an in-plane optical link [110, 113, 114].

## Micro-disk lasers

Microdisk lasers are based on whispering gallery modes around the edge of a thin semiconductor disk. First optically pumped lasing operation at was reported by Bell lab. in 1992[115]. A thin GaInAsP/InP disk with 3–10 μm diameter was suspended by an InP


**Figure 1.40** Micrisdisk laser integrated in silicon photonics platform. Light output characteristics.[33, 116]

pedestal. A threshold power of 100 μW and 1.55 μm-band lasing wavelength were obtained. Electrically pumped whispering gallery mode microdisk lasers were realized in a same year [117]. The threshold current of 0.95 mA and single mode lasing were obtained by injection current pulse with 0.3 μs width and duty ratio of 300:1 at room temperature. Low threshold current continuous operation with 40 μA threshold was achieved in 2000 [118]. A symmetric pedestal mesa structure fabricated by $Cl_2$/Xe inductively-coupled-plasma (ICP) etching remarkably reduced the threshold current. However, it is difficult for microdisk lasers to out couple the light to an output waveguide to the disk structure cavity. Vertically coupled microdisk laser and bus waveguide was reported in 2003 [119]. InP based microdisk lasers on a silicon-on-insulator (SOI) output waveguide was reported [116]. Although both low-threshold current operation at 0.5 mA and integration of an

output waveguide were obtained, the continuous output power of the laser was below 10 μW which was not enough for on-chip optical communication.

## Plasmon, metallic cavity laser

To overcome conventional dielectric confinement cavity with a dimension on the micrometer scale, the use of metallic cladding cavity[120] is an effective method. As the cavity size becomes wavelength scale, optical confinement to the conventional cavity becomes difficult. The metallic cavity provides sub-wavelength scale optical confinement. However, overcoming the losses inherent to metals remains a fundamental challenge in the application for the laser cavity. Remarkable progress of the metal cladding laser is boosted by proposals of spacers [121] and core-shell structure [122]. First continuous electrical injection operation of the metallic cavity laser at 77K was demonstrated in 2007[123]. The device had the pillar structure with a diameter of 260 nm, a height of 300 nm as shown in Figure 1.41. The obtained threshold current of 6 μA at 77K proved the low-threshold capability of metallic cavity laser. After this report, several reports on electrically pumped CW operation was emerged such as pedestal pillar structure with

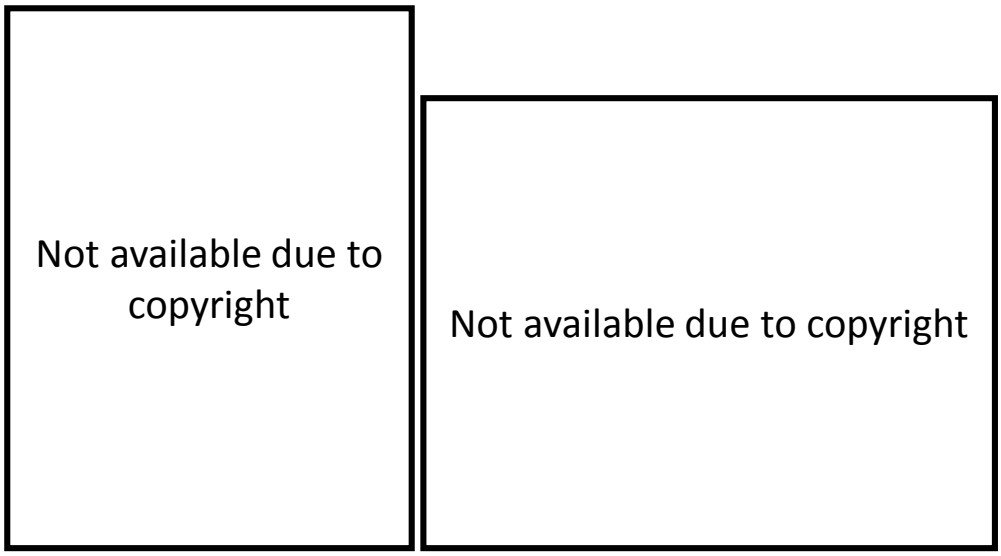


**Figure 1.41** Structure of the cavity formed by a semiconductor pillar encapsulated in gold. [123].

threshold current of 50 μA at 77K [124], rectangular pillar structure with threshold current of 620 μA at 260K.[125]. Room-temperature CW operation of metallic cavity laser was realized in 2012 [126]. The device consist of rectangular semiconductor pillar encapsulated in silver. The threshold current is estimated to be 1000 μA obtained from a linewidth of the spectrum. The record performance at RT-CW condition was reported from the same group in 2013 [127] as shown in Figure 1.42. The Light current characteristics shows a clear threshold around 1100 μA. The spectrum linewidth of 0.5 nm is attained at 2020 μA in RT-CW condition. As an attractive property of metallic cavity laser, a thresholdless lasing was realized by its high spontaneous emission coupling factor [128]. These interesting characters of metallic cavity laser pave a way to application for the ultra-low power consumption light source in communication. Although the metallic cavity overcomes hurdle for electrically pumping and RT-CW operation, there are still remain the problems related to an output power, coupling structure to the waveguide and direct modulation performance, etc.


**Figure 1.42** Structure of the metallic-cavity semiconductor laser with a rectangular cross section pillar encapsulated in silver. [127]

## Photonic crystal lasers

Photonic crystal has a periodic photonic structure which generates photonic band. Recent research was triggered by work in 1987 by E. Yablonovitch at Bell Lab.[129]. The


**Figure 1.43** Cross-sectional SEM image of photonic crystal laser.[130]

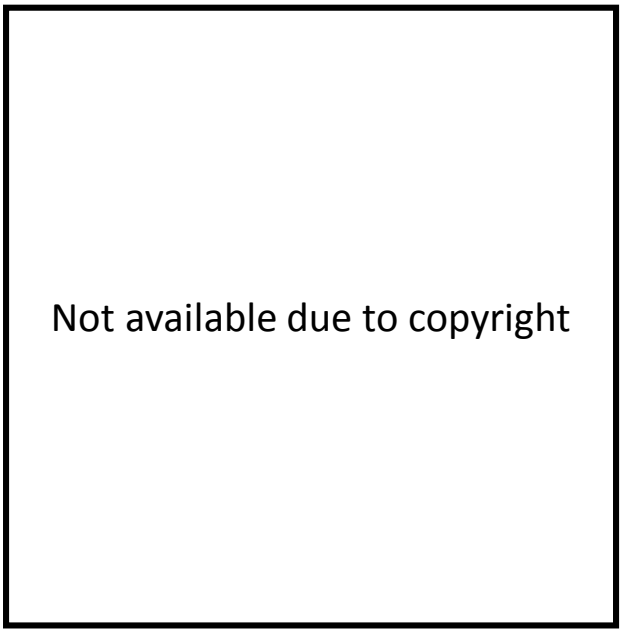


**Figure 1.44** Light output characteristics of the photonic crystal laser [65].

paper extend the conventional one dimensional periodic photonic structure into more than two dimensional ones. The defect in periodic structure can rearrange the optical characteristics of photonic crystals. A strong confiment optical cavity can be realized by photonic crystal defect cavity. Ultra-high Q cavities which use the defect structure with experimental values of higher than $10^5$ and theoretical values of higher than $10^7$ were demonstrated. Ultra-low threshold laser by strong confiment cavity is expected using photonic crystal structure. The first photonic crystal laser using two dimensional photonic

band gap defect mode cavity was demonstrated by optical pumping in 1999 [131]. The laser cavity had half-wavelength scale core layer including GaInAsP 4QWs active layer. The two-dimensional photonic crystal and air bridge structure resulted in strong optical confiment in λ-scale cavity. Electrical injection operation of photonic crystal lasers was also demonstrated under RT-pulsed conditions[132-134], RT-CW conditions[130, 135]. These results showed that photonic crystal cavity enable sub-mA threshold operation thanks to small active volume. However, typical active region of photonic crystal lasers does not have buried hetero structure, which causes poor carrier confinement to the active region and poor thermal characteristics. To overcome these problems, photonic crystal laser with buried hetero structure was reported by NTT [136-138]. The SEM image of the structure and cavity field is shown in Figure 1.43. The periodic air holes were formed at both sides of the buried active region and the membrane structure with an air bridge was used. In-plane output waveguide could be integrated by using a defect mode waveguide. The light output of photonic crystal laser was coupled to a photonic crystal output waveguide. RT-CW operation by current injection was realized with a threshold current of 390 μA [130]. This device adopted the lateral-current-injection structure fabricated by thermal Zn diffusion and Si ion implantation. Significant threshold reduction was achieved by introducing AlInAs sacrificial layer to suppress the leakage current through the substrate. The threshold current was reduced to be 4.8 μA, which is the lowest threshold current of photonic crystal laser under RT-CW electrical injection [139]. High speed direct modulation measurement shows 4.4 fJ/bit energy consumption operation at data-rate of 10Gbit/s. However, at the driving condition of 4.4 fJ/bit operation, the bit-error-rate characteristics showed error floor due to a low light output power of 2.17 μW. In addition, the avalanche photodiode used in the measurement consumed relatively large power. Recently, the photonic crystal laser was fabricated on a Si substrate by oxygen-plasma assisted bonding [140]. Photonic crystal lasers can be easily integrated with other optical components. However, controlling the out coupling efficiency is not so easy due to the complicated trade off of photonic crystal design. Therefore, the low light output power is a problem for the on-chip application.

## Distributed feedback (DFB), distributed-reflector (DR) lasers

The distributed feedback (DFB) laser is a most basic dynamic single mode (DSM) laser widely used in fiber optical communication or sensing. The resonance wavelength in DFB laser can be selected by a periodic refractive index or gain structure produced by grating formation. The DFB structure was first proposed and spontaneously formed in a dye laser by H. Kogelnik and C. V. Shank at Bell Lab.[80]. Semiconductor DFB laser was first fabricated by M. Nakamura at Cal. Tech. using holographic lithography in 1973 [82]. The idea of phase-shifted grating improved a single-mode yield of DFB laser [141]. Typical DFB lasers use only real part of coupling coefficient. In contrast, the gain coupled DFB laser utilizes imaginary part of coupling coefficient. As a combination of these, complex coupled DFB laser using both real and imaginary part of coupling coefficient was proposed [142]. The single mode properties of the DFB lasers strongly affected by the phase at the cleaved facet of the cavity [143, 144]. However, the facet phase cannot be controlled because the grating period is typically in the order of hundreds nm and the position of cleaved facet is not exactly determined. Commercially available uniform grating and $\lambda/4$-shifted DFB lasers have high-reflection(HR)/anti-reflection (AR) and

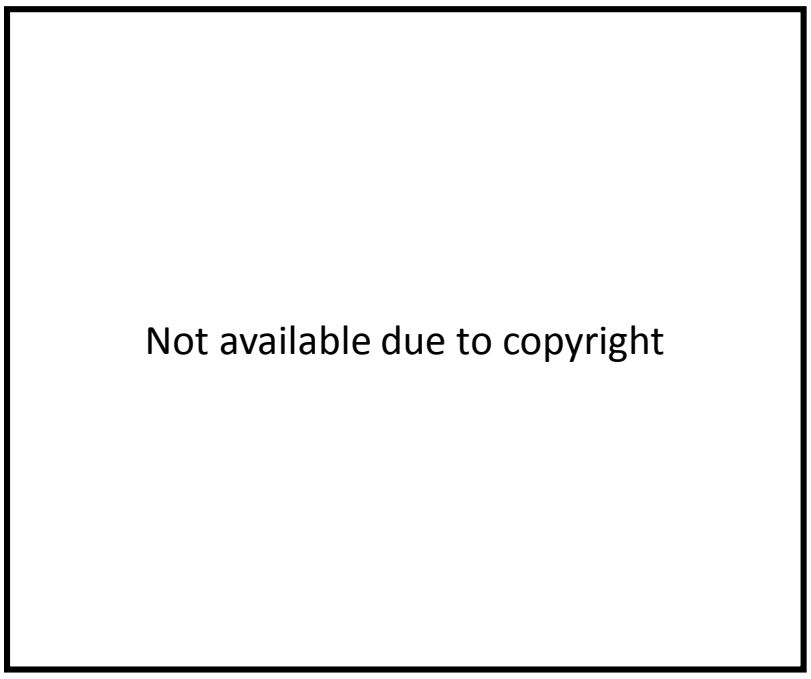


**Figure 1.45** Light output characteristics of wire-like active region DFB laser [145].

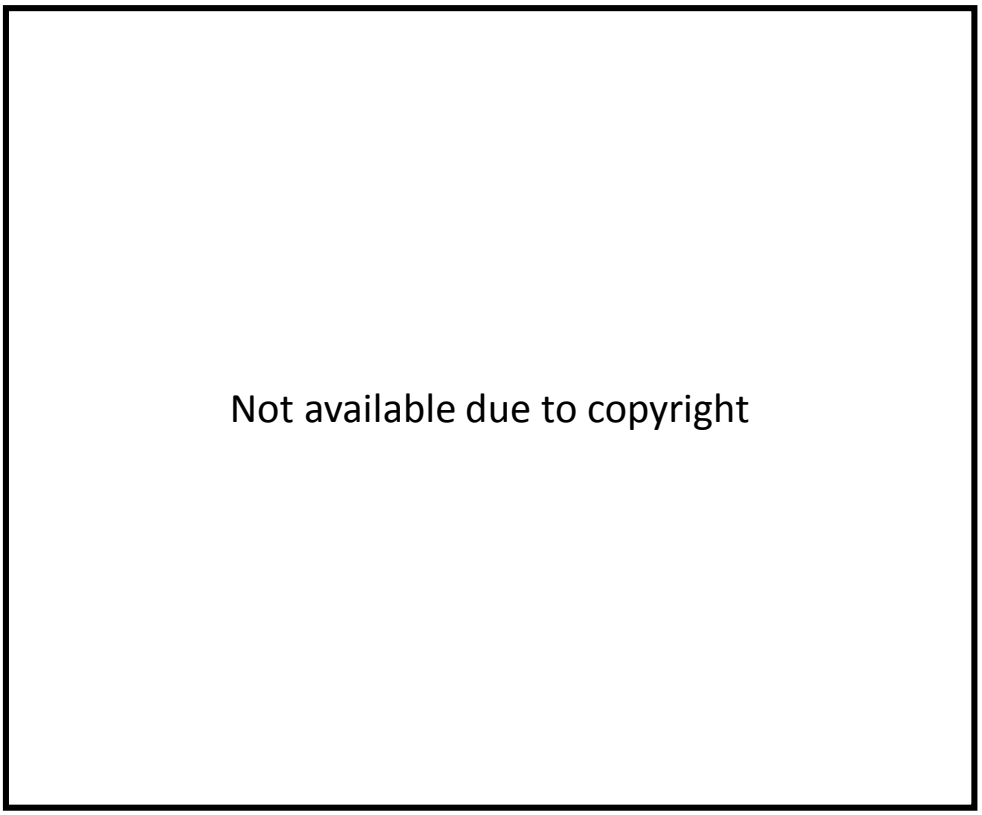


**Figure 1.46 S**chematic diagram of DR laser and cross-sectional structure of wirelike active regions. [146]

AR/AR coating on its facets to suppress the output facet reflection. While the complex coupled DFB laser needs relatively complicated fabrication process than that of index coupled DFB laser, it has advantages on single mode yield [147] and immunity to the facet phase [148]. To obtain single facet output and avoid the facet phase problem without any optical coatings, the distributed-reflector (DR) laser, which consists of an active DFB section and a passive DBR section, was proposed in 1988 [149, 150]. A two times larger output ratio of the DR laser than that of the DFB laser was achieved [151]. Recently, a number of company such as Furukawa Electric., Sumitomo Electric. and Fujitsu etc. adopted the DR structure in their developed devices [152-155].

In our group, complex coupled DFB lasers made by top-down process were proposed and developed by using low damage reactive ion etching technology and organo-metallic vapor phase epitaxy (OMVPE) regrowth [156-158]. The wire-like active region

fabricated by vertical etching of quantum wells leads reduction of the active volume and results in low threshold current operation and strong index coupling. In 2000, a record low threshold current of 0.7mA was achieved (Figure 1.45) [145, 159]. In order to obtain a higher efficiency, the DR laser consisting of wire-like active region DFB laser and quantum wire DBR section was demonstrated [160]. This structure utilized blue shift by quantum confiment effect in narrow width wire-like grating as shown in Figure 1.46. In 2009, low threshold current of 0.9 mA and high efficiency of 48% operation was obtained for the DR laser with wire-like active region [146]. High speed direct modulation using non-return-to zero 10 Gbit/s and 25 Gbit/s signals were demonstrated [161, 162]. The energy cost for transmission was approximately 1.7 pJ/bit for 10 Gbit/s operation. However, even if we attempt to reduce the energy consumption, the weak coupling coefficient of approximately 400 $cm^{-1}$ was not enough to reduce the operating current for on-chip interconnection.

### 1.5.2 Integration methods on silicon

When implementing on-chip optical interconnections into LSI circuits, we should consider not only to the power consumption but also to the integration method. The current CMOS process use 300-mm to 450-mm diameters silicon substrate. Since silicon has an indirect transition bandgap as is well known, its weak emission intensity is not suitable for a light source. Therefore, a technique for integrating a laser consists a conventional III-V semiconductor on a Si substrate is necessary while maintaining the crystallinity of the III-V active layer as grown on III-V substrate. Previously researched integration methods can be roughly categorized into crystal growth based and bonding based methods. Hereinafter, the technique and the semiconductor laser integrated on the Si substrate will be described.

**Direct growth on silicon**

When III-V semiconductors such as InP or GaAs are grown on Si substrate, large dislocations and defects are generated at the interface due to large lattice constant mismatch and difference of thermal expansion coefficient between them, and it is difficult to obtain good crystalline quality. Growth of polar III-V group crystals on nonpolar Group IV crystals causes anti-phased domain (APD) which is an exchange of atomic arrangement. However, since the high performance laser on Si substrate is attractive from the viewpoint of laser integration with an electric circuit, it has been studied for a long time to fabricate a laser directly on a Si substrate. Directly grown III-V laser on a Si substrate for the first time was reported in 1984. A seed layer of Ge on a Si substrate was used to form a GaAs / AlGaAs layer and low temperature pulse lasing achieved [163]. In this way, in order to form a laser by direct growth on a Si substrate, it is necessary to prepare a nanostructure or introduce a buffer layer. In recent years, it has been reported that using quantum dots as an active layer to reduce the portion of threading dislocation penetrating the active layer. Figure 1.47 shows the layer structure of the quantum dot laser

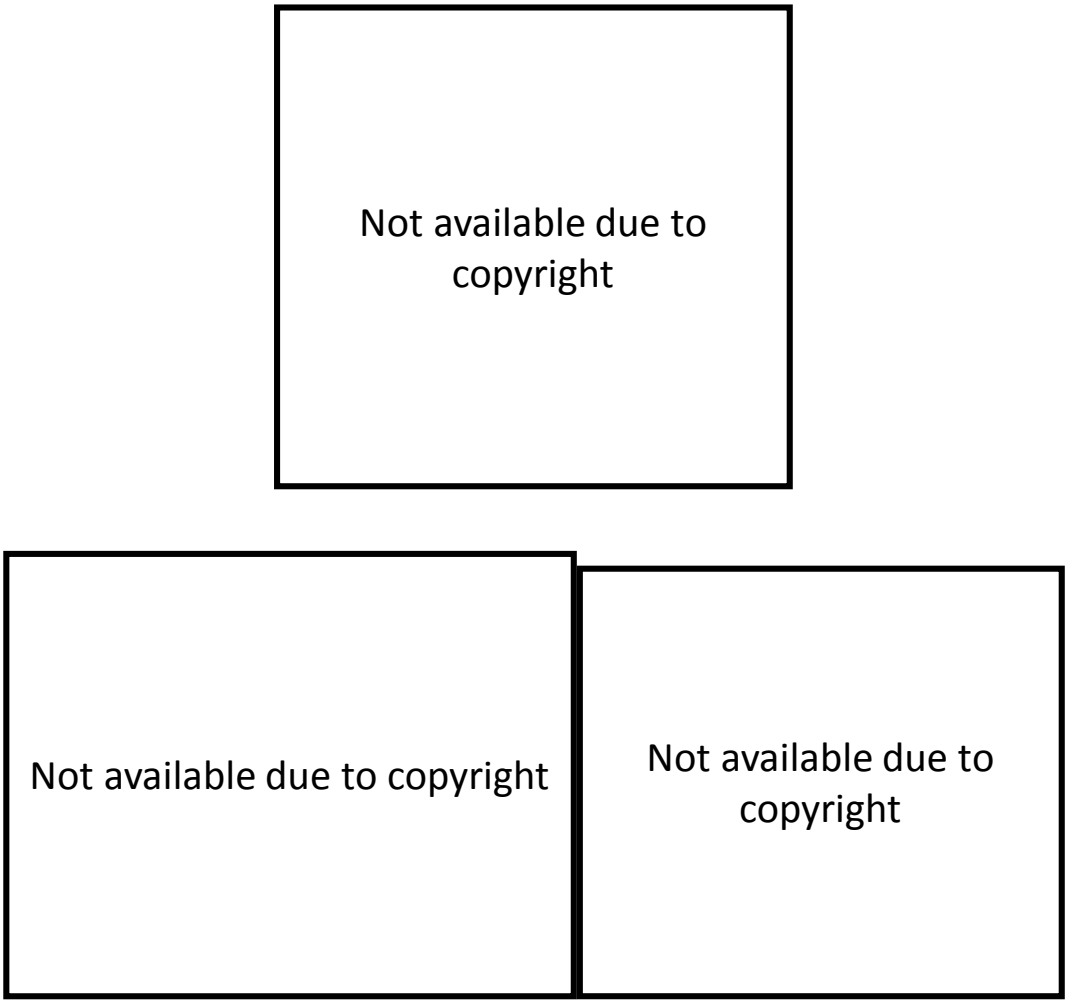


**Figure 1.47** The layer structure of quantum dot laser grown on Si substrate and its light output characteristics [164].

directly grown on a Si substrate. Room-temperature continuous oscillation up to 119 ° C and threshold current of 19 mA maximum output 176 mW have been obtained from CSB[164]. The possibility to fabricate a laser on a large wafer scale Si substrate with a performance comparable to that of conventional lasers. However, since these devices required a growth process at high temperature or annealing process, there is a problem that the process temperature at the back end of line (BEOL) CMOS process exceed the allowable temperature.

**Direct bonding (Plasma activated bonding)**

Plasma activated bonding (PAB) is a method that activate the stable surface crystal by inert gas plasma and bonding the substrates with the activated surface. In the conventional direct bonding method, since substrates are bonded at a high temperature of around 600°C. or more, the difference in thermal expansion coefficient degrade the bonded interface and induce the dislocation into the substrate. In particular, when strong stress or strain is produced at the bonded interface of a III-V semiconductor used for a optical device, degradation in emission efficiency and an emission wavelength peak shift due to an increased dislocation or strain are concerned. By using PAB method, as it is possible to bond at near room-temperatures, connecting the wires between different circuit chip is suggested [165]. In a photonics application, PAB is getting attention as a method to integrate a III-V material in silicon photonics because III-V material can be formed in large area on a SOI substrate which has a passive silicon circuit. Room temperature continuous operation of electrically pumped AlGaInAs/InP hybrid laser using $O_2$ PAB of

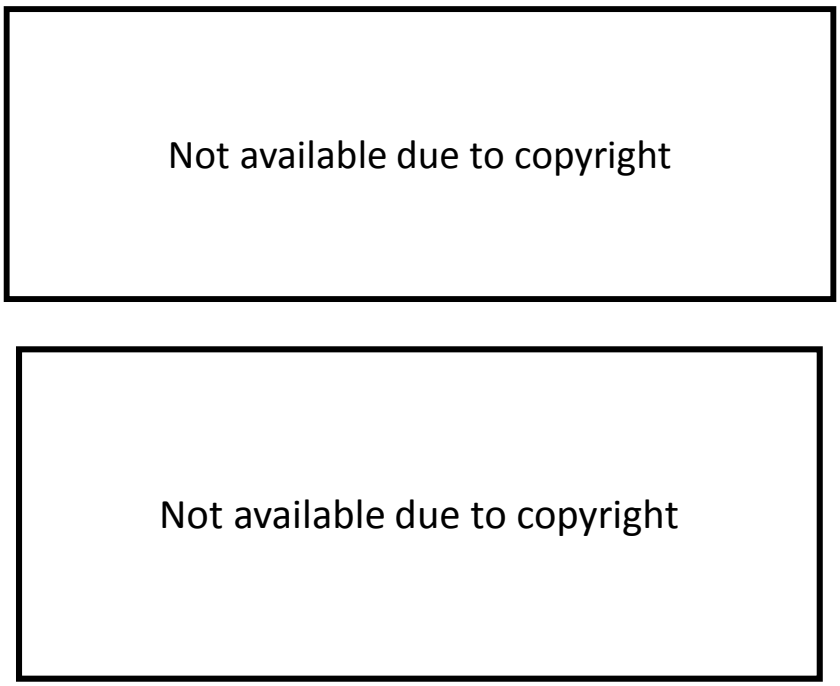


**Figure 1.48** Cross section of the hybrid laser fabricated by $O_2$ PAB [166].

III-V substrate onto SOI substrate has been reported from UCSB and Intel (Figure 1.48)[166, 167]. Our group has reported low threshold current density operation of a GaInAsP/InP/SOI hybrid laser fabricated by $N_2$ PAB [168]. NTT reported a membrane DFB laser which has buried heterostructure formed after bonding a GaInAsP/InP substrate on Si substrate with thermal oxide by using $O_2$ PAB [169] However, PAB is a method to directly bonding the substrates to each other and is sensitive to the surface flatness and conditions. For this reason, it becomes difficult to bond the substrates after complicated process steps [170].

**Benzocyclobuten (BCB) bonding**

Unlike direct bonding, BCB bonding is one of the methods using intermediate adhesive layer. Thermoplastic polymers such as PMMA,SU-8, and thermosetting polymers such as SOG (spin-on glass), polyimide and BCB [171] have been investigated as an intermediate layer. BCB is studied as a potential candidate because BCB has a high glass transition temperature of about 350°C and a low curing temperature of about 250°C. Bonding method using BCB has been originally used in the field of electrical circuits. Compering with the other adhesive materials, BCB emits small amount of outgas during the cure and has long term reliability. And transparent characteristics for communication wavelength becomes a booster of the BCB as a photonics application. Our group started the research associating with BCB bonding since 2000. Figure 1.49 shows recently obtained III-V layer fabricated on Si substrate by BCB bonding. As a activity from another group, room temperature continuous lasing with a threshold current of 0.8 mA was reported for a microdisk laser with a diameter of 7.5 μm integrated with a Si waveguide intermediated by BCB [172]. BCB can alleviate the flatness of the surface and its adhesive property is insensitive to the surface state. Therefore, it can be considered that this method is effective to integrate a substrate of electrical circuit and optical interconnect which have significantly different properties. Therefore, I have adopted the

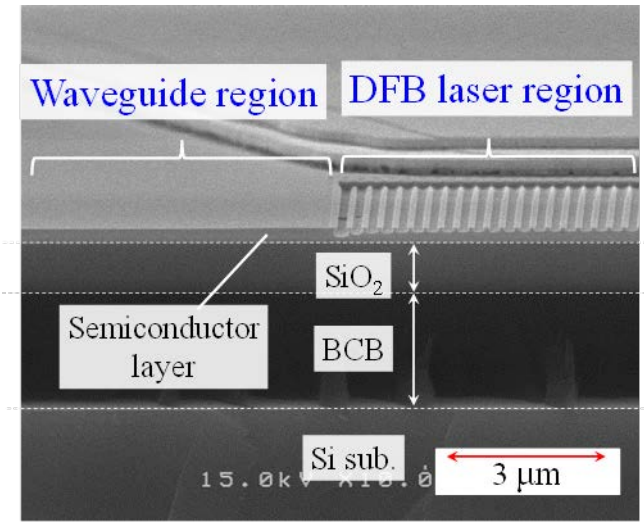


**Figure 1.49** SEM image of the InP-based membrane structure fabricated on a Si substrate using BCB bonding [173].

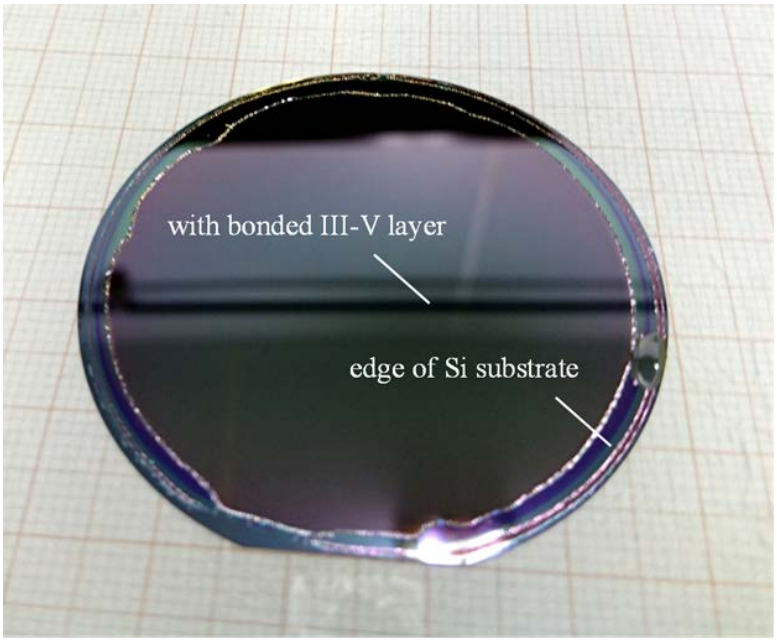


**Figure 1.50** 2 inch wafer consists of III-V layer on Si substrate fabricated by using BCB bonding.

BCB bonding as a method to integrate a laser on a Si substrate in this thesis. In next section, a fundamental property of the membrane DFB structure which is focus in this thesis will be discussed.

## 1.6 Semiconductor membrane DFB structure

### 1.6.1 Features of membrane DFB structure

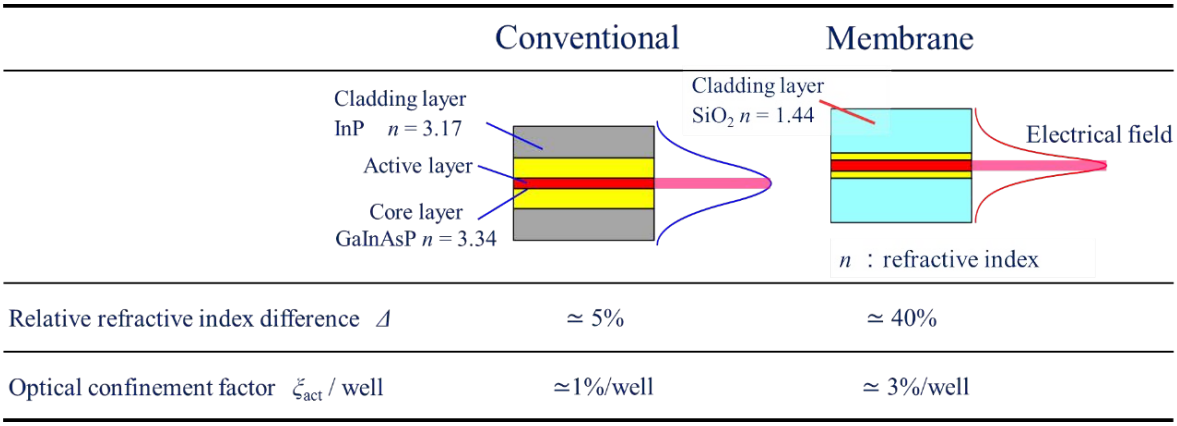


**Figure 1.51** Comparison of the optical confinement between the semiconductor laser and membrane laser.

As discussed in the previous sections, ultra-low power consumption lasers and efficient coupling structures are required for on-chip optical interconnections. Membrane distributed-feedback (DFB) laser—DFB laser consists of thin semiconductor layers—is a promising candidate as light sources for on-chip optical interconnection. Its edge-emitting structure with no requirement to form facets of the DFB laser is well suited for in-plane integration, and is widely used as the light source in photonic integrated circuits. Although the typical operating current of conventional DFB lasers is of several tens of mA, the membrane structure is a solution for low-power consumption operation. The wavelength of light source is not specified in optical interconnection. However it is preferred that the laser is operated by low-driving voltage because LSIs is difficult to produce the voltage higher than power supply. The turn-on voltages for typical wavelength laser are 0.8 V for 1.55 μm, 1.17 V for 1060 nm and 1.46 V for 850 nm. Long-wavelength laser has advantageous over minimum operating voltage which is compatible with supply voltage of LSIs. Therefore, 1.55 μm was adopted as operating wavelength of membrane DFB laser. Figure 1.51 shows the comparison between layer structures of the typical conventional semiconductor laser and membrane laser. The conventional structure

has semiconductor core and cladding layers. In the case for typical 1.55 μm wavelength InP based laser, a material of the core and the cladding layers are GaInAsP and InP, respectively. The relative refractive index difference Δ, is defined as follows:

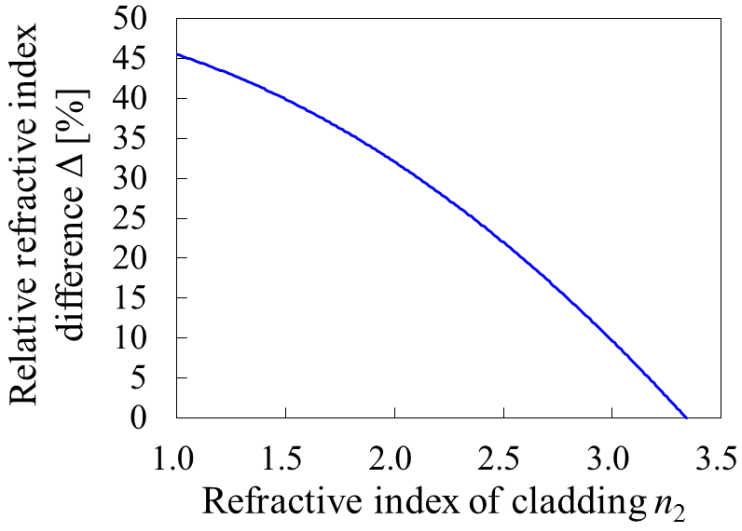


**Figure 1.52** Relative refractive index difference as a function of refractive index of cladding material.

$$\Delta = \frac{n_1^2 - n_2^2}{2n_1^2} \tag{1.7}$$

Figure 1.52 shows the relative refractive index difference as a function of refractive index of cladding material. The $\Delta$ for InP ($n$ = 3.17) cladding structure can be calculated to be approximately 5%. The small index difference resulted in a small optical confiment factor of 1% for single quantum well. These characteristics make conventional laser difficult to operate low-power consumption. In contrast to this, the membrane structure consists of low refractive index cladding layers such as $SiO_2$ ($n$ = 1.44), Benzocycrobutene (BCB) ($n$ = 1.54) or air ($n$ = 1). A thin semiconductor layer sandwiched by dielectric claddings has a large refractive-index difference between the core and cladding layers. $\Delta$ for the membrane structure is calculated to be approximately 40%. And the optical confinement factor of the active layers is enhanced to be 3% per quantum well. A large refractive-index difference between the core and cladding layers results in strong grating index-coupling. Figure 1.53 shows the relative refractive index coupling coefficient $\kappa_i$ of the membrane

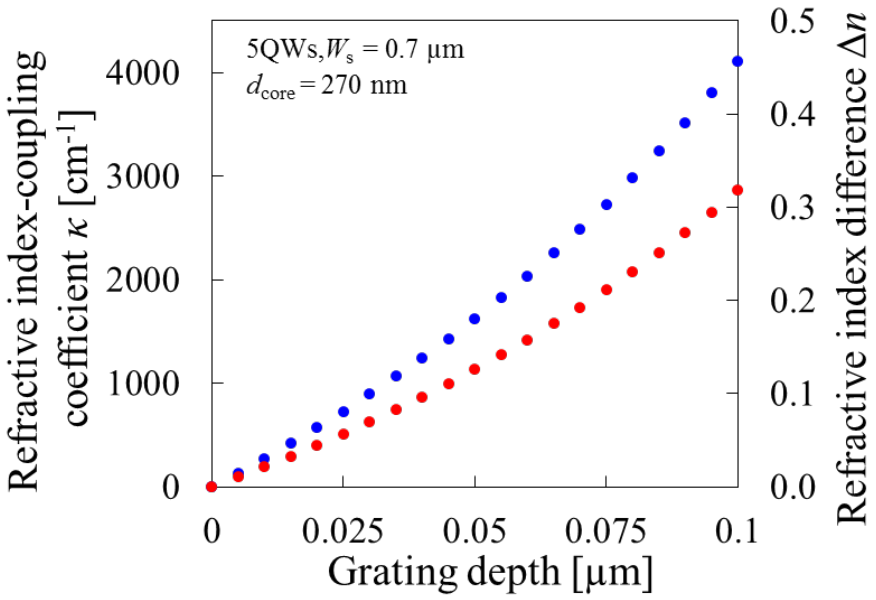


**Figure 1.53** Relative refractive index coupling coefficient of membrane DFB structure as a function of grating depth.

DFB structure as a function of grating depth. The index coupling coefficient can be reach to 2000 cm$^{-1}$ and 4000 cm$^{-1}$ with a grating depth of 60 nm and 100 nm respectively. These values are about one order magnitude larger than that of the conventional semiconductor cladding type laser with a high coupling coefficient [145, 146]. These properties make the membrane DFB laser a candidate for an ultra-low energy consumption operation. Furthermore, membrane structure pushes advantages to not only lasers but also other optical devices. An InP-based wire waveguide can achieve a small bending radius below 10 μm. For a photodiode, an absorption length is expected to be reduced by strong optical confinement factor of the absorption layer.

### 1.6.2 Research history of membrane lasers

In this section, the history of membrane lasers is described. Our group had started the initial consideration of membrane DFB structure since around 1999. The history was divided into six era. As a consequence, problems in the previous works will be clarified.

**Optically pumped membrane DFB lasers (2001~2007)**

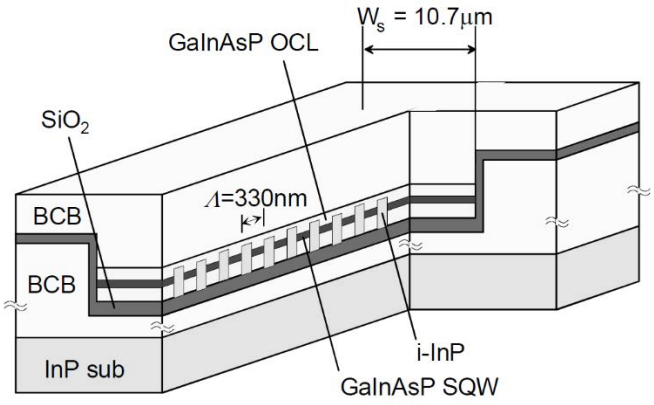


**Figure 1.54** Schematic structure of the first membrane DFB laser operated by optical pumping [174].

The concept and performance calculation were proposed in early 2001 [175]. First room-temperature continuous-wave operation of a membrane DFB laser with wire-like active region was demonstrated by optical pumping condition in end of 2001 [174]. Figure 1.54 shows a schematic structure of the membrane DFB laser. The threshold pump power was 38 mW for a 10.7 μm wide and 40 μm long device. 4-μm-thick BCB was used to form membrane structure on an InP host substrate. Single-mode operation with SMSR of 36 dB [176] and low-threshold pump power of 0.64 mW [177] was achieved by adopting a narrow stripe structure and narrow pump beam. Evaluation of the accuracy of lasing wavelength of fifteen membrane DFB lasers with same cavity design was performed [178]. Multiple-wavelength laser arrays with maximum wavelength range of 75 nm were demonstrated by modulating the grating period, duty ratio and stripe width[179, 180]. The temperature characteristics of membrane DFB lasers were

investigated. Athermal effect of BCB cladding structure was studied and achieved reduced temperature dependence of lasing wavelength with coefficient of $2.45\times10^{-2}$ nm/°C, which was approximately 20–30% of that for conventional semiconductor lasers[181]. Continuous-wave optical pumping operation was obtained up to 85°C by introducing Bragg wavelength detuning[182].The lowest threshold power under optical pumping was 0.34 mW obtained in 2007[183]. The device had cavity length of 80 μm and high-index coupling coefficient of 4200 $cm^{-1}$ by adopting a surface corrugating grating structure.

**Membrane DFB lasers on SOI substrate (2006~2009)**

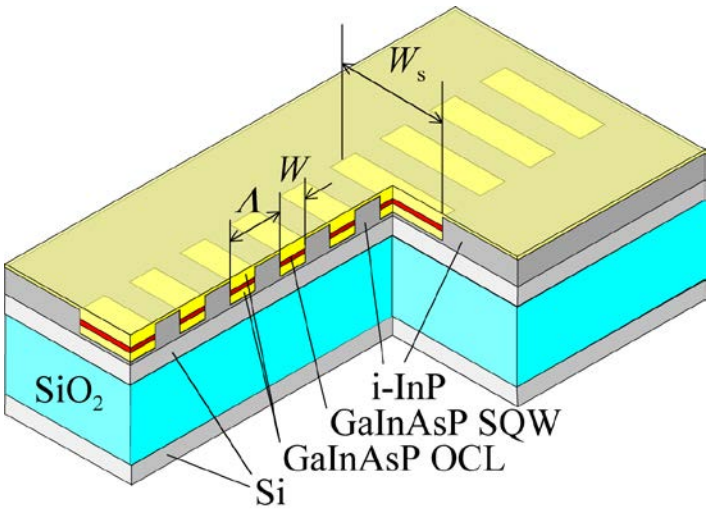


**Figure 1.55** Schematic structure of the membrane DFB laser bonded on SOI substrate fabricated by hydrophilic bonding [184].

Membrane DFB lasers are attractive for light source of SOI platform. In 2006, the direct wafer bonding of GaInAsP/InP membrane structure onto a silicon on insulator (SOI) substrate was performed by a hydrophilic bonding method[185]. Continuous and single-mode operation of membrane DFB laser on SOI substrate by optical pumping was achieved with threshold pump power of 2.8 mW[184]. Membrane DFB laser on SOI substrate with rib-waveguide structure was fabricated in 2007[186]. An injection type GaInAsP/InP DFB laser on SOI substrate was realized in 2009[187]. The threshold

current was 104 mA under room-temperature pulsed condition. SMSR of 28dB. I should note that this device did not have a GaInAsP/InP membrane structure.

**Membrane DFB lasers with air-bridge structure (2006~2008)**

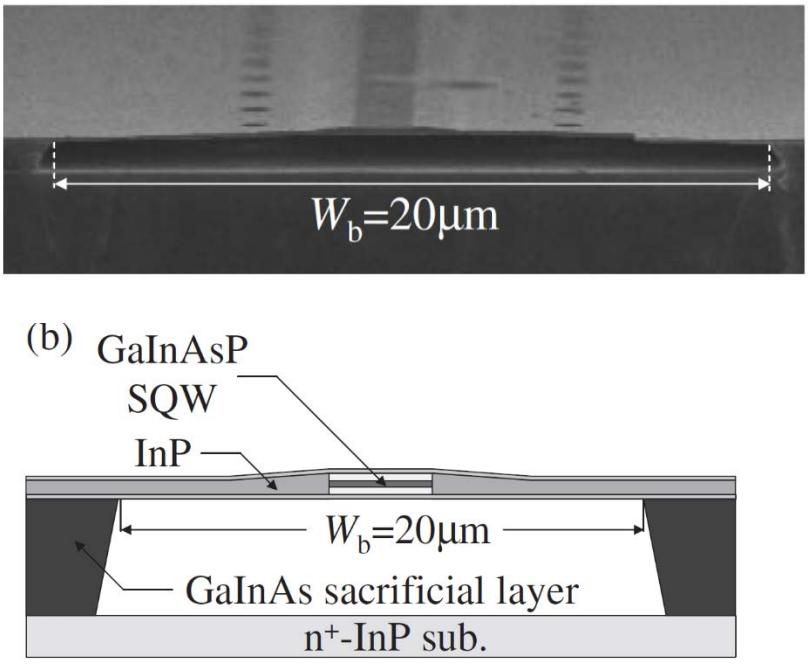


**Figure 1.56** Cross-sectional SEM view of membrane DFB laser with air-bridge structure and its schematic diagram.

Fabrication of membrane structure without complicated wafer bonding process is of interest for easy preparation of membrane structure. Air-bridge structure was fabricated by removing the sacrificial layer underneath the core layer by selective wet chemical etching. GaInAsP/InP BH-membrane DFB laser was fabricated on n-InP substrate using GaInAs sacrificial layer. Continuous-wave optical pumping operation was achieved with threshold pump power of 4.3 mW at 20°C [188]. Lasing operation was obtained up to 80°C and reduced thermal resistance compared with bonded membrane DFB laser was confirmed.

**Lateral-current–injection (LCI) lasers for injection type membrane DFB laser (2008~2012)**

First, I introduce the brief history of lateral-current-injection lasers. A lateral-current-injection lasers have long history since 1970s. Monolithic integration of high-speed electronic devices and photonic devices is thought to be important technology for high-speed communication. Such optoelectronic integrated circuits (OEICs) requires in-plane structure semiconductor laser which is differ from conventional semiconductor laser with perpendicular p-i-n structure for current injection. The first transverse junction stripe (TJS) laser was developed in 1974[189]. The pn junction was formed on AlGaAs/GaAs substrate by selective Zinc diffusion. In 1980s, AlGaAs/GaAs lateral current injection (LCI) type laser with lateral p-i-n junction was demonstrated[190]. The LCI structure was used for the aim of integrating other electrical semiconductor devices for signal processing. The threshold current was 27 mA for the active layer width of 0.5 μm. In addition, a low capacitance of 0.6 pF was also obtained. In 1994, a successful operation of 1.5 μm GaInAsP/InP LCI laser was demonstrated by 2-steps LPE regrowth by K. Oe et al at NTT [191]. Lateral BH structure consisting of 0.1-μm-thick bulk active layer and regrown p-, n-InP was used. RT-CW operation with 10 mA threshold current and a maximum output power of more than 10 mW/facet were obtained.

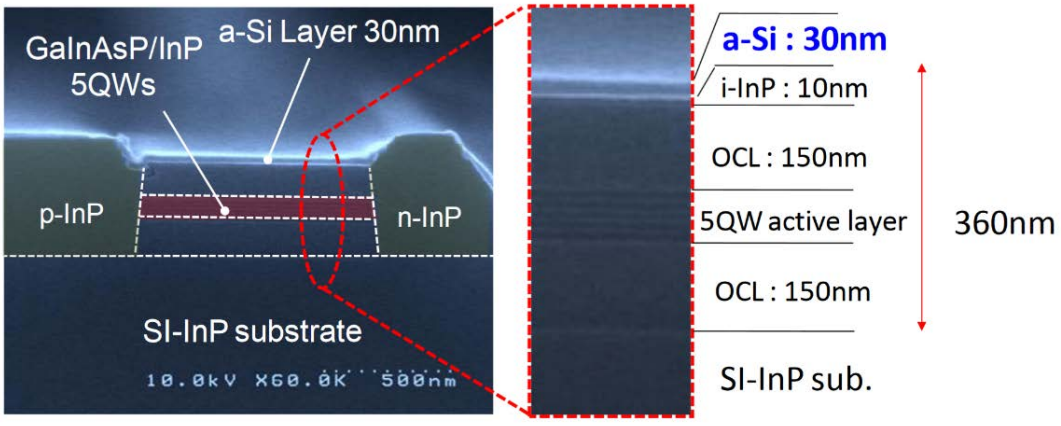


**Figure 1.57** Cross-sectional SEM image of LCI-DFB laser with a-Si surface grating [192].

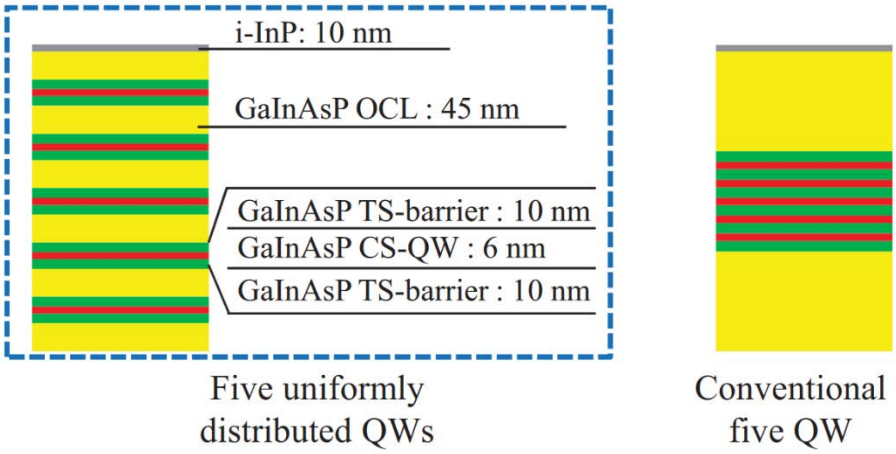


**Figure 1.58** Structural comparison between the distributed quantum well and the conventional multi-quantum well[193].

Using vertical current injection via pn junction is difficult for the membrane structure because this structure has insulating dielectric cladding layers on the thin semiconductor in vertical direction. The LCI structure will be a solution for this problem. The p-i-n diode structure formed in transverse direction is compatible with many types of membrane active device such as membrane DFB lasers, air-bridge type photonic crystal lasers [130, 194-198]. These reports used an implantation of Si for *n*-type doping and an ion implantation of Be or thermal Zinc diffusion for *p*-type doping.

Our research group developed a LCI laser fabricated by two-step OMVPE regrowth. Fundamental properties of a LCI laser were investigated through evaluating the LCI lasers on semi-insulating InP substrate. The first top-air-clad LCI laser with 400-nm-thick core layer was operated with threshold current of 49 mA under RT-pulsed condition[199]. RT-CW operation at threshold current of 11 mA was obtained by modifying the structural design [200]. In 2011, LCI-DFB laser with a-Si surface grating was demonstrated [192] (Figure 1.57). A low threshold current of 7.0 mA and high external differential quantum efficiency of 43% from the front facet were obtained for the device with 2.0-μm stripe width and 300-μm cavity length in RT-CW conditions. $\lambda/4$ shifted LCI-DFB laser with a-Si surface grating [201] and LCI-DFB laser with wire-like active region [202] were

successfully operated. In spite of operation in RT-CW conditions, there were still problems that a low internal quantum efficiency of LCI structure. The internal quantum efficiency of the device was evaluated, however, the value was as low as 40% for the 1.7 μm stripe device which is approximately half of that of the typical semiconductor laser. The methods for increasing the internal quantum efficiency was experimentally investigated. A one approach was distributed quantum well structure [193] as shown in Figure 1.58. The leakage current through the optical confinement layer (OCL) degrade the injection efficiency into the active region. Because the thick OCL layer was origin of leakage current, the current was uniformly injected into each quantum well by distributing the quantum well in the core layer. As a result, an internal quantum efficiency of 70% was realized. Another approach is reduction of surface recombination by using thick InP cap structure [203]. InP has wider bandgap energy than OCL layer. For suppressing the surface recombination, keeping the carriers away from the surface of semiconductor is needed. Thick InP cap layer (50 nm) resulted in enhancement of an internal quantum efficiency to 66%. These results proved that the LCI lasers have internal quantum efficiency comparable to that of the conventional vertical current injection type lasers.

**Membrane waveguides and lateral junction photodiodes (2007~)**

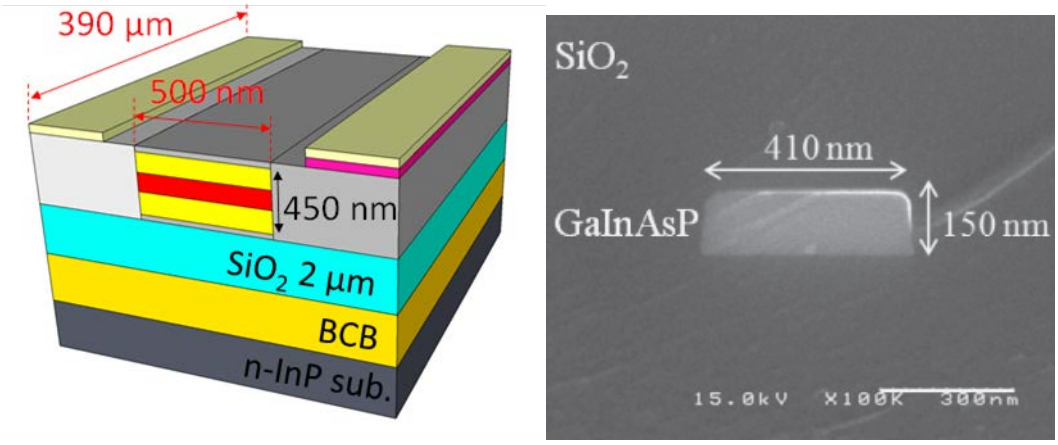


**Figure 1.59** (left) Lateral junction membrane photodiode[204]. (right) GaInAsP membrane wire waveguide [205].

As an essential component for optical interconnection, a waveguide and photodiode for membrane optical interconnect have demonstrated. The lateral junction photodiode on semi-insulating InP substrate was demonstrated using the fabrication process developed for LCI-laser [206]. The photodiode had the absorption layer consisting of GaInAsP 5MQW. The successful photo detection and high speed signal detection of 6 Gbit/s optical signals with bit-error-rate less than $10^{-12}$. The lateral junction photodiode with GaInAs absorption layer was fabricated on semi-insulating InP substrate [207]. The device shows responsivity of 0.39 W/A and clear eye opening at 10 Gbit/s signal. The lateral junction membrane photodiode was demonstrated in 2012 and passed the mask test of 10 Gbit/s Ethernet [204].

First GaInAsP membrane waveguide was reported in 2009 [208]. However, poor bonding quality degraded the waveguide loss to 21 dB/cm. The improvement of bonding condition reduced the waveguide loss to 17 dB/cm [209]. In 2012, by changing resist for electron beam lithography from negative resist of ma-N2405 to positive resist of ZEP520A/ZEP-$C_{60}$, the waveguide loss of GaInAsP membrane waveguide was reduced to be 4 dB/cm. The membrane waveguide had a bending radius of 10 μm which indicated the potential for high density integration of membrane optical devices.

**LCI-membrane lasers (2011~)**

Membrane DFB laser with LCI structure was fabricated for current injection operation of membrane DFB laser. First lasing operation of the LCI membrane DFB laser was realized in 2011[210]. The active region has wire-like active region grating. The lateral pn junction for LCI structure was prepared by two step OMVPE regrowth. 470-nm-thick core layer was bonded onto a SOI substrate. The threshold current was 83 mA under RT-pulsed operation. However, low-threshold current operation was not achieved at this time. Membrane DFB laser with surface etched grating was fabricated, and a threshold current of 11 mA was obtained under the RT-pulse condition [211]. For the

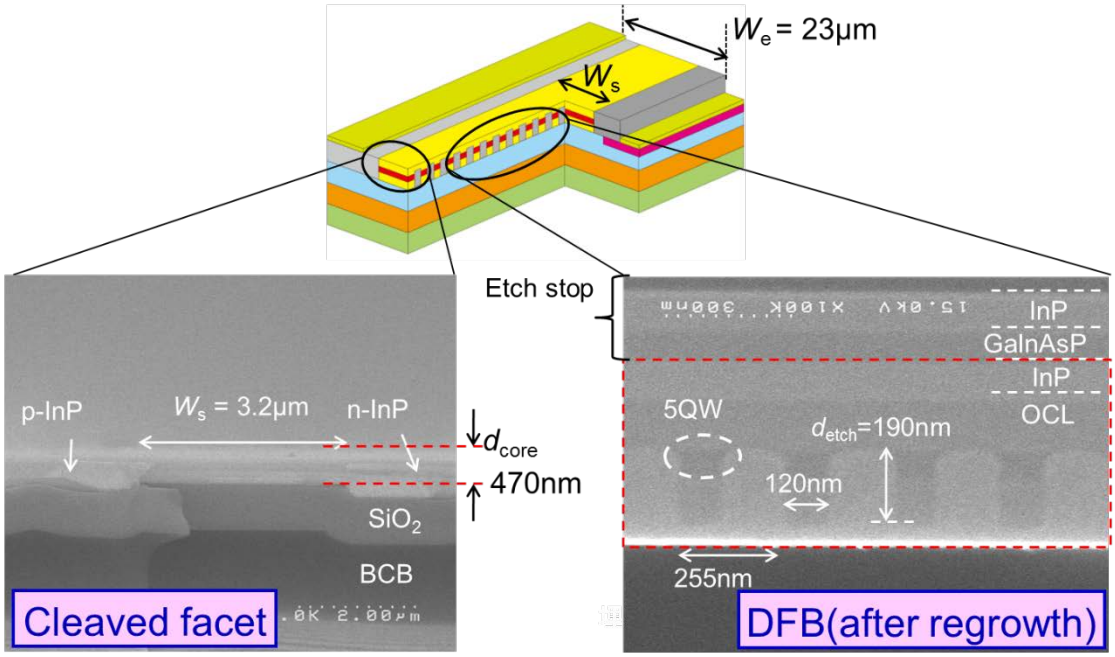


**Figure 1.60** First injection type LCI-membrane DFB laser with wire-like active region [210]

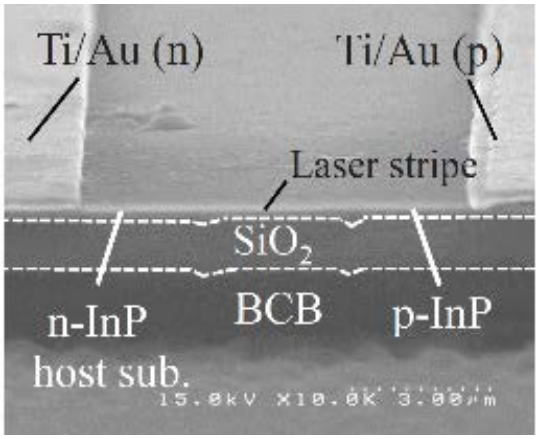


**Figure 1.61** LCI-membrane Fabry-Perot laser bonded on a InP substrate operated in room-temperature continuous condition [212].

performance improvement of membrane laser, complicated fabrication should be simplified. Be-doped GaInAs contact layer was introduced for the suppression of dopant diffusion [213]. Reduction of threshold current to 3.8 mA under the RT-pulse condition was obtained. To realize RT-CW operation, the thermal properties of membrane DFB laser was analyzed [214]. According to the analysis, thinner BCB layer structure can reduce the thermal resistance of a membrane laser. By reducing the BCB thickness from

6 μm to 2 μm for the reduction of thermal resistance, RT-CW operation of membrane Fabry-Perot laser bonded on an InP substrate at threshold current of 3.5 mA was demonstrated in 2013[212]. Subsequently, RT-CW operation of membrane Fabry-Perot laser on a Si substrate was achieved [215]. Form the cavity length dependence of lasing characteristics, an internal quantum efficiency of LCI-membrane laser was estimated to be 75%. Thermal properties of membrane laser were experimentally confirmed and the results were well agreed with calculation results [216].

Figure 1.62 shows time series of research for membrane laser. At the time that I am writing this thesis, highly efficient $\eta_d$ = 36% operation of membrane distributed reflector laser has been realized by co-worker of Dr. Hiratani. My research to be described in following chapter contributes to the low-threshold operation, high-speed direct modulation and integration of membrane optical devices.

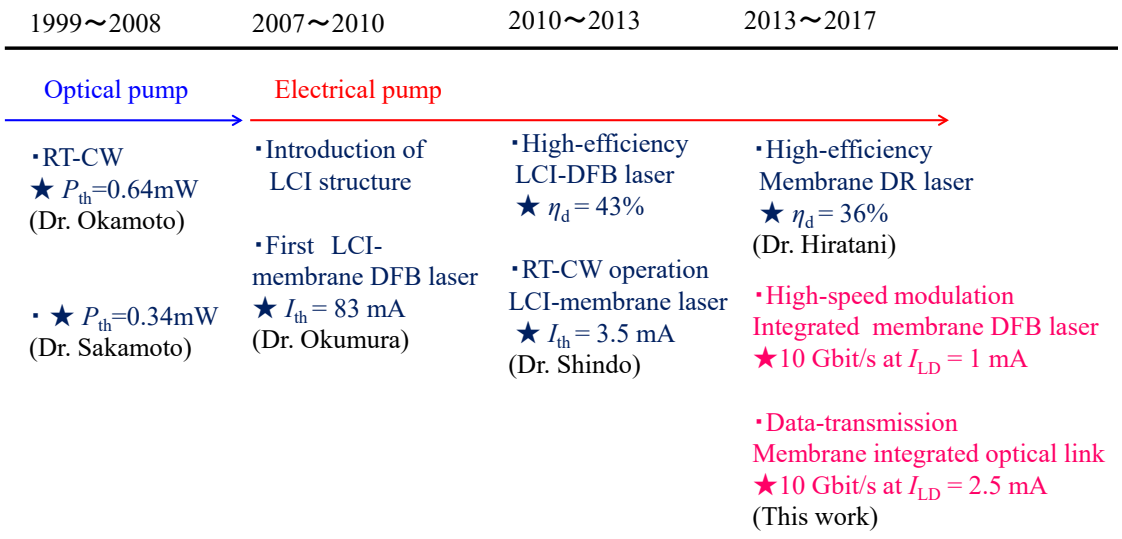


**Figure 1.62** The history of research for membrane laser

## 1.7 Objective and outline of this thesis

As mentioned in this introduction chapter, the appearance of an ultra-low energy consumption semiconductor laser can boost the application of on-chip optical interconnection. Membrane DFB lasers have capability of low-energy consumption operation proven in the theoretical analysis [217, 218]. Successful current injection and RT-CW operation of membrane lasers were reported in previous works. According to the aforementioned research history, the remained problems for membrane DFB laser are as follows. The component devices for an optical link, such as light source, waveguide and photodiode, were realized in membrane platform. However, the lack of integration method is still problem and should be discussed. The theoretically estimated low-threshold performance and high speed modulation characteristics were not investigated experimentally.

Hence, the objectives of this thesis are given as follows;

**[Object 1]** To establish the design and fabrication of integration structure for membrane optical devices.

(a) Calculation of coupling efficiency and back reflection

(b) Fabrication of membrane butt-jointed built-in (BJB) structure

**[Object 2]** To realize low-threshold and high-speed direct modulation of membrane DFB laser

(a) Investigation of fabrication process

(b) Characterization of static and dynamic properties

**[Object 3]** To realize data-transmission through optical link using membrane DFB laser.

(a) Investigation of electrical isolation process

(b) Characterization of static and dynamic properties

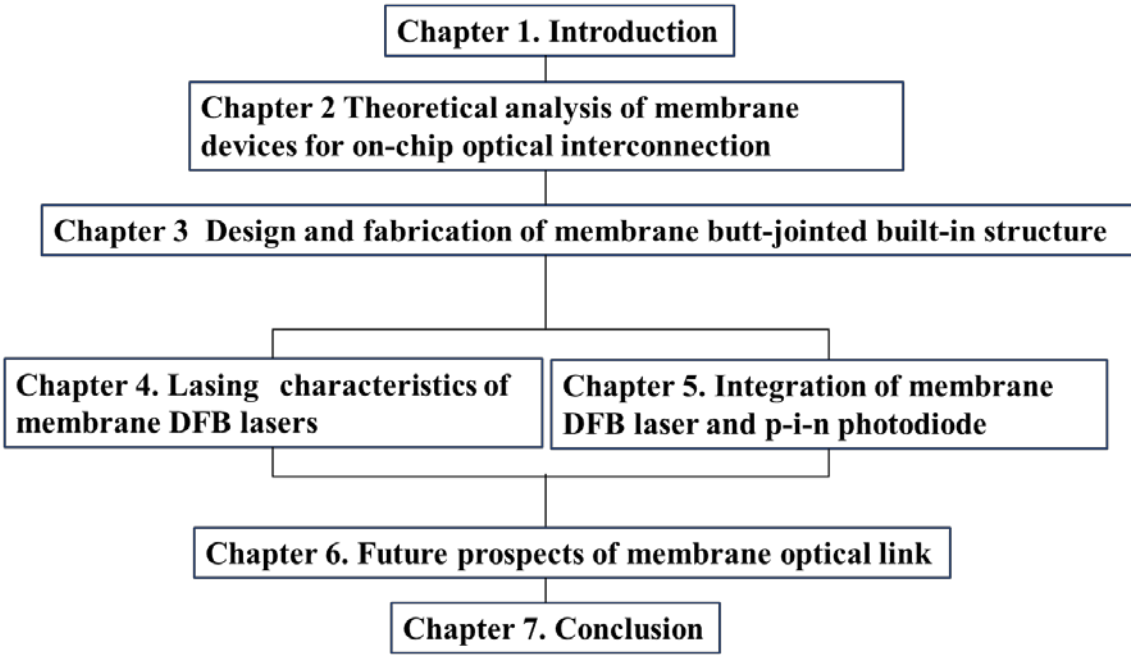


**Figure 1.63** Outline of this thesis.

Figure 1.63 shows the outline of this thesis. In Chapter 2, optical link properties on required optical power for the laser and the expected modulation performance of membrane DFB lasers are analytically discussed. In Chapter 3, butt-jointed built-in (BJB) structure are investigated for integrating membrane optical devices. Coupling characteristics of BJB structure is analyzed by a numerical calculation. And, fabrication process for membrane BJB structure is experimentally studied. In Chapter 4, membrane DFB laser integrated with BJB waveguide are described. In Chapter 5, the integration of the membrane DFB and p-i-n photodiode by a BJB structure is conducted. The works for isolating each device and optical link measurement are described. In Chapter 6, I describe the future prospects of membrane optical link for on-chip optical interconnection. Finally, In Chapter 7, the summary of this thesis will be given.

## References

[1] B. J. Copeland, "Colossus: its origins and originators," *IEEE Annals of the History of Computing,* vol. 26, pp. 38-45, 2004.

[2] W. F. Brinkman, D. E. Haggan, and W. W. Troutman, "A history of the invention of the transistor and where it will lead us," *IEEE Journal of Solid-State Circuits,* vol. 32, pp. 1858-1865, 1997.

[3] C. S. Wallace, "A suggestion for a fast multiplier," *IEEE Transactions on electronic Computers,* vol. EC-13, pp. 14-17, 1964.

[4] Intel. *Intel "Processor History".* Available: http://download.intel.com/pressroom/kits/IntelProcessorHistory.pdf

[5] E. Vittoz, B. Gerber, and F. Leuenberger, "Silicon-gate CMOS frequency divider for electronic wrist watch," *IEEE Journal of Solid-State Circuits,* vol. 7, pp. 100-104, 1972.

[6] G. E. Moore, "Cramming more components onto integrated circuits," *Proceedings of the IEEE,* vol. 86, pp. 82-85, 1998.

[7] R. H. Dennard, F. H. Gaensslen, V. L. Rideout, E. Bassous, and A. R. LeBlanc, "Design of ion-implanted MOSFET's with very small physical dimensions," *IEEE Journal of Solid-State Circuits,* vol. 9, pp. 256-268, 1974.

[8] D. A. Patterson and J. L. Hennessy, *Computer organization and design: the hardware/software interface*: Newnes, 2013.

[9] F. Kaufman, D. Thompson, R. Broadie, M. Jaso, W. Guthrie, D. Pearson, and M. Small, "Chemical - mechanical polishing for fabricating patterned W metal features as chip interconnects," *Journal of The Electrochemical Society,* vol. 138, pp. 3460-3465, 1991.

[10] M. Datta, "Electrochemical processing technologies in chip fabrication: challenges and opportunities," *Electrochimica Acta,* vol. 48, pp. 2975-2985, 2003.

[11] N. A. Kurd, S. Bhamidipati, C. Mozak, J. L. Miller, T. M. Wilson, M. Nemani, and M. Chowdhury, "Westmere: A family of 32nm IA processors," in *Solid-State Circuits Conference Digest of Technical Papers (ISSCC), 2010 IEEE International*, 2010, pp. 96-97.

[12] S. M. Merchant, S. H. Kang, M. Sanganeria, B. van Schravendijk, and T. Mountsier, "Copper interconnects for semiconductor devices," *JOM Journal of the Minerals, Metals and Materials Society,* vol. 53, pp. 43-48, 2001.

[13] H. Li, S. Bhunia, Y. Chen, T. Vijaykumar, and K. Roy, "Deterministic clock gating for microprocessor power reduction," in *High-Performance Computer Architecture, 2003. HPCA-9 2003. Proceedings. The Ninth International Symposium on*, 2003, pp. 113-122.

[14] D.-S. Chiou, S.-H. Chen, S.-C. Chang, and C. Yeh, "Timing driven power gating," in *Proceedings of the 43rd annual design automation conference*, 2006, pp. 121-124.

[15] S. A. Tawfik and V. Kursun, "Low power and high speed multi threshold voltage interface circuits," *IEEE transactions on very large scale integration (VLSI) systems,* vol. 17, pp. 638-645, 2009.

[16] J. L. Shin, K. Tam, D. Huang, B. Petrick, H. Pham, C. Hwang, H. Li, A. Smith, T. Johnson, and F. Schumacher, "A 40nm 16-core 128-thread CMT SPARC SoC processor," in *Solid-State Circuits Conference Digest of Technical Papers (ISSCC), 2010 IEEE International*, 2010, pp. 98-99.

[17] S. Jain, S. Khare, S. Yada, V. Ambili, P. Salihundam, S. Ramani, S. Muthukumar, M. Srinivasan, A. Kumar, and S. K. Gb, "A 280mV-to-1.2 V wide-operating-range IA-32 processor in 32nm CMOS," in *Solid-State Circuits Conference Digest of Technical Papers (ISSCC), 2012 IEEE International*, 2012, pp. 66-68.

[18] C. Auth, A. Cappellani, J.-S. Chun, A. Dalis, A. Davis, T. Ghani, G. Glass, T. Glassman, M. Harper, and M.

Hattendorf, "45nm high-k+ metal gate strain-enhanced transistors," in *VLSI Technology, 2008 Symposium on*, 2008, pp. 128-129.

[19] D. J. Wouters, J.-P. Colinge, and H. E. Maes, "Subthreshold slope in thin-film SOI MOSFETs," *IEEE Transactions on Electron Devices,* vol. 37, pp. 2022-2033, 1990.

[20] Soitec. Available: https://www.soitec.com/en

[21] A. S. Brown, "Fast films [ic interconnect insulation]," *IEEE Spectrum,* vol. 40, pp. 36-40, 2003.

[22] S. Adee, "Winner: Semiconductors the ultimate dielectrics is... nothing," *IEEE Spectrum,* vol. 45, pp. 39-42, 2008.

[23] D. Hisamoto, T. Kaga, Y. Kawamoto, and E. Takeda, "A fully depleted lean-channel transistor (DELTA)-a novel vertical ultra thin SOI MOSFET," in *Electron Devices Meeting, 1989. IEDM'89. Technical Digest., International*, 1989, pp. 833-836.

[24] J. Kavalieros, B. Doyle, S. Datta, G. Dewey, M. Doczy, B. Jin, D. Lionberger, M. Metz, W. Rachmady, and M. Radosavljevic, "Tri-gate transistor architecture with high-k gate dielectrics, metal gates and strain engineering," in *VLSI Technology, 2006. Digest of Technical Papers. 2006 Symposium on*, 2006, pp. 50-51.

[25] A. Matsuzawa, "Interconnection technology for IC design; Overview, Issues, and Future," in *IEICE, Silicon photonics reserch meeting*, Tokyo, 2008.

[26] N. Magen, A. Kolodny, U. Weiser, and N. Shamir, "Interconnect-power dissipation in a microprocessor," in *Proceedings of the 2004 international workshop on System level interconnect prediction*, 2004, pp. 7-13.

[27] V. Adler and E. G. Friedman, "Repeater design to reduce delay and power in resistive interconnect," *IEEE Transactions on Circuits and Systems II: Analog and Digital Signal Processing,* vol. 45, pp. 607-616, 1998.

[28] J. W. Goodman, F. J. Leonberger, S.-Y. Kung, and R. A. Athale, "Optical interconnections for VLSI systems," *Proceedings of the IEEE,* vol. 72, pp. 850-866, 1984.

[29] S. Iijima, "Helical microtubules of graphitic carbon," *nature,* vol. 354, p. 56, 1991.

[30] N. Srivastava and K. Banerjee, "Performance analysis of carbon nanotube interconnects for VLSI applications," in *Proceedings of the 2005 IEEE/ACM International conference on Computer-aided design*, 2005, pp. 383-390.

[31] C. Schoenenberger, A. Bachtold, Strunk, J.-P. Salvetat, and L. Forro, "Interference and Interaction in multi-wall carbon nanotubes," *Applied Physics A: Materials Science & Processing,* vol. 69, pp. 283-295, 1999.

[32] A. Naeemi and J. D. Meindl, "Design and performance modeling for single-walled carbon nanotubes as local, semiglobal, and global interconnects in gigascale integrated systems," *IEEE Transactions on Electron Devices,* vol. 54, pp. 26-37, 2007.

[33] N. Srivastava, H. Li, F. Kreupl, and K. Banerjee, "On the applicability of single-walled carbon nanotubes as VLSI interconnects," *IEEE Transactions on Nanotechnology,* vol. 8, pp. 542-559, 2009.

[34] G. F. Close, S. Yasuda, B. Paul, S. Fujita, and H.-S. P. Wong, "A 1 GHz integrated circuit with carbon nanotube interconnects and silicon transistors," *Nano Letters,* vol. 8, pp. 706-709, 2008.

[35] N. Miura, T. Shidei, Y. Yuan, S. Kawai, K. Takatsu, Y. Kiyota, Y. Asano, and T. Kuroda, "A 0.55 V 10 fJ/bit inductive-coupling data link and 0.7 V 135 fJ/cycle clock link with dual-coil transmission scheme," *IEEE Journal of Solid-State Circuits,* vol. 46, pp. 965-973, 2011.

[36] K. Osada, M. Saen, Y. Okuma, K. Niitsu, Y. Shimazaki, Y. Sugimori, Y. Kohama, K. Kasuga, I. Nonomura, and N. Irie, "3D system integration of processor and multi-stacked SRAMs by using inductive-coupling links," in *VLSI Circuits, 2009 Symposium on*, 2009, pp. 256-257.

[37] H. Ito, J. Seita, T. Ishii, H. Sugita, K. Okada, and K. Masu, "A low-latency and high-power-efficient on-chip LVDS transmission line interconnect for an RC interconnect alternative," in *IEEE International Interconnect Technology Conferencee 2007*, 2007, pp. 193-195.

[38] T. Maekawa, H. Ito, and K. Masu, "An 8Gbps 2.5 mW on-chip pulsed-current-mode transmission line

interconnect with a stacked-switch Tx," in *34th European Solid-State Circuits Conference 2008 (ESSCIRC 2008)*, 2008, pp. 474-477.

[39] S.-K. Lee, S.-H. Lee, D. Sylvester, D. Blaauw, and J.-Y. Sim, "A 95fJ/b current-mode transceiver for 10mm on-chip interconnect," in *Solid-State Circuits Conference Digest of Technical Papers (ISSCC), 2013 IEEE International*, 2013, pp. 262-263.

[40] E. Mensink, D. Schinkel, E. A. Klumperink, E. Van Tuijl, and B. Nauta, "Power efficient gigabit communication over capacitively driven RC-limited on-chip interconnects," *IEEE journal of solid-state circuits,* vol. 45, pp. 447-457, 2010.

[41] R. Ho, T. Ono, R. D. Hopkins, A. Chow, J. Schauer, F. Y. Liu, and R. Drost, "High speed and low energy capacitively driven on-chip wires," *IEEE Journal of Solid-State Circuits,* vol. 43, pp. 52-60, 2008.

[42] M. H. Nazari and A. Emami-Neyestanak, "A 20Gb/s 136fJ/b 12.5 Gb/s/µm on-chip link in 28nm CMOS," in *Radio Frequency Integrated Circuits Symposium (RFIC), 2013 IEEE*, 2013, pp. 257-260.

[43] J. Chen, "Self-calibrating on-chip interconnects," Stanford University, 2012.

[44] R. A. Soref and J. P. Lorenzo, "All-silicon active and passive guided-wave components for lambda= 1.3 and 1.6 microns," *IEEE Journal of Quantum Electronics,* vol. 22, pp. 873-879, 1986.

[45] K. K. Lee, D. R. Lim, H.-C. Luan, A. Agarwal, J. Foresi, and L. C. Kimerling, "Effect of size and roughness on light transmission in a Si/SiO 2 waveguide: Experiments and model," *Applied Physics Letters,* vol. 77, pp. 1617-1619, 2000.

[46] K. K. Lee, D. R. Lim, L. C. Kimerling, J. Shin, and F. Cerrina, "Fabrication of ultralow-loss Si/SiO 2 waveguides by roughness reduction," *Optics letters,* vol. 26, pp. 1888-1890, 2001.

[47] A. Sakai, T. Fukazawa, and B. Toshihiko, "Low loss ultra-small branches in a silicon photonic wire waveguide," *IEICE transactions on electronics,* vol. 85, pp. 1033-1038, 2002.

[48] A. Sakai, G. Hara, and T. Baba, "Propagation characteristics of ultrahigh-Δ optical waveguide on silicon-on-insulator substrate," *Japanese Journal of Applied Physics,* vol. 40, p. L383, 2001.

[49] A. Liu, R. Jones, L. Liao, D. Samara-Rubio, D. Rubin, O. Cohen, R. Nicolaescu, and M. Paniccia, "A high-speed silicon optical modulator based on a metal–oxide–semiconductor capacitor," *Nature,* vol. 427, pp. 615-618, 2004.

[50] T. Yin, R. Cohen, M. M. Morse, G. Sarid, Y. Chetrit, D. Rubin, and M. J. Paniccia, "31GHz Ge nip waveguide photodetectors on Silicon-on-Insulator substrate," *Optics Express,* vol. 15, pp. 13965-13971, 2007.

[51] G. Dehlinger, S. Koester, J. Schaub, J. Chu, Q. Ouyang, and A. Grill, "High-speed germanium-on-SOI lateral PIN photodiodes," *IEEE Photonics Technology Letters,* vol. 16, pp. 2547-2549, 2004.

[52] O. Boyraz and B. Jalali, "Demonstration of a silicon Raman laser," *Optics express,* vol. 12, pp. 5269-5273, 2004.

[53] H. Rong, R. Jones, A. Liu, O. Cohen, D. Hak, A. Fang, and M. Paniccia, "A continuous-wave Raman silicon laser," *Nature,* vol. 433, pp. 725-728, 2005.

[54] L. Chen, K. Preston, S. Manipatruni, and M. Lipson, "Integrated GHz silicon photonic interconnect with micrometer-scale modulators and detectors," *Optics express,* vol. 17, pp. 15248-15256, 2009.

[55] N. Ophir, K. Padmaraju, A. Biberman, L. Chen, K. Preston, M. Lipson, and K. Bergman, "First demonstration of error-free operation of a full silicon on-chip photonic link," in *Optical Fiber Communication Conference and Exposition (OFC/NFOEC), 2011 and the National Fiber Optic Engineers Conference*, 2011, pp. 1-3.

[56] X. Xiao, H. Xu, X. Li, Z. Li, Y. Yude, and Y. Jinzhong, "High-speed on-chip photonic link based on ultralow-power microring modulator," in *Optical Fiber Communications Conference and Exhibition (OFC), 2014*, 2014, pp. 1-3.

[57] E. Timurdogan, Z. Su, K. Settaluri, S. Lin, S. Moazeni, C. Sun, G. Leake, D. D. Coolbaugh, B. Moss, and M. Moresco, "An ultra low power 3D integrated intra-chip silicon electronic-photonic link," in *Optical Fiber*

*Communication Conference*, 2015, p. Th5B. 8.

[58] C. Sun, M. T. Wade, Y. Lee, J. S. Orcutt, L. Alloatti, M. S. Georgas, A. S. Waterman, J. M. Shainline, R. R. Avizienis, and S. Lin, "Single-chip microprocessor that communicates directly using light," *Nature,* vol. 528, pp. 534-538, 2015.

[59] E. Timurdogan, C. M. Sorace-Agaskar, J. Sun, E. S. Hosseini, A. Biberman, and M. R. Watts, "An ultralow power athermal silicon modulator," *Nature communications,* vol. 5, 2014.

[60] K. Chen, Q. Huang, J. Zhang, J. Cheng, X. Fu, C. Zhang, K. Ma, Y. Shi, D. Van Thourhout, and G. Roelkens, "Wavelength-Multiplexed Duplex Transceiver Based on III-V/Si Hybrid Integration for Off-Chip and On-Chip Optical Interconnects," *IEEE Photonics Journal,* vol. 8, pp. 1-10, 2016.

[61] T. Spuesens, J. Bauwelinck, P. Regreny, and D. Van Thourhout, "Realization of a compact optical interconnect on silicon by heterogeneous integration of III–V," *Photon. Technol. Lett,* vol. 25, pp. 1332-1335, 2013.

[62] K. Ohira, H. Uemura, N. Iizuka, H. Yoshida, H. Uemura, Y. Kurita, H. Furuyama, and M. Ezaki, "High-speed and stable operation of highly unidirectional III-V/silicon microring lasers for on-chip optical interconnects," in *Lasers and Electro-Optics (CLEO), 2015 Conference on*, 2015, pp. 1-2.

[63] D. A. Miller, "Device requirements for optical interconnects to silicon chips," *Proceedings of the IEEE,* vol. 97, pp. 1166-1185, 2009.

[64] J. Van Campenhout, P. R. Binetti, P. R. Romeo, P. Regreny, C. Seassal, X. J. Leijtens, T. de Vries, Y. S. Oei, R. P. van Veldhoven, and R. Notzel, "Low-footprint optical interconnect on an SOI chip through heterogeneous integration of InP-based microdisk lasers and microdetectors," *IEEE Photonics Technology Letters,* vol. 21, pp. 522-524, 2009.

[65] K. Takeda, T. Sato, A. Shinya, K. Nozaki, W. Kobayashi, H. Taniyama, M. Notomi, K. Hasebe, T. Kakitsuka, and S. Matsuo, "Few-fJ/bit data transmissions using directly modulated lambda-scale embedded active region photonic-crystal lasers," *Nature Photonics,* vol. 7, pp. 569-575, 2013.

[66] K. Takeda, T. Sato, A. Shinya, K. Nozaki, H. Taniyama, M. Notomi, K. Hasebe, T. Kakitsuka, and S. Matsuo, "Integrated on-chip optical links using photonic-crystal lasers and photodetectors with current blocking trenches," in *Optical Fiber Communication Conference and Exposition and the National Fiber Optic Engineers Conference (OFC/NFOEC), 2013*, 2013, pp. 1-3.

[67] T. Sato, K. Takeda, A. Shinya, M. Notomi, K. Hasebe, T. Kakitsuka, and S. Matsuo, "Photonic crystal lasers for chip-to-chip and on-chip optical interconnects," *IEEE Journal of Selected Topics in Quantum Electronics,* vol. 21, pp. 728-737, 2015.

[68] K.-H. Koo, P. Kapur, and K. C. Saraswat, "Compact performance models and comparisons for gigascale on-chip global interconnect technologies," *IEEE Transactions on Electron Devices,* vol. 56, pp. 1787-1798, 2009.

[69] L. A. Coldren, S. W. Corzine, and M. L. Mashanovitch, *Diode lasers and photonic integrated circuits*. New York, NY, USA: Wiley-Interscience, 1995.

[70] I. Hayashi, M. Panish, P. Foy, and S. Sumski, "Junction lasers which operate continuously at room temperature," *Applied Physics Letters,* vol. 17, pp. 109-111, 1970.

[71] M. Panish, I. Hayashi, and S. Sumski, "DOUBLE‐HETEROSTRUCTURE INJECTION LASERS WITH ROOM‐TEMPERATURE THRESHOLDS AS LOW AS 2300 A/cm," *Applied Physics Letters,* vol. 16, pp. 326-327, 1970.

[72] F. Kapron, D. B. Keck, and R. D. Maurer, "Radiation losses in glass optical waveguides," *Applied Physics Letters,* vol. 17, pp. 423-425, 1970.

[73] T. Izawa, S. Sudo, and F. Hanawa, "Continuous fabrication process for high-silica fiber preforms," *IEICE Transactions (1976-1990),* vol. 62, pp. 779-785, 1979.

[74] M. Horiguchi and H. Osanai, "Spectral losses of low-OH-content optical fibres," *Electronics Letters,* vol. 12, pp. 310-312, 1976.

[75] T. Miya, Y. Terunuma, T. Hosaka, and T. Miyashita, "Ultimate low-loss single-mode fibre at 1.55 μm," *Electronics Letters,* vol. 15, pp. 106-108, 1979.

[76] T. Yamamoto, K. Sakai, S. Akiba, and Y. Suematsu, "Fast pulse behaviour of InGaAsP/InP double-heterostructure lasers emitting at 1.27 μm," *Electronics Letters,* vol. 13, pp. 142-143, 1977.

[77] K. Oe and K. Sugiyama, "GaInAsP-InP double heterostructure lasers prepared by a new LPE apparatus," *Japanese Journal of Applied Physics,* vol. 15, pp. 2003–2004, 1976.

[78] S. Arai, Y. Suematsu, and Y. Itaya, "1.67 m Ga_0. 47In_0. 53As/InP DH Lasers Double Cladded with InP by LPE Technique," *Japanese Journal of Applied Physics,* vol. 18, pp. 709-710, 1979.

[79] S. Akiba, K. Sakai, Y. Matsushima, and T. Yamamoto, "Room temperature cw operation of InGaAsP/InP heterostructure lasers emitting at 1.56 μm," *Electronics Letters,* vol. 15, pp. 606-607, 1979.

[80] H. Kogelnik and C. Shank, "Stimulated emission in a periodic structure," *Applied Physics Letters,* vol. 18, pp. 152-154, 1971.

[81] H. Kogelnik and C. Shank, "Coupled-wave theory of distributed feedback lasers," *Journal of Applied Physics,* vol. 43, pp. 2327-2335, 1972.

[82] M. Nakamura, A. Yariv, H. Yen, S. Somekh, and H. Garvin, "Optically pumped GaAs surface laser with corrugation feedback," *Applied Physics Letters,* vol. 22, pp. 515-516, 1973.

[83] H. Soda, K.-i. Iga, C. Kitahara, and Y. Suematsu, "GaInAsP/InP surface emitting injection lasers," *Japanese Journal of Applied Physics,* vol. 18, p. 2329, 1979.

[84] F. Koyama, S. KINOSHITA, and I. Kenichi, "Room temperature cw operation of GaAs vertical cavity surface emitting laser," *IEICE TRANSACTIONS (1976-1990),* vol. 71, pp. 1089-1090, 1988.

[85] F. Koyama, S. Kinoshita, and K. Iga, "Room‐temperature continuous wave lasing characteristics of a GaAs vertical cavity surface‐emitting laser," *Applied Physics Letters,* vol. 55, p. 221, 1989.

[86] N. Holonyak, R. Kolbas, R. Dupuis, and P. Dapkus, "Quantum-well heterostructure lasers," *IEEE Journal of Quantum Electronics,* vol. 16, pp. 170-186, 1980.

[87] A. Adams, "Band-structure engineering for low-threshold high-efficiency semiconductor lasers," *Electronics Letters,* vol. 22, pp. 249-250, 1986.

[88] E. Yablonovitch and E. Kane, "Reduction of lasing threshold current density by the lowering of valence band effective mass," *Journal of Lightwave Technology,* vol. 4, pp. 504-506, 1986.

[89] P. J. Thijs, L. F. Tiemeijer, P. Kuindersma, J. Binsma, and T. Van Dongen, "High-performance 1.5 mu m wavelength InGaAs-InGaAsP strained quantum well lasers and amplifiers," *IEEE journal of quantum electronics,* vol. 27, pp. 1426-1439, 1991.

[90] P. Thijs, J. Binsma, L. Tiemeijer, and T. Van Dongen, "Submilliamp threshold current (0.62 mA at 0° C) and high output power (220 mW) 1.5 μm tensile strained InGaAs single quantum well lasers," *Electronics Letters,* vol. 28, pp. 829-830, 1992.

[91] C.-E. Zah, R. Bhat, B. N. Pathak, F. Favire, W. Lin, M. Wang, N. C. Andreadakis, D. Hwang, M. Koza, and T.-P. Lee, "High-performance uncooled 1.3-/spl mu/m Al/sub x/Ga/sub y/In/sub 1-xy/As/InP strained-layer quantum-well lasers for subscriber loop applications," *IEEE Journal of Quantum Electronics,* vol. 30, pp. 511-523, 1994.

[92] C. Zah, R. Bhat, and T. Lee, "High temperature operation of AlGaInAs/InP lasers," in *Indium Phosphide and Related Materials, 1995. Conference Proceedings., Seventh International Conference on*, 1995, pp. 14-17.

[93] H. Lu, C. Blaauw, and T. Makino, "Single-mode operation over a wide temperature range in 1.3/spl mu/m InGaAsP/InP distributed feedback lasers," *Journal of lightwave technology,* vol. 14, pp. 851-859, 1996.

[94] K. Uomi, "Modulation-doped multi-quantum well (MD-MQW) lasers. I. Theory," *Japanese journal of applied physics,* vol. 29, p. 81, 1990.

[95] K. Uomi, T. Mishima, and N. Chinone, "Modulation-doped multi-quantum well (MD-MQW) lasers. II.

Experiment," *Japanese journal of applied physics,* vol. 29, p. 88, 1990.

[96] T. Tadokoro, T. Yamanaka, F. Kano, H. Oohashi, Y. Kondo, and K. Kishi, "Operation of a 25-Gb/s Direct Modulation Ridge Waveguide MQW-DFB Laser up to 85°C," *IEEE Photonics Technology Letters,* vol. 21, pp. 1154-1156, 2009.

[97] A. Nakanishi, T. Nakajima, N. Sasada, S. Hayakawa, Y. Sakuma, M. Mukaikubo, R. Washino, K. Naoe, K. Nakahara, and K. Uomi, "120° C, 25.8-Gbps operation of 1.3-μm directly modulated InGaAlAs-MQW DFB lasers," in *Semiconductor Laser Conference (ISLC), 2016 International*, 2016, pp. 1-2.

[98] W. Kobayashi, T. Ito, T. Yamanaka, T. Fujisawa, Y. Shibata, T. Kurosaki, M. Kohtoku, T. Tadokoro, and H. Sanjoh, "50-Gb/s direct modulation of a 1.3-μm InGaAlAs-based DFB laser with a ridge waveguide structure," *IEEE Journal of Selected Topics in Quantum Electronics,* vol. 19, p. 1500908, 2013.

[99] S. Imai, K. Takaki, S. Kamiya, H. Shimizu, J. Yoshida, Y. Kawakita, T. Takagi, K. Hiraiwa, T. Suzuki, and N. Iwai, "Recorded low power dissipation in highly reliable 1060-nm VCSELs for “Green” optical interconnection," *IEEE Journal of Selected Topics in Quantum Electronics,* vol. 17, pp. 1614-1620, 2011.

[100] C. Schow and A. Rylyakov, "30 Gbit/s, 850 nm, VCSEL-based optical link," *Electronics letters,* vol. 47, pp. 1035-1036, 2011.

[101] D. Pienkowski, V. Subramanian, and G. Boeck, "A 0.7 V, 23 GHz, low cost BiCMOS amplifier with 2.8 mW power consumption," in *Wireless Technology, 2006. The 9th European Conference on*, 2006, pp. 71-74.

[102] J. A. Tatum, D. Gazula, L. A. Graham, J. K. Guenter, R. H. Johnson, J. King, C. Kocot, G. D. Landry, I. Lyubomirsky, and A. N. MacInnes, "VCSEL-based interconnects for current and future data centers," *Journal of Lightwave Technology,* vol. 33, pp. 727-732, 2015.

[103] L. A. Graham, H. Chen, D. Gazula, T. Gray, J. K. Guenter, B. Hawkins, R. Johnson, C. Kocot, A. N. MacInnes, and G. D. Landry, "The next generation of high speed VCSELs at Finisar," in *SPIE OPTO*, 2012, pp. 827602-827602-10.

[104] R. Tucker, J. Wiesenfeld, P. Downey, and J. Bowers, "Propagation delays and transition times in pulse‐modulated semiconductor lasers," *Applied physics letters,* vol. 48, pp. 1707-1709, 1986.

[105] D. Huffaker, D. Deppe, C. Lei, and L. Hodge, "Sealing AlAs against oxidative decomposition and its use in device fabrication," *Applied physics letters,* vol. 68, pp. 1948-1950, 1996.

[106] Y. Hayashi, T. Mukaihara, N. Hatori, N. Ohnoki, A. Matsutani, F. Koyama, and K. Iga, "Lasing characteristics of low-threshold oxide confinement InGaAs-GaAlAs vertical-cavity surface-emitting lasers," *IEEE Photonics Technology Letters,* vol. 7, pp. 1234-1236, 1995.

[107] F. Koyama, K. Tomomatsu, and K. Iga, "GaAs surface emitting lasers with circular buried heterostructure grown by metalorganic chemical vapor deposition and two‐dimensional laser array," *Applied physics letters,* vol. 52, pp. 528-529, 1988.

[108] G. Yang, M. MacDougal, and P. Dapkus, "Ultralow threshold current vertical-cavity surface-emitting lasers obtained with selective oxidation," *Electronics Letters,* vol. 31, pp. 886-888, 1995.

[109] K. Iga, "Iga's reserch note," March 22 1977.

[110] C.-T. Chen, P.-K. Shen, T.-Z. Zhu, C.-C. Chang, S.-S. Lin, M.-Y. Zeng, C.-Y. Chiu, H.-L. Hsiao, H.-C. Lan, and Y.-C. Lee, "Chip-Level 1 2 Optical Interconnects Using Polymer Vertical Splitter on Silicon Substrate," *IEEE Photonics Journal,* vol. 6, pp. 1-10, 2014.

[111] P. Moser, W. Hofmann, P. Wolf, J. Lott, G. Larisch, A. Payusov, N. Ledentsov, and D. Bimberg, "81 fJ/bit energy-to-data ratio of 850 nm vertical-cavity surface-emitting lasers for optical interconnects," *Applied Physics Letters,* vol. 98, pp. 231106-231106-3, 2011.

[112] P. Moser, J. Lott, P. Wolf, G. Larisch, H. Li, N. Ledentsov, and D. Bimberg, "56 fJ dissipated energy per bit of oxide-confined 850 nm VCSELs operating at 25 Gbit/s," *Electronics letters,* vol. 48, pp. 1292-1294, 2012.

[113] P.-K. Shen, C.-T. Chen, R.-H. Chen, S.-S. Lin, C.-C. Chang, H.-L. Hsiao, H.-C. Lan, Y.-C. Lee, Y.-S. Lin,

and M.-L. Wu, "Chip-Level Optical Interconnects Using Polymer Waveguide Integrated With Laser/PD on Silicon," *IEEE Photonics Technology Letters,* vol. 27, pp. 1359-1362, 2015.

[114] P.-K. Shen, C.-T. Chen, C.-H. Chang, C.-Y. Chiu, S.-L. Li, C.-C. Chang, and M.-L. Wu, "Implementation of Chip-Level Optical Interconnect With Laser and Photodetector Using SOI-Based 3-D Guided-Wave Path," *IEEE Photonics Journal,* vol. 6, pp. 1-10, 2014.

[115] S. McCall, A. Levi, R. Slusher, S. Pearton, and R. Logan, "Whispering‐gallery mode microdisk lasers," *Applied Physics Letters,* vol. 60, p. 289, 1992.

[116] J. Van Campenhout, P. Rojo-Romeo, P. Regreny, C. Seassal, D. Van Thourhout, S. Verstuyft, L. Di Cioccio, J.-M. Fedeli, C. Lagahe, and R. Baets, "Electrically pumped InP-based microdisk lasers integrated with a nanophotonic silicon-on-insulator waveguide circuit," *Optics Express,* vol. 15, pp. 6744-6749, 2007.

[117] A. Levi, R. Slusher, S. McCall, T. Tanbun-Ek, D. Coblentz, and S. Pearton, "Room temperature operation of microdisc lasers with submilliamp threshold current," *Electronics Letters,* vol. 28, pp. 1010-1012, 1992.

[118] M. Fujita, R. Ushigome, and T. Baba, "Continuous wave lasing in GaInAsP microdisk injection laser with threshold current of 40 μA," *Electronics Letters,* vol. 36, pp. 790-791, 2000.

[119] S. J. Choi, K. Djordjev, S. J. Choi, and P. D. Dapkus, "Microdisk lasers vertically coupled to output waveguides," *IEEE Photonics technology letters,* vol. 15, pp. 1330-1332, 2003.

[120] S. A. Maier, "Effective mode volume of nanoscale plasmon cavities," *Optical and Quantum Electronics,* vol. 38, pp. 257-267, 2006.

[121] D. J. Bergman and M. I. Stockman, "Surface plasmon amplification by stimulated emission of radiation: quantum generation of coherent surface plasmons in nanosystems," *Physical review letters,* vol. 90, p. 027402, 2003.

[122] A. Maslov and C. Ning, "Size reduction of a semiconductor nanowire laser by using metal coating," in *Integrated Optoelectronic Devices 2007*, 2007, p. 64680I.

[123] M. T. Hill, Y.-S. Oei, B. Smalbrugge, Y. Zhu, T. De Vries, P. J. Van Veldhoven, F. W. Van Otten, T. J. Eijkemans, J. P. Turkiewicz, and H. De Waardt, "Lasing in metallic-coated nanocavities," *Nature Photonics,* vol. 1, pp. 589-594, 2007.

[124] J. H. Lee, M. Khajavikhan, A. Simic, Q. Gu, O. Bondarenko, B. Slutsky, M. P. Nezhad, and Y. Fainman, "Electrically pumped sub-wavelength metallo-dielectric pedestal pillar lasers," *Optics express,* vol. 19, pp. 21524-21531, 2011.

[125] K. Ding, Z. Liu, L. Yin, H. Wang, R. Liu, M. T. Hill, M. J. Marell, P. J. Van Veldhoven, R. Nötzel, and C.-Z. Ning, "Electrical injection, continuous wave operation of subwavelength-metallic-cavity lasers at 260 K," *Applied physics letters,* vol. 98, p. 231108, 2011.

[126] K. Ding, Z. Liu, L. Yin, M. Hill, M. Marell, P. Van Veldhoven, R. Nöetzel, and C.-Z. Ning, "Room-temperature continuous wave lasing in deep-subwavelength metallic cavities under electrical injection," *Physical Review B,* vol. 85, p. 041301, 2012.

[127] K. Ding, M. Hill, Z. Liu, L. Yin, P. Van Veldhoven, and C.-Z. Ning, "Record performance of electrical injection sub-wavelength metallic-cavity semiconductor lasers at room temperature," *Optics express,* vol. 21, pp. 4728-4733, 2013.

[128] M. Khajavikhan, A. Simic, M. Katz, J. Lee, B. Slutsky, A. Mizrahi, V. Lomakin, and Y. Fainman, "Thresholdless nanoscale coaxial lasers," *Nature,* vol. 482, pp. 204-207, 2012.

[129] E. Yablonovitch, "Inhibited spontaneous emission in solid-state physics and electronics," *Physical Review Letters,* vol. 58, pp. 2059-2062, 1987.

[130] S. Matsuo, K. Takeda, T. Sato, M. Notomi, A. Shinya, K. Nozaki, H. Taniyama, K. Hasebe, and T. Kakitsuka, "Room-temperature continuous-wave operation of lateral current injection wavelength-scale embedded active-region photonic-crystal laser," *Optics Express,* vol. 20, pp. 3773-3780, 2012.

[131] O. Painter, R. Lee, A. Scherer, A. Yariv, J. O'brien, P. Dapkus, and I. Kim, "Two-dimensional photonic band-gap defect mode laser," *Science,* vol. 284, pp. 1819-1821, 1999.

[132] W. Zhou, J. Sabarinathan, B. Kochman, E. Berg, O. Qasaimeh, S. Pang, and P. Bhattacharya, "Electrically injected single-defect photonic bandgap surface-emitting laser at room temperature," *Electronics Letters,* vol. 36, pp. 1541-1542, 2000.

[133] H.-G. Park, S.-H. Kim, S.-H. Kwon, Y.-G. Ju, J.-K. Yang, J.-H. Baek, S.-B. Kim, and Y.-H. Lee, "Electrically driven single-cell photonic crystal laser," *Science,* vol. 305, pp. 1444-1447, 2004.

[134] K.-Y. Jeong, Y.-S. No, Y. Hwang, K. S. Kim, M.-K. Seo, H.-G. Park, and Y.-H. Lee, "Electrically driven nanobeam laser," *Nature communications,* vol. 4, p. 2822 2013.

[135] D. Ohnishi, T. Okano, M. Imada, and S. Noda, "Room temperature continuous wave operation of a surface-emitting two-dimensional photonic crystal diode laser," *Optics Express,* vol. 12, pp. 1562-1568, 2004.

[136] S. Matsuo, A. Shinya, T. Kakitsuka, K. Nozaki, T. Segawa, T. Sato, Y. Kawaguchi, and M. Notomi, "High-speed ultracompact buried heterostructure photonic-crystal laser with 13 fJ of energy consumed per bit transmitted," *Nature Photonics,* vol. 4, pp. 648-654, 2010.

[137] S. Matsuo, A. Shinya, C.-H. Chen, K. Nozaki, T. Sato, Y. Kawaguchi, H. Taniyama, and M. Notomi, "20-Gbit/s directly modulated photonic crystal nanocavity laser with ultra-low power consumption," *Optics Express,* vol. 19, pp. 2242-2250, 2011.

[138] S. Matsuo, K. Takeda, T. Sato, M. Notomi, A. Shinya, K. Nozaki, K. Hasebe, and T. Kakitsuka, "10-Gbit/s direct modulation of electrically driven photonic crystal nanocavity laser," in *Optical Fiber Communication Conference*, 2012.

[139] K. Takeda, T. Sato, A. Shinya, K. Nozaki, W. Kobayashi, H. Taniyama, M. Notomi, K. Hasebe, T. Kakitsuka, and S. Matsuo, "Few-fJ/bit data transmissions using directly modulated lambda-scale embedded active region photonic-crystal lasers," *Nature Photonics,* vol. 7, pp. 569–575, 2013.

[140] K. Takeda, T. Sato, T. Fujii, E. Kuramochi, M. Notomi, K. Hasebe, T. Kakitsuka, and S. Matsuo, "Heterogeneously integrated photonic-crystal lasers on silicon for on/off chip optical interconnects," *Optics Express,* vol. 23, pp. 702-708, 2015.

[141] K. Utaka, S. Akiba, K. Sakai, and Y. Matsushima, "$\lambda/4$-shifted InGaAsP/InP DFB lasers by simultaneous holographic exposure of positive and negative photoresists," *Electronics Letters,* vol. 20, pp. 1008-1010, 1984.

[142] E. Kapon, A. Hardy, and A. Katzir, "The effect of complex coupling coefficients on distributed feedback lasers," *IEEE Journal of Quantum Electronics,* vol. 18, pp. 66-71, 1982.

[143] W. Streifer, R. Burnham, and D. Scifres, "Effect of external reflectors on longitudinal modes of distributed feedback lasers," *IEEE Journal of Quantum Electronics,* vol. 11, pp. 154-161, 1975.

[144] K. Utaka, S. Akiba, K. Sakai, and Y. Matsushima, "Effect of mirror facets on lasing characteristics of distributed feedback InGaAsP/InP laser diodes at 1.5 μm range," *IEEE Journal of Quantum Electronics,* vol. 20, pp. 236-245, 1984.

[145] N. Nunoya, M. Nakamura, M. Morshed, S. Tamura, and S. Arai, "High-performance 1.55-μm wavelength GaInAsP-InP distributed-feedback lasers with wirelike active regions," *IEEE Journal of Selected Topics in Quantum Electronics,* vol. 7, pp. 249-258, 2001.

[146] T. Shindo, S. Lee, D. Takahashi, N. Tajima, N. Nishiyama, and S. Arai, "Low-threshold and high-efficiency operation of distributed reflector laser with wirelike active regions," *IEEE Photonics Technology Letters,* vol. 21, pp. 1414-1416, 2009.

[147] K. David, G. Morthier, P. Vankwikelberge, and R. Baets, "Yield analysis of non-AR-coated DFB lasers with combined index and gain coupling," *Electronics Letters,* vol. 26, pp. 238-239, 1990.

[148] B. Borchert, K. David, B. Stegmuller, R. Gessner, M. Beschorner, D. Sacher, and G. Franz, "1.55 μm gain-

coupled quantum-well distributed feedback lasers with high single-mode yield and narrow linewidth," *IEEE Photonics Technology Letters,* vol. 3, pp. 955-957, 1991.

[149] K. Komori, S. Arai, Y. Suematsu, and I. Arima, "Proposal of distributed reflector (DR) structure for high efficiency dynamic single mode (DSM) lasers," *IEICE Transactions,* vol. 71, pp. 318-320, 1988.

[150] K. Komori, S. Arai, Y. Suematsu, I. Arima, and M. Aoki, "Single-mode properties of distributed-reflector lasers," *IEEE Journal of Quantum Electronics,* vol. 25, pp. 1235-1244, 1989.

[151] J.-I. Shim, K. Komori, S. Arai, I. Arima, Y. Suematsu, and R. Somchai, "Lasing characteristics of 1.5 μm GaInAsP-InP SCH-BIG-DR lasers," *IEEE journal of quantum electronics,* vol. 27, pp. 1736-1745, 1991.

[152] G. Kobayashi, K. Kiyota, T. Kimoto, and T. Mukaihara, "Narrow linewidth tunable light source integrated with distributed reflector laser array," in *Optical Fiber Communication Conference*, 2014, p. Tu2H. 2.

[153] Y. Matsui, T. Pham, W. A. Ling, R. Schatz, G. Carey, H. Daghighian, T. Sudo, and C. Roxlo, "55-GHz bandwidth short-cavity distributed reflector laser and its application to 112-Gb/s PAM-4," in *Optical Fiber Communications Conference and Exhibition (OFC), 2016*, 2016, pp. 1-3.

[154] M. Matsuda, A. Uetake, T. Simoyama, S. Okumura, K. Takabayashi, M. Ekawa, and T. Yamamoto, "1.3-μm-wavelength AlGaInAs multiple-quantum-well semi-insulating buried-heterostructure distributed-reflector laser arrays on semi-insulating InP substrate," *IEEE Journal of Selected Topics in Quantum Electronics,* vol. 21, pp. 241-247, 2015.

[155] H. Matsuura, T. Kaneko, K. Tanizawa, E. Banno, K. Uesaka, H. Kuwatsuka, S. Namiki, and H. Shoji, "Suppression of channel-by-channel variation in wavelength switching time of TDA-CSG-DR laser," in *Optical Fibre Technology, 2014 OptoElectronics and Communication Conference and Australian Conference on*, 2014, pp. 296-298.

[156] N. Nunoya, M. Nakamura, H. Yasumoto, S. Tamura, and S. Arai, "Low Threshold GaInAsP/InP Distributed Feedback Lasers with Periodic Wire Active Regions Fabricated by $CH_4/H_2$ Reactive Ion Etching," *Japanese Journal of Applied Physics,* vol. 38, pp. L1323-L1326, 1999.

[157] N. Nunoya, H. Yasumoto, H. Midorikawa, S. Tamura, and S. Arai, "Low threshold current density operation of GaInAsP/InP lasers with strain-compensated multiple-layered wirelike active regions," *Japanese Journal of Applied Physics,* vol. 39, pp. 1042-1045, 2000.

[158] N. Nunoya, M. Nakamura, H. Yasumoto, S. Tamura, and S. Arai, "GaInAsP/InP multiple-layered quantum-wire lasers fabricated by $CH_4/H_2$ reactive-ion etching," *Japanese Journal of Applied Physics,* vol. 39, pp. 3410-3415, 2000.

[159] N. Nunoya, M. Nakamura, H. Yasumoto, M. Morshed, K. Fukuda, S. Tamura, and S. Arai, "Sub-milliampere operation of 1.55 μm wavelength high index-coupled buried heterostructure distributed feedback lasers," *Electronics Letters,* vol. 36, pp. 1213-1214, 2000.

[160] K. Ohira, T. Murayama, M. Hirose, H. Yagi, S. Tamura, and S. Arai, "Low-threshold and high-efficiency operation of 1.5 μm distributed reflector laser with DFB grating and Q-wire DBR sections," *Electronics Letters,* vol. 40, pp. 1269-1270, 2004.

[161] S. Lee, D. Takahashi, T. Shindo, K. Shinno, T. Amemiya, N. Nishiyama, and S. Arai, "Low-Power-Consumption High-Eye-Margin 10-Gb/s Operation by GaInAsP/InP Distributed Reflector Lasers With Wirelike Active Regions," *IEEE Photonics Technology Letters,* vol. 23, pp. 1349-1351, 2011.

[162] D. Takahashi, S. Lee, M. Shirao, T. Shindo, K. Shinno, T. Amemiya, N. Nishiyama, and S. Arai, "Carrier-Transport-Limited Modulation Bandwidth in Distributed Reflector Lasers With Wirelike Active Regions," *IEEE Journal of Quantum Electronics,* vol. 48, pp. 688-695, 2012.

[163] T. Windhorn, G. Metze, B. Y. Tsaur, and J. C. Fan, "AlGaAs double‐heterostructure diode lasers fabricated on a monolithic GaAs/Si substrate," *Applied Physics Letters,* vol. 45, pp. 309-311, 1984.

[164] A. Y. Liu, C. Zhang, J. Norman, A. Snyder, D. Lubyshev, J. M. Fastenau, A. W. Liu, A. C. Gossard, and J. E.

Bowers, "High performance continuous wave 1.3 μm quantum dot lasers on silicon," *Applied Physics Letters,* vol. 104, p. 041104, 2014.

[165] A. Shigetou, T. Itoh, M. Matsuo, N. Hayasaka, K. Okumura, and T. Suga, "Bumpless interconnect through ultrafine Cu electrodes by means of surface-activated bonding (SAB) method," *IEEE transactions on advanced packaging,* vol. 29, pp. 218-226, 2006.

[166] A. W. Fang, H. Park, O. Cohen, R. Jones, M. J. Paniccia, and J. E. Bowers, "Electrically pumped hybrid AlGaInAs-silicon evanescent laser," *Optics Express,* vol. 14, pp. 9203-9210, 2006.

[167] H. Park, A. W. Fang, S. Kodama, and J. E. Bowers, "Hybrid silicon evanescent laser fabricated with a silicon waveguide and III-V offset quantum wells," *Optics Express,* vol. 13, pp. 9460-9464, 2005.

[168] Y. Hayashi, R. Osabe, K. Fukuda, Y. Atsumi, J. Kang, N. Nishiyama, and S. Arai, "Low threshold current density operation of a GaInAsP/Si hybrid laser prepared by low-temperature $N_2$ plasma activated bonding," *Japanese Journal of Applied Physics,* vol. 52, p. 060202, 2013.

[169] S. Matsuo, T. Fujii, K. Hasebe, K. Takeda, T. Sato, and T. Kakitsuka, "Directly modulated buried heterostructure DFB laser on SiO 2/Si substrate fabricated by regrowth of InP using bonded active layer," *Optics express,* vol. 22, pp. 12139-12147, 2014.

[170] 須賀唯知, "常温接合による銅バンプレスインタコネクトと三次元集積化," ***電子情報通信学会論文誌*** *C,* vol. 91, pp. 519-526, 2008.

[171] D. Burdeaux, P. Townsend, J. Carr, and P. Garrou, "Benzocyclobutene (BCB) dielectrics for the fabrication of high density, thin film multichip modules," *Journal of Electronic Materials,* vol. 19, pp. 1357-1366, 1990.

[172] G. Roelkens, L. Liu, D. Liang, R. Jones, A. Fang, B. Koch, and J. Bowers, "III‐V/silicon photonics for on‐chip and intra‐chip optical interconnects," *Laser & Photonics Reviews,* vol. 4, pp. 751-779, 2010.

[173] D. Inoue, J. Lee, T. Hiratani, Y. Atsuji, T. Amemiya, N. Nishiyama, and S. Arai, "Sub-milliampere threshold operation of butt-jointed built-in membrane DFB laser bonded on Si substrate," *Optics express,* vol. 23, pp. 7771-7778, 2015.

[174] T. Okamoto, N. Nunoya, Y. Onodera, S. Tamura, and S. Arai, "Continuous wave operation of optically pumped membrane DFB laser," *Electronics Letters,* vol. 37, pp. 1455-1457, 2001.

[175] 松井研輔, 岡本健志, 布谷伸浩, and 荒井滋久, "半導体薄膜活性層分離型 DFB レーザの閾値電流解析," ***第48 回応用物理学会関係連合講演会*** 2001.

[176] T. Okamoto, N. Nunoya, Y. Onodera, S. Tamura, and S. Arai, "Single-mode operation of optically pumped membrane buried heterostructure distributed-feedback lasers," *Japanese Journal of Applied Physics,* vol. 41, pp. L249-L251, 2002.

[177] T. Okamoto, N. Nunoya, Y. Onodera, S. Tamura, and S. Arai, "Low-threshold singlemode operation of membrane BH-DFB lasers," *Electronics Letters,* vol. 38, pp. 1444-1446, 2002.

[178] T. Okamoto, N. Nunoya, Y. Onodera, T. Yamazaki, S. Tamura, and S. Arai, "Optically pumped membrane BH-DFB lasers for low-threshold and single-mode operation," *IEEE Journal of Selected Topics in Quantum Electronics,* vol. 9, pp. 1361-1366, 2003.

[179] T. Okamoto, T. Yamazaki, S. Sakamoto, S. Tamura, and S. Arai, "Low-threshold membrane BH-DFB laser arrays with precisely controlled wavelength over a wide range," *IEEE Photonics Technology Letters,* vol. 16, pp. 1242-1244, 2004.

[180] S. Sakamoto, T. Okamoto, T. Yamazaki, S. Tamura, and S. Arai, "Multiple-wavelength membrane BH-DFB laser arrays," *IEEE Journal of Selected Topics in Quantum Electronics,* vol. 11, pp. 1174-1179, 2005.

[181] S. Sakamoto, H. Kawashima, H. Naitoh, S. Tamura, T. Maruyama, and S. Arai, "Reduced temperature dependence of lasing wavelength in membrane buried heterostructure DFB lasers with polymer cladding layers," *IEEE Photonics Technology Letters,* vol. 19, pp. 291-293, 2007.

[182] S. Sakamoto, H. Naitoh, M. Ohtake, Y. Nishimoto, T. Maruyama, N. Nishiyama, and S. Arai, "85 °C

continuous-wave operation of GaInAsP/InP-membrane buried heterostructure distributed feedback lasers with polymer cladding layer," *Japanese Journal of Applied Physics,* vol. 46, pp. L1155-L1157, 2007.

[183] S. Sakamoto, H. Naitoh, M. Ohtake, Y. Nishimoto, S. Tamura, T. Maruyama, N. Nishiyama, and S. Arai, "Strongly index-coupled membrane BH-DFB lasers with surface corrugation grating," *IEEE Journal of Selected Topics in Quantum Electronics,* vol. 13, pp. 1135-1141, 2007.

[184] T. Maruyama, T. Okumura, S. Sakamoto, K. Miura, Y. Nishimoto, and S. Arai, "GaInAsP/InP membrane BH-DFB lasers directly bonded on SOI substrate," *Optics Express,* vol. 14, pp. 8184-8188, 2006.

[185] T. Maruyama, T. Okumura, and S. Arai, "Direct wafer bonding of GaInAsP/InP membrane structure on silicon-on-insulator substrate," *Japanese Journal of Applied Physics,* vol. 45, pp. 8717-8718, 2006.

[186] T. Okumura, T. Maruyama, M. Kanemaru, S. Sakamoto, and S. Arai, "Single-mode operation of GaInAsP/InP-membrane distributed feedback lasers bonded on silicon-on-insulator substrate with rib-waveguide structure," *Japanese Journal of Applied Physics,* vol. 46, pp. L1206-L1208, 2007.

[187] T. Okumura, T. Maruyama, H. Yonezawa, N. Nishiyama, and S. Arai, "Injection-type GaInAsP–InP–Si distributed-feedback laser directly bonded on silicon-on-insulator substrate," *IEEE Photonics Technology Letters,* vol. 21, pp. 283-285, 2009.

[188] H. Naitoh, S. Sakamoto, M. Ohtake, T. Okumura, T. Maruyama, N. Nishiyama, and S. Arai, "GaInAsP/InP membrane buried heterostructure distributed feedback laser with air-bridge structure," *Japanese Journal of Applied Physics,* vol. 46, pp. L1158-L1160, 2007.

[189] H. Namizaki, H. Kan, M. Ishii, and A. Ito, "Transverse‐junction‐stripe‐geometry double‐heterostructure lasers with very low threshold current," *Journal of Applied Physics,* vol. 45, pp. 2785-2786, 1974.

[190] A. Furuya, M. Makiuchi, O. Wada, T. Fujii, and H. Nobuhara, "AlGaAs/GaAs lateral current injection (LCI)-MQW laser using impurity-induced disordering," *Japanese Journal of Applied Physics,* vol. 26, pp. L134-L135, 1987.

[191] K. Oe, Y. Noguchi, and C. Caneau, "GaInAsP lateral current injection lasers on semi-insulating substrates," *Photonics Technology Letters, IEEE,* vol. 6, pp. 479-481, 1994.

[192] T. Shindo, T. Okumura, H. Ito, T. Koguchi, D. Takahashi, Y. Atsumi, J. Kang, R. Osabe, T. Amemiya, and N. Nishiyama, "GaInAsP/InP lateral-current-injection distributed feedback laser with a-Si surface grating," *Optics Express,* vol. 19, pp. 1884-1891, 2011.

[193] M. Futami, T. Shindo, T. Koguchi, K. Shinno, T. Amemiya, N. Nishiyama, and S. Arai, "GaInAsP/InP Lateral Current Injection Laser With Uniformly Distributed Quantum-Well Structure," *IEEE Photonics Technology Letters,* vol. 24, pp. 888-890, 2012.

[194] C. M. Long, A. V. Giannopoulos, and K. D. Choquette, "Modified spontaneous emission from laterally injected photonic crystal emitter," *Electronics Letters,* vol. 45, p. 227, 2009.

[195] B. Ellis, T. Sarmiento, M. Mayer, B. Zhang, J. Harris, E. Haller, and J. Vuckovic, "Electrically pumped photonic crystal nanocavity light sources using a laterally doped pin junction," *Applied Physics Letters,* vol. 96, p. 181103, 2010.

[196] C. M. Long, A. V. Giannopoulos, and K. D. Choquette, "Lateral current injection photonic crystal membrane light emitting diodes," *Journal of Vacuum Science & Technology B: Microelectronics and Nanometer Structures,* vol. 28, pp. 359-364, 2010.

[197] B. Ellis, M. A. Mayer, G. Shambat, T. Sarmiento, J. Harris, E. E. Haller, and J. Vučković, "Ultralow-threshold electrically pumped quantum-dot photonic-crystal nanocavity laser," *Nature Photonics,* vol. 5, pp. 297-300, 2011.

[198] G. Shambat, B. Ellis, J. Petykiewicz, M. A. Mayer, A. Majumdar, T. Sarmiento, J. S. Harris, E. E. Haller, and J. Vuckovic, "Electrically driven photonic crystal nanocavity devices," *IEEE Journal of Selected Topics in*

*Quantum Electronics,* vol. 18, pp. 1700-1710, 2012.

[199] T. Okumura, M. Kurokawa, M. Shirao, D. Kondo, H. Ito, N. Nishiyama, T. Maruyama, and S. Arai, "Lateral current injection GaInAsP/InP laser on semi-insulating substrate for membrane-based photonic circuits," *Optics Express,* vol. 17, pp. 12564-12570, 2009.

[200] T. Okumura, H. Ito, D. Kondo, N. Nishiyama, and S. Arai, "Continuous wave operation of thin film lateral current injection lasers grown on semi-insulating InP substrate," *Japanese Journal of Applied Physics,* vol. 49, p. 040205, 2010.

[201] T. Shindo, T. Okumura, H. Ito, T. Koguchi, D. Takahashi, Y. Atsumi, J. Kang, R. Osabe, T. Amemiya, and N. Nishiyama, "Lateral-current-injection distributed feedback laser with surface grating structure," *IEEE Journal of Selected Topics in Quantum Electronics,* vol. 17, pp. 1175-1182, 2011.

[202] T. Shindo, T. Okumura, M. Futami, R. Osabe, H. Ito, T. Koguchi, T. Amemiya, N. Nishiyama, and S. Arai, "Lateral current injection distributed feedback laser with wirelike active regions," in *Compound Semiconductor Week (CSW/IPRM), 2011 and 23rd International Conference on Indium Phosphide and Related Materials*, 2011, pp. 1-4.

[203] M. Futami, K. Shinno, T. Shindo, T. Amemiya, N. Nishiyama, and S. Arai, "Improved quantum efficiency of GaInAsP/InP top air-clad lateral current injection lasers," in *2012 IEEE Optical Interconnects Conference*, 2012, pp. 34-35.

[204] 山原佳晃, 二見充輝, 進藤隆彦, 李智恩, 土居恭平, 雨宮智宏, 西山伸彦, and 荒井滋久, "GaInAsP 横方向接合型薄膜フォトダイオードの特性評価," ***電子情報通信学会ソサイエティ大会講演論文集*** vol. 2012, p. 225, 2012.

[205] J. Lee, Y. Maeda, Y. Atsumi, Y. Takino, N. Nishiyama, and S. Arai, "Low-Loss GaInAsP Wire Waveguide on Si Substrate with Benzocyclobutene Adhesive Wafer Bonding for Membrane Photonic Circuits," *Japanese Journal of Applied Physics,* vol. 51, p. 042201, 2012.

[206] T. Okumura, D. Kondo, H. Ito, S. Lee, T. Amemiya, N. Nishiyama, and S. Arai, "Lateral junction waveguide-type photodiode grown on semi-insulating InP substrate," *Japanese Journal of Applied Physics,* vol. 50, p. 020206, 2011.

[207] T. Shindo, T. Koguchi, M. Futami, K. Doi, Y. Yamahara, J. Lee, T. Amemiya, N. Nishiyama, and S. Arai, "10 Gbps Operation of Top Air-Clad Lateral Junction Waveguide-Type Photodiodes," *Japanese Journal of Applied Physics,* vol. 52, p. 118002, 2013.

[208] H. Enomoto, K. Inoue, T. Okumura, H. D. Nguyen, N. Nishiyama, Y. Atsumi, S. Kondo, and S. Arai, "Properties of high index-contrast wired GaInAsP waveguides with Benzocyclobutene on Si substrate," in *Indium Phosphide & Related Materials, 2009. IPRM'09. IEEE International Conference on*, 2009, pp. 347-350.

[209] Y. Maeda, J. Lee, Y. Atsumi, N. Nishiyama, and S. Arai, "Uniform BCB bonding process toward low propagation loss in GaInAsP photonic wire waveguide on Si wafer," in *Compound Semiconductor Week (CSW/IPRM), 2011 and 23rd International Conference on Indium Phosphide and Related Materials*, 2011, pp. 1-4.

[210] T. Okumura, T. Koguchi, H. Ito, N. Nishiyama, and S. Arai, "Injection-type GaInAsP/InP membrane buried heterostructure distributed feedback laser with wirelike active regions," *Applied Physics Express,* vol. 4, p. 042101, 2011.

[211] T. Shindo, M. Futami, T. Okumura, R. Osabe, T. Koguchi, T. Amemiya, N. Nishiyama, and S. Arai, "Lateral-Current-Injection Type Membrane DFB Laser With Surface Grating," *IEEE Photonics Technology Letters,* vol. 25, pp. 1282-1285, 2013.

[212] K. Doi, T. Shindo, M. Futami, J. Lee, T. Hiratani, D. Inoue, S. Yang, T. Amemiya, N. Nishiyama, and S. Arai, "Room-temperature continuous-wave operation of lateral current injection membrane laser," presented at the

The 25th International Conference on Indium Phosphide and Related Materials (IPRM2013), Kobe, Japan, 2013.

[213] M. Futami, T. Shindo, K. Doi, T. Amemiya, N. Nobuhiko, and A. Shigehisa, "Low-threshold operation of LCI-membrane-DFB lasers with Be-doped GAInAs contact layer," presented at the The 24th International Conference on Indium Phosphide and Related Materials (IPRM2012), Santa Barbara, CA, USA, 2012.

[214] K. Doi, T. Shindo, J. Lee, T. Amemiya, N. Nishiyama, and S. Arai, "Thermal analysis of lateral-current-injection membrane distributed feedback laser," *IEEE Journal of Quantum Electronics,* vol. 50, pp. 321-326, 2014.

[215] D. Inoue, J. Lee, K. Doi, T. Hiratani, Y. Atsuji, T. Amemiya, N. Nishiyama, and S. Arai, "Room-temperature continuous-wave operation of GaInAsP/InP lateral-current-injection membrane laser bonded on Si substrate," *Applied Physics Express,* vol. 7, p. 072701, 2014.

[216] T. Hiratani, K. Doi, J. Lee, D. Inoue, T. Amemiya, N. Nishiyama, and S. Arai, "Thermal properties of lateral-current-injection semiconductor membrane Fabry–Perot laser under continuous-wave operation," *Japanese Journal of Applied Physics,* vol. 54, p. 042701, 2015.

[217] T. Hiratani, T. Shindo, K. Doi, Y. Atsuji, D. Inoue, T. Amemiya, N. Nishiyama, and S. Arai, "Energy cost analysis of membrane distributed-reflector lasers for on-chip optical interconnects," *IEEE Journal of Selected Topics in Quantum Electronics,* vol. 21, pp. 299-308, 2015.

[218] T. Shindo, M. Futami, K. Doi, T. Amemiya, N. Nishiyama, and S. Arai, "Design of Lateral-Current-Injection-Type Membrane Distributed-Feedback Lasers for On-Chip Optical Interconnections," *IEEE Journal of Selected Topics in Quantum Electronics,* vol. 19, p. 1502009, 2013.

# Chapter 2
# Theoretical analysis of membrane devices for on-chip optical interconnection

2.1 Introduction 88
2.2 Effect of link loss on required optical power 91
2.3 Analysis on membrane DFB laser performance 96
2.3.1 Threshold current characteristics of DFB structure 100
2.3.2 High modulation efficiency characteristics 106
2.4 Conclusion 115
References

## 2.1 Introduction

On-chip optical interconnection is characterized by transmitter and receiver and link loss. It is easy to use the same transmitter and receiver devices regardless of the wiring length from the viewpoint of process and design easiness. Therefore, the performances of the transmitter and the receiver are key factors defining the performance of the optical interconnection. The threshold current of the laser gives the lower limit of the achievable bias current of the laser. The modulation efficiency which is the slope of the laser relaxation oscillation frequency with respect to the bias current above threshold gives the required bias current for obtaining the necessary 3dB bandwidth of the laser. The integration structure that couples the each optical device also has influence on the optical link performance. Figure 2.1 shows the schematic of membrane optical link consisting of a membrane DFB laser, a passive waveguide and a membrane p-i-n photodiode. The coupling efficiency between the active devices and the passive waveguide has a role to determine the ratio at which the optical output power can be effectively used for

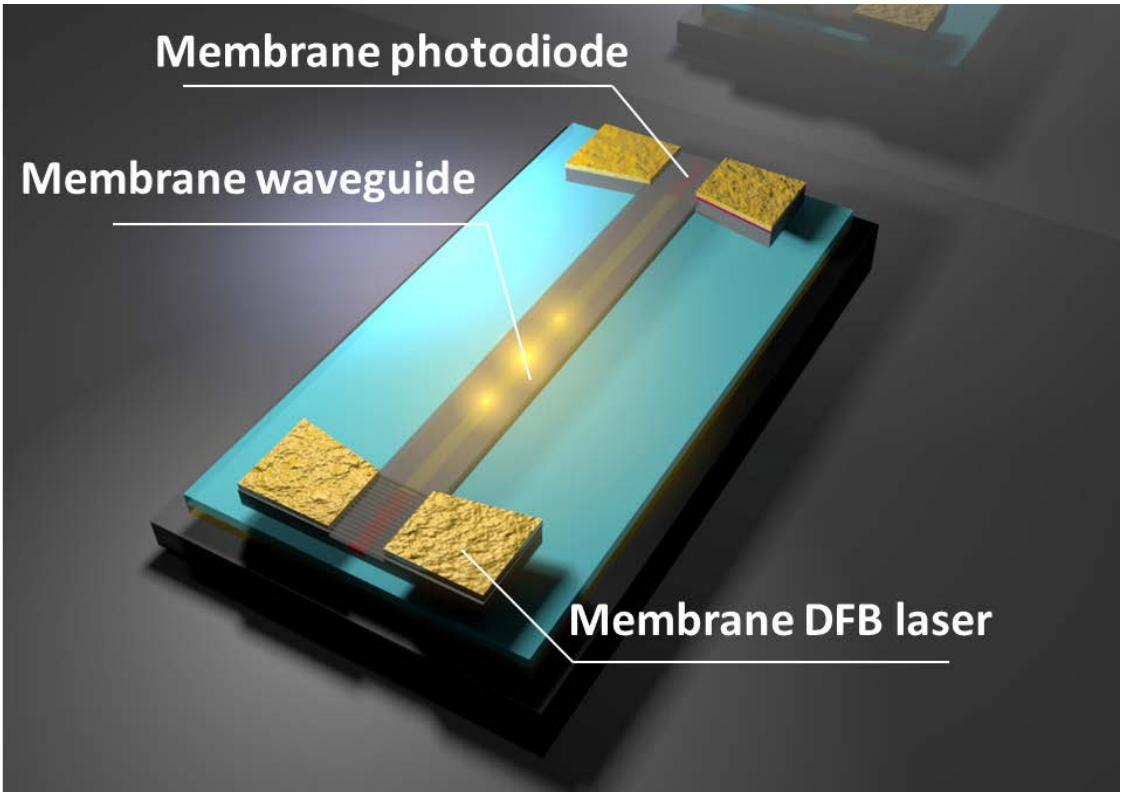


**Figure 2.1** Membrane optical link consisting of a membrane DFB laser, a passive waveguide and membrane p-i-n photodiode.

communication. Propagation loss plays a major role in indicating the superiority of optical wiring to electrical wiring especially for long wiring length. This is because it is necessary to realize a low loss propagation waveguide in order to reduce the impact on power consumption even if the propagation length becomes long distance. Table 2.1 (same as Table 1.4) shows the assumption of coupling efficiency and propagation loss to calculate required laser output power. By clarifying the relationship behind these factors, we will show the characteristics necessary for the devices consisting the optical link required for low power consumption. In section the 2.2, the coupling efficiency of the link integration structure and the influence of the propagation loss on the output requirement of the laser are examined. The section 2.3 shows the characteristics of membrane DFB lasers. From the calculation, the threshold current obtained by high index coupling coefficient and short cavity length will be shown. Respecting to the volume of the active layer, the possible modulation efficiency obtained in membrane DFB laser will

be shown. Finally, I will show that it is possible to enhance the modulation efficiency by reducing the active layer volume without weakening the optical confiment inside the cavity by utilizing the high coupling coefficient obtained by using membrane structure.

**Table 2.1** Light output power requirement for on-chip optical interconnection.

| | | |
|---|---|---|
| Requirement | Minimum received power | 50 μW (-13dBm) |
| Assumptions | Coupling loss between LD and waveguide | -1.5dB (-30%) |
| | Propagation loss for 2 cm-long waveguide | -2dB (-1dB/cm) |
| | Coupling loss between LD and waveguide | -1.5dB (-30%) |
| **Calculated value** | **Required light output power of LD** | **160 μW (-8dBm)** |

## 2.2 Effect of link loss on required optical power

The coupling loss and the propagation loss of optical link structure are investigated assuming the wiring length of 1–2 cm which is possible longest length for on-chip wiring. Figure 2.2 shows the optical link properties and loss together with the whole link structure using membrane platform. When the signal with SNR of 28 dB is received by a system terminated by impedance of 50 Ω with a bandwidth of 5 GHz for 10 Gbit/s and is amplified by an amplifier having noise figure of 6 dB. The minimum received power $P_{\mathrm{rec}}$ necessary for receiving the non-return-to-zero 10 Gbit/s signals with the bit-error-rate of $10^{-9}$ is considered to be -13 dBm (50 μW).

Minimum received power $$P_{\mathrm{rec}} = -13\ [\mathrm{dBm}] \tag{2.1}$$

The coupling loss for a single joint is defined as following constant;

Coupling loss $$\alpha_{\mathrm{coup}}\ [\mathrm{dB}] \tag{2.2}$$

The propagation loss is given by the attenuation per unit length $\alpha_{\mathrm{prop}}$ multiplied by the propagation distance $L$ as follows;

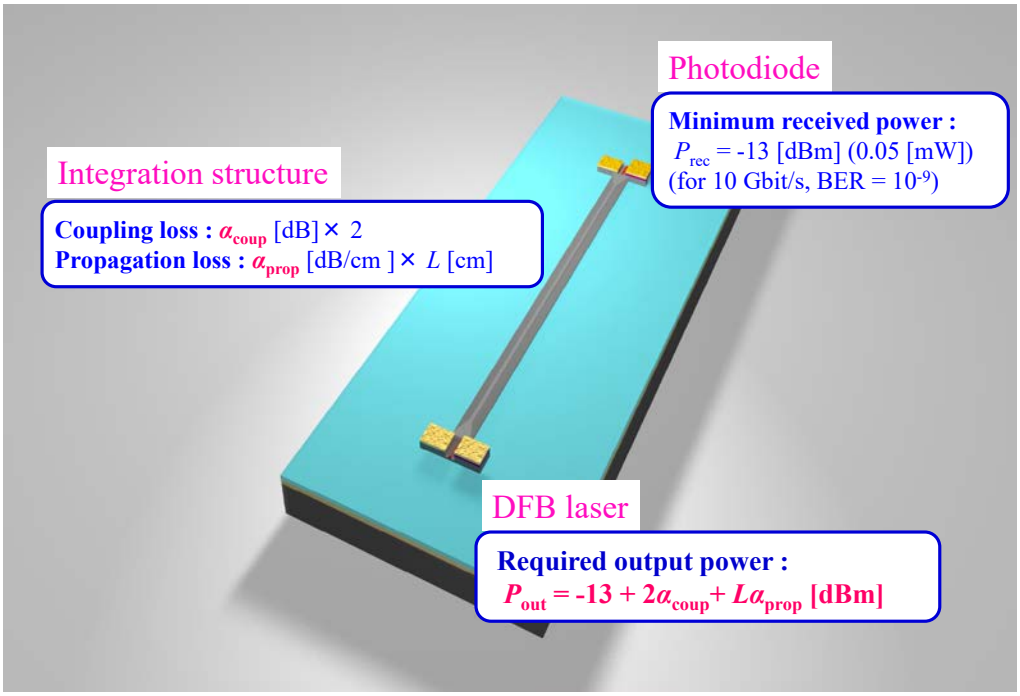


**Figure 2.2** Schematic of membrane optical link and the losses in optical link.

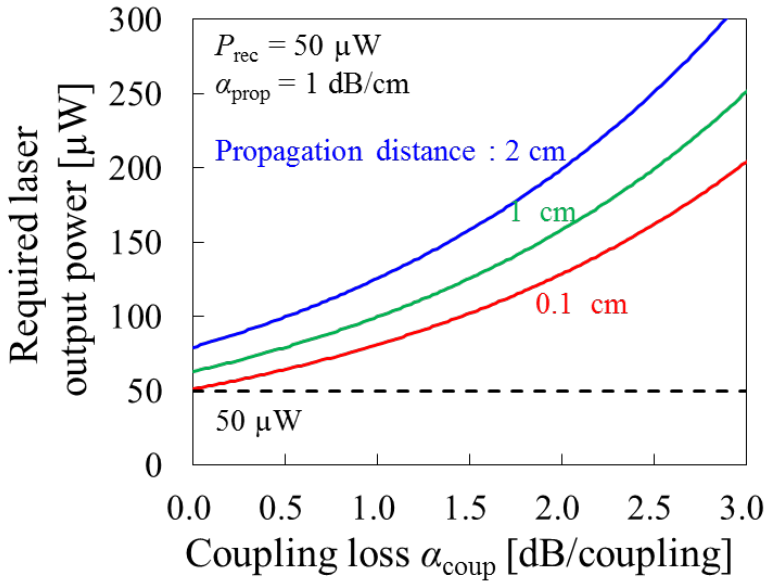


**Figure 2.3** Required laser output power versus coupling loss

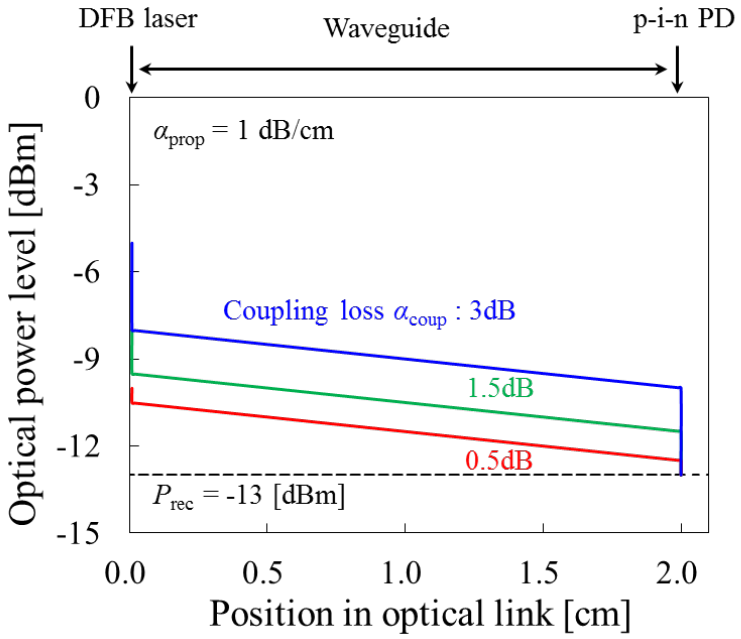


**Figure 2.4** Optical power level in wiring as a function of propagation distance for different coupling loss.

$$\text{Propagation loss} \qquad \alpha_{\text{prop}}[\text{dB/cm}] \times L\ [\text{cm}] \qquad (2.3)$$

According to these loss factors, the output power necessary for the laser is as follows;

$$\text{Required output power} \qquad P_{out} = -13 + 2\alpha_{\text{coup}} + \alpha_{\text{prop}} \times L\ [\text{dBm}] \qquad (2.4)$$

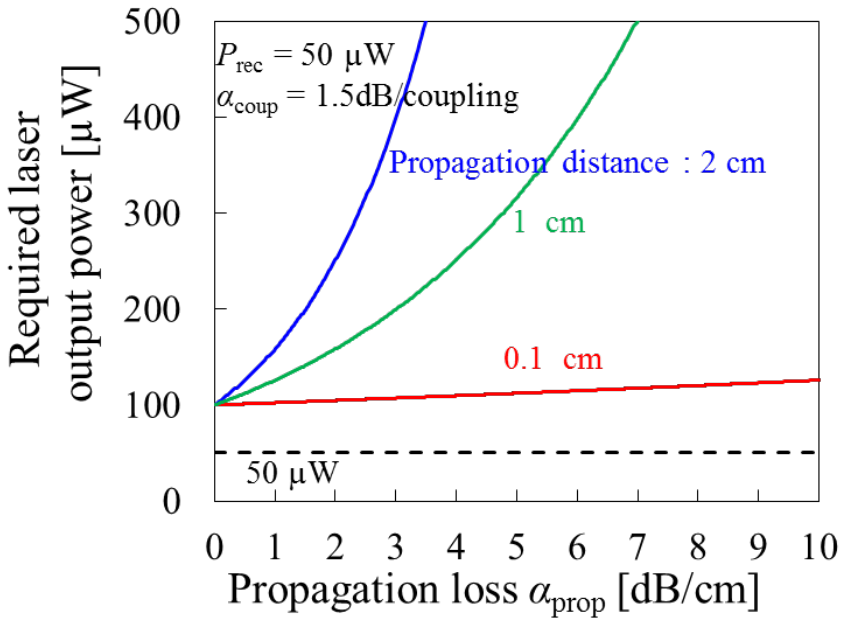


**Figure 2.5** Required laser output power versus propagation loss

Based on this equation, we will study the rolls of integrated properties on required optical power at laser. Figure 2.3 shows required laser output power versus single coupling loss $\alpha_{coup}$ characteristics for the propagation length of 0.1, 0.5 and 1.0 cm. The calculation was done using the propagation loss of 1 dB/cm. The coupling loss affects equally on required power not depending on the wiring length. Since it is an integrated structure of the laser, the waveguide and the photodetector, two connection interfaces are necessary at two places. Figure 2.4 shows the attenuation of the optical power level in an interconnection as a function of position in the optical link. The attenuation of optical power is shown for different coupling losses. At the origin, initial power level is set so that the power after 2 cm propagation becomes the minimum received power of -13 dBm. Coupling losses are occurred at the origin and end point of the wiring. For the optical link with low efficiency coupling, high input power is required even for short length wiring. To realize highly efficient coupling structure, mode fields of both laser and waveguide side should be matched. Even when there is a large mode field mismatch, high coupling efficiency can be obtained by introducing tapered structure which convert the optical field adiabatically [1]. In general, however, it requires precise fabrication accuracy and long taper length.

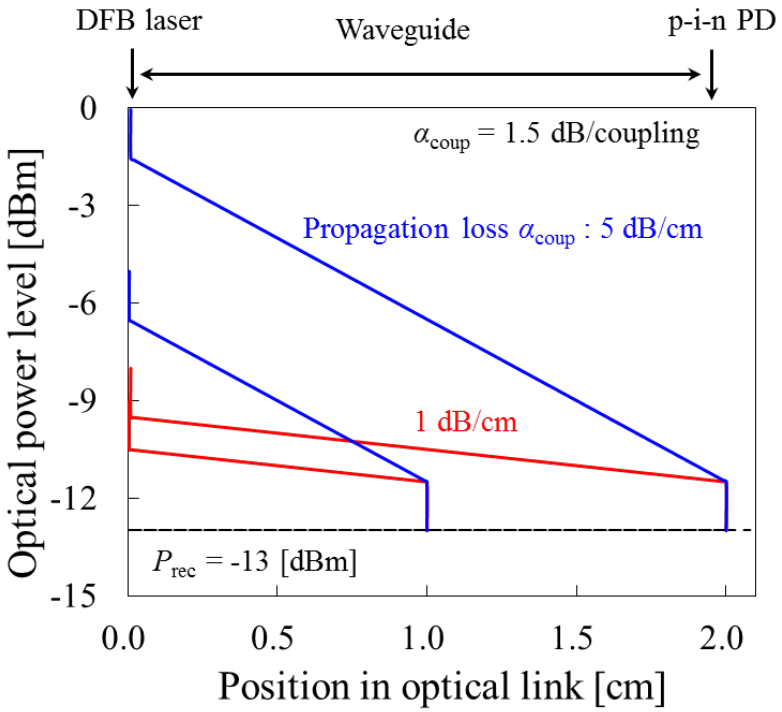


**Figure 2.6** Optical power level in wiring as a function of propagation distance for different propagation loss.

Figure 2.5 shows required laser output power versus propagation loss for various propagation length of 0.1, 0.5 and 1 cm. The coupling efficiency of 1.5 dB was used in the calculation. When the wiring length is short such as 0.1 and 0.5 cm, there is almost no influence on the requirement power even if the waveguide has a high propagation loss. On the other hand, as propagation length becomes 1 cm, the required power abruptly rises as the propagation loss increase. Figure 2.6 shows optical power level in wiring as a function of position in optical link distance for different propagation loss. Because the wiring length of around 2 cm is possible for on-chip wiring, the graph shows lines for the propagation length of 1 and 2 cm. For such long wiring, the propagation loss of 1–2 dB/cm or less is preferred in order to suppress the required optical output power of the laser. Such propagation loss is realized in a waveguide such as planar-light-circuit (PLC) [2]or InP monolithic integrated circuit [3] platform which has weak optical confinement of the waveguide core. Although, in order to obtain micro bending radius on the chip,

strong optical confinement waveguide is necessary that can be bent with macro meter order curvature radius. Si wire waveguide is capable of sufficiently small bending as on-chip wiring. The propagation loss of Si wire waveguide is generally reported to be about 2 dB/cm for the foundry which conducts CMOS process is reported [4]. Since the strong optical confinement is needed only the bend region, propagation loss below 1 dB/cm has been reported by expanding the waveguide width in the straight section [5] or by using rib structure waveguide [4]. If a highly efficient link structure can be obtained by structural investigation, the required optical output power becomes small. According to the results of Chapter 3, the coupling structure with coupling loss below -0.1dB will be obtained by numerical calculation and experimental ways. When a propagation loss of 1 dB/cm and a coupling loss of 0.1dB/coupling are obtained as a highly efficient optical link, the required power for the wiring length of 2 cm is calculated as follows.

Required output power

$$P_{out} = -13 + 2\alpha_{\mathrm{coup}} + \alpha_{\mathrm{prop}} \times L \ [\mathrm{dBm}] \quad (2.5)$$

$$= -13 + 2 \times 0.1 + 1 \times 2 \ [\mathrm{dBm}]$$

$$= -10.8 \ [\mathrm{dBm}] \ (83 \ [\mu\mathrm{W}])$$

Table 2.2 summarizes output power requirement for on-chip optical interconnection assuming possible efficient structure.

**Table 2.2** Light output power requirement for on-chip optical interconnection.

| | | |
|---|---|---|
| Required power | Minimum received power | 50 μW (-13dBm) |
| New assumptions | Coupling loss | -0.1dB |
| | Propagation loss for 2 cm | -2dB (-1dB/cm) |
| **Calculated value** | **Required light output power of LD** | **83 μW (-10.8dBm)** |

## 2.3 Analysis on membrane DFB laser performance

In this section, calculation results for the expected performance of membrane DFB laser will be shown. Figure 2.7 shows the schematic diagram of cross section of membrane DFB laser with surface grating used for calculation. This structure is close to the structure showing good lasing characteristics in Fabry-Perot cavity [6], only difference is that the 100-nm-thick InP cap layer is adopted to form the surface grating. The semiconductor core layer is sandwiched by dielectric cladding layers of air and $SiO_2$.

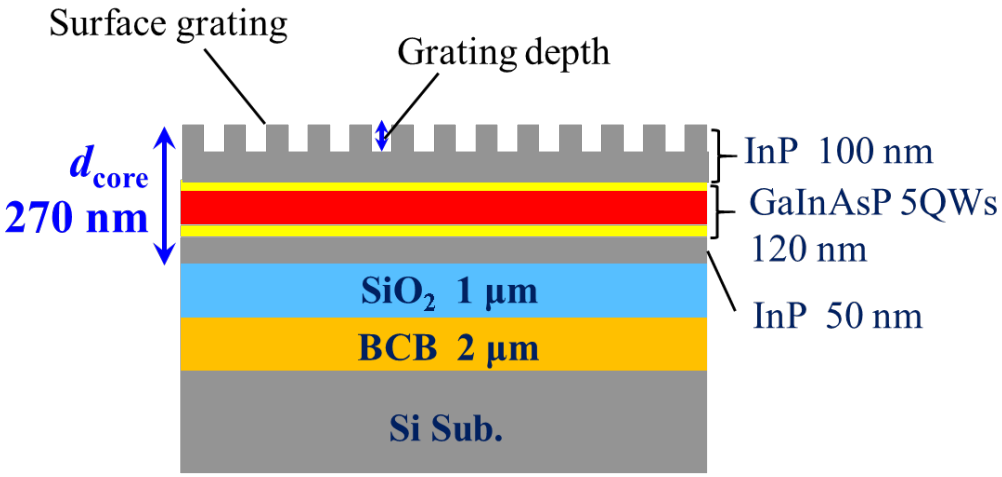


(a)

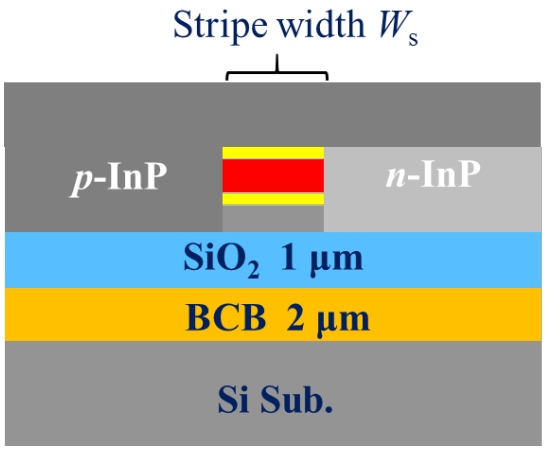


(b)

**Figure 2.7** Required laser output power versus propagation loss.

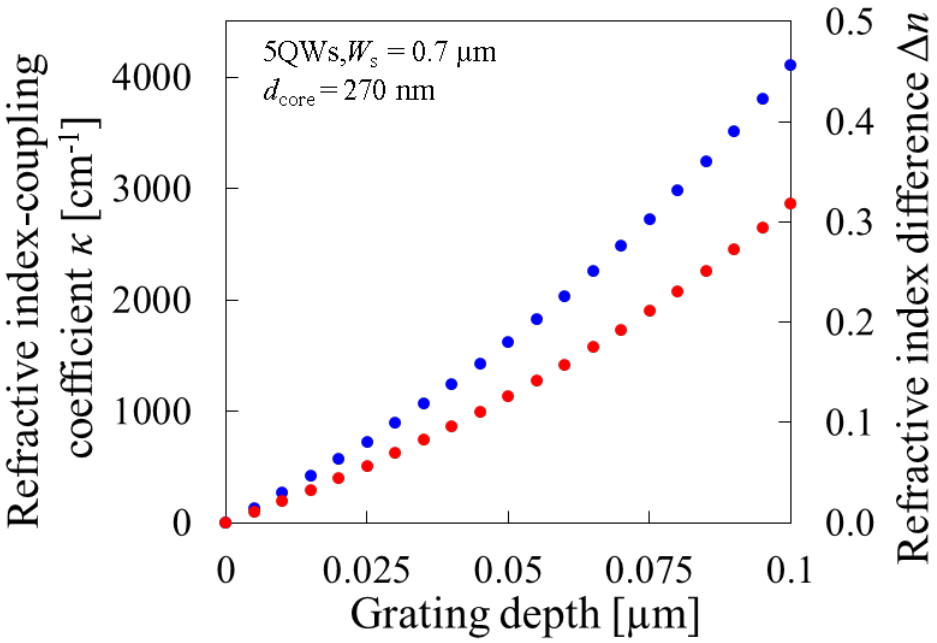


**Figure 2.8** Grating depth and refractive index coupling coefficient

The thickness of core layer is 270 nm including five multi quantum well active layers. The grating producing the refractive index perturbation is formed on a top surface InP layer.

First, a fundamental equations characterizing a DFB laser is described. Since the detail derivations are available in many papers and books [7-10], I do not discuss the derivation of each equation. In this section, the coupled-wave mode theory is adopted for calculation of membrane DFB structure because it can be applied to high-refractive index difference structure with several % error [8].When the refractive index in the waveguide is modulated by the periodically formed grooves, the independently propagated optical modes are coupled to each other. In the field of DFB lasers, the coupling coefficient representing the strength of the coupling between the forward wave and the backward wave is expressed as follows;

$$\kappa = \kappa_i + i\kappa_g \tag{2.6}$$

$$= \frac{1}{\pi}\sin(\pi\frac{W}{\Lambda})(k_0\Delta n) + i\frac{\Delta g}{2}) \tag{2.7}$$

where, $\kappa$ is the optical complex coupling coefficient, $\kappa_i$ is the refractive index coupling coefficient, $\kappa_g$ is the gain coupling coefficient, $W$ is the width of grating, $\Lambda$ is the grating period, $k_0$ is the wavenumber in vacuum, $\Delta n$ is the equivalent refractive index perturbation by grating and $\Delta g$ is the gain perturbation by grating. Gain coupling coefficient can be obtained by forming the gratin into active region. However, since the perturbation of the only refractive index is much large value in the surface grating structure, the gain coupling coefficient is not considered in the subsequent calculation. Figure 2.8 shows refractive index-coupling coefficient $\kappa_i$ and refractive index difference $\Delta n$ as a function of grating depth. In conventional laser structure, the coupling coefficient is 200–300 $cm^{-1}$ at most because of small relative refractive index difference of the waveguide structure. In contrast, membrane structure has large relative index difference, and can obtain large index perturbation by small grating depth. For the grating depth of 60 nm and 100 nm, $\kappa_i$ of 2000$cm^{-1}$ and 4000 $cm^{-1}$ are obtained, respectively. The strength of the optical confinement to the DFB cavity is expressed as $\kappa L$ using the cavity length $L$. Large $\kappa$ can provide strong cavity confinement even with the short cavity length. From coupled-mode equations representing the interaction between the forward-wave and the backward-wave, the resonance condition of the DFB laser should satisfy the following relation.

$$\gamma_c^2 = \kappa^2 + (\alpha - i\Delta\beta)^2 \tag{2.8}$$

where, $\gamma_c$ is complex propagation constant, $\alpha$ is imaginary part of complex wave number and $\Delta\beta$ is detuning from Bragg wavelength. This relation is transcendental equation. The solutions are obtained using numerical solving method such as Newton-Raphson method. Then, we obtaine the combination of the wavelength and threshold gain $g_{th}$ satidfiyng the resonant condition. When the threshold gain is once calculated, threshold current is given by

$$I_{th} = \frac{eV_a B_{eff}}{\eta_i}\left(N_g + \frac{g_{th}}{\frac{dg}{dN}}\right)^2 \tag{2.9}$$

where, $I_{th}$ is the threshold current, $e$ is the electron charge, $V_a$ is the active medium volume, $B_{eff}$ is the effective recombination coefficient, $N_g$ is the transparent carrier density, $\eta_i$ is

the internal quantum efficiency and d$g$/d$N$ is the differential gain. Expression for frequency response of the laser is obtained by performing small-signal analysis in rate-equation. The frequency response M($f$) for the modulation signal is expressed by the following equation;

$$\frac{M(f)}{M(0)} = \frac{f_r^2}{\sqrt{(f^2 - f_r^2) + \frac{f^2\gamma^2}{(2\pi)^2}}} \tag{2.10}$$

$$f_r = \frac{1}{2\pi}\sqrt{\xi\frac{dg}{dN}\frac{v_g\eta_i}{eV_a}}\sqrt{I_b - I_{th}} \tag{2.11}$$

$$\gamma = \xi\frac{dg}{dN}v_g S_0 + \frac{1}{\tau_s} = Kf_r^2 + \frac{1}{\tau_s} \tag{2.12}$$

where, $\gamma$ is the damping factor, $v_g$ is the group velocity, $I_b$ is the bias current, $S_0$ is the photon density in a cavity, $\tau_s$ is the carrier lifetime and $K$ is the $K$-factor. It can be seen that the relaxation oscillation frequency is increased by increasing the bias current. The slope is expressed by the following equation;

$$\text{Modulation efficiency} = \frac{f_r}{\sqrt{I_b - I_{th}}} \tag{2.13}$$

$$= \frac{1}{2\pi}\sqrt{\xi\frac{dg}{dN}\frac{v_g\eta_i}{eV_a}} \tag{2.14}$$

This is called modulation efficiency which is slope of $f_r$ as a function of the bias current. This is an important index for obtaining high-speed operation with low bias current condition. The 3dB bandwidth is given at a frequency at which the power of the response is halved;

$$\left|\frac{M(f_{3\text{dB}})}{M(0)}\right|^2 = \frac{1}{2} \tag{2.15}$$

The $f_{3\text{dB}}$ is related to the $f_r$ as following valid in low damping condition;

$$f_{3\text{dB}} \cong 1.55 f_r \tag{2.16}$$

The theoretical maximum 3dB bandwidth is given by using $K$-factor as follows;

$$f_{3\mathrm{dB\ max}} = \sqrt{2}\,\frac{2\pi}{K} \tag{2.17}$$

Based on the discussion for the rise time and the fall time of the large signal response of the semiconductor laser [11], the relationship between the 3dB bandwidth and the maximum achievable data rate for non-return-to-zero (NRZ) signal is

$$\mathrm{Datarate} = 1.3 f_{3\mathrm{dB}} \tag{2.18}$$

This relation gives the information for the large signal modulation from the bandwidth.

### 2.3.1 Threshold current characteristics of DFB structure

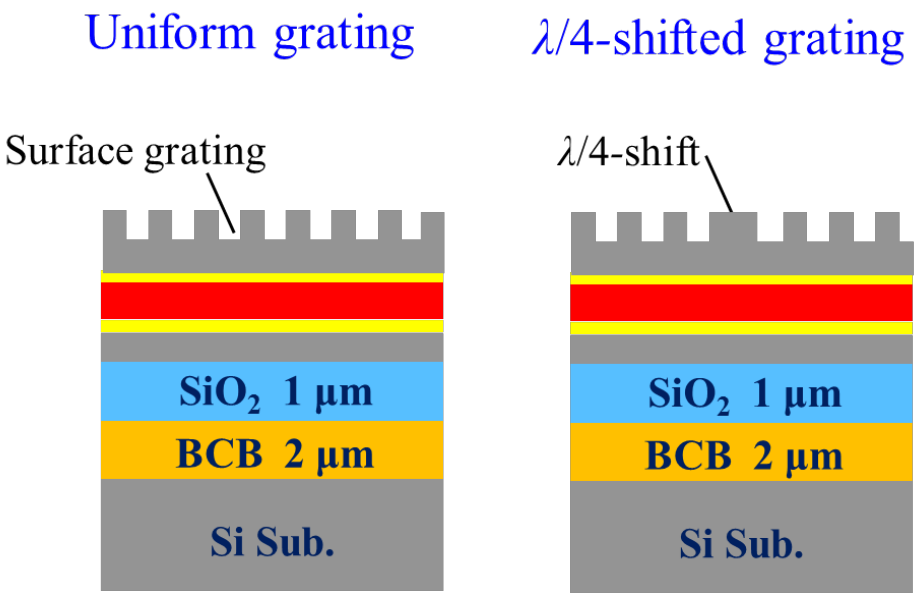


**Figure 2.9** Structure comparison between the uniform grating and λ/4-shifted grating.

In this subsection, I analyzed the threshold current of membrane DFB laser. Reduction of the threshold can be obtained by reducing active cavity volume and enhancing optical confinement in the cavity. Here, analysis results on the following two type DFB structure will be shown.

(1) Uniform grating DFB laser

(2) λ/4-shifted grating DFB laser

Figure 2.9 shows the structure comparison between the uniform grating and λ/4-shifted grating. By introducing the λ/4 phase shift, it is possible to obtain a strong cavity confinement due

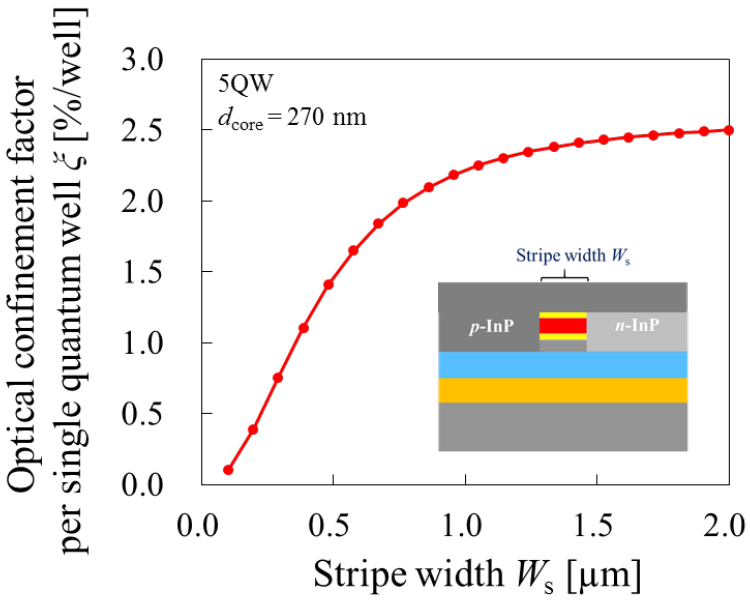


**Figure 2.10** Optical confinement factor for single quantum well versus stripe width.

to modifying the resonant condition.

First, it is necessary to determine the active layer stripe width used in the calculations. According to the previous study, it is shown that in the lateral-current-injection structure with wide stripe width, the recombination emission profile becomes non-uniform due to the difference between the hole mobility and the electron mobility. In order to obtain uniform reconbination emission in the active region, a stripe width of less than 1 μm is needed [12]. Figure 2.10 shows the optical confinement factor per single quantum well as a function of the stripe width. The calculation was performed for a 5QW structure. Narrower stripe results in lower optical confinement factor. In the calculation after here, the stripe width of 0.7 μm is adopted. Table 2.3 summarizes the parameters used in following calculations. Figure 2.11 shows threshold current and differential quantum efficiency as a function of cavity length for different coupling coefficient $\kappa$ values. The $\kappa$ of 2000, 3000 and 4000 correspond to the grating depth of 60 nm, 80 nm and 100 nm, respectively. With larger refractive index coupling coefficient, strong optical confinement can be obtained even with a short cavity length. This is because sufficient cavity strength

$\kappa L$ can be obtained in a short cavity region. As a consequence, lower threshold current is expected for short cavity device by reduction of the active volume. When the refractive index coupling coefficient is 2000 $cm^{-1}$, the minimum threshold current becomes 0.17 mA around the cavity length of 60 μm and the external differential quantum efficiency of 22%/facet can be expected. When the refractive index coupling coefficient is 4000 $cm^{-1}$, the minimum threshold current becomes 0.1 mA around the cavity length of 35 μm. and the external differential quantum efficiency of 23%/facet can be expected.

**Table 2.3** Parameters for calculation

| | | |
|---|---|---|
| Differential gain | $dg/dN$ | $6.0\times10^{-16}$ $cm^2$ |
| Transparent carrier density | $N_g$ | $1.5\times10^{18}$ $cm^{-2}$ |
| Effective recombination coefficient | $B_{eff}$ | $1.5\times10^{-10}$ $cm^3/s$ |
| Internal quantum efficiency | $\eta_i$ | 0.75 |
| Well thickness | $d$ | 6 nm |

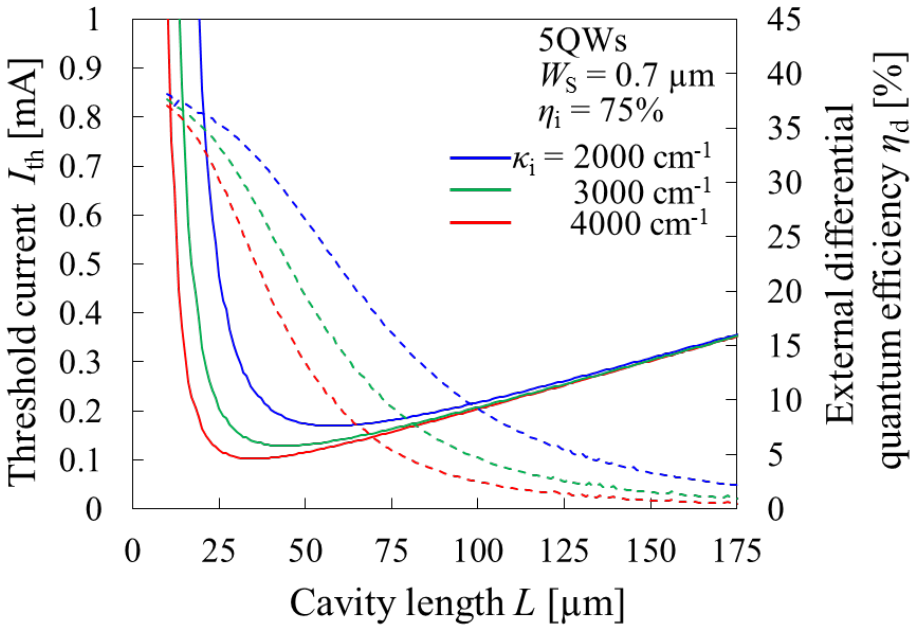


**Figure 2.11** Threshold current and external differential quantum efficiency versus cavity length for uniform grating membrane DFB laser.

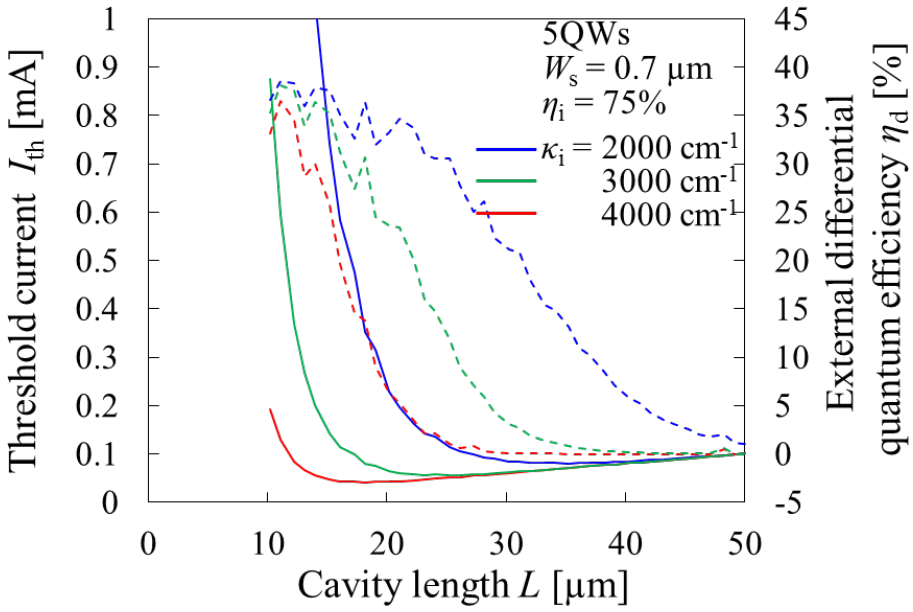


**Figure 2.12** Threshold current and external differential quantum efficiency versus cavity length for $\lambda/4$-shifted grating membrane DFB laser.

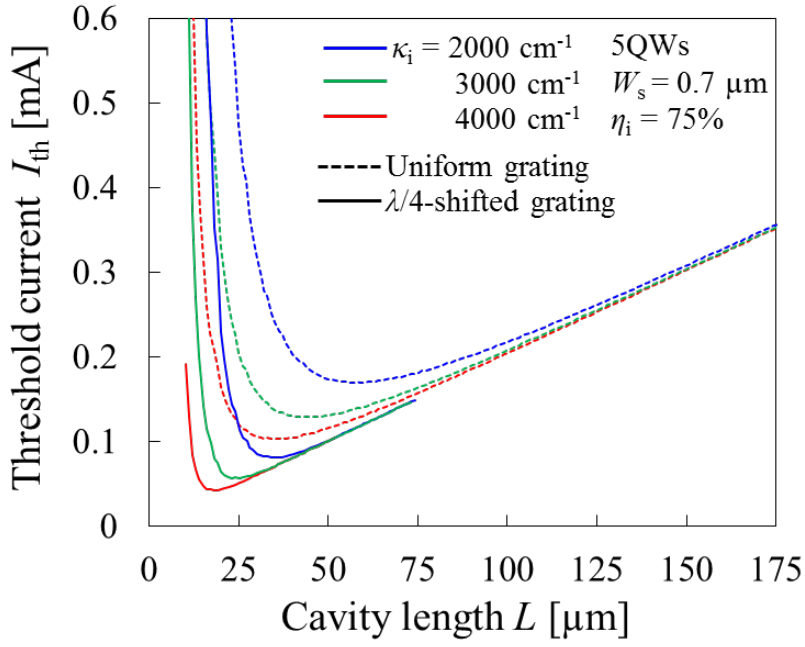


**Figure 2.13** Comparison of the threshold current between the uniform and λ/4-shifted grating membrane DFB lasers.

Next, the calculation results for the membrane DFB laser with $\lambda/4$ shift region at the center of the cavity is shown. Improvement of single-mode characteristics by phase shift has been pointed out from the early research on DFB laser. As shown in the Figure 2.9, calculation was performed to confirm possibility of shortening the cavity length by introducing phase shift at the cavity center. A $\lambda/4$ phase shift that can expect the largest effect was introduced. Figure 2.12 shows threshold current and external differential quantum efficiency versus cavity length for $\lambda/4$-shifted grating membrane DFB laser. For the refractive index coupling coefficient of 2000 $cm^{-1}$, the lowest threshold current can be obtained around cavity length of 35 μm, which is shorter length than that of the structure using a uniform grating. For the refractive index coupling coefficient of 4000 $cm^{-1}$, the cavity length of 19 μm is possible with significant low threshold current. Figure 2.13 shows the comparison of the threshold current between the uniform and $\lambda/4$-shifted grating membrane DFB lasers.

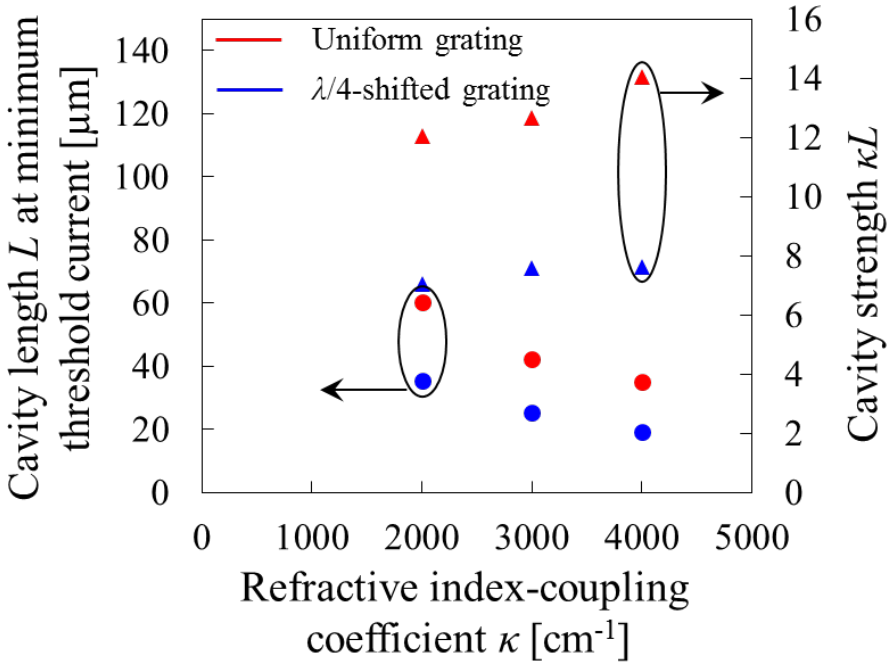


**Figure 2.14** Cavity length at minimum threshold current versus refractive index-coupling coefficient. The red dots show the uniform grating, and the blue dots show the $\lambda/4$-shifted grating.

Figure 2.14 shows cavity length $L$ to obtain minimum $I_{th}$ as a function of $\kappa$ for uniform grating and $\lambda/4$-shifted grating. The cavity strength $\kappa L$ for minimum $I_{th}$ is found to be around 12 and 7 for uniform and $\lambda/4$-shifted grating, respectively. This relationship can be used as a guide in designing the cavity length and grating depth.

### 2.3.2 Modulation efficiency characteristics

The modulation efficiency is a slope of relaxation oscillation frequency $f_r$ as a function of a square root bias current expressed in a unit of GHz/mA$^{1/2}$. The $f_r$ is directly related to the high speed property of the semiconductor lasers. Significant high modulation efficiency is required for high-speed direct modulation with low-bias current. In a membrane structure, the modulation efficiency is enhanced from two factors as following sentence. The modulation efficiency is proportional to the squared root of the product of an optical confinement factor and a differential gain.

$$\sqrt{\xi \frac{dg}{dN}} \tag{2.19}$$

and an inverse of square root of an active volume

$$\sqrt{\frac{1}{V_a}} \tag{2.20}$$

It is assumed that the cavity volume is equal to the active volume in a membrane DFB structure. The strong optical confinement factor in the membrane structure can enhance the modulation efficiency by the term in equation (2.19). In addition, by a large coupling coefficient $\kappa$, it is possible to shorten the cavity length while keeping the cavity strength $\kappa L$ constant. This enable us to reduce active volume $V_a$, thus term in equation (2.20) can be enhanced. Figure 2.15 shows the modulation efficiency as a function of the active volume. The differential gain d$g$/d$N$ of $6\times10^{-16}$ cm$^2$ is used in this calculation. This value is obtained at carrier density of $3\times10^{18}$ cm$^3$ for GaInAsP-based strained QW. The value of modulation efficiency abruptly rises as active volume decreases. Because the modulation efficiency increases with the reciprocal of the active volume, the smaller the active layer volume is, the higher the differential coefficient of its curve increases. In particular, the significantly high value is obtained in the region of less than 1 μm$^3$. For 10 Gbit/s and the energy consumption of 100 fJ/bit operation, 3dB bandwidth of 7.7 GHz is required at a bias current of 1 mA according to equation (2.18). In this sense, at least the

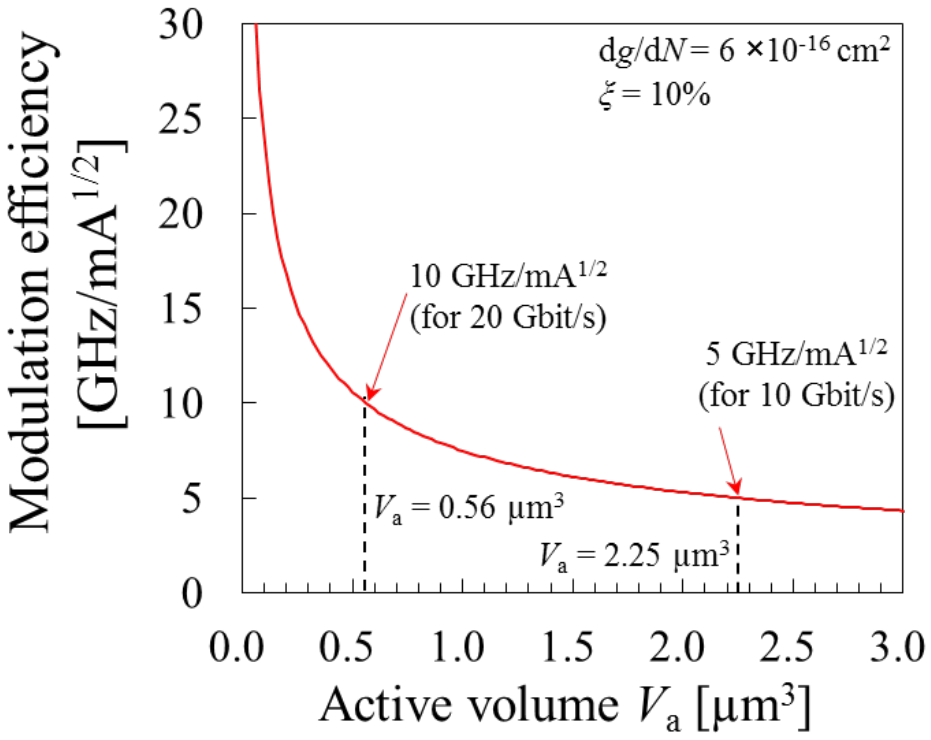


**Figure 2.15** Modulation efficiency as a function of active volume.

modulation efficiency must be higher than 5 GHz/mA$^{1/2}$ from equation (2.16). The modulation efficiency becomes 5 GHz/mA$^{1/2}$ when the active layer volume is less than 2.25 μm$^3$. Actually, the laser is necessary to have higher modulation efficiency than 5 GHz/mA$^{1/2}$ considering that relaxation oscillation occurs above the threshold current. As a modulation efficiency for 20 Gbit/s operation, 10 GHz/mA$^{1/2}$ is obtained at active volume of 0.56 μm$^3$. We consider the cavity design that realizes such small active layer volume. Figure 2.16 shows the active volume versus cavity length with maintaining constant $\kappa L$ of 10. The redline shows required $\kappa$ value at

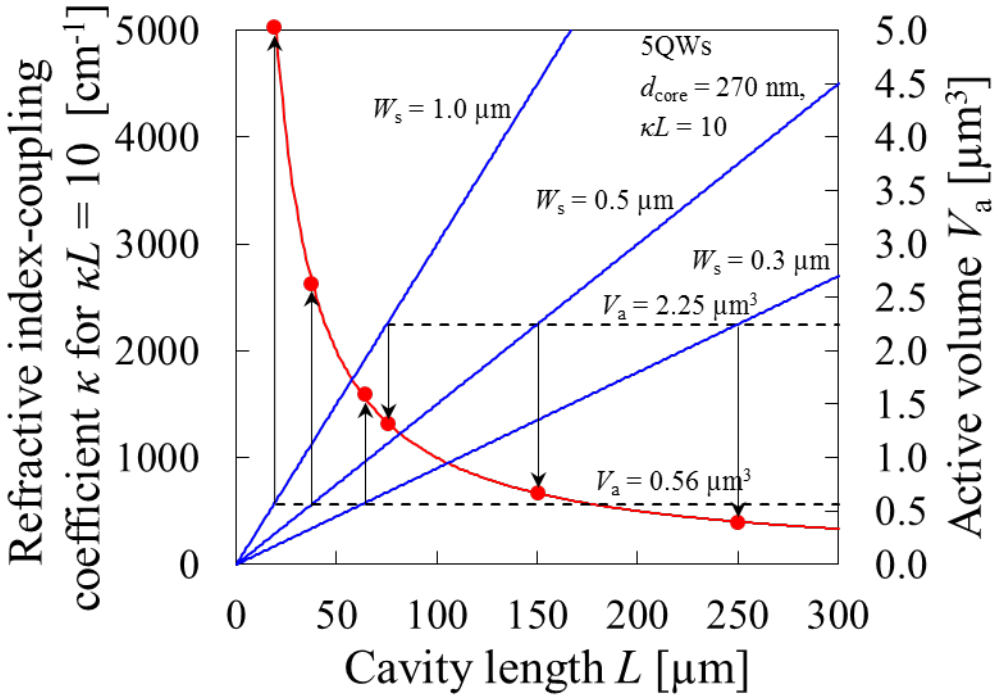


**Figure 2.16** Active volume as a function of cavity length with constant $\kappa L$ of 10. The redline shows $\kappa$ needed at each cavity length.

**Table 2.4** Summary of calculation in Figure 2.16

| Stripe width $W_s$ | Cavity length for $V_a$ of 2.25 μm$^3$ / 0.56μm$^3$ | Required $\kappa$ for $\kappa L$ of 10 |
|---|---|---|
| 1.0 μm | 75 μm | 1333 cm$^{-1}$ |
| | 19 μm | 5260 cm$^{-1}$ |
| 0.5 μm | 150 μm | 667 cm$^{-1}$ |
| | 38 μm | 2630 cm$^{-1}$ |
| 0.3 μm | 250 μm | 400 cm$^{-1}$ |
| | 62 μm | 1610 cm$^{-1}$ |

each cavity length to achieved $\kappa L$ of 10. The blue lines which showing the active volume represent for different stripe width of 0.3 μm, 0.5μm and 1 μm. The active volume $V_a$ is calculated by following relation;

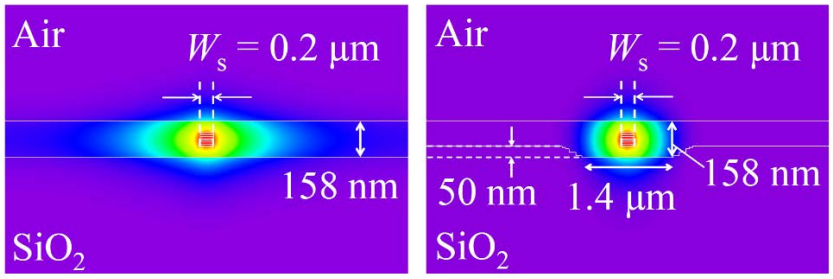


**Figure 2.17** Lateral optical confiment structure to realize the narrow stripe design [13]. (a) flat structure ,(b) selective regrowth structure.

$$V_a = W_s L d_{5Qw} \tag{2.21}$$

where $d_{5QW}$ is the total thickness for 5QW. Small active layer volume can be easily realized with a narrow stripe width. For the stripe width of 1.0 μm, 0.5μm and 0.3μm, the active volume of 2.25 $\mu m^3$ to obtain the modulation efficiency of 5 $GHz/mA^{1/2}$ is achieved at a cavity length of 75 μm, 150 μm and 250 μm, respectively. The active volume of 0.56 $\mu m^3$ to obtain the modulation efficiency of 10 $GHz/mA^{1/2}$ is achieved at a cavity length of 19 μm, 38 μm and 62 μm, respectively. Table 2.4 summarizes the relationships between the stripe width, cavity length for $V_a$ of 2.25 and 0.56 $\mu m^3$ and required coupling coefficients $\kappa$. The wider stripe design needs shorter cavity length to reduce the $V_a$. In addition, it is important to note that the coupling coefficient required at that case becomes significant large value. For example, to obtain $V_a$ of 0.56 $\mu m^3$, stripe width of 1.0 μm requires coupling coefficient of 5260 $cm^{-1}$. However, narrow stripe width of 0.3 μm weaken the optical confinement factor as shown in Figure 2.10. To maintain optical confinement factor even in narrow stripe design, lateral optical confinement structure should be introduced [13]. As shown in Figure 2.17, the narrow strip of 0.2 μm was experimentally realized by introducing the lateral optical confiment structure fabricated by selective are regrowth process.

Next, I investigated the enhancement in modulation efficiency arose from a differential gain. Figure 2.18 shows the modulation efficiency versus differential gain calculated for different active volumes. The optical confinement factor of 10% for the five quantum

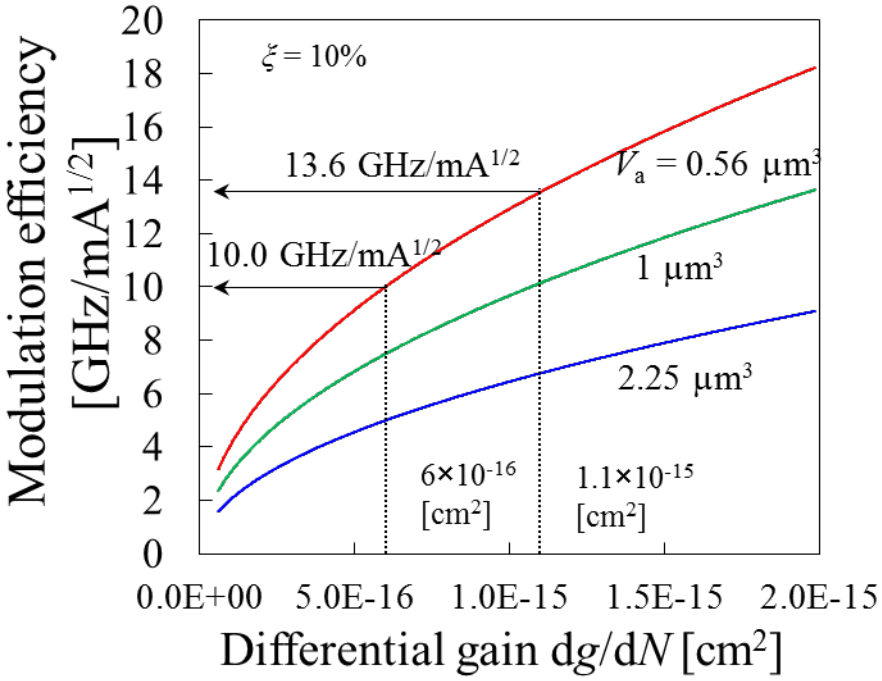


**Figure 2.18** Modulation efficiency as a function of differential gain.

wells was assumed. The compressed strained GaInAsP quantum well designed in our laboratory has a differential gain of $6\times10^{-16}$ cm$^2$. It is well known that the differential gain becomes maximum at the short wavelength side of the gain peak. A higher differential gain for the same quantum well design is possible by selecting a lasing wavelength that maximizes the differential gain for the DFB laser. In AlGaInAs system based quantum-well which can create deep conduction band offset, a differential gain higher than GaInAsP-based quantum-well was reported. The differential gain of $1.1\times10^{-15}$ cm$^2$ has been experimentally realized [14]. Using this differential gain, the modulation efficiency of 13.6 GHz/mA$^{1/2}$ can be obtained for the active volume of 0.56 μm$^3$.

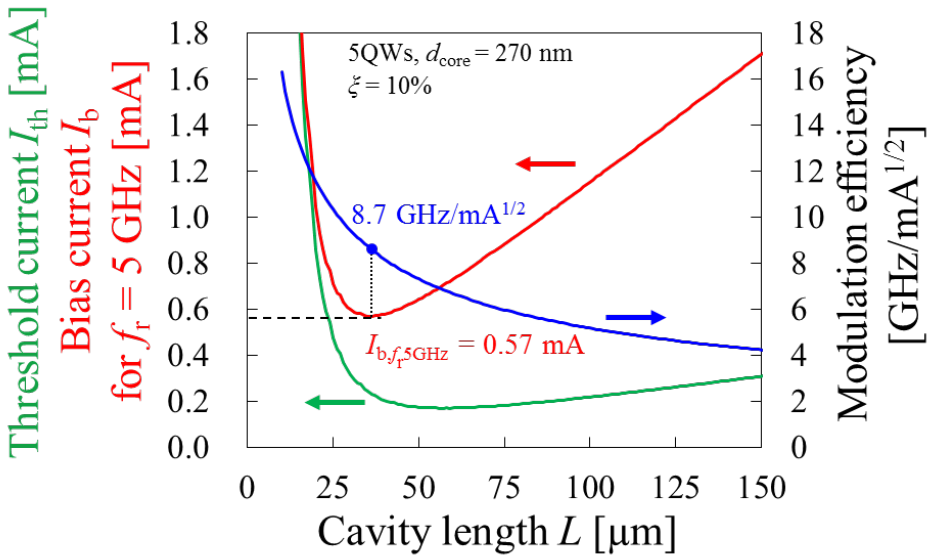


**Figure 2.19** Required bias current $I_b$ to obtain $f_r$ of 5 GHz ($\kappa$ = 2000 cm$^{-1}$, d$g$/d$N$ = 6 × 10$^{-16}$ cm$^2$, $W_s$ = 0.7 μm).

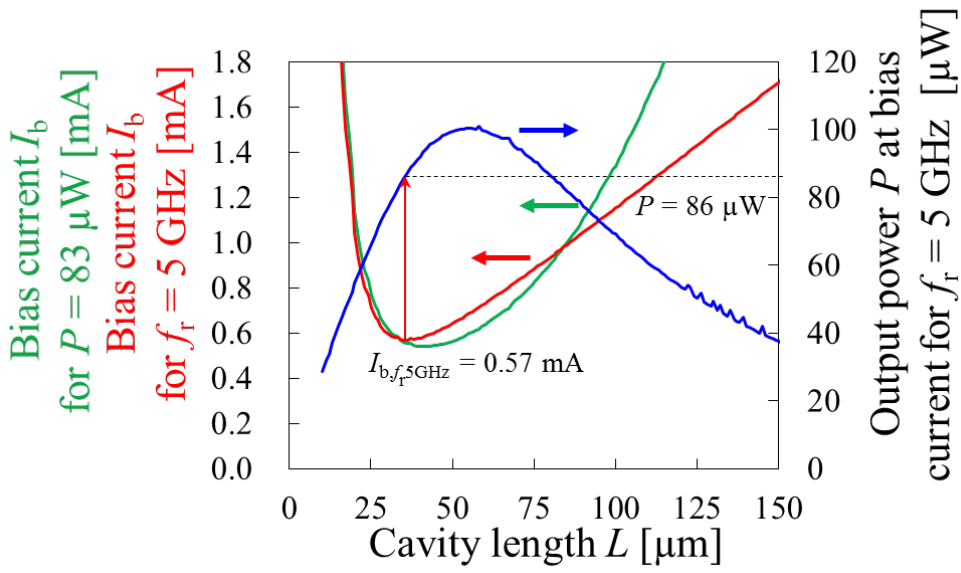


**Figure 2.20** Bias current $I_b$ to obtain $f_r$ of 5GHz (red line) and to obtain output power of 83 μW (green line). The blue line represents the output power at the bias current for $f_r$ of 5 GHz. ($\kappa$ = 2000 cm$^{-1}$, d$g$/d$N$ = 6 × 10$^{-16}$ cm$^2$, $W_s$ = 0.7 μm).

I have calculated the characteristics of the modulation efficiency with respect to the active volume and the differential gain. By calculating the modulation efficiency and the threshold current dependence on the cavity lengths, the bias current to obtain the certain bandwidth can be known. As already mentioned, the relaxation oscillation frequency $f_r$

needed for 10 Gbit/s is 5 GHz from equation (2.16) and (2.18). The value of the bias current required to obtain the $f_r$ can be calculated from the equation (2.13) as follows

Bias current to obtain the $f_r$

$$I_b = I_{th} + \frac{f_r^2}{\text{modulation effieicnry}^2} \tag{2.22}$$

In the case that the nonlinearity of the differential gain was ignored, the modulation efficiency monotonically increases as the cavity length reduced. The cavity length dependence of the threshold current has the local minimum value. Taking into consideration these facts, it can be predicted that the bias current required to obtain a certain relaxation oscillation frequency value varies so as to have a local minimum at a specific cavity length. Figure 2.19 shows the required bias current $I_b$ to obtain $f_r$ of 5 GHz. The $\kappa$ of 2000 $cm^{-1}$, d$g$/d$N$ of $6 \times 10^{-16}$ $cm^2$ and $W_s$ of 0.7 μm were used. The green and blue lines shows the calculated threshold current and the modulation efficiency. Using these two values, the bias current for the $f_r$ of 5 GHz at each cavity length depicted as red line can be calculated. The bias current takes the minimum value in the vicinity of the cavity length where the threshold current also becomes the minimum. At the cavity length of 35 μm, the threshold current and the modulation efficiency were 0.24 mA and 8.7 $GHz/mA^{1/2}$, respectively. Then, the required bias current was calculated to be 0.57 mA. Addition to the bandwidth requirement, a sufficient optical output power of 83 μW is simultaneously needed as discussed in the section 2.2. Figure 2.20 shows the bias current $I_b$ to obtain $f_r$ of 5GHz (red line) and to obtain output power of 83 μW (green line). The blue line represents the output power at the bias current for $f_r$ of 5 GHz. At the cavity length of 35 μm, a relationship between the current for $f_r$ of 5 GHz, $I_{b,fr5GHz}$, and the current for output power $P$ of 83 μW , $I_{b,P83\mu W}$ was

$$I_{b,fr5GHz} > I_{b,P83\mu W} \tag{2.23}$$

Therefore, when the bias current to obtain $f_r$ of 5GHz is injected, a sufficient output power for the photoreceiver is simultaneously obtained. The bias current of 0.57 mA can realize an energy cost of 57 fJ/bit when assuming a data-rate of 10 Gbit/s and an operating voltage of 1 V.

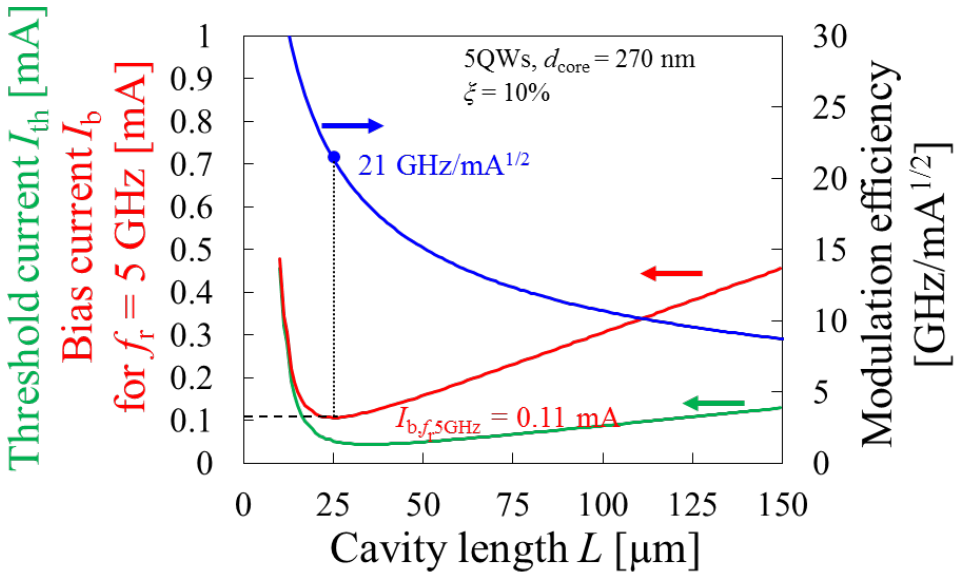


**Figure 2.21** Required bias current $I_b$ to obtain $f_r$ of 5 GHz ($\kappa$ = 4000 cm$^{-1}$, d$g$/d$N$ = 1.1 × 10$^{-15}$ cm$^2$, $W_s$ = 0.3 μm).

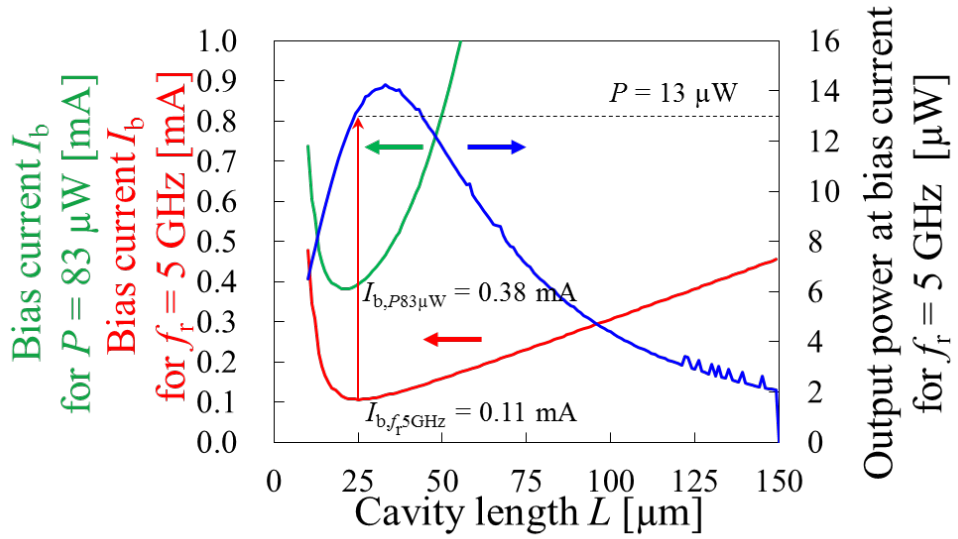


**Figure 2.22** Bias current $I_b$ to obtain $f_r$ of 5GHz (red line) and to obtain output power of 83 μW (green line). The blue line represents the output power at the bias current for $f_r$ of 5 GHz. ($\kappa$ = 4000 cm$^{-1}$, d$g$/d$N$ = 1.1 × 10$^{-15}$ cm$^2$, $W_s$ = 0.3 μm).

To realize further energy reduction, Figure 2.21 shows calculation result of bias current for $f_r$ of 5 GHz using the possible parameters for high modulation efficiency. The $\kappa$ of 4000 cm$^{-1}$, d$g$/d$N$ of 1.1 × 10$^{-15}$ cm$^2$ and $W_s$ of 0.3 μm were used. At the cavity length of 25 μm, the threshold current and the modulation efficiency were 0.05 mA and 21

GHz/mA$^{1/2}$, respectively. The bias current for $f_r$ of 5 GHz, $I_{b,fr5GHz}$, was 0.11 mA. Figure 2.22 shows the bias current $I_{b,fr5GHz}$ (red line) and $I_{b,P83\mu W}$ as a function of cavity length. In this case, at a bias current $I_{b,fr5GHz}$ of 0.11 mA, the optical output power $P$ was only 13 μW. This was not sufficient for the required optical power. At the cavity length of 25 μm, the relationship between the $I_{b,fr5GHz}$ and $I_{b,P83\mu W}$ was

$$I_{b,P83\mu W} > I_{b,fr5GHz} \tag{2.24}$$

The bias current is determined by not a value of $f_r$ but the optical output power. The required bias current for output power $P$ of 83 μW was calculated to be 0.38 mA. This results pave the way to achieve an energy cost of 38 fJ/bit operation.

## 2.4 Conclusion

In this section, optical device characteristics for on-chip interconnection was investigated based on a calculation. The link loss in on-chip interconnection has a significant impact on required lase output power. The design of membrane DFB lasers with respects to the modulation efficiency is numerically studied so that satisfy the performance required for on-chip optical interconnections.

In the consideration of link loss, the coupling efficiency and the propagation loss is the most important factors in the case considering the required optical power of the laser. The coupling efficiency has an influence independent on wiring length. Therefore, in a structure in which has low coupling efficiency, the increase in required power is caused even in a short wiring. In contrast, the propagation loss has significant influence on total link loss. In order to realize a long optical wiring that shows advantages for electric wiring, it is necessary to construct the interconnection with a waveguide having a propagation loss of approximately 1 dB/cm. If a highly efficient link structure is obtained, the required light output becomes small. As an example of efficient link, if a propagation loss of 1 dB/cm and a coupling loss of 0.1dB/coupling are achieved, the required laser output power for the wiring length of 2 cm is calculated to be 83 μW.

Threshold current and modulation efficiency were calculated based on the refractive index coupling coefficient obtained in membrane DFB structure. For the structure with a uniform grating with a coupling coefficient of 2000 $m^{-1}$, the minimum threshold current of 0.17 mA was obtained at a cavity length of 60 μm. For the structure with a $\lambda/4$-shifted grating with a coupling coefficient of 2000 $m^{-1}$, the minimum threshold current of 0.08 mA was obtained at a cavity length of 35 μm. The modulation efficiency is the slope of the relaxation oscillation frequency with respect to the bias current above threshold. This has a significant meaning to achieve high speed operation with low bias current. It was considered that the design to obtain the 3dB bandwidth of 7.7 GHz necessary for 10 Gbit/s operation at bias current of 1 mA for 100 fJ/bit energy consumption. At this situation, the modulation efficiency must be at least 5 GHz/$mA^{1/2}$ and for the 20 Gbit/s operation, 10

GHz/mA$^{1/2}$ is needed. From the relationship between the modulation efficiency and the active volume, the modulation efficiency of more than 5 GHz/mA$^{1/2}$ and 10 GHz/mA$^{1/2}$ are obtained for the active layer volume of less than 2.25 μm$^3$ and 0.56 μm$^3$, respectively. When the cavity length was 35 μm with the threshold current and the modulation efficiency of 0.24 mA and 8.7 GHz/mA$^{1/2}$, the bias current required for 10 Gbit/s operation was 0.57 mA. This bias current corresponded to a value that can realize an energy cost of 57 fJ/bit when assuming a data-rate of 10 Gbit/s and a driving voltage of 1 V. Assuming the possible extreme design to realize ultra-low energy consumption, the bias current required for 10 Gbit/s operation was calculated to be 0.38 mA, which was not determined by the $f_r$ but a required optical output power. According to this results, the prospect for realizing the 38 fJ/bit energy consumption operation in a membrane DFB laser was obtained.

# References

[1] G. Kurczveil, P. Pintus, M. J. Heck, J. D. Peters, and J. E. Bowers, "Characterization of insertion loss and back reflection in passive hybrid silicon tapers," *IEEE Photonics Journal,* vol. 5, pp. 6600410-6600410, 2013.

[2] Y. Hibino, H. Okazaki, Y. Hida, and Y. Ohmori, "Propagation loss characteristics of long silica-based optical waveguides on 5 inch Si wafers," *Electronics Letters,* vol. 29, pp. 1847-1848, 1993.

[3] J. Angenent, M. Erman, J. Auger, R. Gamonal, and P. Thijs, "Extremely low loss InP/GaInAsP rib waveguides," *Electronics Letters,* vol. 25, pp. 628-629, 1989.

[4] R. Takei, S. Manako, E. Omoda, Y. Sakakibara, M. Mori, and T. Kamei, "Sub-1 dB/cm submicrometer-scale amorphous silicon waveguide for backend on-chip optical interconnect," *Optics express,* vol. 22, pp. 4779-4788, 2014.

[5] Y. Atsumi, J. Kang, Y. Hayashi, J. Suzuki, N. Nishiyama, and S. Arai, "Analysis of higher-order mode suppressed transmission in low-loss silicon multimode waveguides on silicon-on-insulator substrates," *Japanese Journal of Applied Physics,* vol. 53, p. 078002, 2014.

[6] D. Inoue, J. Lee, K. Doi, T. Hiratani, Y. Atsuji, T. Amemiya*, et al.*, "Room-temperature continuous-wave operation of GaInAsP/InP lateral-current-injection membrane laser bonded on Si substrate," *Applied Physics Express,* vol. 7, p. 072701, 2014.

[7] H. Ghafouri-Shiraz, *Distributed feedback laser diodes and optical tunable filters*: John Wiley & Sons, 2004.

[8] L. A. Coldren, S. W. Corzine, and M. L. Mashanovitch, *Diode lasers and photonic integrated circuits*. New York, NY, USA: Wiley-Interscience, 1995.

[9] H. Kogelnik and C. Shank, "Coupled-wave theory of distributed feedback lasers," *Journal of Applied Physics,* vol. 43, pp. 2327-2335, 1972.

[10] S. Hansmann, "Transfer matrix analysis of the spectral properties of complex distributed feedback laser structures," *IEEE journal of quantum electronics,* vol. 28, pp. 2589-2595, 1992.

[11] R. Tucker, J. Wiesenfeld, P. Downey, and J. Bowers, "Propagation delays and transition times in pulse‐modulated semiconductor lasers," *Applied physics letters,* vol. 48, pp. 1707-1709, 1986.

[12] M. Futami, T. Shindo, T. Okumura, R. Osabe, D. Takahashi, T. Koguchi*, et al.*, "Stripe width dependence of internal quantum efficiency and carrier injection delay in lateral current injection GaInAsP/InP lasers," in *Opto-Electronics and Communications Conference (OECC), 2011 16th*, 2011, pp. 468-469.

[13] Y. Atsuji, K. Doi, T. Hiratani, D. Inoue, J. Lee, Y. Atsumi*, et al.*, "Low-threshold-current operation of membrane distributed-feedback laser with surface grating bonded on Si substrate," *Japanese Journal of Applied Physics,* vol. 54, p. 080301, 2015.

[14] T. Ishikawa, T. Higashi, T. Uchida, T. Fujii, T. Yamamoto, H. Shoji*, et al.*, "Evaluation of differential gain of 1.3/spl mu/m AlGaInAs/InP strained MQW lasers," in *Indium Phosphide and Related Materials, 1998 International Conference on*, 1998, pp. 729-732.

# Chapter 3
# Design and fabrication of membrane butt-jointed built-in structure

3.1 Introduction 118
3.2 Method of monolithic photonic integration 119
3.3 Butt-jointed built-in (BJB) structure 126
3.3.1 Selective area regrowth 126
3.3.2 BJB structure in photonic integration 128
3.4 Calculation of membrane BJB structure 133
3.4.1 Calculation method for BJB coupling 133
3.4.2 Analysis on coupling efficiency and back reflection 137
3.5 Process investigation of membrane BJB structure 145
3.5.1 Growth process 145
3.5.2 Dependence on regrowth mask shape 152
3.5.3 Dependence on island fabrication process 159
3.5.4 Evaluation of regrown layer by photoluminescence 164
3.6 Conclusion 170
References

## 3.1 Introduction

In order to integrate each membrane optical components, high coupling efficiency and low back reflection structure as well as negligible optical absorption at the passive region are necessary. These can be achieved by appropriate coupling structure design and optimum material design in terms of bandgap energy. There has been several approaches to integrating photonic devices, such as butt-joint built-in (BJB) structure, selective area growth (SAG), offset quantum-well (OQW) and quantum-well intermixing (QWI) to

name just a few. However, SAG, OQW and QWI are difficult to fabricate with membrane structure or to achieve rapid band gap change at the active-passive interface. Therefore, in this chapter, I employed the BJB structure using organo-metallic vapor phase epitaxy (OMVPE) as an integration method, and established the technologies, which satisfies the requirements above for membrane integration. First, the overview of photonic integration technique will be given. Moreover in the calculation, the coupling efficiency and the back reflection of the butt-joint interface were estimated using the finite difference method (FDM) and the eigen-mode expansion method (EME). Fabrication process of BJB structure in membrane semiconductor layer was investigated. The dependence of butt-joint growth results on the protect mask shape and the etching process before regrowth were studied. As a result, a flat regrown surface without degradation in crystalline quality was obtained.

## 3.2 Method of monolithic photonic integration

The concept of photonic integrated circuit was first proposed in early stage of a planer optics [1]. Semiconductor integrated optical devices were appeared in 1970s soon after the invention of RT-CW operated semiconductor laser [2]. The demand for integration of optical devices comes from need for small system footprint, low assembly cost, packaging cost and power reduction in the system using many optical component. The alignment between two optical devices typically requires sub-μm-order position accuracy. When the number of optical components reaches hundreds or thousands, the time consumption and cost for aligning all devices becomes impractical amount. In some cases such as using an optical amplifier, the power consume optical/electronic/optical converting process can be bypassed. And, the integration allows us to simultaneously align the many optical components by using a lithography.

We are now considering the way to integrate the membrane structure optical devices on a Si platform. There are several integrated optics platform based on a glass, an organic material and a semiconductor. I introduce the semiconductor integrated optics platform

classified into “hybrid” and “monolithic” integration. The hybrid integration was emerged in middle of 2000s. The name of hybrid is derived from the combination of III-V and IV group material. This is a method of integrating the III-V semiconductors on the IV semiconductor by using a wafer bonding or flip-chip bonding technique. The monolithic integration is composed of only III-V materials and is used in early integrated laser. It is typically difficult to obtain a high index difference waveguide in monolithic integration. In this section, some of monolithic integration method will be described.

## Monolithic integration method


**Figure 3.1** Monolithic integration method [3].

In monolithic integration, it is necessary to fabricate lasers, modulators, detectors and waveguide requiring semiconductor materials with different bandgap energy in the same plane. Especially, a passive waveguide should consist of a material with larger bandgap than that of active regions to avoid the absorption loss. As famous approaches of monolithic integration, offset quantum well, selective area growth, quantum well intermixing and butt-jointed built-in structure will be mentioned. Figure 3.1 summarizes a cross-sectional view of each integration method. In the following, the features,

advantages and disadvantages of these methods will be explain.

## Offset quantum wells (OQW)

An offset Quantum Wells (OQW) [4-6] structure has an initial growth structure consisted of the active region onto the passive layer. Unnecessary active layer is to be removed by etching during the fabrication process before the regrowth of upper cladding layer. The use of the OQW enable the integration of active and passive sections with only one regrowth process. This method makes the fabrication process of integrated device easy and simple procedure. However, it is difficult to obtain a large modal gain because the offset between the active region and center of waveguide prevents efficient overlap of optical field. The integration of more than two different bandgap requires additional regrowth steps. Figure 3.2 shows a schematic diagram of sampled grating DBR laser using OQW [3].


**Figure 3.2** Sampled-grating DBR laser using offset quantum well structure [3].

## Selective area growth (SAG)

In a selective are growth [7-11] the bandgap of the grown layer is controlled by a mask covering nearby the area to be grown. The dielectric mask promotes the flow of diffusion of metal organic precursors. The thickness and composition of grown layer is strongly affected by the design of the mask geometry. Using SAG integration, epitaxial layers with

different bandgaps for each region can be formed by only one growth. However, for precise control of desired grown layer, many analysis on experimental data and model of growth mechanisms are needed and considerable effort should be paid for calibrations [12].


**Figure 3.3** Mask design for SAG indicated by hatched lines [13].

## Quantum well intermixing (QWI)

A quantum well intermixing (QWI) is a method to make a bandgap shift by diffusing the materials consisting a QW. The selective removal of the intermixing catalyst enable us to make the different bandgap region in a same plane. There are many reports on achieving the compositional intermixing of QW, such as impurity-induced disordering (IID) [14], impurity-free vacancy-enhanced disordering (IFVD) [15], photoabsorption-induced disordering (PAID) [16], and implantation-enhanced interdiffusion [17]. Although this method has an advantage that the etching and regrowth process is not necessary, it is difficult to obtain a large emission wavelength difference of more than 150 nm while maintaining the crystalline quality. Several groups reported integrated photonics devices using quantum well intermixing [18-21].


**Figure 3.4** Emission peak wavelength of photoluminescence induced by QWI as a function of anneal times [22].

## Butt-jointed built-in (BJB) structure

A butt-jointed built-in structure (BJB) consists of the butt-coupling between the active and passive section by selective removal of unnecessary region and butt-joint regrowth [23-27]. This method can utilizes the well sophisticated etching and regrowth process in semiconductor laser manufacturing. A good bandgap controllability is available due to the regrown layer formed by organometallic vapor phase epitaxy (OMVPE). As a negative aspect, when the number of desired different bandgap regions increases, the regrowth is required as many as the number of required bandgap regions. The BJB structure is adopted as a standard integration method for manufacturing the productive integrated lasers in many company [28-33]. The thickness and bandgap of regrown layer are controlled by equipment for OMVPE.


**Figure 3.5** 1.6 μm DBR laser integrated by butt-jointed built-in structure [23].

Table 3.1 summarizes the above mentioned monolithic integration methods. The offset quantum well needs the stacked active and passive layers structure, and has a relatively thick waveguide core. As a result, the strong optical confinment effect in a membrane structure is obscured by OQW integrated structure. Therefore the compatibility of offset quantum well in membrane structure is not so good. The SAG method will serve as the superior integration platform once the calibration is completed. However, establishment of growth condition will require considerable effort and spending a large amount of time. It is considered difficult to apply the SAG to integration of membrane optical devices in restricted time at this thesis. The QWI based on IFVD had been investigated for integrating the membrane optical devices in our group [22, 23]. Tradeoff between the crystalline quality and bandgap shift was a primary problem. BJB structure is expected to offer the appropriate integration platform in membrane structure. In a membrane structure, it is preferred that the integrated structure has a flat joint section to avoid the scattering

**Table 3.1** Comparison of the monolithic integration methods.

| Method | Compatibility in membrane structure | Thickness controllability | Bandgap controllability | Process complexity |
|---|---|---|---|---|
| Offset quantum well | poor | good | good | easy |
| SAG | good | moderate | moderate | moderate |
| QWI | good | good | moderate | easy |
| BJB | good | good | good | moderate |

loss. Thickness of regrown layer is precisely controlled by growth time during OMVPE regrowth. The properties of regrown layer is expected to same as grown on bulk substrate if an appropriate pretreatment is performed. In addition, we can utilize the already established etching and regrowth process established for preparing the lateral *pn*-junction. In this thesis, I focus on the BJB structure as an integration method of membrane optical devices. The next section describes core technologies of the selective area regrowth and BJB structure in the membrane platform.

## 3.3 Butt-jointed built-in (BJB) structure for membrane photonic integrated circuits

The BJB structure has feature which are wished for integration method of membrane optical devices. To fabricate a fine BJB structure, selective area regrowth conducted by OMVPE is a key technology. The optimization of etching and growth can be done by experimental try and error sequence because it is difficult to simulate the mechanism of growth phenomena associated with a structured surface and precursor diffusion from the mask. Each research group developed a structure based on its own empirical accumulation of knowledge. First the principle of the selective area regrowth technique will be introduced.

### 3.3.1 Selective area regrowth

During OMVPE growth process, the grown region can be selected by covering the semiconductor surface with dielectric film such as $SiO_2$ or SiN. On the dielectric film, reactant does not make bond, but continue to diffuse a long distance to find energy stable position. Utilizing this fact, after once epitaxial growth performed, the region to be protected is covered with a dielectric mask. Then the unnecessary region is removed by etching, we can form a desired semiconductor material on selective region by repeating epitaxial growth. This selective area regrowth can be used for fabrication of buried-hetero structure and integrated lasers. Figure 3.6 shows possible diffusion path of precursors in selective area regrowth. It is known that diffusion paths of precursors on a dielectric film are divided into surface diffusion that migrates the surface of substrate, lateral vapor phase diffusion that diffuses from the top of the substrate to lateral direction in the vapor phase and vertical vapor phase diffusion that diffuses in the vertical direction to the substrate [34, 35]. Surface diffusion affects the diffusion length of approximately several μm from the edge of the mask region. Lateral vapor phase diffusion affects from the edge of the mask region to a distance of several 10 μm. In a growth of quaternary compound semiconductor such as GaInAsP, a compositnal deviation occurs in the vicinity of the mask owing to a difference in diffusion length between the Ga reactant and the In reactant.

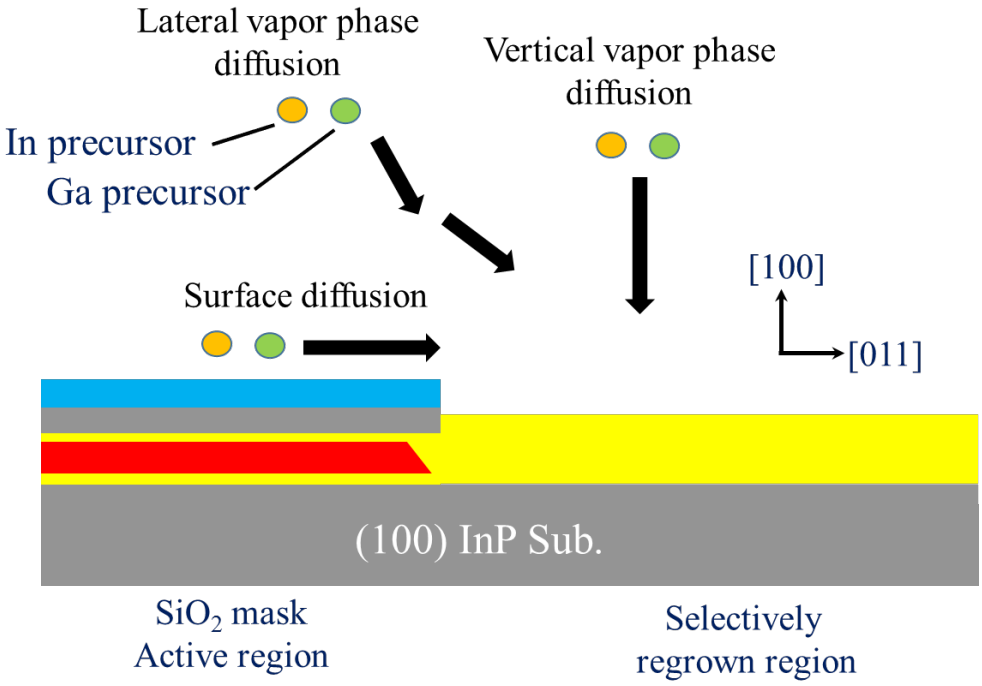


**Figure 3.6** Possible diffusion paths of precursors in selective area regrowth.

[36]. If the compositional deviation causes the lattice mismatch exceeds the critical thickness, the polycrystallization of grown material is occurred. To perform successful regrowth, following points are necessary;

(1) Exposing clean surface

(2) Forming undercut region beneath the mask to suppress over-regrowth

(3) Selecting proper crystalline orientation to form mesa

The brief explanation is given as follows. (1) When the unnecessary region is etched by accelerated plasma with high energy such as reactive ion etching, significant damage remains on the semiconductor surface. Growing performed on the damaged surface, defects and abnormal growth may be created. (2) This is to prevent abnormal growth due to transported precursors diffused from the dielectric mask region. In the region of near mask edge where group III reactant diffused from the mask, excessive mass transportation of III reactant occurs. Then the growth is proceeded with a higher growth rate than the growth rate of planar region. By forming undercut region by using selective wet etching under the dielectric mask, a space for reactant flowing in is formed. As a result, a flat regrowth structure can be obtained even in the vicinity of the mask. (3) Depending on the

orientation of the mesa of the covered region, the difference in growth shape depending on the crystalline orientation appears near the mesa. This is because the direction of the bonding of the group III element and the group V element differs depending on the plane orientation exposed by the etching, so that the energy stability for incoming reactant is different. Generally, when the $(011)$ plane is exposed, it tends to form a groove in the vicinity of the mask, and when the $(0\bar{1}1)$ plane is exposed, the growth tends to be exciting [37].

In the next subsection, after reviewing examples of formation of BJB structures, I will describe the structure required for the integration of membrane optical devices.

### 3.3.2 BJB structure in photonic integration

The previous reports on fabrication of the BJB structure in conventional semiconductor platform are introduced. While the BJB structure can be fabricated by using molecular beam epitaxy[38], the small mass transport and diffusion of precursor result in poor growth results compared with BJB structure fabricated by OMVPE. Therefore, most of the currently conducted butt-joint regrowth is performed by OMVPE. The BJB structure requires increment of the number of regrowth steps. To reduce the growth steps, sometimes butt-joint growth accompanies the growth of cladding layer [39]. As shown in


**Figure 3.7** BJB structure accompanied with cladding layer growth [39].


**Figure 3.8** BJB coupling between the two MQW regions formed before the growth of the cladding layer [24].

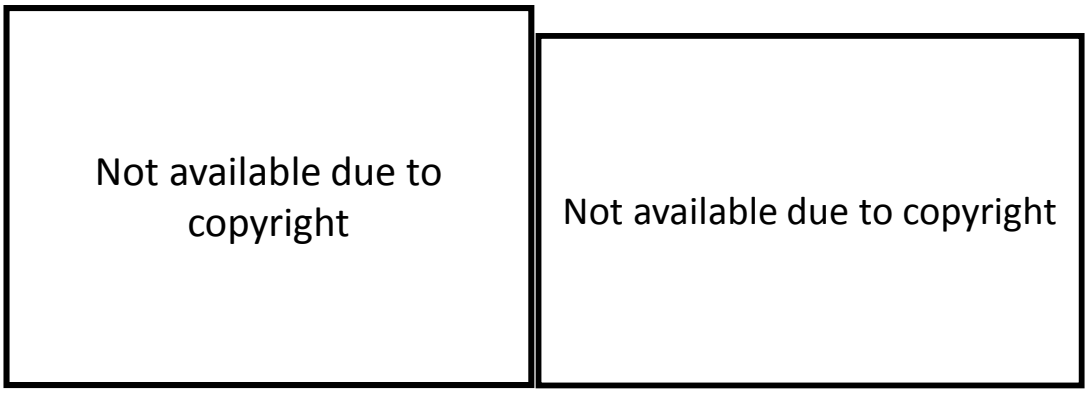


(a) (b)

**Figure 3.9** Undercut structures and growth results using (a) selective etchant and (b) non-selective etchant [40].

Figure 3.7, however, thickness at the vicinity of the mask is largely deviated from the planar region by mass transport effect. To fabricate a planar BJB structure, it is preferred that the growth of cladding layer is performed after the fabricating the BJB structure on initial epitaxial structure [24, 40-43]. Figure 3.8 shows the BJB structure integrating the laser and electro-absorption region fabricated before the growth of cladding layer. As a good aspect, cladding layer growth performed entirely over the jointed region helps the surface planarization. To alleviate the growth rate enhancement effect by the mask, the formation of side etching under beneath


**Figure 3.10** (left) The mask layout for tilted butt-joint growth. (right) The growth results for tilted mesa [26].


**Figure 3.11** SEM images of butt-joint growth formed in (a) $[\mathbf{0\bar{1}1}]$ direction observed from $(\mathbf{011})$ plane and (b) $[\mathbf{011}]$ direction observed from $(\mathbf{0\bar{1}1})$ plane [25].

the dielectric mask is known as effective approach [40, 44]. The ref. [40] investigated the effect of side etching before the growth using selective and non-selective etchant as shown in Figure 3.9. The

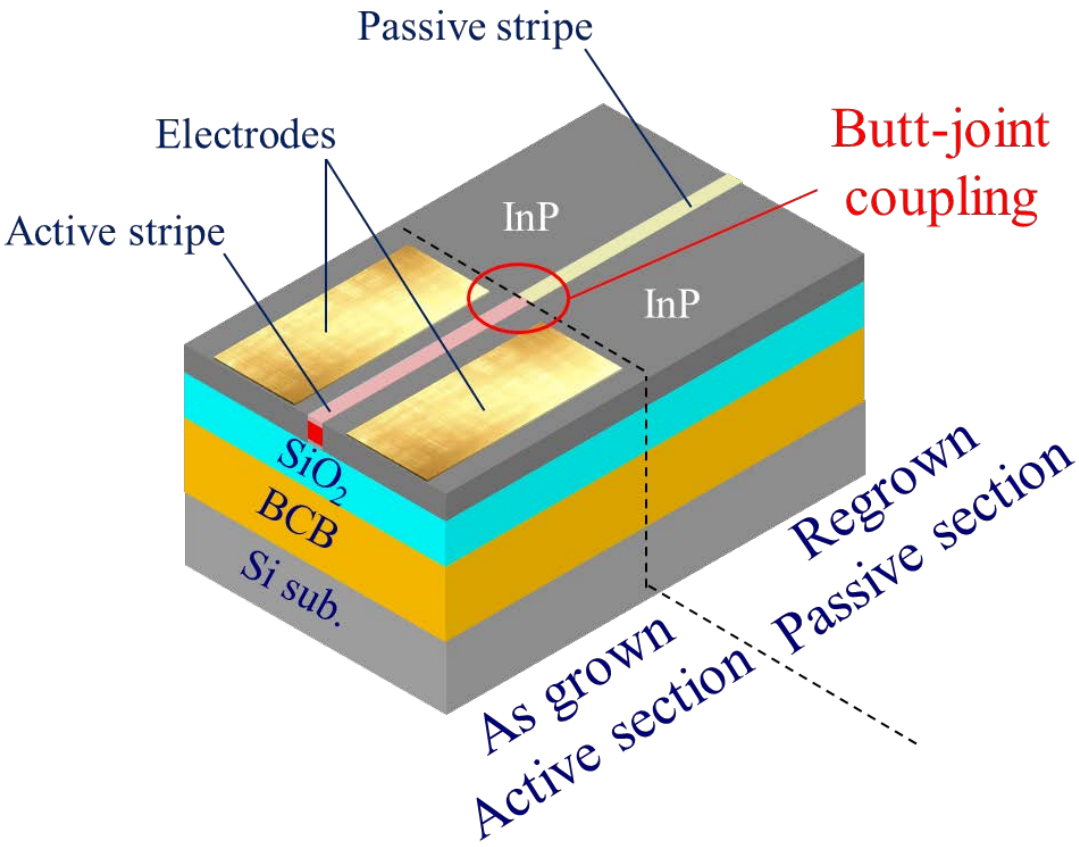


**Figure 3.12** Schematic of membrane BJB structure bonded on Si substrate.

selective and non-selective etchant were $H_2SO_4 : H_2O_2 : H_2O = 1 : 1 : 8$ and $HBr : H_2O_2 : H_2O = 1 : 1 : 10$, respectively. In both cases, the top lnP on the active layer was selectively etched by $HCl : H_2O = 4 : 1$ at 4°C. Figure 3.9 shows the undercut structures and growth results for selective and non-selective etchant. When the deep under etching was formed using selective etchant, the formation of InP, InP-rich alloy or void leaving at the undercut becomes problem. The side etching depth should be carefully chose to avoid these problems. Using non-selective etchant, the active layer and InP cap layer are both etched. Although the sidewall had thick InP layer grown with enhanced growth rate, there is no void left beneath the undercut and no compositional variations are expected. The orientation of the mesa significantly change the growth shape. The investigation of growth results of butt-joint regrowth are performed with mask oriented in the direction of [011] and $[0\bar{1}1]$ [25] (Figure 3.10), or tilted direction [26](Figure 3.11). According the

ref. [25], the tendency of the excitation at the joint formed in $[0\bar{1}1]$ direction than $[011]$ direction. The tilted mask layout forming mesa can change the growth shape depending on crystallographic graphic direction. The active region removal process has an influence on the growth results [25]. Depending on the used etching method of reactive ion etching, wet etching or these combination, different growth results are obtained and typically use of manly wet chemical etching is preferred to avoid damage induced by dry etching [45, 46].

In a membrane BJB structure, the structural requirements different from the conventional BJB integrated structure are as follows;

(1) A thin regrowth thickness of 100–200 nm

(2) Surface flat joint section

(3) No subsequent cladding regrowth available

(1) The butt-joint regrowth for membrane structure should complete with a growth thickness of 100–200 nm. (2) The optical filed in membrane structure is sensitive to the surface object due to the large refractive index difference between the core and cladding layer. To avoid the scattering loss at the joint section, the regrown structure should be connected with the as-grown active region with smooth surface. (3) Planarization process by growing cladding layer is unavailable because the membrane structure has dielectric cladding layers. In order to obtain a structure satisfying these requirements, growth structure change can be accomplished using the method as described above. Figure 3.12 shows schematic of membrane BJB structure aiming in this thesis. BJB structure is formed in a membrane semiconductor layer on Si substrate. In next subsection, I will describe an analysis on characteristics of BJB coupling in membrane structure.

## 3.4 Calculation of membrane BJB structure

A coupling efficiency and reflection ratio are the fundamental characteristics of joint interfaces of two sections. The expected coupling characteristics of a membrane BJB structure is analyzed by numerical calculation in this section. A tolerance for layer thickness variation is considered for calculation. Back reflection ratio at the interface is also investigated because the reflection between the laser and the waveguide become an important factor hindering stable operation of the laser. Therefore, it is studied that the structure of the membrane BJB structure which can obtain high coupling efficiency and sufficiently small back reflection toward fabricating integrated membrane optical devices.

### 3.4.1 Calculation method for BJB coupling

Numerical calculations are performed using the FIMMWAVE and FIMMPROP released by Photon Design Inc [47]. A full-vectorial finite-difference-method (FDM) is used to calculate mode profiles including full-vectors and the effective indices for all eigenmodes of the waveguide. The obtained eigenmode profiles are incorporated in eigenmode-expansion (EME) method calculation performed by FIMMPROP, then scattering matrix including joint section is obtained. A brief theoretical principle of these calculation methods are introduced.

**Finite-difference-method**

First, finite-difference-method (FDM) [48, 49] basically uses a calculation procedure similar to finite-difference-time domain method (FDTD) [50, 51]. By differentiating the Maxwell's equation with respect to the space, the electric and magnetic fields for each region can be found. The only difference from FDTD is to neglect the difference of time. It is possible to calculate the existing electromagnetic field distribution so called mode profile of each mode from the cross-sectional structure of the waveguide by using FDM. Various parameters such as the equivalent refractive index of the waveguide and the


**Figure 3.13** $TE_{01}$ mode in an optical fiber as calculated by FIMMWAVE [47].

optical confinement factor can be obtained from the mode profile. Figure 3.13 shows an example of the FDM calculation for a mode-profile of an optical fiber. It is also used as the calculation method of the eigenmode in the EME.

**Eigenmode-expansion (EME) method**

EME method can deal with a rigorous solution of Maxwell's equations with very long propagation structure. Assuming a single wavelength and time dependence of the form exp(iωt), solutions of Maxwell's equation are descripted as follows;

$$\mathrm{E(x,y,z)} = e_m(x,y) \cdot e^{i\beta_m z} \tag{4.1}$$

We can find that a mode has a simple harmonic dependence for $z$, and this fact enable EME method to solve slowly varying structures quickly and efficiency. In typical waveguide, there are several guided modes and infinite radiation modes. A complete basic set, which can express any solution of Maxwell's equation in a waveguide, consists of superposition of the guided and radiation modes including both the forward and backward propagation modes. The electric and magnetic field can be expanded as following equations.

$$\mathbf{E}(\mathrm{x,y,z}) = \sum_{k=1}^{M}(a_k e^{i\beta_k z} + b_k e^{-i\beta_k z})\mathbf{E_k}(\mathrm{x,y}) \quad \text{Electrical field} \tag{4.2}$$

$$\mathbf{H}(\mathrm{x,y,z}) = \sum_{k=1}^{M}(a_k e^{i\beta_k z} + b_k e^{-i\beta_k z})\boldsymbol{H_k}(\mathrm{x,y}) \quad \text{Magnetic field} \tag{4.3}$$

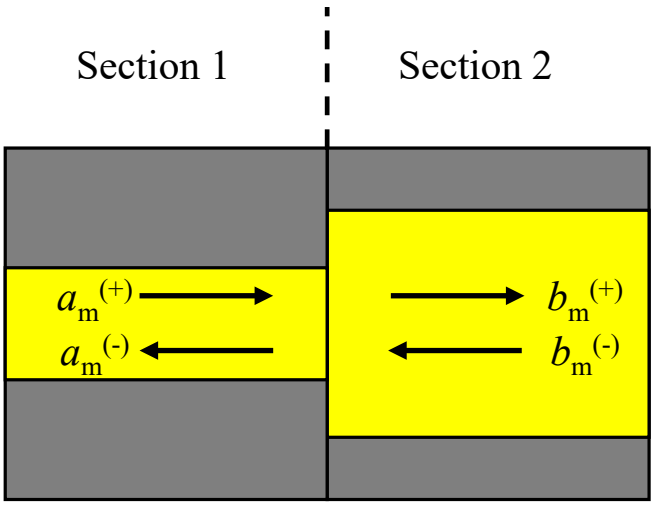


**Figure 3.14** Scattering coefficient at a waveguide joint.

These equations give exact solution of Maxwell's equation in a linear medium. Next, to analyze jointed optical waveguide structure, a joint section between two waveguide will be introduced.

The boundary conditions at a joint of two media are derived from the continuity conditions Maxwell's equation. The tangential component of electrical fields must be equal on each side of the jointed interface. According to the expanded expression of the electrical fields, the mathematical expression for boundary conditions are as follows;

$$\sum_{k=1}^{M}\left(a_k^{(+)}e^{i\beta_k z}-a_k^{(-)}e^{-i\beta_k z}\right)\boldsymbol{E}_k^{(+)}(\mathrm{x,y})=\sum_{k=1}^{M}(b_k^{(+)}e^{i\beta_k z}-b_k^{(-)}e^{-i\beta_k z})\boldsymbol{E}_k^{(-)}(\mathrm{x,y}) \qquad (4.4)$$

Also, the boundary conditions for longitudinal electrical and magnetic fields become

$$\int \mathbf{E}_{x,j}\cdot\mathbf{H}_{x,j}-\mathbf{E}_{\boldsymbol{y},j}\cdot\mathbf{H}_{\boldsymbol{y},j})\cdot dS=\delta_{jk} \qquad (4.5)$$

Here, I used the fact that the all modes are orthonormal each other. After some mathematical operations, a relationship between the coefficients are represented as the form;

$$\begin{pmatrix}a^{(-)}\\ b^{(+)}\end{pmatrix}=\mathbf{S}_J\begin{pmatrix}a^{(+)}\\ b^{(-)}\end{pmatrix} \qquad (4.6)$$

In this matrix equation $S_J$ is a scattering matrix for the waveguide joint. The evolution in the simple propagation section is represented as

$$\begin{pmatrix} e^{i\beta_1 z} & \mathbf{0} & \cdots \\ \mathbf{0} & e^{i\beta_2 z} & \cdots \\ \vdots & \vdots & \ddots \end{pmatrix} \tag{4.7}$$

Calculation for this diagonalized matrix can be conducted very quickly when eigenmodes are once obtained. In EME method, first, the eigenmodes in each region are calculated, and the electromagnetic field distribution is deduced by calculating the scattering matrix of the joint section between each propagating region.

A combination of modal analysis based on FDM and propagation analysis based on EME method enable us to an accurate and time efficient numerical calculation of a waveguide.

### 3.4.2 Analysis on coupling efficiency and back reflection

Prior to the showing the coupling structure to be analyzed, a brief fabrication procedure of the membrane BJB structure is shown. Figure 3.15 shows a fabrication process of the membrane BJB structure. The process start with an initial growth InP wafer including MQWs layer. The island shape $SiO_2$ mask is formed by using plasma-enhanced chemical vaper phase deposition and photolithography. The mask pattern is transferred on MQWs layer by etching. Then, a GaInAsP/InP waveguide layer is regrown by OMVPE. Subsequently, n- and p-InP layers are regrown using stripe shape $SiO_2$ mask. Finnaly the InP substrate is bonded on a Si substrate with $SiO_2$ cladding layer intermediated by BCB adhesive. The variable parameters for designing the coupling structure is considered to be a refractive index of waveguide as well as composition of GaInAsP or growth thickness. However, the equivalent refractive index of the waveguide can be easily changed by thickness control rather than the material composition change. For this reason, the growth thickness, which can be easily controlled by a growth time, is chosen as a parameter to be designed.

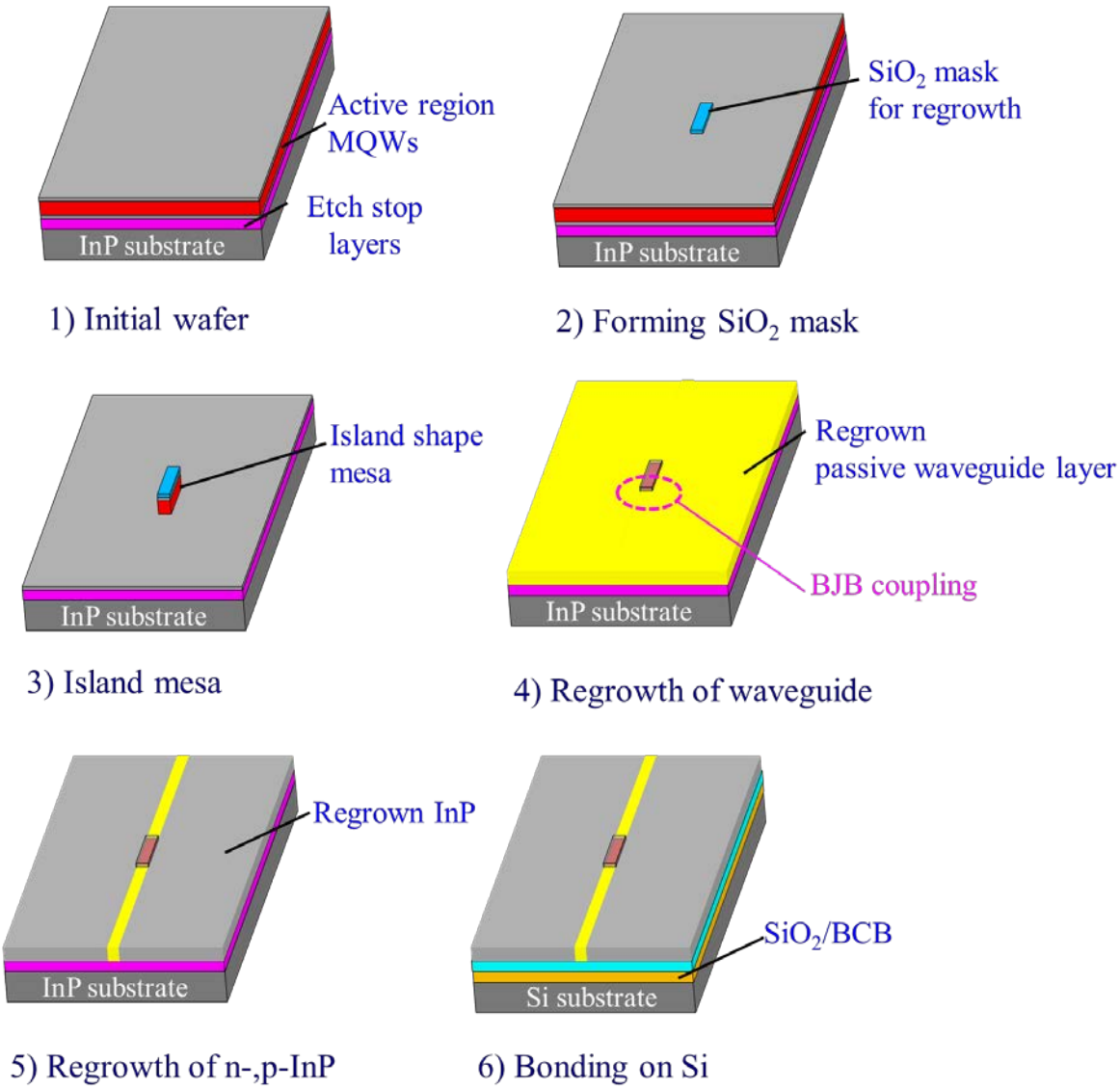


**Figure 3.15** Schematics of fabrication process of membrane BJB structure.

Figure 3.16 shows the calculation model of the membrane BJB structure in perpendicular to the direction to the propagation direction. The stripe width is 0.8 μm, which satisfies the single mode in the both active and passive section and can expect good laser characteristics. The active section consists of 5 multi quantum-wells buried by side InP cladding layer. The passive section has also side InP cladding layer. The growth thickness of GaInAsP layer $d$ can be a parameter. The total core thickness of the passive waveguide is defined as $D = d$ + 100 nm (top InP) + 20 nm (bottom InP). Figure 3.17

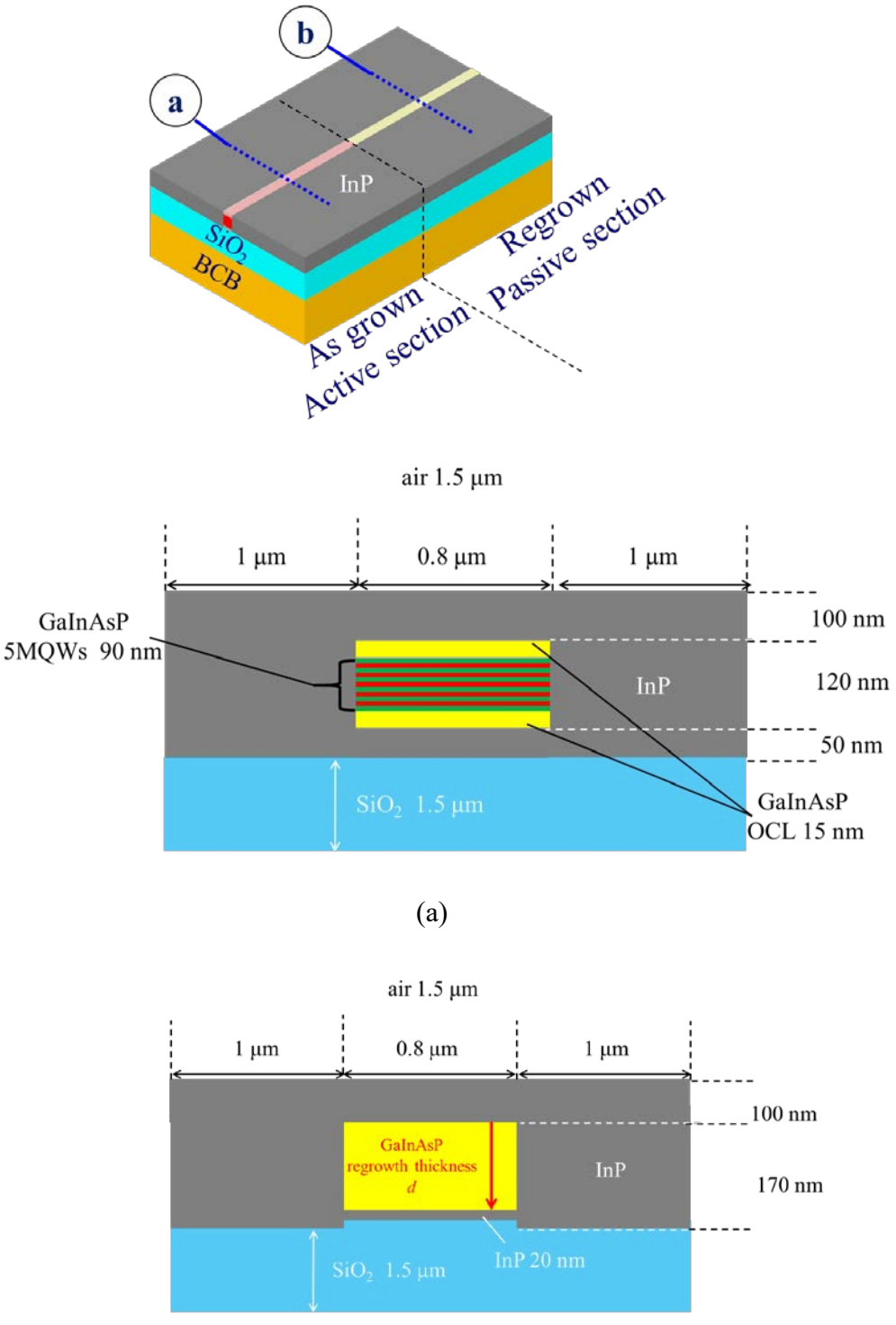


**Figure 3.16** Calculation model of the membrane BJB structure in perpendicular to the direction to the propagation direction. (a) Cross section of an active region. (a) Cross section of a passive region

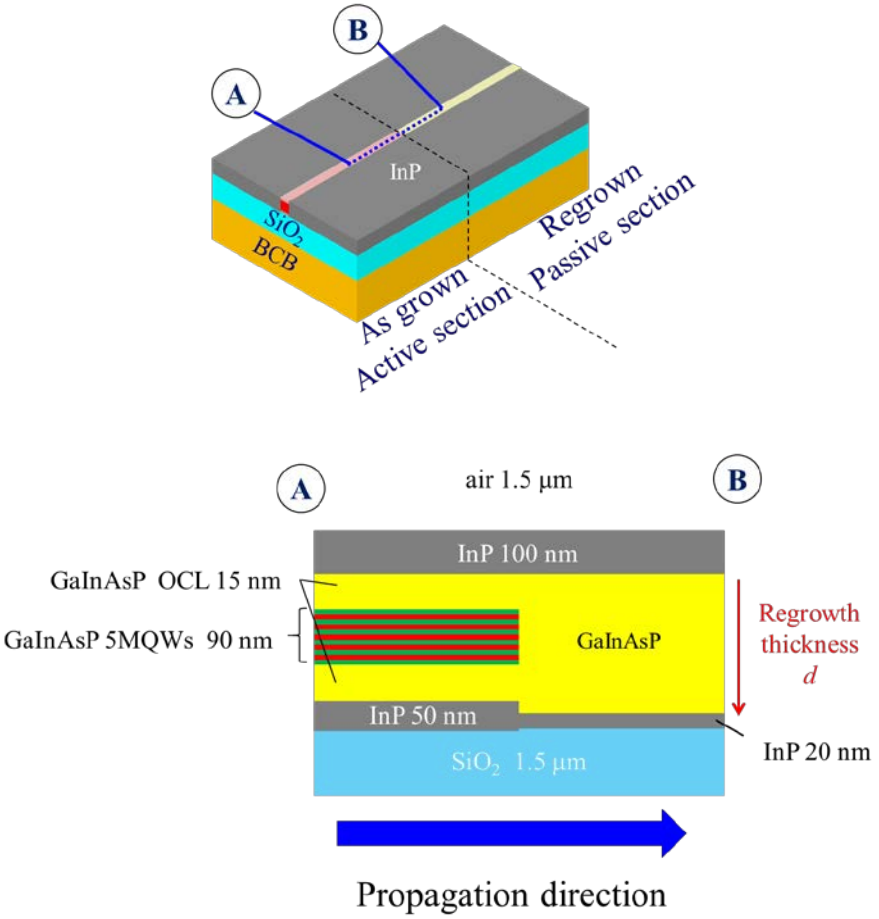


**Figure 3.17** Calculation model of the membrane BJB structure in horizontal direction to the propagation direction.

shows the calculation model of the membrane BJB structure in the direction parallel to the propagation direction. It is assumed that two regions are joined by abrupt interface without any transition structure. Actually, such abrupt joint is difficult to fabricate because of the growth phenomena during the OMVPE regrowth. After observing the experimentally obtained BJB structure in next section, coupling efficiency is again calculated. The cladding layers of 1.5 μm-thick of $SiO_2$ and air are used because the optical field does not exist outside these cladding layers. The calculations are performed using wavelength of 1.55 μm which is the target operating wavelength of the membrane laser. Table 3.2 summarizes the used parameters for the calculation at the wavelength of

**Table 3.2**Refractive index parameters in the calculations at 1.55 μm.

| Material | Refractive index |
|---|---|
| Air | 1.00 |
| $G_{0.21}In_{0.79}As_{0.46}P_{0.54}$ (OCL) | 3.35 |
| $G_{0.22}In_{0.78}As_{0.81}P_{0.19}$ (well) | 3.54 |
| $G_{0.26}In_{0.74}As_{0.49}P_{0.51}$ (barrier) | 3.35 |
| $SiO_2$ | 1.44 |
| InP | 3.17 |

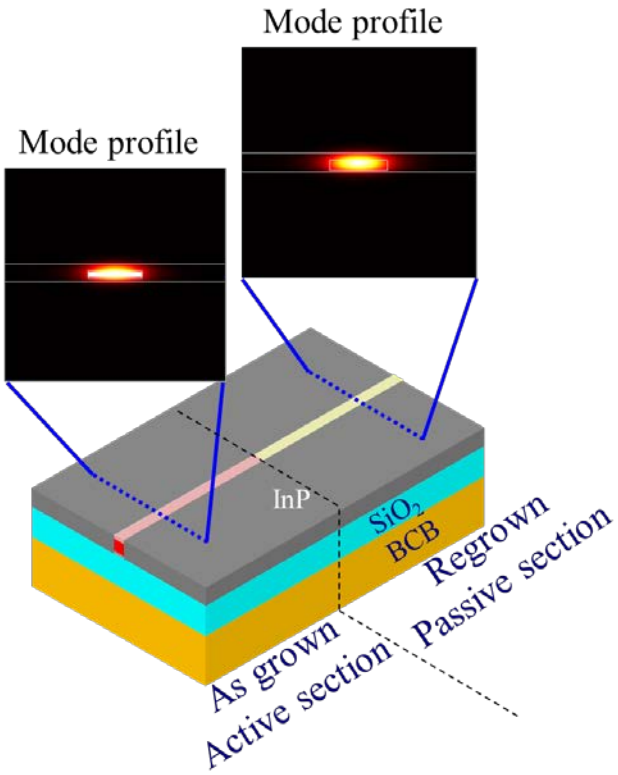


**Figure 3.18** Mode profiles at the active and passive sections.

1.55 μm. The refractive index of quaternary materials are calculated by modified single effective oscillator method (MSEO) [52]. Figure 3.18 shows calculated mode profiles at the active and passive sections with regrowth thickness *d* of 150 nm, that is when the thickness of the active and passive sections are matched. These profiles have almost same

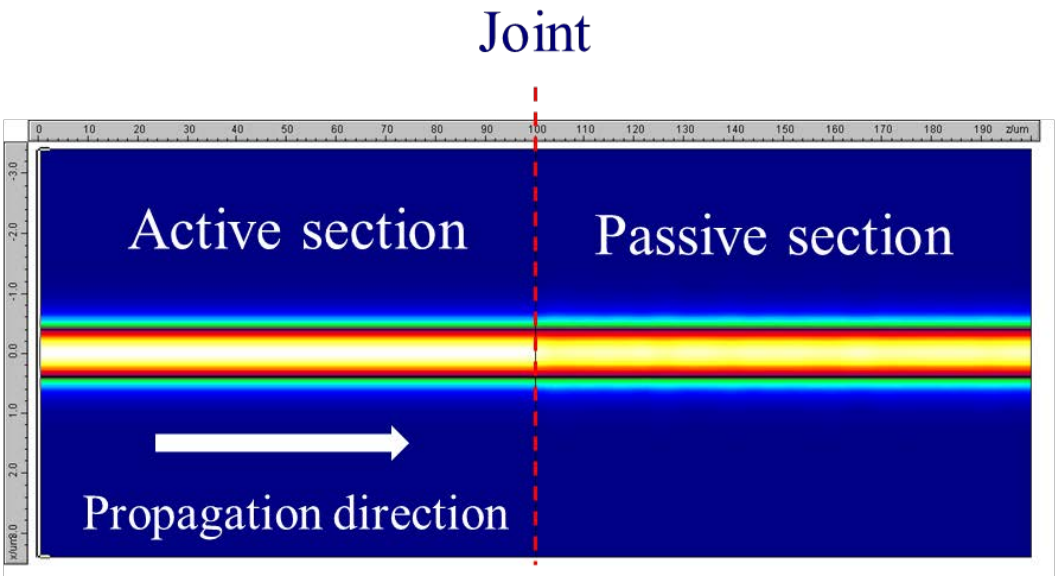


(a)

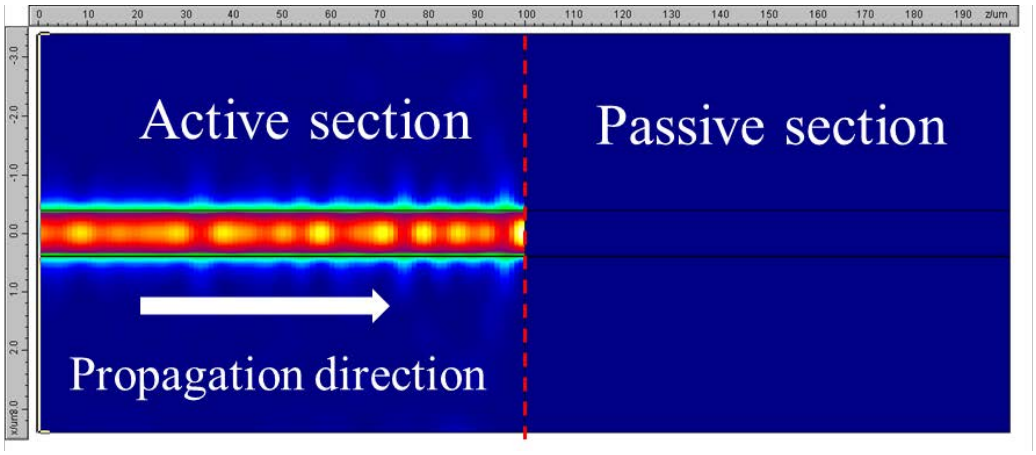


(b)

**Figure 3.19** Propagation intensity profile calculated by EME method. (a) Forward propagating power, (b) Backward propagating power.

shape which is thanks to the BJB integration structure. Figure 3.19 shows result for propagation intensity profile calculated by EME method. The incident optical mode was TE-like 0th-order. The passive regrowth thickness *d* of 150 nm was used in this calculation. As shown in the (a), the forward propagating field is well coupled to the passive section. The backward propagating field is shown in the (b). Although the almost

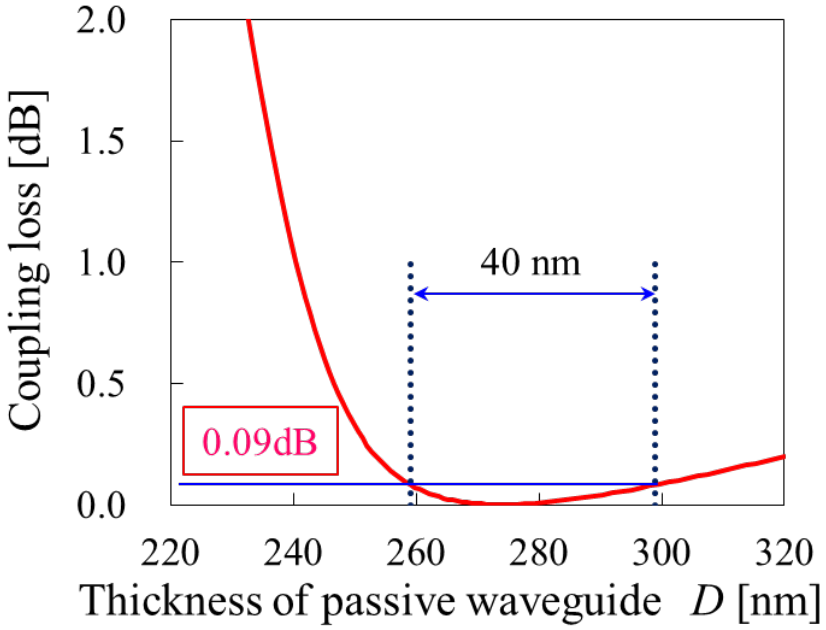


**Figure 3.20** Coupling loss of the BJB coupling between the active and passive sections.

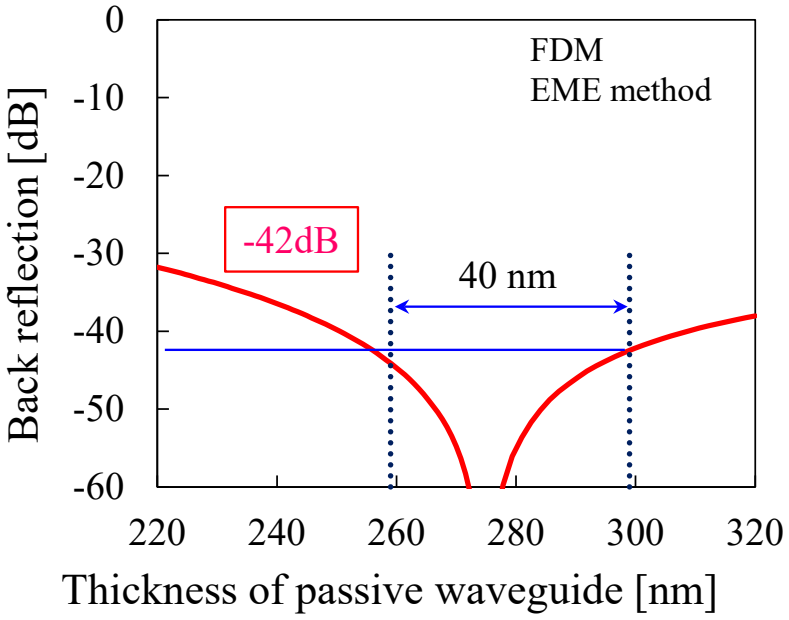


**Figure 3.21** Back reflection ratio at the BJB coupling.

propagating power is coupled to the passive section, there exits back reflection portion. Figure 3.20 shows the coupling loss of the active-passive BJB coupling as a function of the total thickness of passive waveguide *D*. We consider the ± 20 nm thickness as a possible deviation during fabrication. Choosing the thickness of 279 nm as the center, it

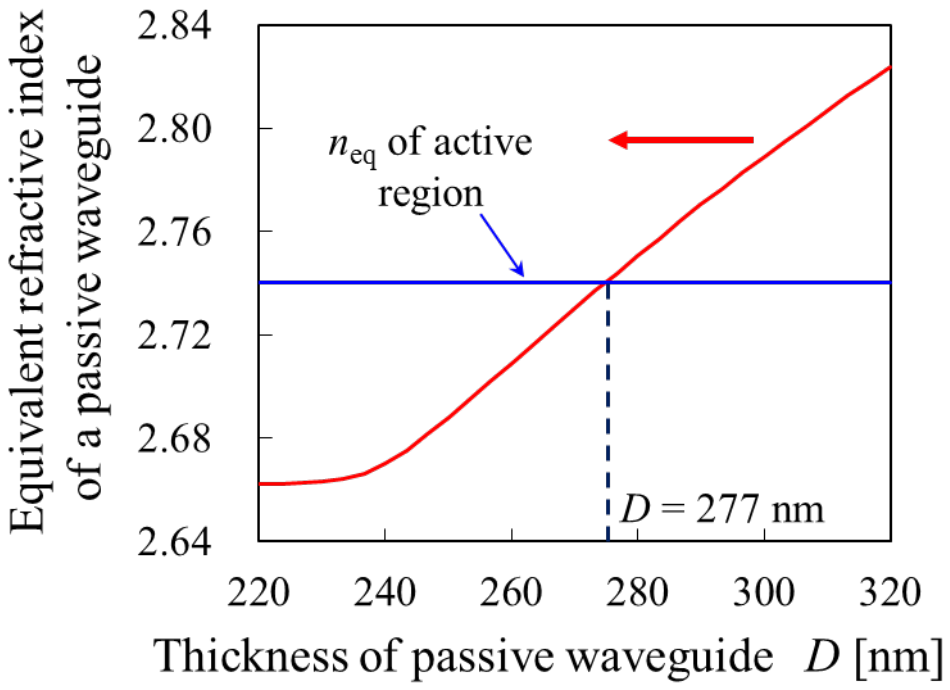


**Figure 3.22** Equivalent refractive index of the passive waveguide section as function of the thickness.

can be seen that the coupling loss of less than 0.09 dB (2%) is obtained in the deviation of ± 20 nm. The reason of the rapid increase of loss in the less thickness region is large mode mismatch between the two sections. As for the back reflection ratio shown in Figure 3.21, the value of less than -42dB is expected within the aforementioned thickness deviation range. This is a value is considered to not disturb the stable operation of the laser [53]. In order to verify the reason of why the minimum coupling loss occurred at the thickness of 279 nm, an equivalent refractive index as a function of the passive waveguide thickness is calculated. Figure 3.22 shows the equivalent refractive index of the passive waveguide as a function of the waveguide thickness. The equivalent refractive index of the passive section is monotonically increased as increasing the waveguide thickness. The indices of the active and passive regions are becomes equal when the passive waveguide thickness is 277 nm. At this thickness, back reflection becomes small due to a little index mismatch. In addition to the refractive index matching, the mode profiles of two regions are almost same shape.

## 3.5 Process investigation of membrane BJB structure

In section 3.5, process investigation of a butt-joint regrowth using OMVPE will be described. To obtain flat buried structure, I investigated the crystal geometry depending on two approaches as follows;

(1) Dependence on regrowth mask shape

(2) Dependence on island fabrication process

The obtained layers were evaluated by scanning-electron microscope image and photoluminescence measurements.

### 3.5.1 Growth process

The experimental procedure for butt-joint regrowth is described.

**Organo-metallic vapor phase epitaxy (OMVPE)**

Figure 3.23 shows the appearance of OMVPE system （NIPPON SANSO currently TAIYO NIPPON SANSO CORPORATION ： HR3255）used for regrowth and initial wafer growth in this experiments. This OMVPE has a horizontal reactor and a load lock chamber. As a material source, group-III material (metal organic) of tri-ethyl-gallium (TEG), tri-methyl-aluminum (TMA), and

**Figure 3.23** OMVPE equipment of HR3255.

**Table 3.3** specification list of HR3255

| | | | | | | |
|---|---|---|---|---|---|---|
| System type | Lateral type MOCVD system MODEL HR3255 | | | | | |
| Gas control | Metal organic | TEG | TMG | TMA | TMI | $CBr_4$ |
| | | 100 sccm | 10 sccm | 50 sccm | 500 sccm | 500 sccm |
| | gas | 100% $AsH_3$ | 1% $AsH_3$ | 100% $PH_3$ | $Si_2H_6$ | DMZn |
| | | 100 sccm | 1000 sccm | 500 sccm | 500 /10 sccm | 520 sccm |
| | Carrier gas： 2 lines（$H_2$） | | | | | |
| | Vent gas： 2 lines（$N_2$） | | | | | |
| Reactor System | Lateral type reactor (silica base)<br>Rotation type Susceptor (SiC coted graphite base)<br>A single 2-inch wafer | | | | | |
| Annealing system | High Frequency Induction Heating, 450 ~ 1000 °C (susepter temperature) | | | | | |
| Gas purifier | $H^2$ purifier： LS20 ($2.0m^3/h$)<br>$N^2$ purifier： MANN02 ($2.7m^3/h$) | | | | | |

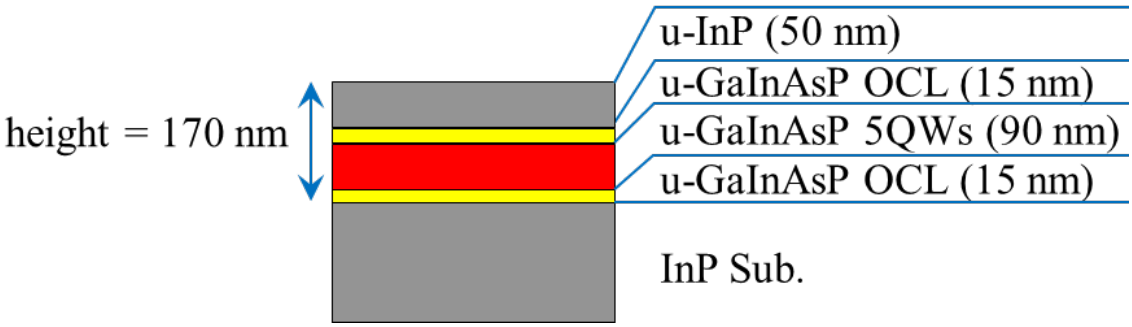


**Figure 3.24** Initial wafer structure used in experiment for butt-joint regrowth.

tri-methyl-gallium (TMG) and group-V material of $AsH_3$ (arsine) and $PH_3$ (phosphine) are implemented. Dopants of di-metyl-zinc (DMZ), di-silane (Si2H6) and carbon tetrabromide ($CBr_4$) are available. The all epitaxial growth was done on a carbon

**Table 3.4 P**roperties of initial epitaxial layers

| Layer | Material | Emission wavelength [ nm ] | Thickness [ nm ] | |
|---|---|---|---|---|
| Cap | u-InP | | 50 | |
| OCL | $Ga_{0.21}In_{0.79}As_{0.46}P_{0.54}$ | 1200 | 15 | |
| TS-0.15% barrier | $Ga_{0.26}In_{0.74}As_{0.49}P_{0.51}$ | 1200 | 10 | ×5 |
| CS1.0% well | $Ga_{0.21}In_{0.79}As_{0.8}P_{0.2}$ | 1520 | 6 | |
| TS-0.15% barrier | $Ga_{0.26}In_{0.74}As_{0.49}P_{0.51}$ | 1200 | 10 | |
| OCL | $Ga_{0.21}In_{0.79}As_{0.46}P_{0.54}$ | 1200 | 15 | |
| InP substrate | n-InP | | | |

susceptor coated with SiC under the pressure of 82 Torr with the substrate rotation speed of 12 rpm. Table 3.3 summarizes the specification of HR3255. Figure 3.24 shows the initial wafer structure used in experiment for membrane butt-joint regrowth. Table 3.4 is a list of the detail properties of the initial epitaxial layers. The epitaxial structure is grown on an n-InP substrate by using OMVPE. The core structure consists of 5 quantum wells (GaInAsP, 6 nm) and 6 barrier layers (GaInAsP, 10nm), which are sandwiched by optical confiment layers (GaInAsP, 15 nm). The top layer is capped by 50-nm-thick undoped-InP layer. This active layers are same structure as that of an initial wafer of membrane lasers in the following chapters.

**Reactive ion etching (RIE)**

Figure 3.25 shows the appearance of reactive-ion-etching system of 10-NR (SAMCO). In RIE system, radicals of the reactive gas are generated by applying a high frequency voltage through parallel plate electrodes. Anisotropic etching is occurred by irradiating

radical plasma gas onto the substrate surface. Although the plasma leaves the damage on

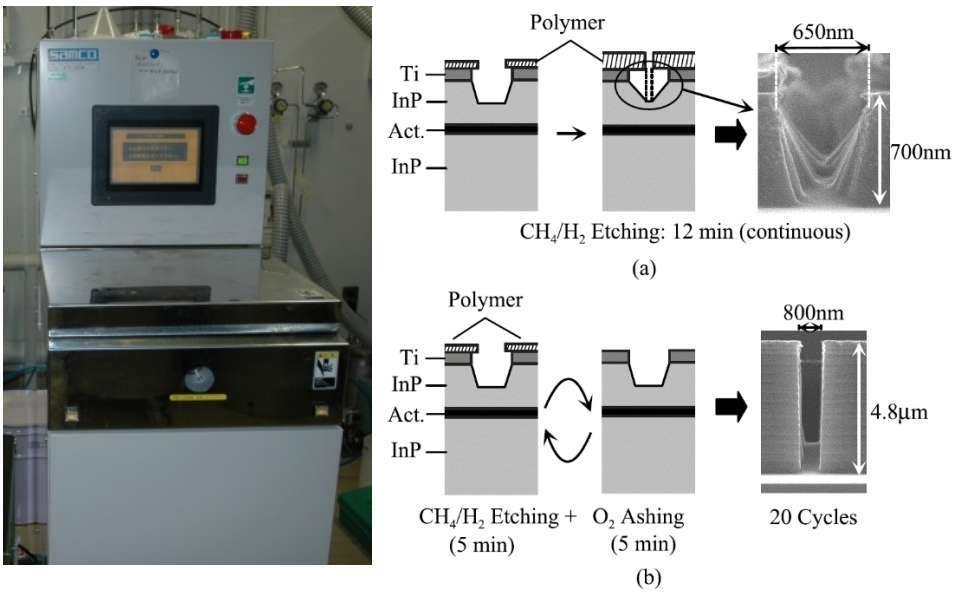


**Figure 3.25** (Left) Reactive-ion-etching system (SAMCO;10-NR). (Right) cycle etching process [54].

**Table 3.5** Etching condition of InP and GaInAsP using $CH_4/H_2$ RIE

| | | 1 cycle | |
|---|---|---|---|
| Parameters | | Step1 | Step2 |
| Gas flow | $CH_4$ | 10 sccm | - |
| | $O_2$ | 40 sccm | 30 sccm |
| RF power | | 100 W | 50 W |
| Pressure | | 6.0 Pa | 10 Pa |
| Irradiation time | | 1 min. | 40 sec. |

**Table 3.6** Etching condition of $SiO_2$ using $CF_4$ RIE

| Parameters | | Step1 |
|---|---|---|
| Gas flow | $CF_4$ | 10 sccm |
| | $O_2$ | - |
| RF power | | 12 W |
| Pressure | | 0.8 Pa |
| Irradiation time | | 27 min. |

an etched surface, the vertically etched profiles can be obtained compared with wet chemical etching. In this thesis, two RIE systems are used in order to generate different gas plasma. The first one is equipped with $CH_4/H_2$ gas lines to etch the III-V semiconductors with $SiO_2$ mask. Another one is equipped with $CF_4$ gas line to etch the $SiO_2$ with photoresist mask. In an etching process with $CH_4/H_2$ gas, the polymer deposition tends to prevent the vertical etching profile as shown in right hand side of Figure 3.25. By inserting the ashing process using $O_2$ plasma between the each $CH_4/H_2$ etching process, and repeating this cycle, the vertical etching profile with several-μm-depth can be obtained [54]. Table 3.5 shows the etching condition of InP and GaInAsP using $CH_4/H_2$ RIE for 1 cycle. Table 3.6 shows the etching condition of $SiO_2$ using $CF_4$ RIE.

Figure 3.26 shows schematic diagram for explanation of experimental procedure observing the $(0\bar{1}1)$ plane.

(1) Initial wafer

The initial epitaxial structure shown in Table 3.4 was grown on a 2-inch n-InP wafer by OMVPE.

(2) Etching InP cap layer

The surface InP cap layer was removed after forming island shape $SiO_2$ mask. The island shape resist patterns were formed by a photoresist of S1818 and an i-line photolithography. Before the spin coating the S1818 on a substrate, hexamethydisilazane (HMDS) was coated as primer coating. The island mask patterns were exposed by i-line lithography with the exposure energy of 92.5 mJ. The resist patters were transferred onto a $SiO_2$ using $CF_4$ reactive ion etching (RIE). The photoresist was removed by boiling in acetone and rinsed in methanol. The InP cap layer was etched by $CH_4/H_2$ RIE using the formed island shape $SiO_2$ mask. The dry etching depth at this process is to be considered in the next subsection.

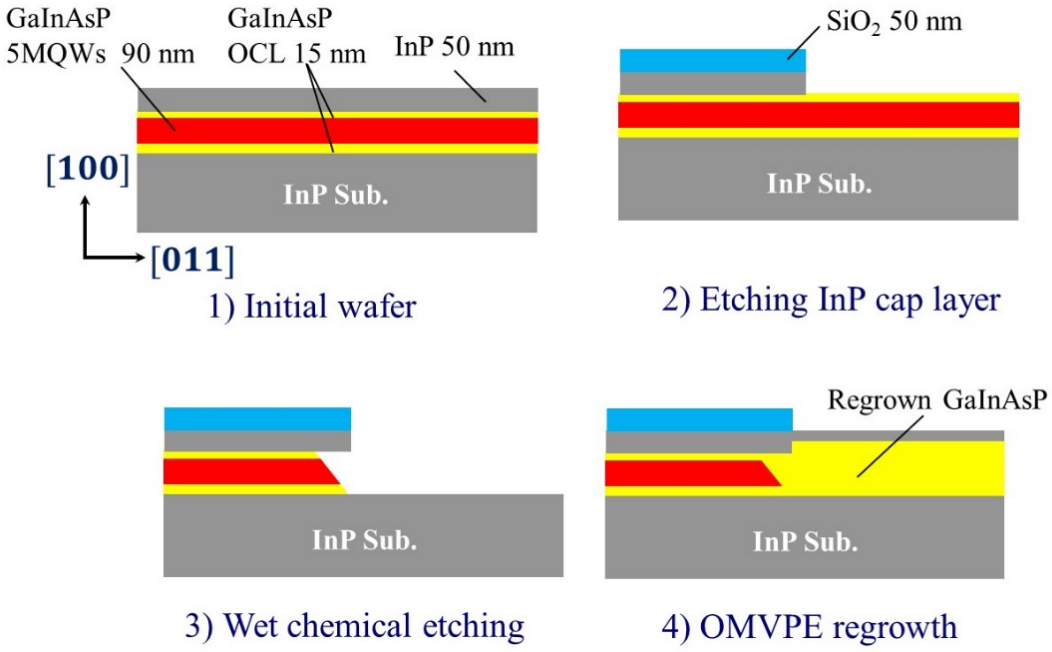


**Figure 3.26** Schematic of fabrication procedure of the membrane BJB structure.

(3) Wet chemical etching

Unnecessary active layer was removed before the regrowth and optimum undercut etching should be performed in this step. A selective chemical solution of $H_2SO_4$ : $H_2O_2$ : $H_2O$ = 1 : 1 : 40 is chosen for the etching because its relatively small etching rate for GaInAsP helps precise control of etching depth with smooth etching surface. During the wet etching, the temperature of the solution was controlled by temperature-controlled water bath.

(4) OMVPE regrowth

The process substrate was regrown in the OMVPE reactor. The substrate was dipped in buffered HF 1% in 3 sec for removing $SiO_2$ particles. After loading the sample into the OMVPE reactor, dehydration baking was conducted for 30 min at 250°C. The epitaxial regrowth was performed for the conditions as shown in Table 3.7. As the first layer, a thin InP is grown for the thickness of 10 nm at 600°C. This buffer growth condition is the same as the buffer condition in previously established regrowth process for regrowth of *n*- and *p*-InP to fabricated LCI structure. After raising the temperature, the 155-nm-thick

GaInAsP core layer and the 20-nm-thick InP cap layer were grown at 650°C. In this growth process, only buffer InP layer was grown at 600 °C to utilize the previously established regrowth process for regrowth of n- and p-InP. Finally, the regrown substrate is cleaved in $(0\bar{1}1)$ plane so as to observe a cross section at BJB coupling by using SEM.

**Table 3.7** Growth condition for butt-jointed built-in structure.

| Layer | Material | Time [ min ] | Thickness [ nm ] | Rate [ nm/min ] | Temperature [ °C ] | V/III ratio |
|---|---|---|---|---|---|---|
| 1. Buffer | InP | 0.5 | 10 | 20 | 600 | 560 |
| Temp. rise | | | | | 600→650 | |
| 2. Core | GaInAsP | 7.2 | 155 | 22 | 650 | 440 |
| 3. Cap | InP | 1 | 20 | 20 | 650 | 560 |

### 3.5.2 Dependence on regrowth mask shape

When performing the butt-joint regrowth, $SiO_2$ mask shapes can be a parameters. The mask area and mask angle respect to the crystal orientation of an InP substrate can be changed to give a difference in the growth shape.

**Consideration of mask area**

First, a butt-joint regrowth using different dimension of mask is conducted to investigate an optimum mask size especially respect to the area. Figure 3.27 shows a top view of $SiO_2$ mask design with fixed width and various length. The mask shape is designed to be a rectangular shape for the simplicity. The mask dimensions are a 2000 μm wide × various length. The length is defined to the parallel direction to the $[011]$ direction of an InP substrate. The arrayed island shape masks are spaced by 1000 μm for the $[011]$ direction and 130 μm for the $[0\bar{1}1]$ direction in order to avoid the interference between adjacent masks. A length of the mask is varied from 50 to 200 μm, which values are chosen assuming a cavity length of membrane DFB lasers. The dry etching time of 5 min (1min × 5cycle) and wet etching time of 1min and 30sec were performed. Figure 3.28 shows SEM images of a cross section of the regrown substrate cleaved in the $(0\bar{1}1)$ plane. The samples are stained by using a solution of $H_2SO_4$ : $H_2O_2$ : $H_2O$ = 1 : 1 : 40 for 40 sec at 20°C. We can see that the roughness and thickness of the grown layer tend to increase as the length of the mask gets longer. The enhanced growth rate is attributed to the excessive diffusion of the reactant from on the $SiO_2$ mask. The thermally decomposed metalorganic material is diffused on the dielectric $SiO_2$ mask with a long diffusion length because the Ga and In reactants cannot form a bond on a dielectric. The reactants diffused for a long time reach the edge of the mask, and then diffused into a semiconductor surface. The amount of diffused reactant is dependent on the mask area of the $SiO_2$ mask. Therefore, the abnormal growth was strongly occurred for a mask with longer length. Such abnormally grown of GaInAsP layer has unpredictable composition and unoriented polycrystalline properties. In addition, dislocations could be generated in the grown layer will degrade the optical properties of

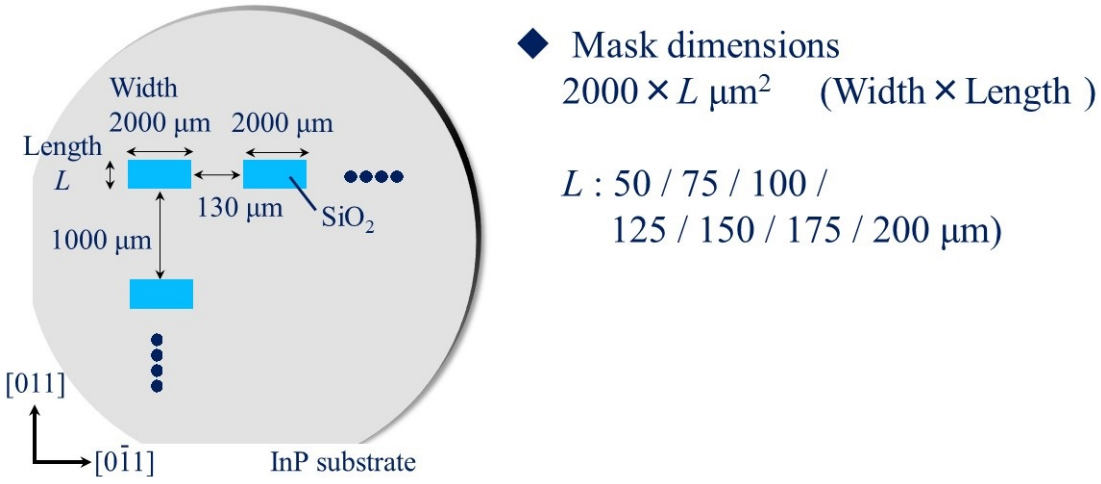


**Figure 3.27** $SiO_2$ regrowth mask layout with the width of 2000 μm and various length.

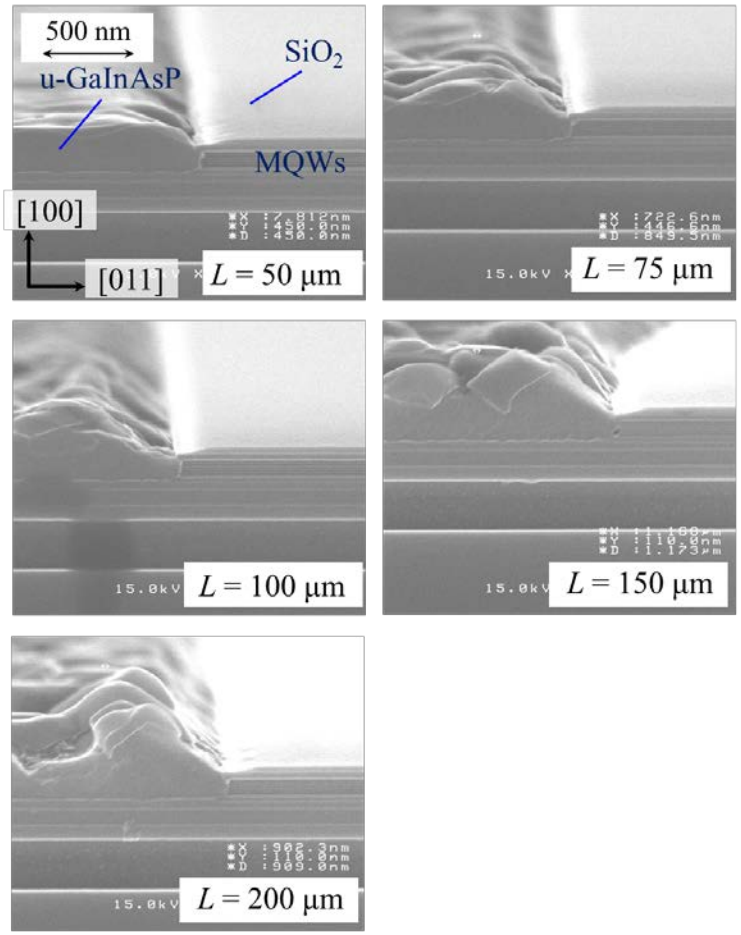


**Figure 3.28** SEM images of a cross section of the regrown substrate cleaved in the $(\mathbf{0\bar{1}1})$ plane.

a GaInAsP as a passive waveguide. According to the aforementioned discussion, the abnormal growth must be avoided in a selective area regrowth for the fabrication of BJB structure. Therefore, the mask width of 2000 μm was too wide as the area of dielectric covered region. Figure 3.29 shows the mask layout with reduced width of 13 μm to avoid the abnormal growth. The mask length is varied from 10 to 500 μm. The patterns are oriented parallel to the [011] direction. In this narrow width design, it is difficult that cleaving the 13-μm-wide masked island to observe the coupling joint formed in the [011] direction. The sample with 90° rotated mask pattern was prepared to observe the cross section of growth results. Because small regrowth mask effect on the growth is expected for this design, the growth results for two masks are assumed to be the same in this experiment. To form the mesa, the dry etching time of 5 min (1 min × 5cycle) and wet etching time of 1 min and 30 sec were performed. Figure 3.30 shows stained SEM image of BJB coupling form in the $(0\bar{1}1)$ plane. As expected from qualitative consideration of mask area design, the growth thickness is almost same as the thickness of the region far from the mask edge. The grown surface morphology is improved to be flat compared with previous results as shown in Figure 3.28. The epitaxial growth with single crystal is expected from the SEM observation. However, there is an air gap between the initially grown active region and regrown passive region. This unembedded region is created by an appearing of the higher order crystalline plane, which has slow growth rate, such as the (111)A plane. It is well known that the butt-joint regrowth to the [011] direction tends to cause the air gap [55]. To perform a butt-joint regrowth without the air gap, not only the regrowth mask area but also other factors such as the mask angle and growth process should be considered.

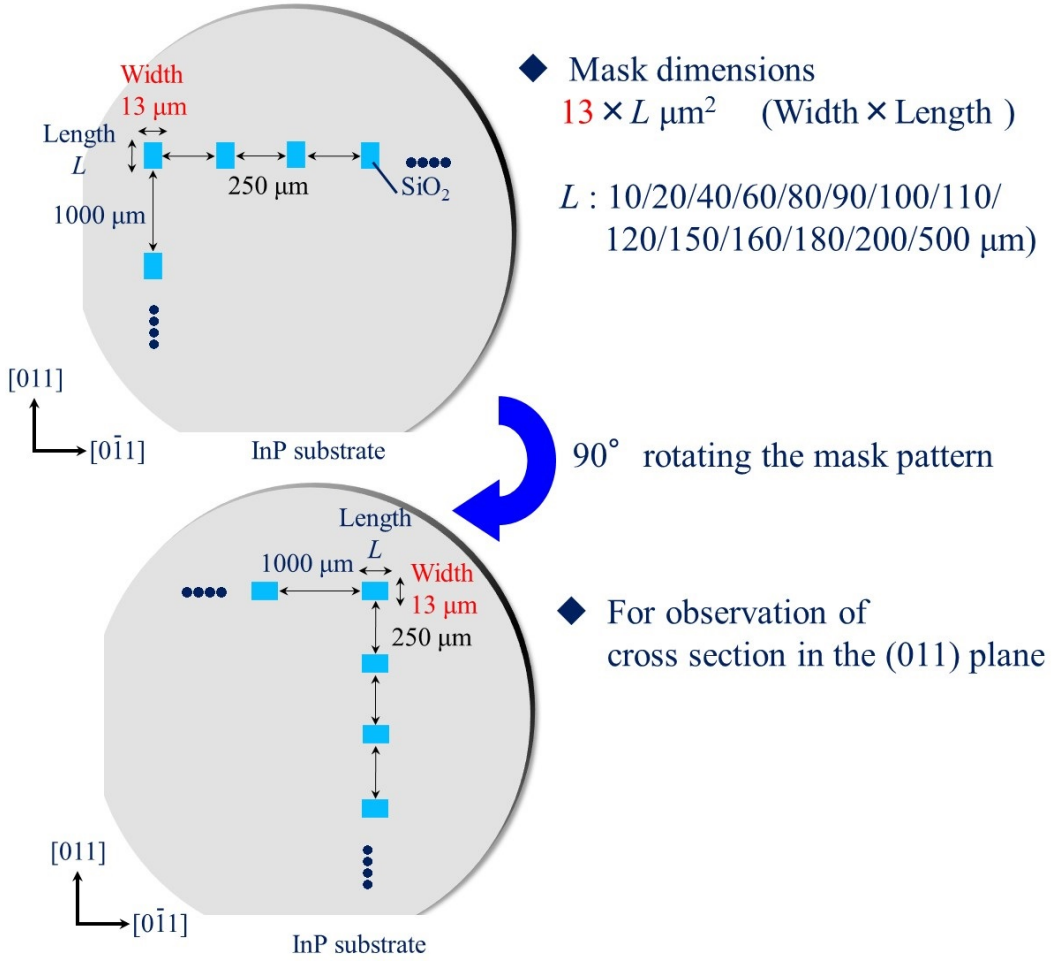


**Figure 3.29** $SiO_2$ regrowth mask layout with reduced width of 13 μm.

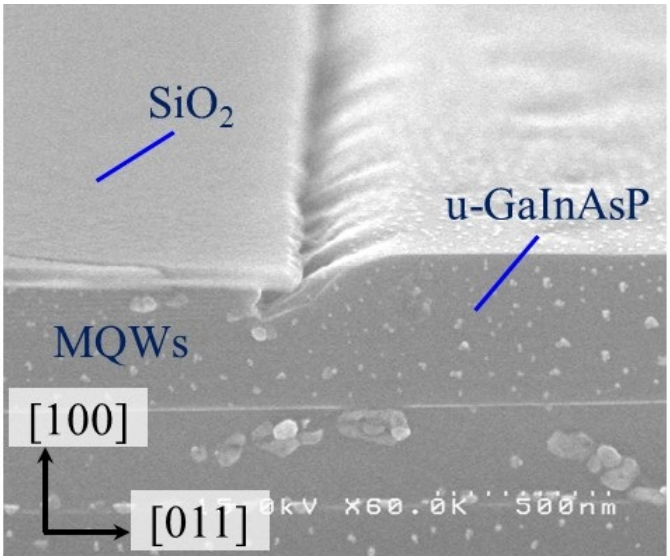


**Figure 3.30** SEM images of a cross section of the regrown substrate cleaved in the $(\mathbf{0\bar{1}1})$ plane.

**Consideration of mask angle**

Subsequently, the dependence on mask orientation with respect to the crystalline direction is investigated through changing the angle of the regrowth mask patterns. The initial wafer structure is as same as the previous experiment shown in Figure 3.24. The mask design is shown in Figure 3.31. The mask shape is a rectangle with a width of 10 μm and a length of 200 μm. The patterns are angled from 90° to 0° stepped by 1°. To form the mesa, the dry etching time of 1min (1 cycle) and wet etching time of 11 min were performed. However, it is difficult to continue to observe the cross section from the facet formed in same crystalline direction. The cleaving direction is divided into two types , As shown in Figure 3.32, SEM observations were performed along with the $[011]$ direction from an angle of 45° to 90° and the $[0\bar{1}1]$ direction from an angle of 0° to 45°. Although the wet etching time before the regrowth is 11 min, the side etching depth under the mask observed from the SEM is approximately 400 nm, which is the depth corresponding to the wet etching time of about 17 min assuming side etching rate of 23 nm/min. Therefore, we should note that there was excessive etching due to insufficient rinse by diluted water after the etching. Figure 3.33 shows the SEM images extracted from the results of regrowth which showing a distinctive appearance. (a) For the result of $\theta = 87°$, the InP as a buffer layer was first grown so that filling the side of the mesa of the active layer with a slope to the region 150 nm away from the mesa. After that, GaInAsP layer grown so as to fill under the mask, then cap InP was grown on the surface. However, there was an air gap left under beneath the $SiO_2$ mask. (b) For the result of $\theta = 64°$, the amount of InP buffer layer grown at the side of mesa was considerably increased. And it was grown to a distance of 315 nm away from the mesa. The GaInAsP layer was grown so as to fill the undercut region. The gap between the GaInAsP and the mask was embedded by the InP cap layer. However, since the cap layer was not grown on the GaInAsP at the mask edge, the desorption of As-atom during the temperature lowering after the growth caused roughened surface. (c) For the result of $\theta = 25°$, the InP buffer was grown to a distance of approximately 200 nm from the mesa, and GaInAsP is grown with keeping a gap from the mask. Although InP was grown on the llyer, the gap was left between the mask and

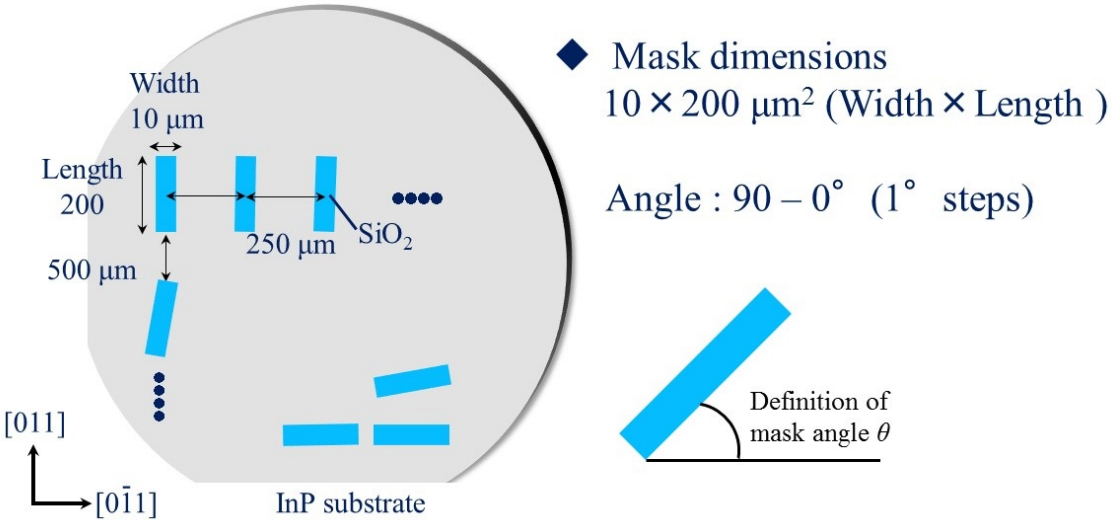


**Figure 3.31** $SiO_2$ regrowth mask layout with various angled.

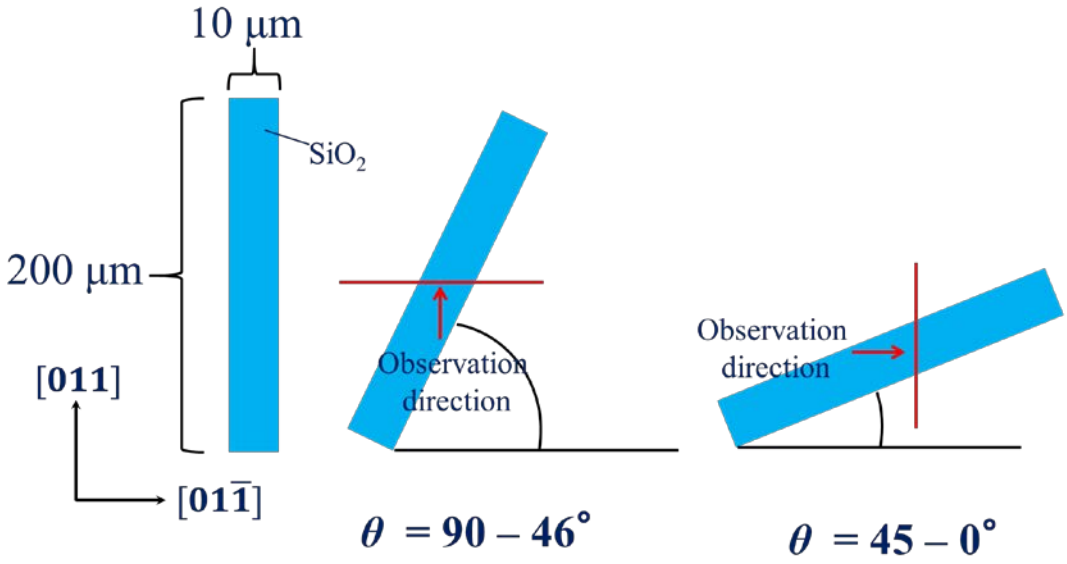


**Figure 3.32** Cleaving direction divided into two types by its angle.

the growth surface. (d) For the result of $\theta = 0°$, the InP buffer was grown to a distance of about 100 nm from the mesa. Particularly noteworthy is that it was grown with the upper layer as a seed layer. The InP buffer grown on the substrate side was grown to the height of only that of the lower OCL of the active layer, and the amount of growth is very small compared with the results for other angles. As GaInAsP approaches the mask side, the

growth thickness becomes thinner in a tapered structure. The InP cap was grown to fill the gap between the mask and the GaInAsP.

In the observation of SEM images, air gap and surface roughness appeared in these samples are confirmed. As the conclusion for this experiments, increase of the growth time of the InP cap layer at an angle of $\theta$ = 75°– 0° will give good butt-joint growth interface which has no air gap and rough surface.

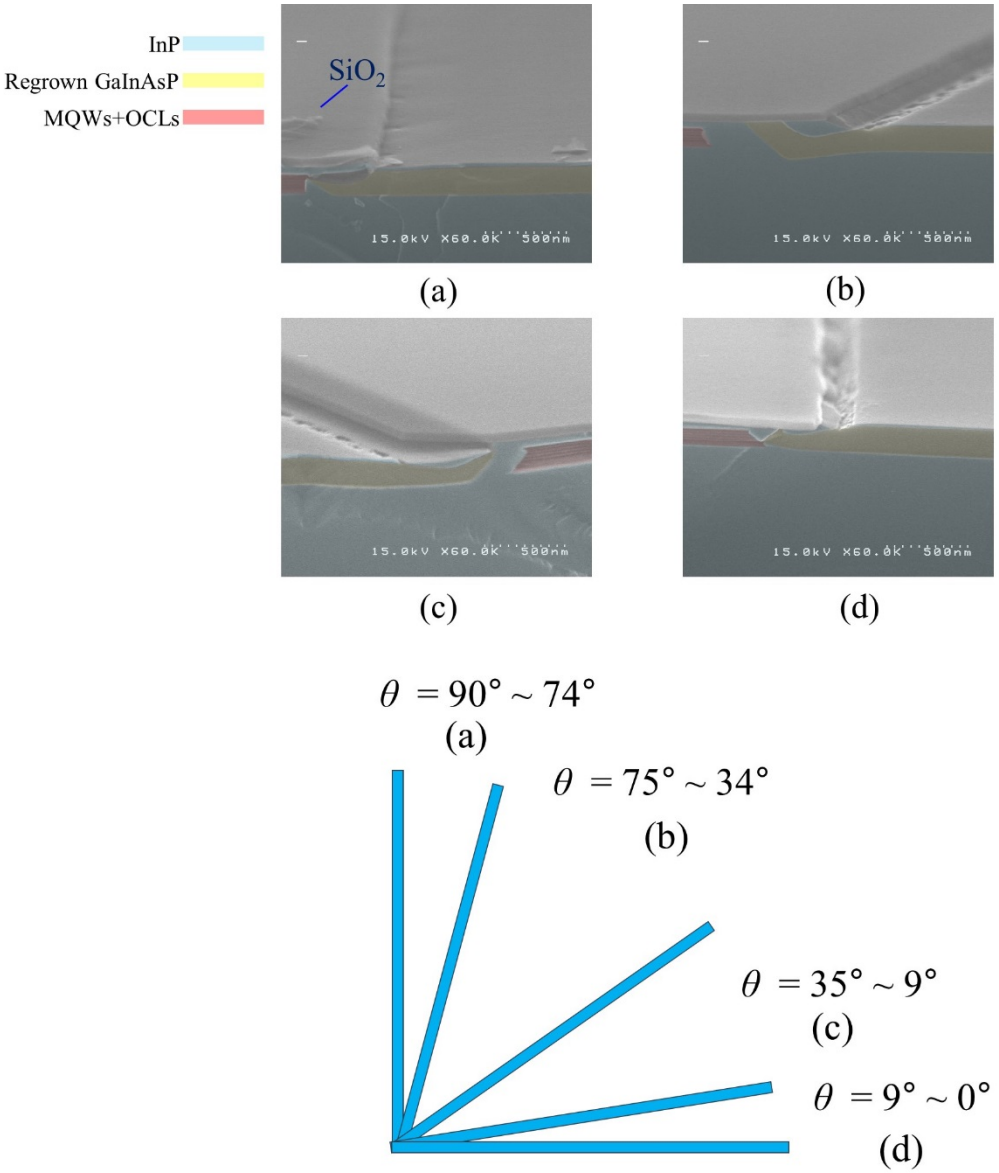


**Figure 3.33** (upper) SEM images of butt-joint regrowth result for different mask angle. (bottom) Group of the growth results categorized by a mask angle. Each semiconductor material is colored by an illustration software.

### 3.5.3 Dependence on island fabrication process

The butt-joint growth structure depending on the island formation process is investigated. The process sequence of the island mesa formation is shown in Figure 3.34. The 50-nm-thick surface InP layer is removed by RIE for 2.5 cycle. The OCL and MQWs layers are etched by using chemical etchant of $H_2SO_4$: $H_2O_2$: $H_2O$ = 1:1:40, then the bottom InP layer is exposed. By changing the wet etching time, the side etch depth under the mask and the mesa formation angle can be controlled. This results in change of regrowth geometry. The definition of side-etch depth and mesa angle is shown in the middle of Figure 3.34. The mask used in the experiments is a rectangle shape oriented in the [011]

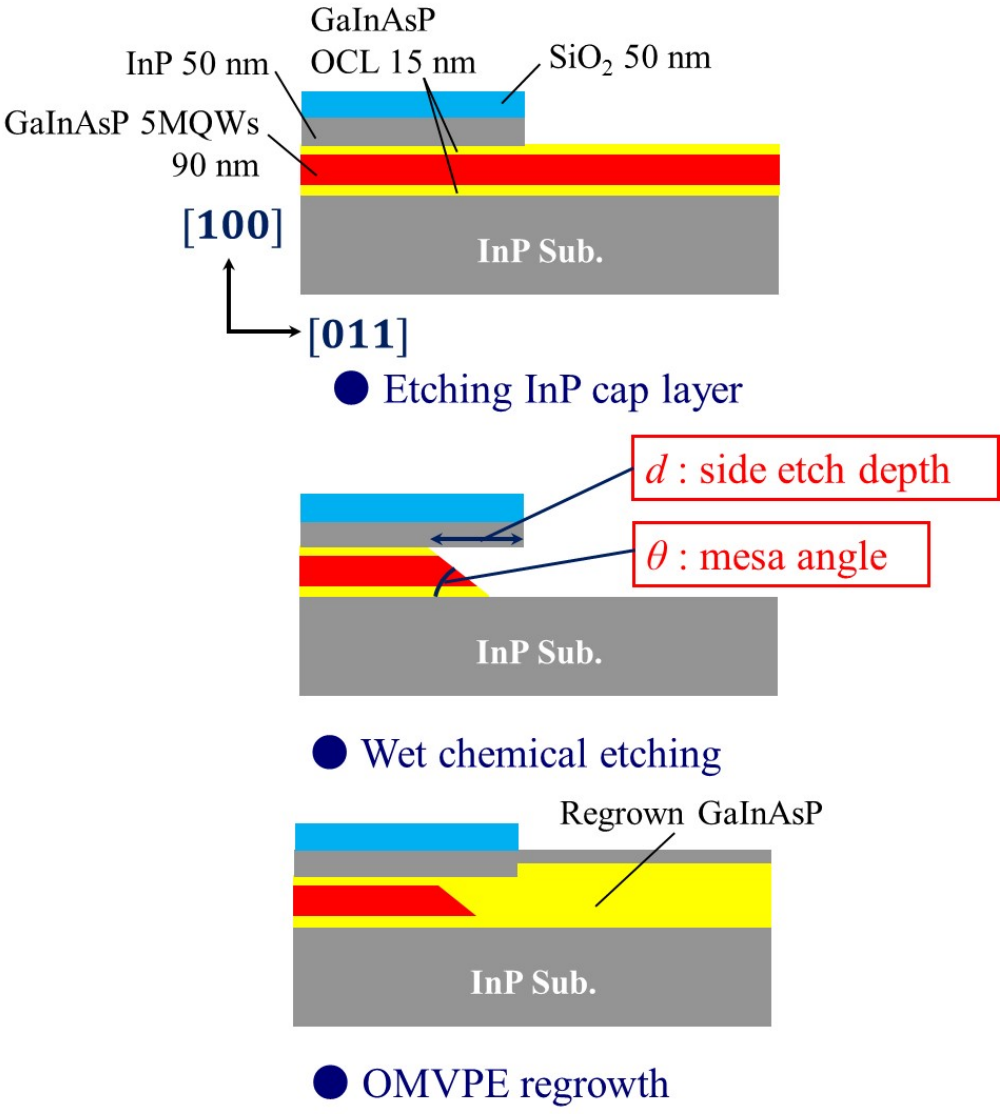


**Figure 3.34** Island shape mesa formation process.

direction. The length is varied from 10 μm to 300 μm, and the stripe width is fixed at 13 μm. Figure 3.35 shows SEM images observing the growth results obtained for different etching time conditions. The results for the wet etching time of 5 min and 7 min show the formation of air gap between the interface of the active and passive regions. In the result of the etching time of 9 min, the embedded and air gap region are simultaneously exist. In the case of wet etching for 20 min, no air gap is formed at the growth joint section, though there is a region where the InP cap layer is not grown on GaInAsP. As a consequence, desorption of As-atom induces the surface roughness. For the etching time of 11 min, flat regrowth result having a butt-joint section completely embedded with GaInAsP/InP and a maximum height deviation of approximately 5 nm from SEM image is obtained. Figure 3.36 shows a graph for depth of side etching and mesa angle for wet etching time. The side etching depth was monotonically increased as an increase of etching time. The mesa angle shows saturation at around 50°. It seems that it approaches the theoretical angle of to 54.736° formed by the (111) plane and the (001) plane. The reason why the structure of the regrowth near the mask changes by changing the time of wet etching is as follows. When the growth is performed for difererent crystalline plane appreared on a surface, crystal growth preferentially occurs on a crystal plane having a low energy barrier because the precursors diffuse from a high energy surface to a low energy crystal surface [56]. As a result, a concentration gradient of the precursors species from the preferentially grown crystal plane to crystal planes where growth is difficult occurs [57]. In the case of InP, the growth rate on the (111) plane is several times slower than that of on the (001) plane. In GaInAs and GaInAsP, the growth rate on the (111) plane is much slower than that on the (001) plane, therefore it can be said that negligible growth is occurred in the growth of thin film [56]. In the results of 5, 7 and 9 min, It is considered that diffusion into the region where the (100) plane exists occurs and hardly grows to the (111)A plane on the mesa side surface of the active region. In the etching time of 20 min, mass transport into the beneath the mask results in enhanced growth rate of InP buffer layer due to the deep side etching depth. Selective growth on a specific

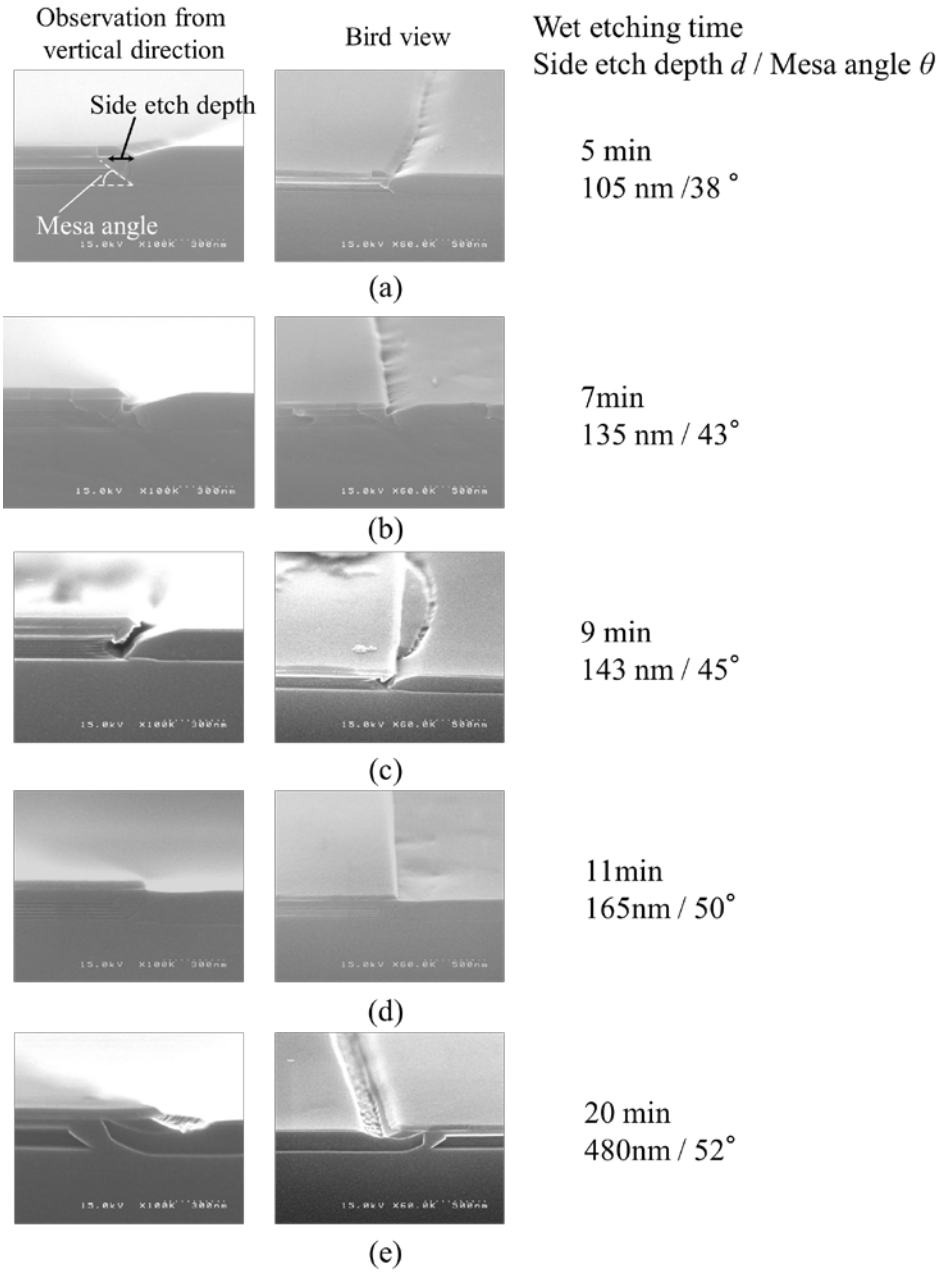


**Figure 3.35** SEM images of cross section of butt-joint regrowth results for different wet etching times.

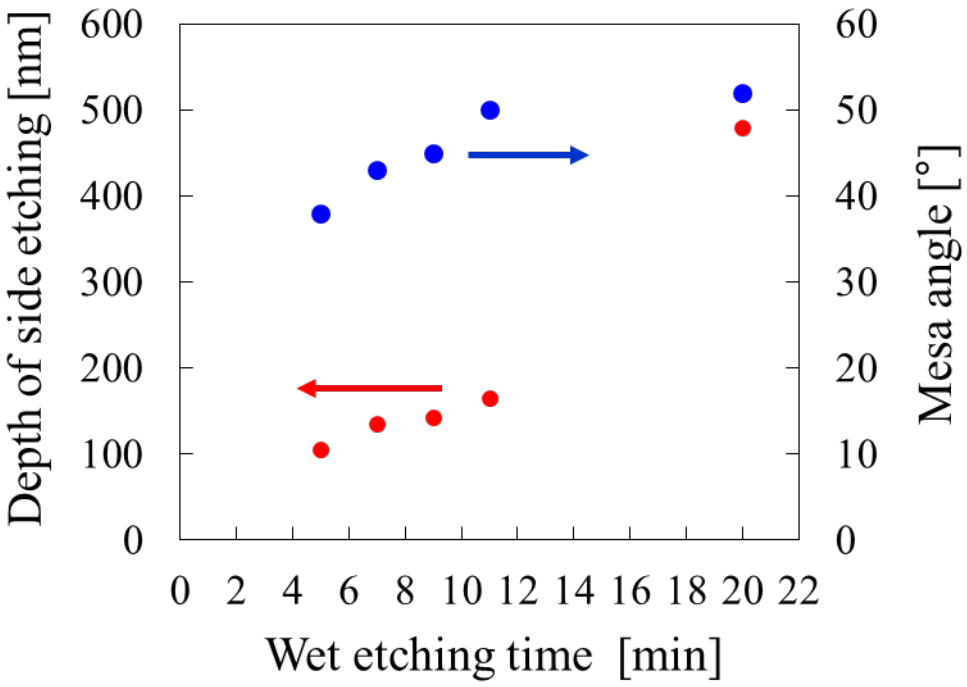


**Figure 3.36** Depth of side etching and mesa angle dependence on etching time.

crystal plane was suppressed by deep undercut and no higher order plane appeared. The InP cap layer is grown so as to embed the gap region, but the growth time is insufficient to cover the GaInAsP surface. From these results, as a condition for obtaining a good butt-joint coupling, wet etching time for 11 min should be adopted as the condition of island formation. Figure 3.37 shows the SEM image of the fabricated BJB structure observed from the $[0\bar{1}1]$ direction using the established conditions. The GaInAsP core layer in the passive section is directly joined to the active region, whereas the surface of the u-InP layer in the passive section is slightly (~20 nm) higher than that in the active section. The top InP cap layer of as-grown active region was slightly deformed after growth. This is att4ributed to the decomposition during dehydration baking or temperature rising in reactor of OMVPE. However, it is considered that there was no influence on growth because no occurrence of voids was observed. The coupling loss of the experimentally obtained structure was calculated. Figure 3.38 shows the calculation model for experimentally obtained membrane BJB structure. The mesa shape of the active region

was approximated by step structure. The calculation method and procedure was as same as those in the section 3.4. As a results, the coupling loss and back reflection of 0.02dB and -47dB were estimated.

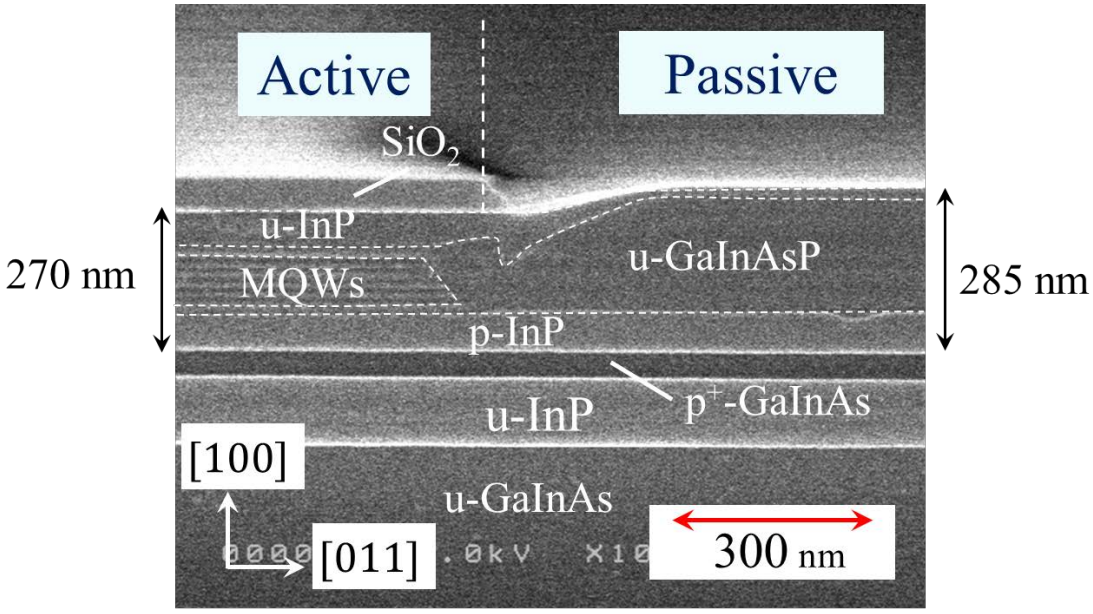


**Figure 3.37** Cross sectional SEM image of the obtained membrane BJB structure.

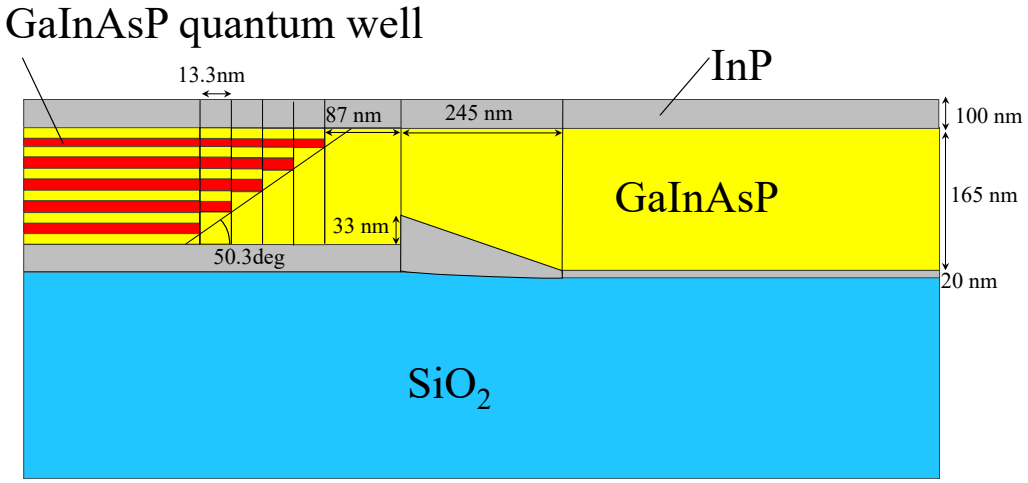


**Figure 3.38** Calculation model for experimentally obtained membrane BJB structure.

### 3.5.4 Evaluation of regrown layer by photoluminescence

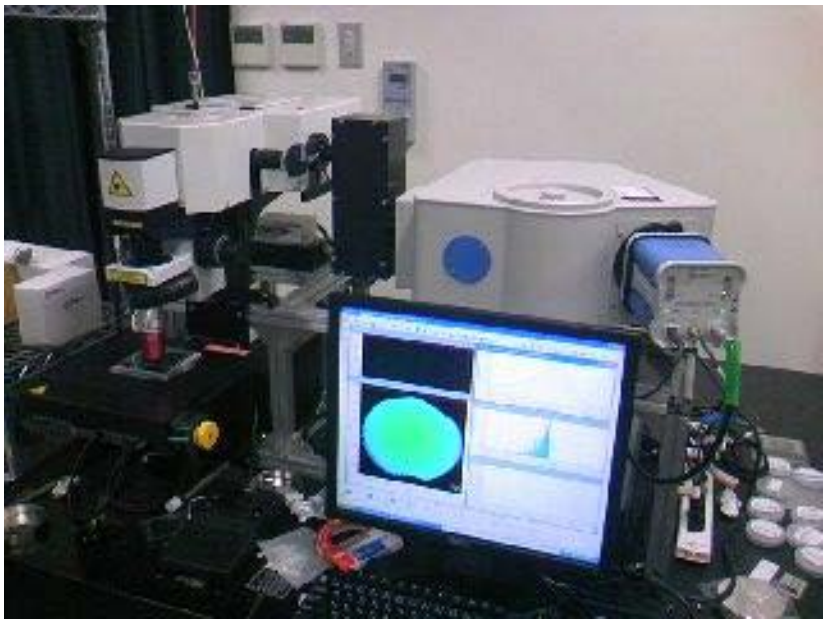

**Figure 3.39** Photoluminescence measurement equipment (HORIBA).

To investigate the optical properties of regrown layer, the photoluminescence characteristics of the regrown GaInAsP were evaluated for the results of the wet etching time of 11 min which showed a good BJB coupling. Photoluminescence (PL) measurement is based on the principle that the carrier is excited by using an excitation light source with the energy larger than the bandgap of interest semiconductor and that carriers are recombined to emit photons. Since the emitted photon corresponds to the intrinsic band gap of each semiconductor material, the emission spectrum can be used to know the optical properties of the material. Figure 3.39 shows the appearance of PL measurement system manufactured by HORIBA. This system consists of excitation layer with wavelength of 640 nm (VORTRAN LASER TECHNOLOGY,INC, Stradus® 640-30 ) and the detector (HORIBA, synapse) and the spectrometer (HORIBA, iHR320). The GaInAs array detector of synapse is cooled to -65°C. In this system, the stage can move with an accuracy of 1 μm and has a mapping function to continuously measure the PL characteristics in the plane. The implemented objective lens is M Plan Apo NIR 10× (Mitutoyo). According to the spot size of 1.3 mm of the laser source and the specs of the

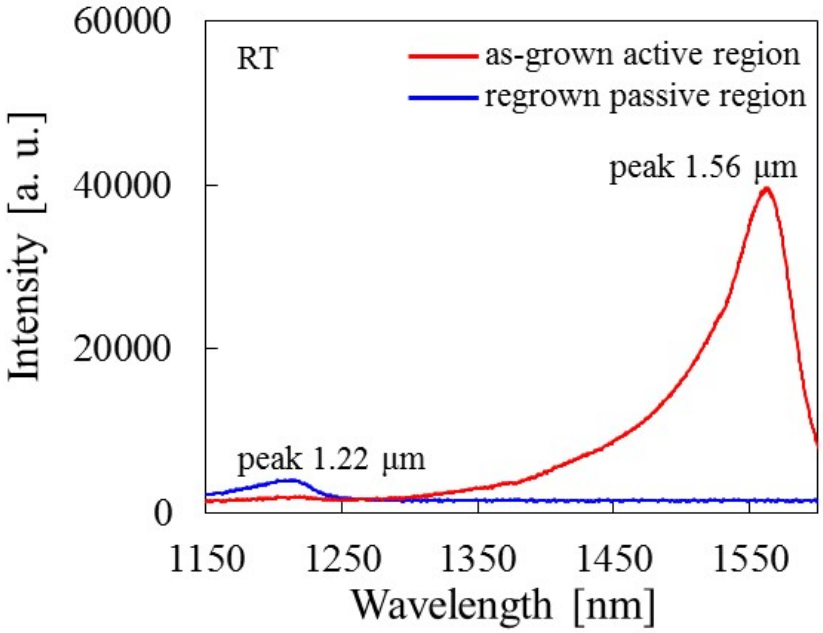


**Figure 3.40** PL spectra of the active region and regrown passive region measured at far from the mask.

objective lens, the spot size of approximately 10 μm is expected on a sample. All measurement was performed at room-temperature. Because we use the 10% attenuation filter for 30 mW laser source was used, the excitation power was approximately 3 mW. Figure 3.40 shows PL spectra of the active region and regrown passive region measured at far from the mask. The active and passive regions have a PL peak at 1.56 μm and 1.22 μm, respectively. In the regrown region, there is a concern that the obtained crystal in the vicinity of the mask has different characteristics compared with the region not affected by the mask. Next, the location dependence of PL characteristics was measured.

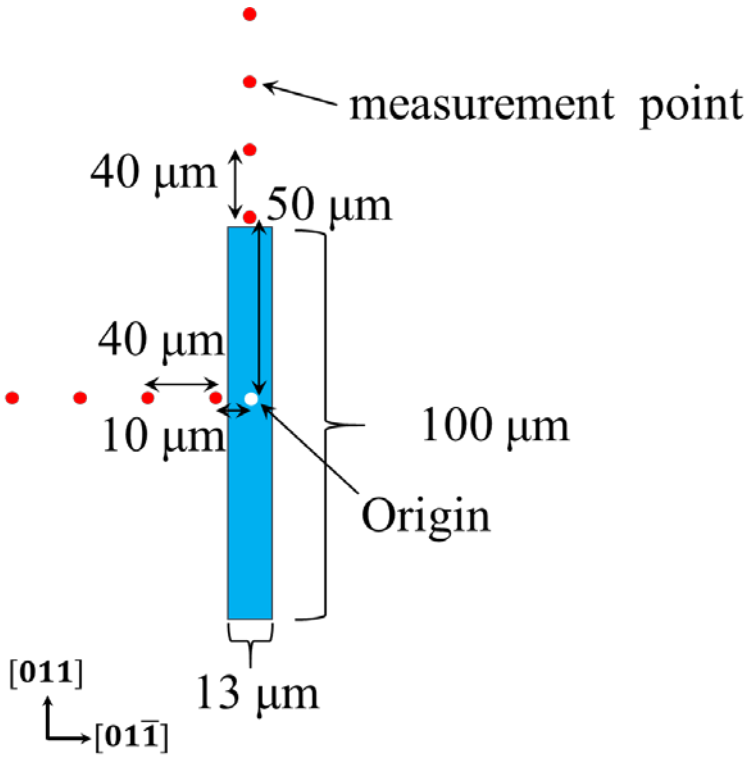


**Figure 3.41** Measured positions around the mask.

Figure 3.41 explains the measured position. The island region with the width of 13 μm and length of 100 μm was used. Measurements were performed at 40 μm intervals in the [011] and [0$\bar{1}$1] directions with the vicinity of the mask as the starting point. Table 3.8 shows the PL intensity, peak wavelength and full-width at half maximum (FWHM) of each measured point. Figure 3.42 shows the superimposed PL spectra for different position. There are no significant difference for both direction. These spectra have slightly different PL intensity but the FWHMs of 58 meV are almost constant over the all measured point. This FWHM of 58 meV is comparable with the FWHM of 57.7 meV for GaInAsP grown on a bulk InP substrate in our previous result, the value of it was 57.7 meV. Next, PL mapping measurement was performed in the region of 200 μm × 200 μm where the possibility that the influence of the mask might be considered. The measured island had a width of 13 μm and length of 40 μm. Figure 3.43 (a) and (b) show the PL peak wavelength and PL peak intensity mapping result respectively. The PL mapping was generated by stepping the 3 μm×3 μm field of view. It was confirmed that the wavelength

**Table 3.8** PL properties for each position.

$[0\bar{1}1]$ direction

| Distance from the origin [μm] | Peak intensity [a. u.] | Peak wavelength [nm] | Full-width at half maximum [meV] |
|---|---|---|---|
| 20 | 51315 | 1222.5 | 59 |
| 60 | 47993 | 1218.5 | 58 |
| 100 | 49000 | 1218.5 | 58 |
| 140 | 51195 | 1217.5 | 59 |

[011] diretion

| Distance from the origin [μm] | Peak intensity [a. u.] | Peak wavelength [nm] | Full-width at half maximum [eV] |
|---|---|---|---|
| 50 | 48979 | 1219.5 | 58 |
| 90 | 51413 | 1218.5 | 59 |
| 130 | 50301 | 1217.5 | 58 |
| 170 | 53320 | 1218.0 | 59 |

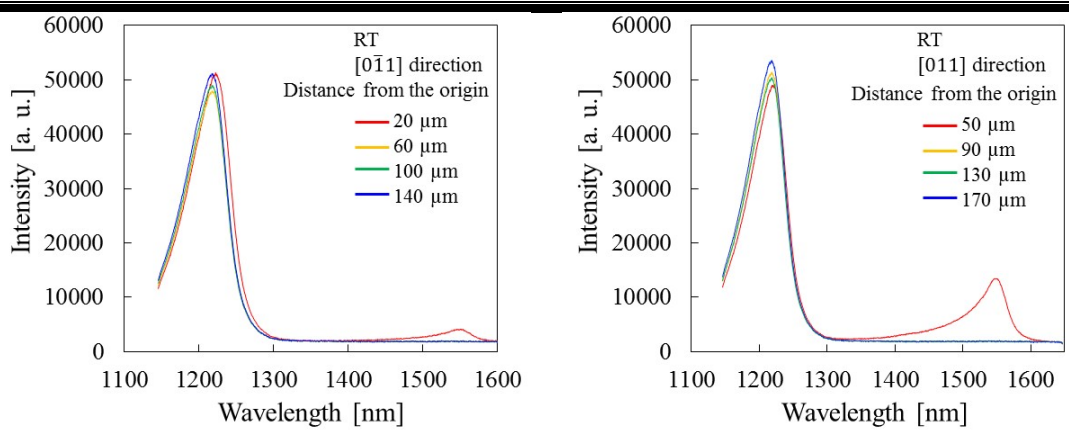


(a) (b)

**Figure 3.42** Superimposed PL spectra for different position. (a) results in the $[0\bar{1}1]$ direction (b) results in the $[011]$ direction.

shift was not occurred even in the vicinity of the island mask. In addition, no transition wavelength was observed in Figure 3.43 (a). I note that the colors indicating intermediate wavelength appear on the boundary between the two regions due to automatic interpolating by the software. From the measurement of the PL peak intensity mapping, it is confirmed that the emission intensity which is the same as the position away from the mask even in the vicinity of the island. According to these measurements, the regrown layer in the vicinity of the active region island has same characteristics as in the region without the influence of the regrowth mask. Therefore, the GaInAsP waveguide grown by the method investigated in this research has sufficient quality to obtain the passive waveguide characteristics.

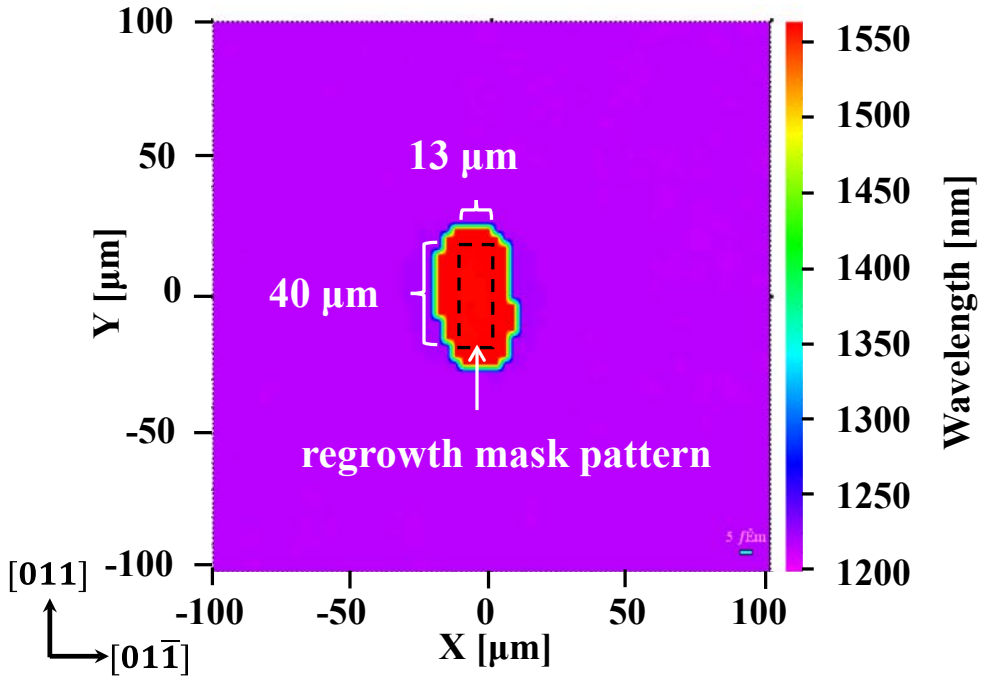


(a)

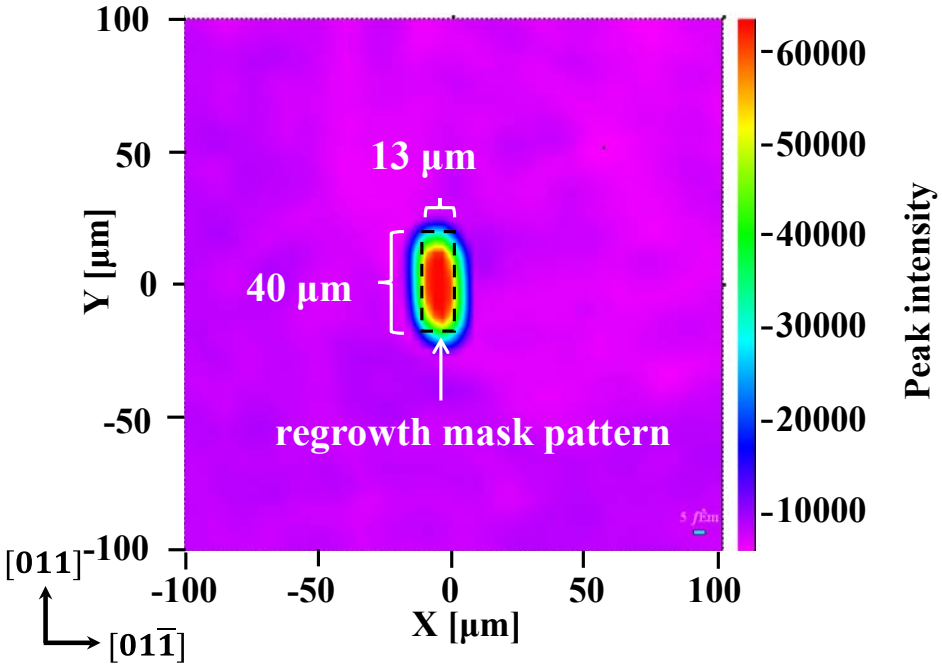


(b)

**Figure 3.43** Photoluminescence mapping of (a) peak intensity, (b)peak wavelength around regrowth mask (13 μm wide and 40 μm long).

## 3.6 Conclusion

This chapter described BJB structure for the integration of membrane optical devices. Section 3.2 given photonic integration methods used in general photonic platform. In monolithic integration platform, many efficient coupling structures, for example offset quantum well, quantum well intermixing and butt-joint regrowth, are available. Section 3.3 described numerical design for the efficient BJB structure in membrane structure. The BJB structure was investigated in the view point of regrowth thickness of u-GaInAsP layer. The numerical calculation based on finite difference method (FDM) and eigenmode expansion (EME) method was performed. As a results, a high coupling loss of 0.09dB (2%) and small back reflection of below -42dB can be simultaneously achieved in the growth deviation range of ±20 nm. This fact is thanks to the mode matching between the active region and a passive region by adopting BJB structure. In section 3.5, experimental investigation to fabricating membrane BJB structure was conducted. The two approaches to obtain a BJB structure were investigated. The reduction of the protect mask are for regrowth improved thickness uniformity of regrown layer. The control of the active mesa structure by a wet etching process enable regrowth to embedding the active and passive section without an air gap. The undercut condition of depth of 165 nm and mesa angle of 50° result in good growth structure with etching time of 11 min. The regrown GaInAsP layer was evaluated by micro photoluminescence. There was no distinguished degradation in pholuminescence intensity around the active region confirmed by mapping measurement. The emission wavelength of regrown layer was same as that of grown on a bulk InP substrate. The FWHM of the regrown layer was 58 meV, which was comparable to the typical FWHM of GaInAsP at room-temperature. As a consequence, is was realized that the membrane BJB structure with efficient coupling of an active and passive section can be expected.

# References

[1] S. E. Miller, "Integrated optics: An introduction," *Bell Labs Technical Journal,* vol. 48, pp. 2059-2069, 1969.

[2] Y. Suematsu, M. Yamada, and K. Hayashi, "A multi-hetero-AIGaAs laser with integrated twin guide," *Proceedings of the IEEE,* vol. 63, pp. 208-208, 1975.

[3] L. A. Coldren, S. C. Nicholes, L. Johansson, S. Ristic, R. S. Guzzon, E. J. Norberg, and U. Krishnamachari, "High performance InP-based photonic ICs—A tutorial," *Journal of Lightwave Technology,* vol. 29, pp. 554-570, 2011.

[4] B. Mason, S. P. DenBaars, and L. A. Coldren, "Tunable sampled-grating DBR lasers with integrated wavelength monitors," *IEEE Photonics Technology Letters,* vol. 10, pp. 1085-1087, 1998.

[5] K. Takeda, M. Takenaka, T. Tanemura, and Y. Nakano, "Experimental study on wavelength tunability of all-optical flip-flop based on multimode-interference bistable laser diode," *IEEE Photonics Journal,* vol. 1, pp. 40-47, 2009.

[6] V. Lai, M. L. Masanovic, J. A. Summers, L. A. Coldren, and D. J. Blumenthal, "40Gbps operation of an offset quantum well active region based widely-tunable all-optical wavelength converter," in *Optical Fiber Communication Conference, 2005. Technical Digest. OFC/NFOEC*, 2005, p. 3 pp. Vol. 4.

[7] Y. Kawakita, T. Saitoh, S. Shimotaya, and K. Shimomura, "A novel straight arrayed waveguide grating with linearly varying refractive-index distribution," *IEEE Photonics Technology Letters,* vol. 16, pp. 144-146, 2004.

[8] K. Kudo, M. Ishizaka, T. Sasaki, H. Yamazaki, and M. Yamaguchi, "1.52-1.59-μm range different-wavelength modulator-integrated DFB-LDs fabricated on a single wafer," *IEEE Photonics Technology Letters,* vol. 10, pp. 929-931, 1998.

[9] M. Aoki, M. Suzuki, H. Sano, T. Kawano, T. Ido, T. Taniwatari, K. Uomi, and A. Takai, "InGaAs/InGaAsP MQW electroabsorption modulator integrated with a DFB laser fabricated by band-gap energy control selective area MOCVD," *IEEE journal of quantum electronics,* vol. 29, pp. 2088-2096, 1993.

[10] J. Decobert, P.-Y. Lagrée, H. Guerault, and C. Kazmierski, "AlGaInAs selective area growth for high-speed EAM-based PIC sources," in *Indium Phosphide and Related Materials (IPRM), 2013 International Conference on*, 2013, pp. 1-2.

[11] J. Darja, M. J. Chan, M. Sugiyama, and Y. Nakano, "Four channel DFB laser array with integrated combiner for 1.55 μm CWDM systems by MOVPE selective area growth," *IEICE Electronics Express,* vol. 3, pp. 522-528, 2006.

[12] N. Dupuis, J. Décobert, P.-Y. Lagrée, N. Lagay, F. Poingt, C. Kazmierski, A. Ramdane, and A. Ougazzaden, "Mask pattern interference in AlGaInAs selective area metal-organic vapor-phase epitaxy: Experimental and modeling analysis," *Journal of Applied Physics,* vol. 103, p. 113113, 2008.

[13] N. Dupuis, J. Decobert, C. Jany, F. Alexandre, A. Garreau, N. Lagay, F. Martin, D. Carpentier, J. Landreau, and C. Kazmierski, "10-Gb/s AlGaInAs colorless remote amplified modulator by selective area growth for wavelength agnostic networks," *IEEE Photonics Technology Letters,* vol. 20, pp. 1808-1810, 2008.

[14] D. G. Deppe and N. Holonyak Jr, "Atom diffusion and impurity‐induced layer disordering in quantum well III‐V semiconductor heterostructures," *Journal of Applied Physics,* vol. 64, pp. R93-R113, 1988.

[15] S. K. Si, D. H. Yeo, H. H. Yoon, and S. J. Kim, "Area selectivity of InGaAsP-InP multiquantum-well intermixing by impurity-free vacancy diffusion," *IEEE Journal of selected topics in quantum electronics,* vol. 4, pp. 619-623, 1998.

[16] B. Qiu, A. Bryce, R. De La Rue, and J. Marsh, "Monolithic integration in InGaAs-InGaAsP multiquantum-

well structure using laser processing," *IEEE Photonics Technology Letters,* vol. 10, pp. 769-771, 1998.

[17] S. Charbonneau, P. Poole, Y. Feng, G. Aers, M. Dion, M. Davies, R. Goldberg, and I. Mitchell, "Band‐gap tuning of InGaAs/InGaAsP/InP laser using high energy ion implantation," *Applied physics letters,* vol. 67, pp. 2954-2956, 1995.

[18] S. R. Jain, M. N. Sysak, G. Kurczveil, and J. E. Bowers, "Integrated hybrid silicon DFB laser-EAM array using quantum well intermixing," *Optics express,* vol. 19, pp. 13692-13699, 2011.

[19] E. J. Skogen, J. S. Barton, S. P. Denbaars, and L. A. Coldren, "A quantum-well-intermixing process for wavelength-agile photonic integrated circuits," *IEEE Journal of selected topics in quantum electronics,* vol. 8, pp. 863-869, 2002.

[20] W. Guo, P. R. Binetti, C. Althouse, M. L. Mašanović, H. P. Ambrosius, L. A. Johansson, and L. A. Coldren, "Two-dimensional optical beam steering with InP-based photonic integrated circuits," *IEEE Journal of Selected Topics in Quantum Electronics,* vol. 19, p. 6100212, 2013.

[21] A. Matsumoto, Y. Takei, K. Akahane, S. Matsui, T. Umezawa, N. Yamamoto, Y. Matsushima, and K. Utaka, "Ar implantation-induced quantum dot intermixing technique for 1550 nm-band highly stacked QD photonic integrated circuit," in *Lasers and Electro-Optics (CLEO), 2016 Conference on*, 2016, pp. 1-2.

[22] E. J. Skogen, J. W. Raring, J. S. Barton, S. P. DenBaars, and L. A. Coldren, "Postgrowth control of the quantum-well band edge for the monolithic integration of widely tunable lasers and electroabsorption modulators," *IEEE Journal of selected topics in quantum electronics,* vol. 9, pp. 1183-1190, 2003.

[23] Y. Abe, K. Kishino, Y. Suematsu, and S. Arai, "GaInAsP/InP integrated laser with butt-jointed built-in distributed-Bragg-reflection waveguide," *Electronics Letters,* vol. 17, pp. 945-947, 1981.

[24] W. Kobayashi, M. Arai, T. Yamanaka, N. Fujiwara, T. Fujisawa, T. Tadokoro, K. Tsuzuki, Y. Kondo, and F. Kano, "Design and fabrication of 10-/40-Gb/s, uncooled electroabsorption modulator integrated DFB laser with butt-joint structure," *Journal of Lightwave Technology,* vol. 28, pp. 164-171, 2010.

[25] R. Strzoda, G. Ebbinghaus, T. Scherg, and N. Emeis, "Studies on the butt-coupling of InGaAsP-waveguides realized with selective area metalorganic vapour phase epitaxy," *Journal of crystal growth,* vol. 154, pp. 27-33, 1995.

[26] J. Binsma, P. Thijs, T. Van Dongen, E. Jansen, A. T. STARING, G. Van den Hoven, and L. Tiemeijer, "Characterization of butt-joint InGaAsP waveguides and their application to 1310 nm DBR-type MQW gain-clamped semiconductor optical amplifiers," *IEICE transactions on electronics,* vol. 80, pp. 675-681, 1997.

[27] M. Wada, H. Okamoto, K. Kishi, Y. Kadota, M. Qkamoto, Y. Kondo, Y. Sakai, H. Oohashi, Y. Suzaki, and Y. Tohmori, "Laser diodes integrated with butt-jointed spotsize converter fabricated on 2-in wafer," *Journal of lightwave technology,* vol. 15, pp. 498-504, 1997.

[28] M. Matsuda, A. Uetake, T. Simoyama, S. Okumura, K. Takabayashi, M. Ekawa, and T. Yamamoto, "1.3-μm-wavelength AlGaInAs multiple-quantum-well semi-insulating buried-heterostructure distributed-reflector laser arrays on semi-insulating InP substrate," *IEEE Journal of Selected Topics in Quantum Electronics,* vol. 21, pp. 241-247, 2015.

[29] W. Kobayashi, T. Ito, T. Yamanaka, T. Fujisawa, Y. Shibata, T. Kurosaki, M. Kohtoku, T. Tadokoro, and H. Sanjoh, "50-Gb/s direct modulation of a 1.3-μm InGaAlAs-based DFB laser with a ridge waveguide structure," *IEEE Journal of Selected Topics in Quantum Electronics,* vol. 19, p. 1500908, 2013.

[30] H. Matsuura, T. Kaneko, K. Tanizawa, E. Banno, K. Uesaka, H. Kuwatsuka, S. Namiki, and H. Shoji, "Suppression of channel-by-channel variation in wavelength switching time of TDA-CSG-DR laser," in *Optical Fibre Technology, 2014 OptoElectronics and Communication Conference and Australian Conference on*, 2014, pp. 296-298.

[31] Y. Sasahata, T. Saito, T. Takiguchi, K. Takagi, K. Matsumoto, T. Nagira, H. Sakuma, D. Suzuki, R. Makita, and M. Takabayashi, "Tunable DFB laser array integrated with Mach–Zehnder modulators for 44.6 Gb/s

DQPSK transmitter," *IEEE Journal of Selected Topics in Quantum Electronics,* vol. 19, p. 1501507, 2013.

[32] N. Yasuhara, S. Yamauchi, Y. Tsunemi, A. Nakamura, Y. Yamaguchi, K. Naoe, and K. Uomi, "Extremely low-voltage (1.0 Vpp) and 28-Gbps uncooled operation up to 85° C in 1.3-μm EA/DFB lasers with high-quality eye opening," in *Semiconductor Laser Conference (ISLC), 2016 International*, 2016, pp. 1-2.

[33] Y. Matsui, T. Pham, T. Sudo, G. Carey, B. Young, and C. Roxlo, "112-Gb/s WDM link using two directly modulated Al-MQW BH DFB lasers at 56 Gb/s," presented at the Optical Fiber Communication Conference, 2015.

[34] Y. Sakata, Y. Inomoto, and K. Komatsu, "Surface migration effect and lateral vapor-phase diffusion effect for InGaAsP/InP narrow-stripe selective metal-organic vapor-phase epitaxy," *Journal of crystal growth,* vol. 208, pp. 130-136, 2000.

[35] O. Kayser, "Selective growth of InP/GaInAs in LP-MOVPE and MOMBE/CBE," *Journal of crystal growth,* vol. 107, pp. 989-998, 1991.

[36] J. S. Chang, K. W. Carey, J. E. Turner, and L. A. Hodge, "Compositional non-uniformities in selective area growth of GaInAs on InP grown by OMVPE," *Journal of Electronic Materials,* vol. 19, pp. 345-348, 1990.

[37] S. Lourdudoss, E. R. Messmer, O. Kjebon, and G. Landgren, "Temporally resolved selective regrowth of InP around [110] and [-110] mesas," *Journal of electronic materials,* vol. 25, pp. 389-394, 1996.

[38] H. Künzel, S. Ebert, R. Gibis, R. Kaiser, H. Kizuki, S. Malchow, and G. Urmann, "Selective MOMBE growth of InP-based waveguide/laser butt-joints," *Journal of crystal growth,* vol. 192, pp. 56-62, 1998.

[39] T. Brenner, E. Gini, and H. Melchior, "Low coupling losses between InP/InGaAsP optical amplifiers and monolithically integrated waveguides," *IEEE photonics technology letters,* vol. 5, pp. 212-214, 1993.

[40] J. Wallin, G. Landgren, K. Streubel, S. Nilsson, and M. Öberg, "Selective area regrowth of butt-joint coupled waveguides in multi-section DBR lasers," *Journal of crystal growth,* vol. 124, pp. 741-746, 1992.

[41] H. Takeuchi, K. Kasaya, and O. Kunishige, "Experimental evaluation of the coupling efficiency between monolithically integrated DFB lasers and waveguides," *IEICE TRANSACTIONS (1976-1990),* vol. 73, pp. 53-58, 1990.

[42] J. Binsma, M. Van Geemert, F. Heinrichsdorff, T. Van Dongen, R. Broeke, and M. Smit, "MOVPE waveguide regrowth in InGaAsP/InP with extremely low butt joint loss," in *Proc. IEEE/LEOS Symposium (Benelux Chapter)*, 2001, pp. 245-248.

[43] Y. Barbarin, E. Bente, T. de Vries, J. den Besten, P. van Veldhoven, M. Sander-Jochem, E. Smalbrugge, F. van Otten, E. Geluk, and M. Heck, "Butt-joint interfaces in InP/InGaAsP waveguides with very low reflectivity and low loss," in *Proc. IEEE/LEOS Symp. Benelux*, 2005, pp. 89-92.

[44] S. Jiang, R. Zhang, L. Dong, N. Zhou, and S. Xie, "Fabrication of widely tunable SGDBR laser using butt-joint technique," in *Photonics and Optoelectronics Meetings*, 2008, pp. 727806-727806-8.

[45] S. H. Oh, C.-W. Lee, J.-M. Lee, K. S. Kim, H. Ko, S. Park, and M.-H. Park, "The design and the fabrication of monolithically integrated GaInAsP MQW laser with butt-coupled waveguide," *IEEE Photonics Technology Letters,* vol. 15, pp. 1339-1341, 2003.

[46] J. Mi, H. Yu, L. Yuan, S. Liang, Q. Kan, and J. Pan, "Fabrication of InGaAs/InP DBR laser with butt-coupled passive waveguide utilizing selective wet etching," in *SPIE/COS Photonics Asia*, 2014, pp. 92670Z-92670Z-7.

[47] Photon Design Product. *FIMMWAVE and FIMMPROP software*. Available: http://www.photond.com.

[48] P. Lusse, P. Stuwe, J. Schule, and H.-G. Unger, "Analysis of vectorial mode fields in optical waveguides by a new finite difference method," *Journal of lightwave technology,* vol. 12, pp. 487-494, 1994.

[49] W. Huang and C. Xu, "Simulation of three-dimensional optical waveguides by a full-vector beam propagation method," *IEEE journal of quantum electronics,* vol. 29, pp. 2639-2649, 1993.

[50] Z. Zhu and T. G. Brown, "Full-vectorial finite-difference analysis of microstructured optical fibers," *Optics*

*Express,* vol. 10, pp. 853-864, 2002.

[51] C.-P. Yu and H.-C. Chang, "Yee-mesh-based finite difference eigenmode solver with PML absorbing boundary conditions for optical waveguides and photonic crystal fibers," *Optics Express,* vol. 12, pp. 6165-6177, 2004.

[52] B. Broberg and S. Lindgren, "Refractive index of $In_{1-x}Ga_xAs_yP_{1-y}$ layers and InP in the transparent wavelength region," *Journal of Applied Physics,* vol. 55, pp. 3376-3381, 1984.

[53] K. Petermann, "External optical feedback phenomena in semiconductor lasers," *IEEE Journal of Selected Topics in Quantum Electronics,* vol. 1, pp. 480-489, 1995.

[54] M. M. Raj, J. Wiedmann, S. Toyoshima, Y. Saka, K. Ebihara, and S. Arai, "High-reflectivity semiconductor/benzocyclobutene Bragg reflector mirrors for GaInAsP/InP lasers," *Japanese Journal of Applied Physics,* vol. 40, p. 2269, 2001.

[55] S. Lourdudoss, E. R. Messmer, O. Kjebon, K. Streubel, J. André, and G. Landgren, "Morphological modifications during selective growth of InP around cylindrical and parallelepiped mesas," *Materials Science and Engineering: B,* vol. 28, pp. 179-182, 1994.

[56] A. Moseley, J. Thompson, P. Kightley, R. Wallis, and D. Stirland, "CODE: a novel single step MOVPE technique for the fabrication of low-dimensional devices, quantum wires and quantum dots," *Journal of crystal growth,* vol. 108, pp. 203-218, 1991.

[57] Y. Galeuchet, P. Roentgen, and V. Graf, "GaInAs/InP selective area metalorganic vapor phase epitaxy for one‐step‐grown buried low‐dimensional structures," *Journal of applied physics,* vol. 68, pp. 560-568, 1990.

# Chapter 4

# Lasing characteristics of membrane DFB lasers

4.1 Introduction 175
4.2 Structure and design of membrane DFB laser 177
4.2.1 Device structure 177
4.2.2 Grating design 180
4.3 Fabrication process 183
4.3.1 Equipment 183
4.3.2 BCB (benzocyclobutene) wafer bonding 188
4.3.3 Grating formation method 194
4.3.4 Fabrication procedure 200
4.4 Static characteristics of membrane DFB laser 207
4.4.1 Uniform grating device 207
4.4.2 $\lambda/4$-shifted grating device 213
4.4.3 Reliability of membrane DFB lasers 217
4.5 Dynamic characteristics of membrane DFB laser 225
4.5.1 Relative intensity noise (RIN) measurement 225
4.5.2 Small signal modulation 230
4.5.3 Eye diagrams and bit-error-rate (BER) measurement 240
4.6 Conclusion 246
References

## 4.1 Introduction

This chapter describes the fabrication process and measurement results of membrane DFB lasers integrated with a BJB waveguide. In the chapter 3, the fabrication process of the membrane BJB structure was established. The BJB structure will be

introduced into the membrane laser to integrate the laser and other function devices in this chapter. Section 4.2 describes the fabricated device structure and grating design. Section 4.3 describes the fabrication procedure and detail process of the membrane DFB laser. The dry etching process during the grating formation which used in previous works in our group significantly degraded the optical property of the active region. Therefore, the grating was formed using wet etching in this research to avoid the damage into the active region. Section 4.4 describes the static characteristics of fabricated membrane DFB lasers. The devices with uniform grating and $\lambda/4$-shifted grating are characterized. To confirm the reliability of membrane DFB laser, the preliminary reliability test is performed. Section 4.5 describes the dynamic characteristics of membrane DFB lasers. Relative intensity noise (RIN) measurement shows the noise spectrum included in the output light of lasers. The relaxation oscillation frequency can be obtained from the peak frequency in RIN spectrum. The modulation bandwidth of the laser was measured by using vector network analyzer (VNA). Finally, the large-signal modulation of membrane DFB laser was performed. The eye diagram and bit-error-rate were recorded and energy consumption for the modulation was estimated.

## 4.2 Structure and design of membrane DFB laser

### 4.2.1 Device structure

First, the device structure fabricated in this chapter is explained. Figure 4.1 shows the schematics of (a) the membrane DFB laser in previous works and (b) the membrane DFB laser integrated with a BJB waveguide in this thesis. The device in the previous works consists of only DFB laser section. The facets should be cleaved to measure the optical output power. The cavity length is define by the cleaved facets. The device in this thesis

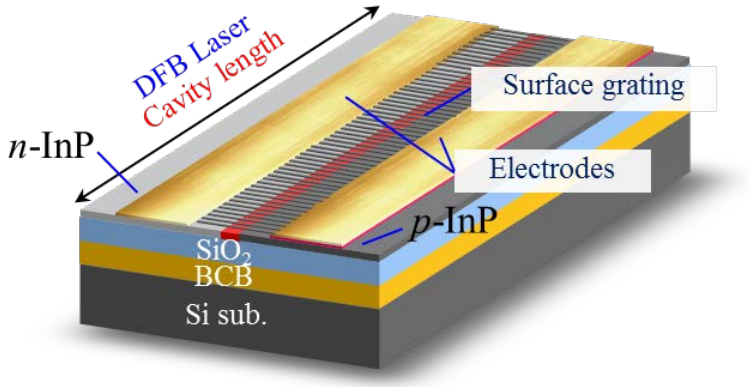


(a)

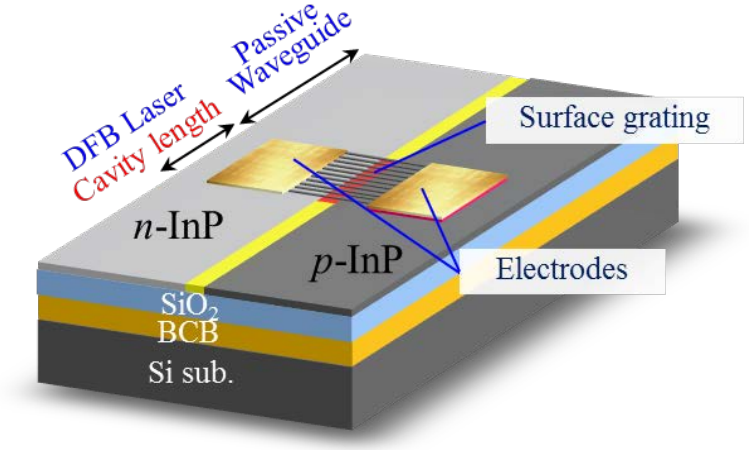


(b)

**Figure 4.1** Schematic structure of membrane DFB laser (a) previous work without output waveguide and (b) this work with integrated output waveguide.

shown in (b) has the output waveguide integrated by the BJB structure. The device consists of a DFB laser section and a passive waveguide section. The facets are formed at the passive waveguide section. The cavity length of this device is defined by a lithography process. Figure 4.2 shows the cross section of the active region and the passive region of membrane DFB laser. A 270-nm-thick semiconductor core layer is bonded on a Si substrate. As an intermediate medium, 1-μm-thick $SiO_2$ cladding layer and 2-μm-thick BCB adhesive layer are inserted. The active region consists of GaInAsP-based five quantum wells. The *n*- and *p*-InP layer are formed both side of the active region to construct the lateral-current-

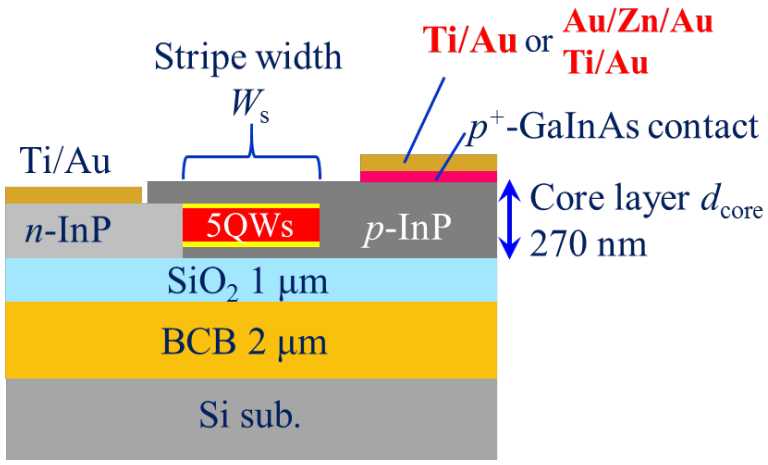


(a)

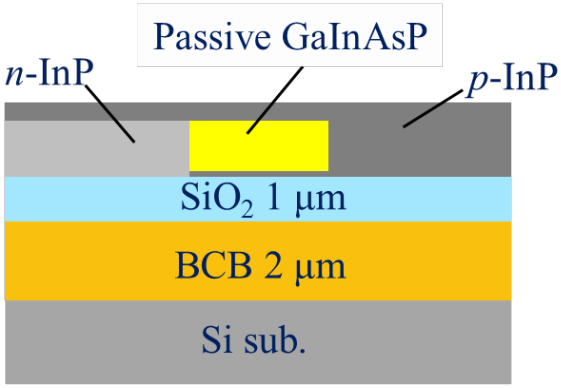


(b)

**Figure 4.2** Cross sectional image of membrane DFB laser at (a) active region and (b) passive region.

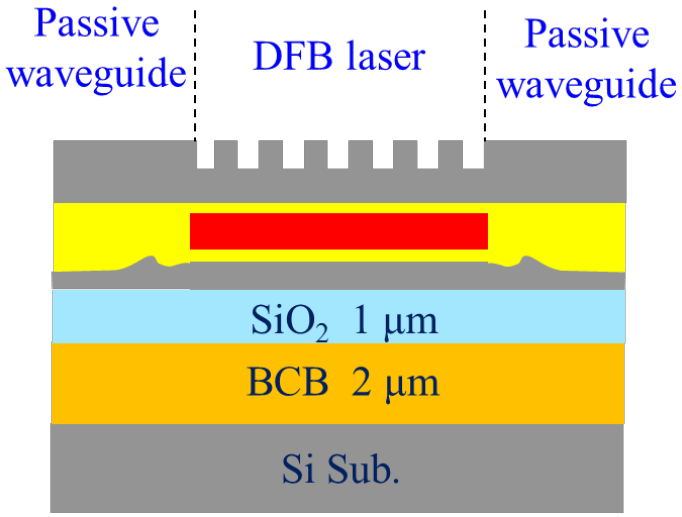


**Figure 4.3** Cross sectional image of membrane DFB laser in a light propagation direction.

injection (LCI) structure. The stripe width $W_s$ of the active layer is indicated in the figure. To obtain efficient radiative recombination, $W_s$ is preferred to be narrower than 1 μm due to the mobility difference between the hole and electron. The top of *p*-InP cladding layer has a $p^{++}$-GaInAs as a contact layer. The electrode metal for contacting *n*-InP is non-alloyed Ti/Au. As an electrode material for *p*-InP, two type electrodes of non-alloyed Ti/Au or alloyed Au/Zn/Au are used. Consequently, alloyed Au/Zn/Au electrode shows better electrical property than Ti/Au electrode for *p*-InP. As shown in Figure 4.2 (b), passive waveguide section has *u*-GaInAsP core layer which is transparent to the wavelength of the DFB laser. The core layer is embedded by *n*- and *p*-InP similar to the active region. Figure 4.3 shows the cross sectional image along to the light propagation direction. The passive waveguides are integrated to the both edges of the DFB laser region by the BJB structure. The surface grating is formed on a top InP layer in the active region.

### 4.2.2 Grating design

The grating design of the membrane DFB laser will be shown. Parameters to be designed are shown in Figure 4.4. We call the convex and concave region in a grating as main region (m-region) and sub region (s-region), respectively. The grating period is expressed as $\Lambda$. The length of m-region is expressed as $l_m$. The grating duty is given by $l_m/\Lambda$. The grating depth is expressed as $d_g$. The relationship between the grating depth $d_g$ and index-coupling coefficient $\kappa$ is already mentioned in the section 2.3. the bragg wavelength of DFB lasers is determined by grating period $\Lambda$ and equivalent refractive index $n_{eq}$ as follows;

$$\lambda_{Bragg} = 2\Lambda n_{eq} \tag{4.1}$$

The $n_{eq}$ represents the index of the longitudinal direction in the cavity. Therefore, this is calculated as following equation;

$$n_{eq} = \frac{l_m}{\Lambda} n_{eqm} + (1 - \frac{l_m}{\Lambda}) n_{eqs} \tag{4.2}$$

where, $n_{eqm}$ is the equivalent refractive index in m-region and $n_{eqs}$ is the equivalent refractive index in s-region. The $n_{eqm}$ and $n_{eqs}$ are calculated by finite-difference-method (FDM) using commercially available software FIMMWAVE. Figure 4.5 shows the TE-like 1st order mode profiles for the m- and s- regions. The calculation was performed using the stripe width $W_s$ of 0.7 μm and grating depth $d_g$ of 50 nm. The $n_{eqm}$ and $n_{eqs}$ are 2.73

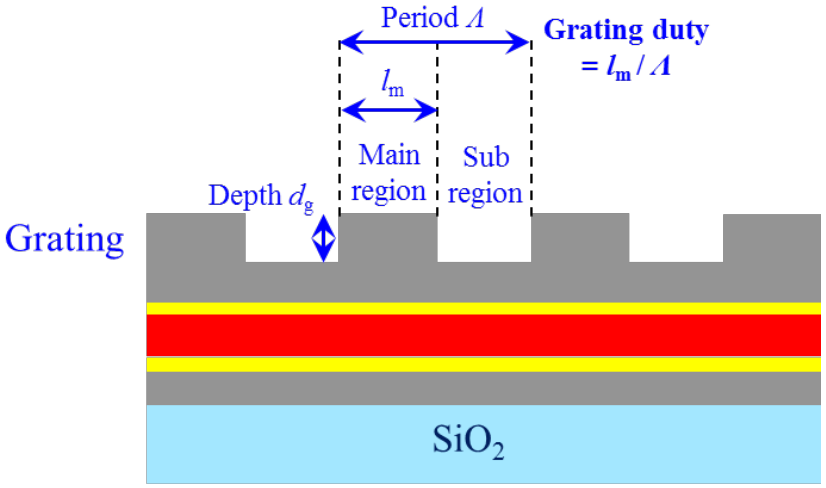


**Figure 4.4** Design parameters of grating.

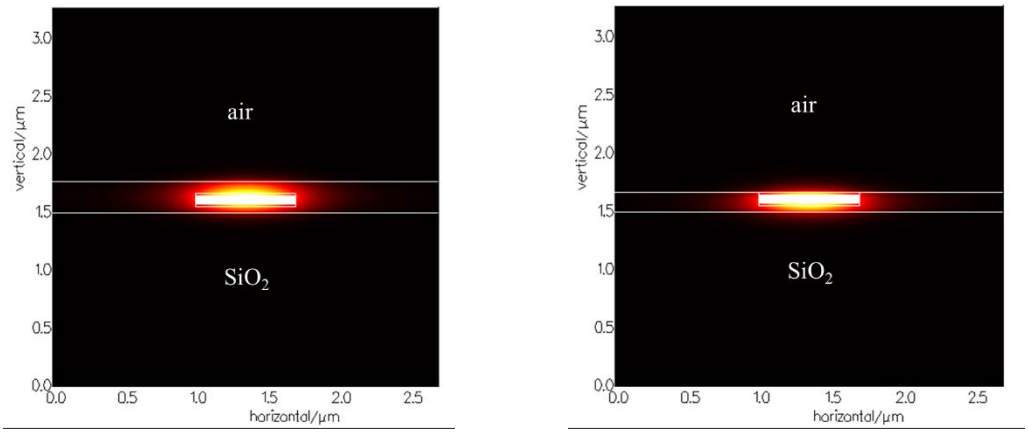


$n_{eqm} = 2.73$ $n_{eqs} = 2.61$

(a) m-region (b) s-region

**Figure 4.5** Mode-field and equivalent refractive index at m-region and s-region,

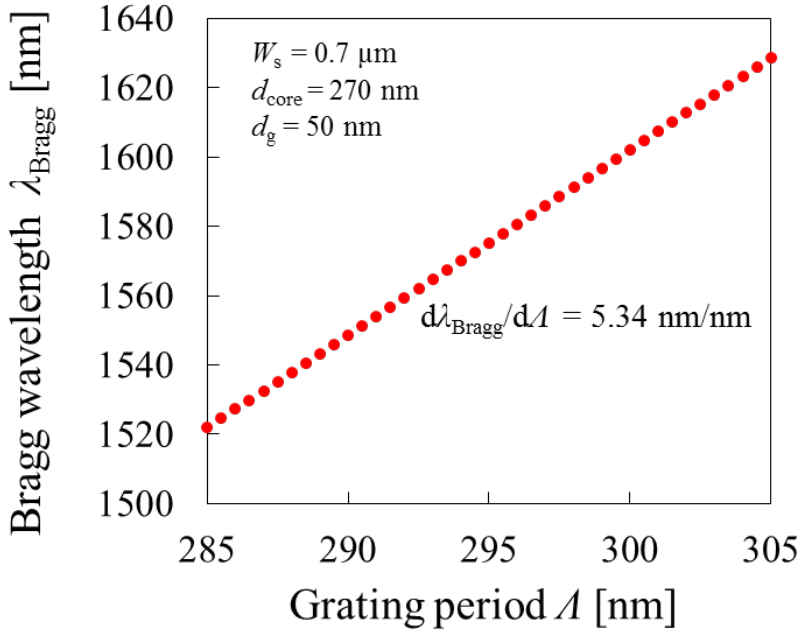


**Figure 4.6** Bragg wavelength versus grating period.

and 2.61, respectively. Then, $n_{eq}$ is calculated to be 2.67 assuming grating duty of 0.5. Figure 4.6 shows the Bragg wavelength versus grating period. The slope of Bragg wavelength as a function of grating period is 5.34 nm/nm. However, the Bragg wavelength dose not satisfy the resonance condition due to the phase characteristics of Bragg reflection. To determine the lasing wavelength, the dispersion relation of DFB laser

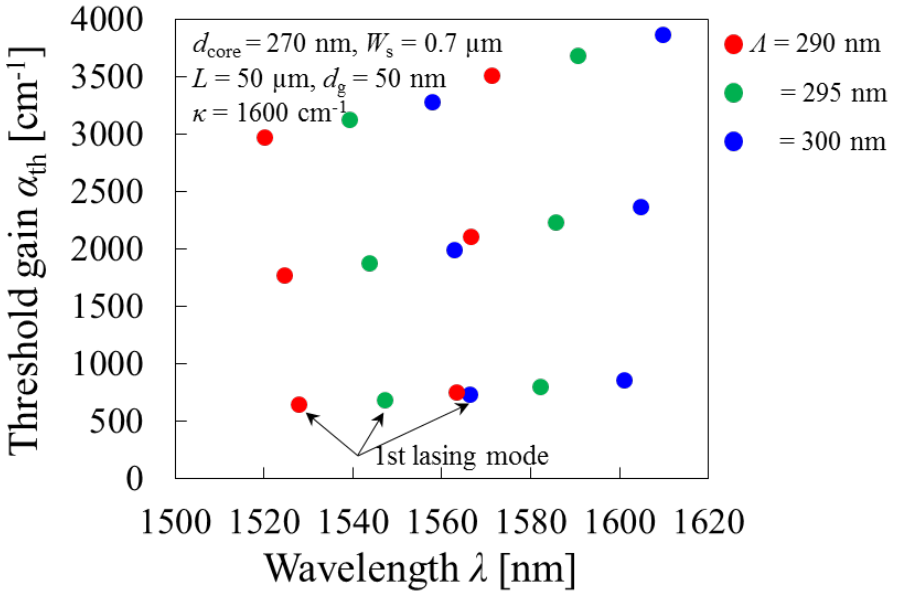


**Figure 4.7** Wavelength satisfying the resonance condition. The vertical axis shows the threshold gain for each mode.

shown in equation (2.9) should be numerically solved. Figure 4.7 shows the wavelength satisfying the resonance condition for the grating period of 290nm, 295 nm and 300 nm. The vertical axis shows the threshold gain for each mode. The cavity length of 50 μm was used for the calculation. The lasing wavelength corresponds to the mode which has the lowest threshold gain indicated by the arrow line. The lasing wavelength is apart from the Bragg wavelength for the amount of half of stop bandwidth. In this thesis, the MQWs active layer with photoluminescence peak wavelength of 1520 nm was used. Therefore the lasing wavelength should be designed to exist within the gain spectrum of the active region.

## 4.3 Fabrication process

In subsection 4.3.1, the equipment used for the fabrication of membrane DFB laser is explained. The key experimental technologies of BCB bonding and grating formation are described in subsections 4.3.2 and 4.3.3. Series of fabrication procedures of membrane DFB laser is described in subsection 4.3.4.

### 4.3.1 Equipment

**Electron beam lithography**

Figure 4.8 shows the appearance of electron-beam (EB) lithography system of JEOL JBX-6300FS. The definition of grating patterns requires nm-order controlling for structural dimension and period. When fabricating fine patterns, the EB lithography offers precise control for desired nano-structure patterns compared with the optical lithography. Table 4.1 shows specifications of the EB lithography systems of JEOL JBX-6300FS. The system is composed of an electron gun, an electron optical system, a moving stage, and a controller unit. The spot-beam scan is adopted as a scanning method to reduce the stitching errors induced by the cassette-stage movement. The main field size is set to as small as 20 μm × 20 μm. The accelerating voltage is fixed at 50 kV (maximum 100 kV) in this thesis. The focused beam sized is approximately 5 nm with FWHM at that voltage. The beam current of 100 pA is used for defining the grating patterns because the exposure with lower beam current results in finer patterning. The minimum beam-shot pitch is 0.25 nm at the accelerating voltage of 50 kV, while actual minimum shot pitch is decided by the beam current and the required dose amount. The dose amount required to expose the resist material depends on the many factors, such as thickness of resist, structure of the substrate and developing time. For the grating formation of membrane DFB laser, 80-nm-thick ZEP 520 positive resist mixed with a $C_{60}$ micro composite was used as EB resist.

**Figure 4.8** Appearance of electron-beam lithography system of JEOL JBX-6300FS.

**Table 4.1** Specifications of JBX-6300FS

| System | JBX-6300FS |
|---|---|
| Electron gun | ZrO/W Shottky type |
| Writing method | Spot beam |
| Accelerating voltage | 25kV/50kV/100kV |
| Beam current | 20 pA ~ 20 nA |
| Beam size | ~ 5nm (@ 50 kV) |
| Scan speed | Up to 50MHz |

**Electron beam evaporation**

Figure 4.9 shows the appearance of electron-beam evaporation system (Eiko Engineering). The metal sources are heated by electron-beams in a vacuum chamber, and evaporated metals are deposited on a target substrate. Comparing with thermal evaporation system utilizing heating by resistive filament, noble metals (Ti) which require high temperature for evaporation are available. Because the deposited thickness is monitored by a quartz crystal unit, nm-order thickness control is easily achieved. Our system has a load-lock

chamber to maintain the pressure of the vacuum chamber. As a metal source, Au, Ti, Pd, Cr and Ni are implemented in electron guns.

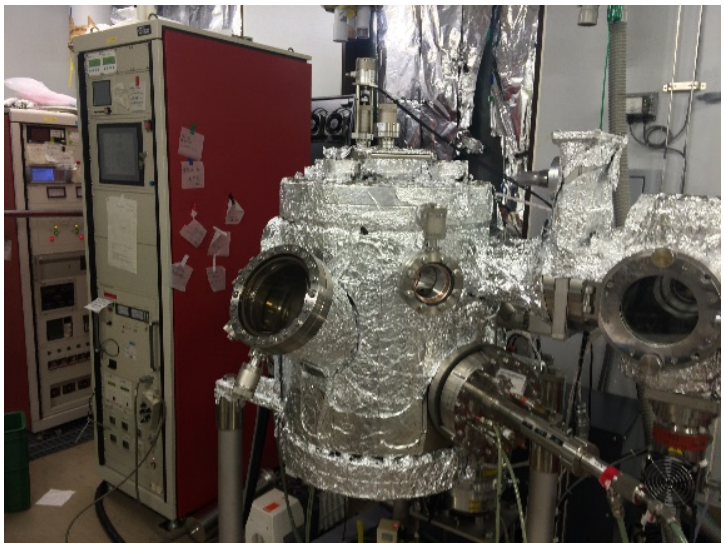

**Figure 4.9** Electron-beam evaporation system (Eiko Engineering).

**Resistive thermal evaporation**

Figure 4.10 shows the appearance of the resistive thermal evaporation system (TOKYO VACUUM, EG-240). In thermal evaporation, the material source is put in a resistive coil. The coil as well as source materials are heated by applying the high current. The thermally

**Figure 4.10** Thermal evaporation system (TOKYO VACUUM, EG-240).

evaporated metal is deposited on a target substrate. The thermal evaporation system is a popular technique to evaporate metals due to its simple structure than electron-beam evaporation system. However, maximum heating temperature is limited by the resistive coil. This system can gradually rise the source material temperature. A low-thermal conductivity metal such as Zn is preferred to be evaporated by thermal evaporation to avoid explosive boiling. During fabrication of membrane DFB laser, thermal evaporation is used to deposit Au/Zn/Au electrode.

**Plasma enhanced chemical vapor phase deposition (PECVD)**

In a PECVD process to deposit $SiO_2$, plasma is generated by applying a high frequency voltage to a parallel plate electrode in a vacuum chamber introduced with tetraethyl orthosilicate (TEOS) and $O_2$. The source materials are decomposed in a plasma and deposited on the substrate surface in a state of $SiO_2$. Figure 4.11 shows the PECVD system of PD-240 manufactured by SAMCO. Two deposition conditions of $SiO_2$ are used in the fabrication process of membrane DFB laser. Table 4.2 shows the deposition condition of 50-nm-thick $SiO_2$ for mesa formation. Table 4.3 shows the deposition condition of 20-nm-thick $SiO_2$ for grating formation. In order to maintain coverage on surface even with thin (20 nm) deposition layer, slow deposition rate of 20 nm/min is used for the mask of a grating.


**Figure 4.11** Plasma-enhanced chemical vapor phase deposition (PECVD) system (SAMCO;PD-240).

**Table 4.2** Deposition condition of 50-nm-thick $SiO_2$ for mesa formation

| Parameters | | Step1 |
|---|---|---|
| Gas flow | TEOS | 3 sccm |
| | $O_2$ | 233 sccm |
| RF power | | 250 W |
| Pressure | | 70 Pa |
| Discharging time | | 1 min. |

**Table 4.3** Deposition condition of 20-nm-thick $SiO_2$ for grating formation

| Parameters | | Step1 |
|---|---|---|
| Gas flow | TEOS | 1 sccm |
| | $O_2$ | 233 sccm |
| RF power | | 250 W |
| Pressure | | 70 Pa |
| Discharging time | | 1 min. |

### 4.3.2 BCB (benzocyclobutene) Wafer bonding

BCB bonding is the essential process to prepare the membrane structure on a Si substrate with CMOS compatible temperature. For the high quality bonding result, the uniform spin coating of liquid BCB and uniformity of applied force during pressing process are important.

**Spin coater (Delta 80 RC)**

Spin coating system of Delta 80 RC (SUSS MicroTec) is used to coating the BCB onto a Si substrate. The rotation speed, rotation acceleration, and rotating time are arbitrary controlled. Delta 80 RC has not only standard rotational stage but also a rotatable cover. After dropping the liquid onto the substrate placed on the rotational stage, the substrate can be spun with closed cover. This equipment configuration suppresses the drying of the resist and the occurrence of turbulence. As a result, high uniformity coating is realized. Figure 4.12 shows the appearance of instrument. The operation and process recipe are configured on a PC software. The figure on the right hand side shows the inside of the rotational stage. The maximum available wafer size is 3-inch wafer. 2-inch Si wafer is used in the fabrication of membrane DFB laser. The BCB with product name of CYCLOTENE 3022-35 is coated on a Si substrate. Table 4.4 shows spin coating condition of Delta 80 RC for CYCLOTENE 3022-35. The coating using this condition results in almost uniform 2-μm-thick BCB layer.

**Figure 4.12** Delta 80 RC (SUSS MicroTec).

**Table 4.4** Spin coating condition of delta 80 for BCB (CYCLOTENE 3022-35)

| Step | Rotation [rpm] | Acceleration [rpm/s] | Cover action | Time [sec] |
|---|---|---|---|---|
| 1 | 0 | 1000 | close | 7 |
| 2. | 500 | 1000 | close | 5 |
| 3 | 1000 | 1000 | close | 16 |
| 4 | 1900 | 5000 | close | 1 |
| 5 | 0 | 5000 | close | 2 |
| 6 | 0 | 1000 | open | 6 |
| 7 | 1000 | 1000 | open | 180 |
| 8 | 0 | 1500 | open | 0 |

**Nano-imprinter**

Figure 4.13 shows the appearance of nano-imprinter (MEISYO KIKO) used for applying the uniform force to a bonded wafer. Our group adopted the nano-imprinter as an instrument to pressing the wafer because this instrument can control the pressing force, the chamber temperature and the pressure during the pressing operation. The wafers to be bonded are set on the top and bottom stage. These wafers are pressing in a vacuum environment with configured temperature and force. Table 4.5 shows the press condition of nano-imprinter for BCB bonding. The applied pressure to the wafers is needed to be

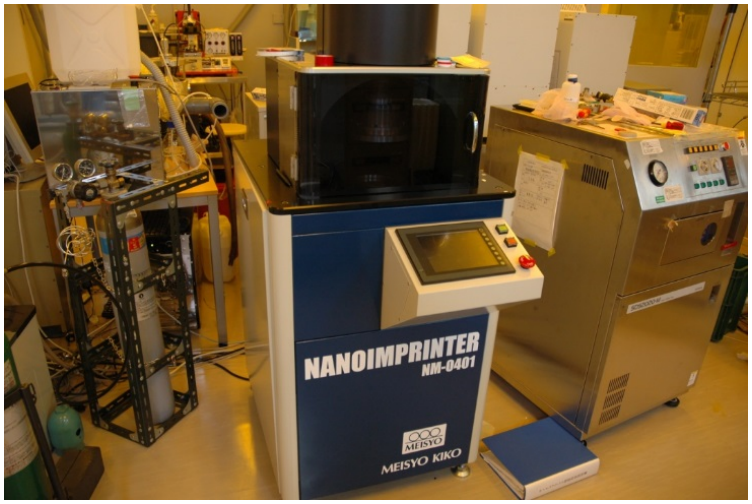


**Figure 4.13** Nano-imprinter NM-0401 (MEISYO-KIKO)

**Table 4.5** Press condition of nano-imprinter for BCB bonding.

| Step | Force[ N ] | Temperature [ °C ] | Time [ min ] |
|---|---|---|---|
| 1 | 0 | 30 | 5 |
| 2 | 12 | 130 | 10 |
| 3 | 12 | 130 | 60 |
| 4 | 0 | 30 | 60 |

calculated from the applied force and the area of substrate.

The whole process flow of BCB bonding is explained as follows.

(1) Deposition of 1-μm-thick $SiO_2$ cladding layer on an epitaxial substrate using PECVD. (Figure 4.14(A))

(2) Spin coating of BCB on a 2-inch Si substrate using the condition in Table 4.4.(Figure 4.14(B))

(3) Pre-baking of BCB-coated Si substrate in a $N_2$ atmosphere using the condition in Table 4.6

(4) Pressing the two wafers in nano-imprinter with condition in Table 4.5. (Figure 4.14(C))

(5) Hard-baking of BCB using the condition in Table 4.7.

(6) Thinning the InP substrate by chemical and mechanical polishing using solution of Br:$CH_3OH$ (Figure 4.14(D)).

(7) Removal of etch stop layers using selective wet etching conditions in Table 4.8 (Figure 4.14(E)).

**Table 4.6** Pre-baking condition

| **Temperature [ °C ]** | **Time [ min ]** | **Atmosphere** | **Phase** |
|---|---|---|---|
| 210 | 47 | $N_2$ | Liquid→Gel |

**Table 4.7** Hard-baking condition.

| **Temperature [ °C ]** | **Time [ min ]** | **Atmosphere** | **Phase** |
|---|---|---|---|
| R.T→250 | | $N_2$ | Gel |
| 250 | 60 | $N_2$ | Gel→Solid |
| 250→R.T. | | $N_2$ | Solid |

**Table 4.8** Removal condition of etch stop layers.

| Material | Etchant | Temperature | Time [min] |
|---|---|---|---|
| InP substrate | $HCl:CH_3COOH = 30:10$ | R.T. | ~60 |
| 300-nm-thick GaInAs | $H_2SO_4:H_2O_2:H_2O = 2:2:80$ | 20°C | 6 |
| 100-nm-thick InP | $HCl:CH_3COOH = 10:40$ | 20°C | 1 |

Figure 4.15 shows a photograph of the 270-nm-thick InP membrane layer fabricated on a Si substrate by BCB bonding. Almost whole 2-inch region except for the edge was successfully bonded. In an actual fabrication process of membrane DFB laser, a rectangular shape substrate with a dimension of 2 cm × 2 cm was used instead of 2-inch wafer.

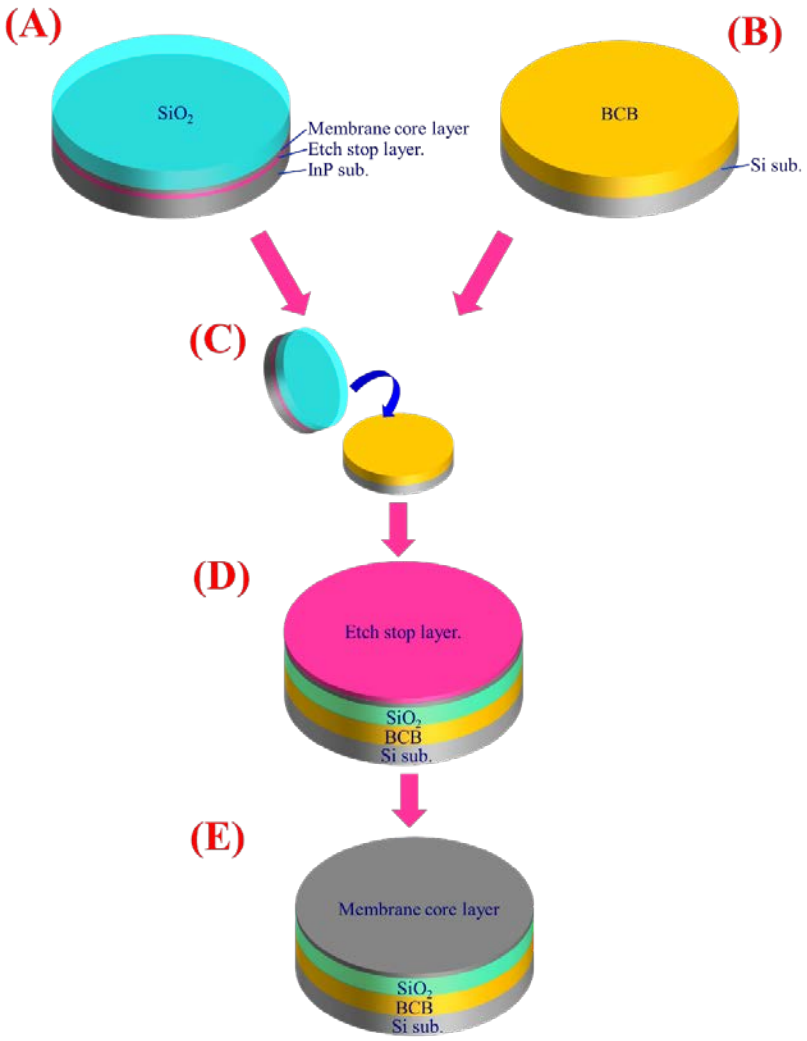


**Figure 4.14** Process flow of BCB bonding

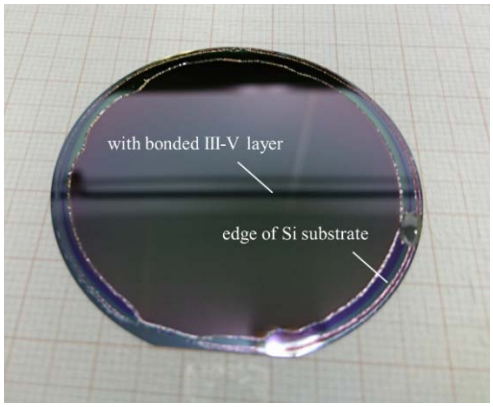


**Figure 4.15** Fabricated 2-inch membrane III-V layer on a Si substrate by BCB bonding.

### 4.3.3 Grating formation method

In a previous work, the $SiO_2$ grating pattern defined by EB lithography was transferred on an InP surface layer by using $CH_4/H_2$ RIE [1]. The SEM top view of the obtained grating pattern on an InP is shown in Figure 4.16. It can be seen that the surface was significantly roughened though the dry etching process. When such damaged layer is placed in close to the active layer, the increment of non-radiative recombination is induced. In generally, the damaged semiconductor surface can be recovered by annealing process to enhance reconstruction or wet cleaning to remove the damaged layer. However, it is preferred that the surface grating is formed using only wet chemical etching, which will not remain the damage on an etched surface. Therefore, here, etching conditions for forming a surface grating using wet etching are investigated.

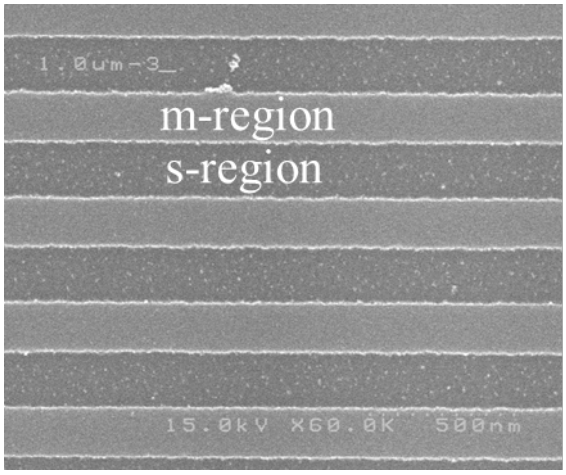


**Figure 4.16** SEM image of top view of surface grating formed by $CH_4/H_2$ RIE [1].

**Selection of chemical solution**

In the grating design of membrane DFB laser, possible grating depth is in the range from 0 nm to 100 nm. In order to perform wet etching with high thickness controllability, a chemical solution with slow etching rate for InP should be chosen. As an experimental procedure, chemical etchant suitable for forming a surface grating is studied by etching the InP substrate with patterns of $SiO_2$. Figure 4.17 shows the difference in mask

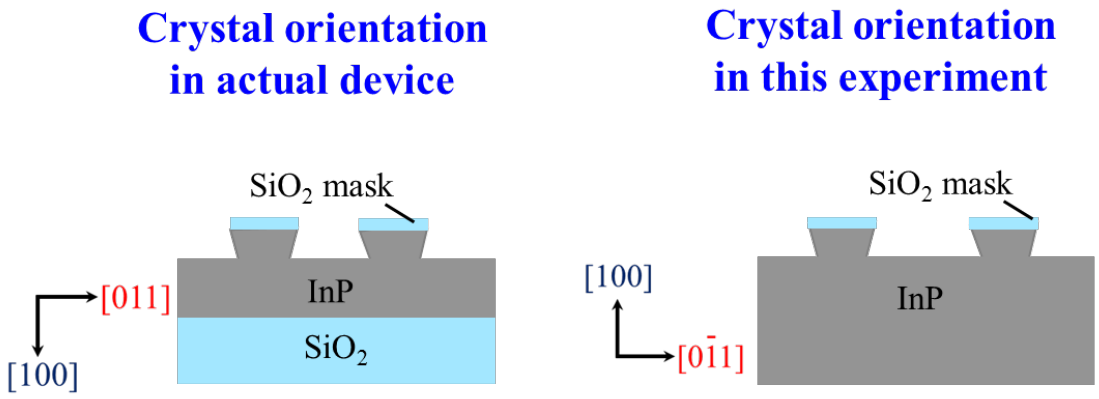


**Figure 4.17** Crystal orientation in actual device and this experiment.

formation direction between in the actual membrane device and in an InP chip used in this experiment. In the membrane structure, the [100] direction face the bottom side because the membrane layer is bonded upside down on a Si substrate. Then the grating is formed in [011] direction. In contrast, the [100] direction of the InP substrate in this experiment faces to top side. To obtain etching profile same as in a membrane device, the grating should be formed in [0$\bar{1}$1] direction.

In the experiments, the following four types of chemical solution were examined.

(1) HCl:$CH_3COOH$

(2) Br:$CH_3OH$

(3) $H_2SO_4$ : HCl : $H_2O_2$

(4) HCl : $CH_3COOH$ : $H_2O_2$ : $H_2O$

First, I considered the typical etchant of HCl:$CH_3COOH$ and Br:$CH_3OH$ used for an etching of an InP. However, these halogen-based etchant has relatively high etching rate (several 100 nm/min) and was difficult to obtained uniform etching depth without etch stop layer. Therefore, the chemical etchant including oxidizing agent is suitable for our purpose. In addition, it is well known in previous research that this type of solution has linear etching rate to the time and smooth etching surface is created.

**$H_2SO_4$ : HCl : $H_2O_2$**

The etching property of solution of $H_2SO_4$ : HCl : $H_2O_2$ = 1: 1: 8 is examined. The temperature of the solution is controlled at 20°C in a water temperature controlling bath. Figure 4.18 shows the SEM images of the cross section of etched InP substrate using $H_2SO_4$ : HCl : $H_2O_2$ = 1 : 1 : 8 @20°C for etching time of 30 sec an 60 sec. Figure 4.19 shows the etching rate for InP using this solution. The etching rate is estimated to be 1.7 nm/sec which is adequately slow rate to form 50-nm-depth grating. Although the

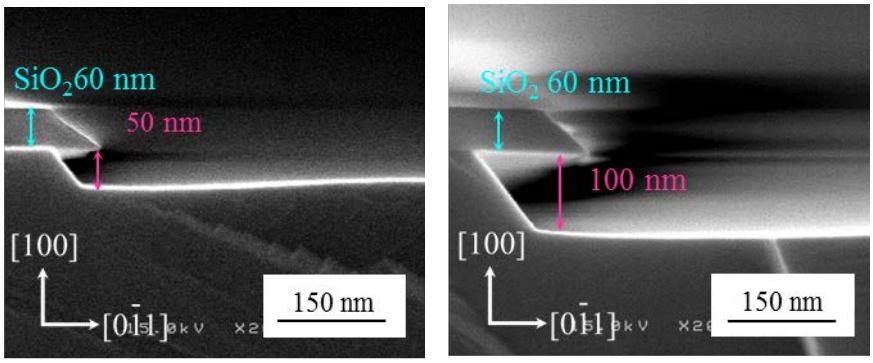


(a) etching time = 30 sec (b) etching time = 60 sec

**Figure 4.18** SEM images of cross section of etched InP substrate using $H_2SO_4$ : HCl : $H_2O_2$ = 1 : 1 : 8 @20°C

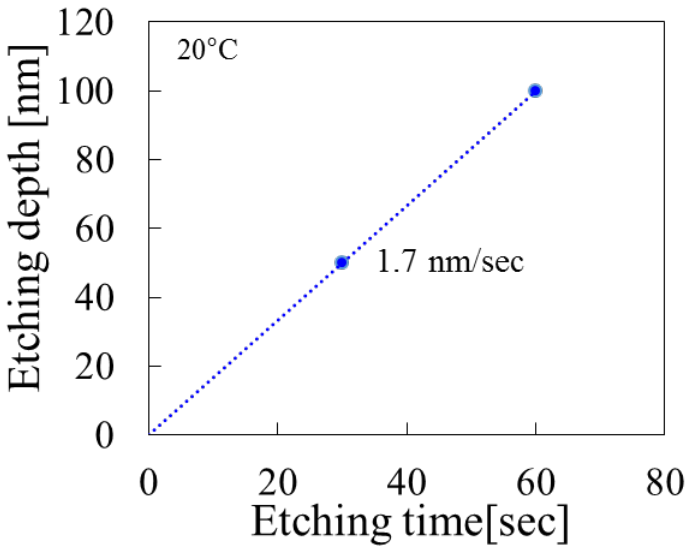


**Figure 4.19** Etching rate of InP using $H_2SO_4$ : HCl : $H_2O_2$ = 1 : 1 : 8 @20°C

uniformly etched and smooth surface were obtained, there was an undercut into the beneath of $SiO_2$ mask with a same depth as vertical etching. When the grating is formed with depth of 50 nm using this etchant, the shrinkage of grating m-region becomes 100 nm. Considering the grating period of membrane DFB laser is around 300 nm, this shrinkage degrades the precise control of grating design. Hence, this solution can provide good depth control and smooth etching profile, it is difficult to fabricate the surface grating of membrane DFB laser. The chemical solution which does not form the undercut is needed.

**$HCl : CH_3COOH : H_2O_2 : H_2O$**

Chemical solution of $HCl : CH_3COOH : H_2O_2 : H_2O$ = 2: 20: 1 :30 is examined. The temperature of the solution is controlled at 10°C in a water temperature controlling bath. Figure 4.20 shows the SEM images of cross section of etched InP substrate using $HCl : CH_3COOH : H_2O_2 : H_2O$ = 2: 20: 1 :30 @10°C for etching time of 3 sec, 6 sec and 9 sec. Figure 4.21 shows the etching rate for InP using this solution. The etching rate has slightly nonlinear characteristics, but by fitting linear approximation, the rate is obtained to be 18 nm/sec. From the etching profiles, there are little undercut into the mask region. The

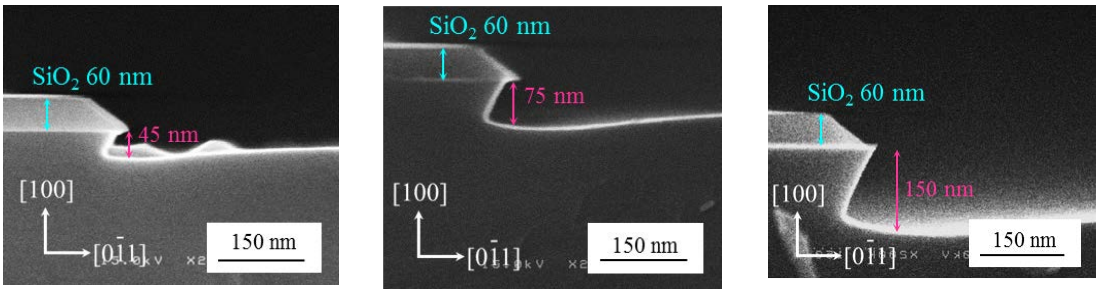


(a) 3sec (b) 6 sec (c) 9 sec

**Figure 4.20** Etching rate of InP using $HCl : CH_3COOH : H_2O_2 : H_2O$ = 2: 20: 1 :30 @10°C

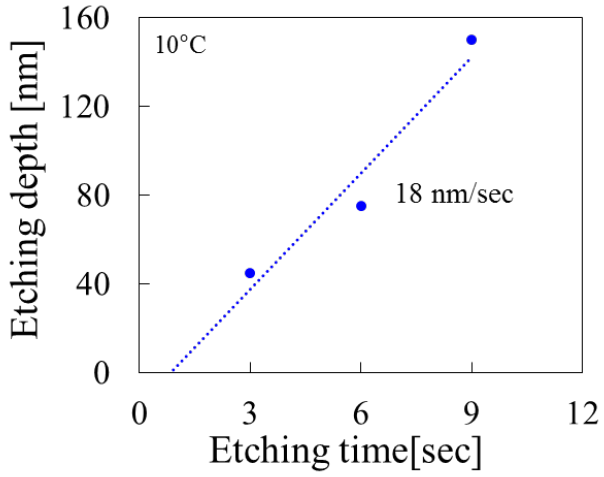


**Figure 4.21** Etching rate of InP using HCl : $CH_3COOH$ : $H_2O_2$ : $H_2O$ = 2: 20: 1 :30 @10°C

**Table 4.9** Comparison of solution for InP etching.

| Solution | Surface smoothness | Etching rate | undercut |
|---|---|---|---|
| HCl:$CH_3COOH$ | bad | fast | little |
| Br : $CH_3OH$ | bad | fast | little |
| $H_2SO_4$ : HCl : $H_2O_2$ | good | slow (1.7 nm/sec) | large |
| HCl : $CH_3COOH$ : $H_2O_2$ : $H_2O$ | good | slow (18 nm/sec) | little |

crystal plane of (111)A was appeared at the side of mesa. This plane prevented the entering of undercut during the etching process. In this solution system, it is considered that wet etching with a precise control of the grading depth and width is simultaneously achieved.

Table 4.9 summarizes the properties of solution examined in this experiment. As a conclusion, the chemical solution of HCl : $CH_3COOH$ : $H_2O_2$ : $H_2O$ = 2: 20: 1 :30 @10°C is adopted for etching of InP surface grating. Figure 4.22 shows the top view of the surface grating formed by chemical solution of HCl : $CH_3COOH$ : $H_2O_2$ : $H_2O$ = 2: 20: 1 :30 @10°C. Comparing with Figure 4.16, smooth and fine grating is successfully formed.

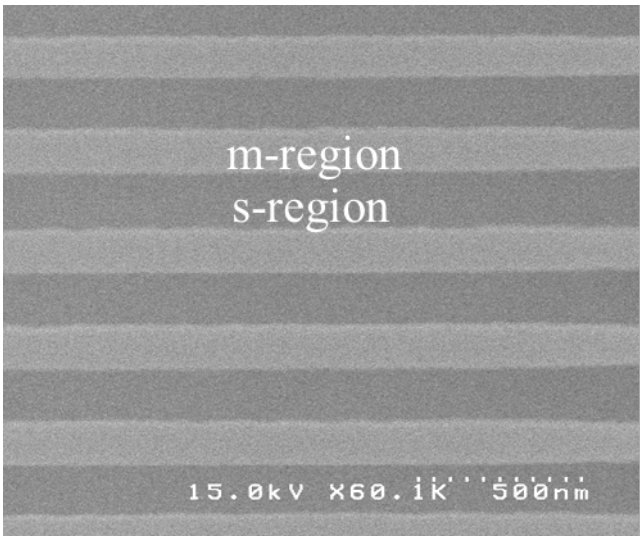


**Figure 4.22** SEM image of top view of surface grating formed by chemical solution of HCl : $CH_3COOH : H_2O_2 : H_2O = 2: 20: 1 :30$ @10°C

### 4.3.4 Fabrication procedure of membrane DFB laser

The initial wafer is grown by gas-source molecular beam epitaxy supplied by foundry service offered by InPACT. Table 4.10 shows the initial wafer structure for fabrication of membrane DFB laser. The initial wafer structure consists of GaInAs (undoped, 300 nm thick) and InP (undoped, 100 nm thick) etch-stop layers, a $p^{++}$-GaInAs contact layer ($N_A = 8 \times 10^{18}$ cm$^{-3}$, 50 nm), a $p$-InP cap layer ($N_A = 1 \times 10^{18}$ cm$^{-3}$, 100 nm), five 1% compressively strained $Ga_{0.22}In_{0.78}As_{0.81}P_{0.19}$ quantum wells (undoped, 6 nm) with six

**Table 4.10** Initial wafer structure (55551) for fabrication of membrane DFB laser.

| Layer | Material | Wavelength [ nm ] | Thickness [ nm ] | Doping level [ cm$^{-3}$ ] |
|---|---|---|---|---|
| Cap | $u$-InP | | 50 | |
| $u$-OCL | $Ga_{0.21}In_{0.79}As_{0.46}P_{0.54}$ | 1200 ± 20 | 15 | |
| TS -0.15% barrier | $Ga_{0.26}In_{0.74}As_{0.49}P_{0.51}$ | 1200 ± 20 | 10 | |
| CS 1.0% well | $Ga_{0.22}In_{0.78}As_{0.81}P_{0.19}$ | 1520 | 6 | |
| TS -0.15% barrier | $Ga_{0.26}In_{0.74}As_{0.49}P_{0.51}$ | 1200 ± 20 | 10 | |
| CS 1.0% well | $Ga_{0.22}In_{0.78}As_{0.81}P_{0.19}$ | 1520 | 6 | |
| TS -0.15% barrier | $Ga_{0.26}In_{0.74}As_{0.49}P_{0.51}$ | 1200 ± 20 | 10 | |
| CS 1.0% well | $Ga_{0.22}In_{0.78}As_{0.81}P_{0.19}$ | 1520 | 6 | |
| TS -0.15% barrier | $Ga_{0.26}In_{0.74}As_{0.49}P_{0.51}$ | 1200 ± 20 | 10 | |
| CS 1.0% well | $Ga_{0.22}In_{0.78}As_{0.81}P_{0.19}$ | 1520 | 6 | |
| TS -0.15% barrier | $Ga_{0.26}In_{0.74}As_{0.49}P_{0.51}$ | 1200 ± 20 | 10 | |
| CS 1.0% well | $Ga_{0.22}In_{0.78}As_{0.81}P_{0.19}$ | 1520 | 6 | |
| TS -0.15% barrier | $Ga_{0.26}In_{0.74}As_{0.49}P_{0.51}$ | 1200 ± 20 | 10 | |
| $u$-OCL | $Ga_{0.21}In_{0.79}As_{0.46}P_{0.54}$ | 1200 ± 20 | 15 | |
| Cap | $p$-InP | | 100 | Be : $1\times10^{18}$ |
| $p$-contact | $p^{++}$-$Ga_{0.47}In_{0.53}As$ | | 50 | Be : $8\times10^{18}$ |
| InP etch stop | $u$-InP | | 100 | |
| GaInAs etch stop | $u$-$Ga_{0.47}In_{0.53}As$ | | 300 | |
| Substrate | $n$-InP | | | |

0.15% tensile strained $Ga_{0.26}In_{0.74}As_{0.49}P_{0.51}$ barriers (undoped, 10 nm) sandwiched by $Ga_{0.21}In_{0.79}As_{0.46}P_{0.54}$ optical confinement layers (OCLs; undoped, 15 nm), and an InP cap layer (undoped, 50 nm). These layers are grown on a (100) n-InP substrate. Using this initial wafer, 270-nm-thick membrane core layer is form in final structure.

The whole fabrication process flow (shown in Figure 4.23 and Figure 4.24) is described as follows;

(1) Initial wafer

The structure is given in Table 4.10.

(2) Island formation + (3) OMVPE regrowth of passive layer

This process is same as BJB growth process described in the section 3.5.1.

(4) Stripe mesa formation

A 7-μm-wide stripe mesa structure is formed by using the same etching method as island formation.

(5) OMVPE regrowth of *n*-InP

An *n*-InP layer ($N_D = 4 \times 10^{18}$ cm$^{-3}$) is regrown at 600°C by OMVPE.

After the growth, $SiO_2$ mask is removed by dipping in buffered HF 7% for 1 min.

(6) Stripe mesa formation

One side of the *n*-InP layer beside the stripe is etched.

(7) OMVPE regrowth of *p*-InP

A *p*-InP layer ($N_A = 4 \times 10^{18}$ cm$^{-3}$) is regrown to form an LCI buried heterostructure with a stripe width of 0.5–2 μm. After the growth, $SiO_2$ mask is removed by dipping in buffered HF 7% for 1 min.

(8) $SiO_2$ cladding layer deposition

After the three-step regrowth process, a 1-μm-thick $SiO_2$ cladding layer is deposited onto the wafer by PECVD.

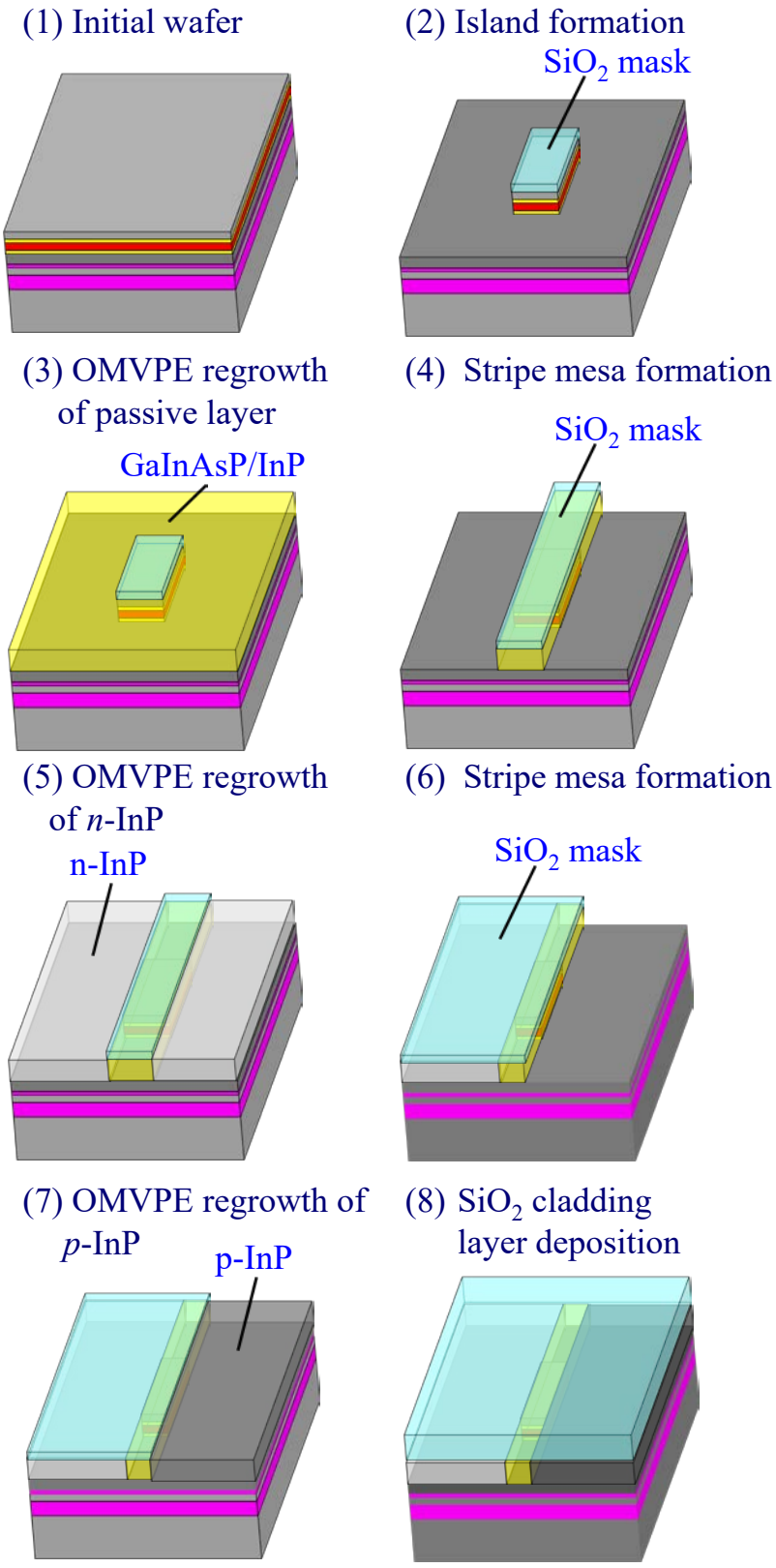


**Figure 4.23** Fabrication procedure of membrane DFB laser (initial wafer ~ $SiO_2$ cladding layer deposition).

(9) BCB bonding + (10) Removing InP substrate and etch stop layer

This process is following the procedure described in section 4.3.2. After removing etch stop layers, the GaInAs contact layer was revealed.

(11) Removing contact layer

The contact layer was etched by selective wet etchant of $H_2SO_4$:$H_2O_2$:$H_2O$ = 1: 1: 40, except for the *p*-side electrode region.

(12) Electrodes deposition

The *p*- and *n*-side electrodes were separately deposited. As a *p*-side electrode, Ti/Au = 25 nm/200 nm evaporated by electron beam evaporation or Au/Zn/Au = 25/50/300 nm evaporated by resistive thermal evaporation are deposited. Only the case for the Au/Zn/Au electrode, the deposited metal was annealed at 350°C for 1 min in $N_2$ ambient to alloying the Au and Zn. Before the *n*-side electrode deposition, the top *p*-InP cap layer at *n*-electrode region was etched by $CH_4/H_2$ RIE for 3 cycle. After that, Ti/Au = 25 nm/200 nm was deposited by electron beam evaporation for both *n*- and *p*-side electrode region.

(13) Grating formation

As an EB lithography resist, 70–80-nm-thick ZEP 520/$C_{60}$ was coated on substrate. A surface grating pattern of $SiO_2$ was formed by electron-beam lithography with dose amount of 180 μC/cm$^2$. After formation of grating pattern $SiO_2$ mask, this pattern was transferred on a surface InP by using the chemical solution of HCl : $CH_3COOH$ : $H_2O_2$ : $H_2O$ = 2: 20: 1 :30 @10°C for 3 sec.

Finally, the processed substrate is cleaved into bar form at the waveguide or DFB laser sections to measure light-output characteristics. The facets have no antireflection coating because the membrane DFB lasers are light source for completely integrated on-chip optical interconnection. Therefore, the facet coating technique is not suitable approach. The residual reflectivity at the facet is calculated to be approximately 20%, which is lower than that for the conventional lasers.

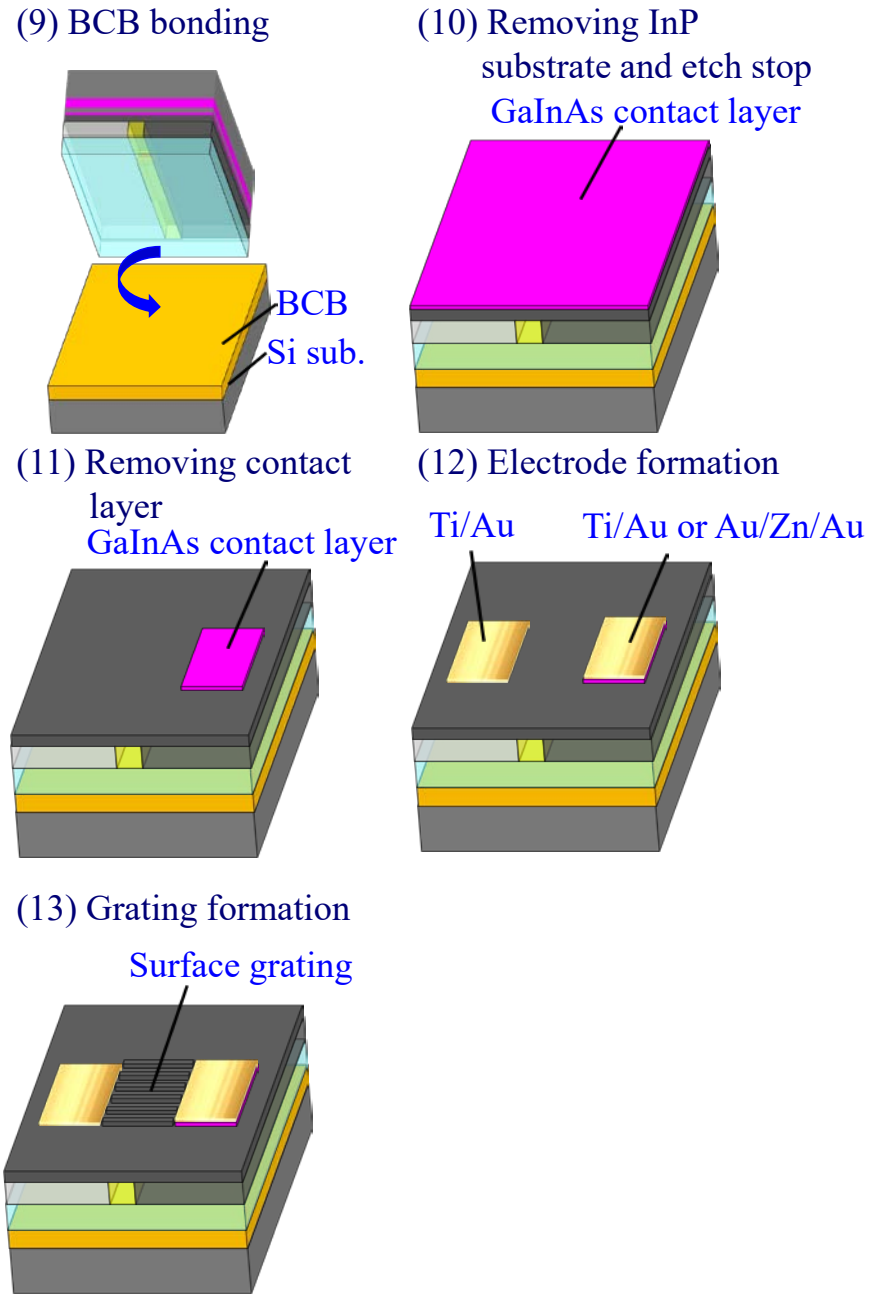


**Figure 4.24** Fabrication procedure of membrane DFB laser (BCB bonding ~ grating formation)

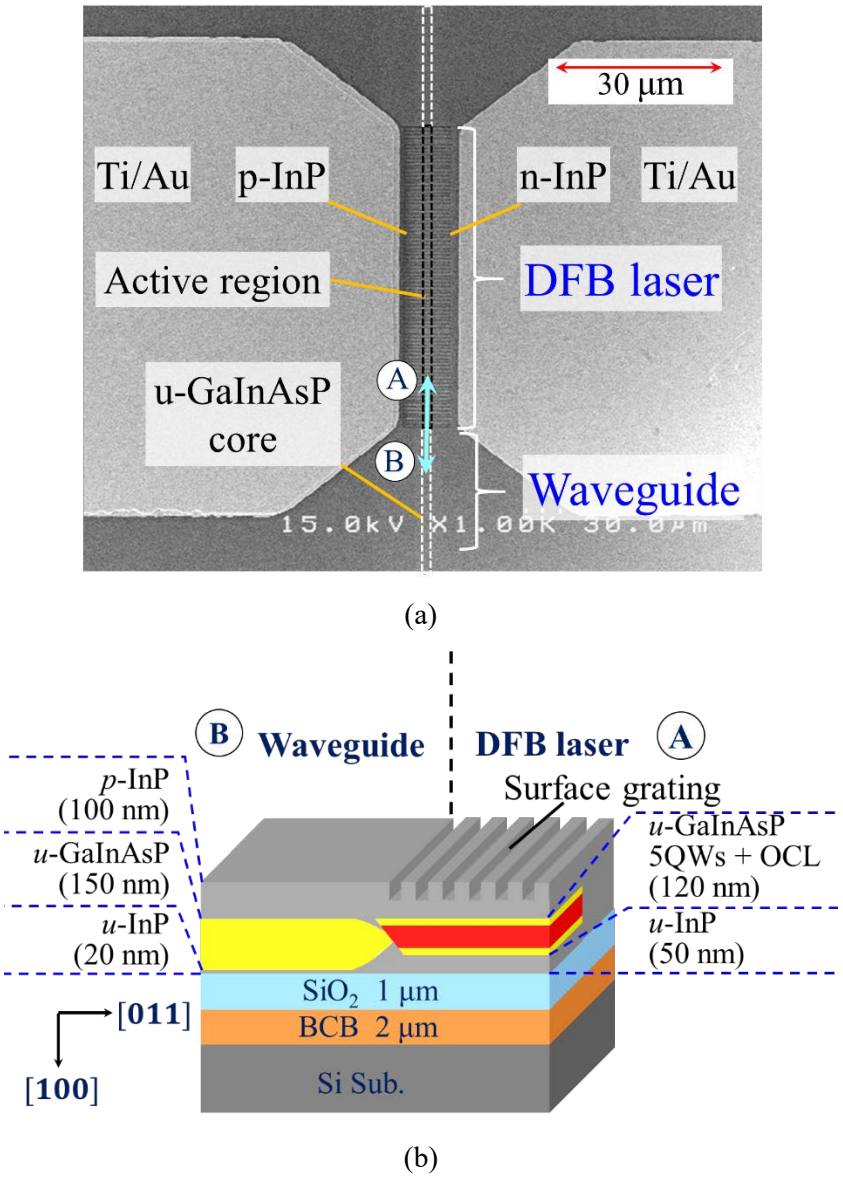


**Figure 4.25** (a) SEM image of the top view of the fabricated membrane DFB laser with BJB integrated structure. (b) Schematic diagram of the cross section parallel to the stripe at the coupling section.

Figure 4.25(a) shows an SEM image of the top view of the fabricated membrane DFB laser integrated with a BJB waveguide. The active region located in the center of the device is sandwiched by *n*-and *p*-InP so as to form a LCI structure. The electrodes are placed outside of the active stripe region. It can be confirmed that surface grating is successfully formed on the active region. Figure 4.25(b) shows a schematic diagram of the cross section parallel to the stripe at the coupling section. The positions corresponding to Figure 4.25(a)

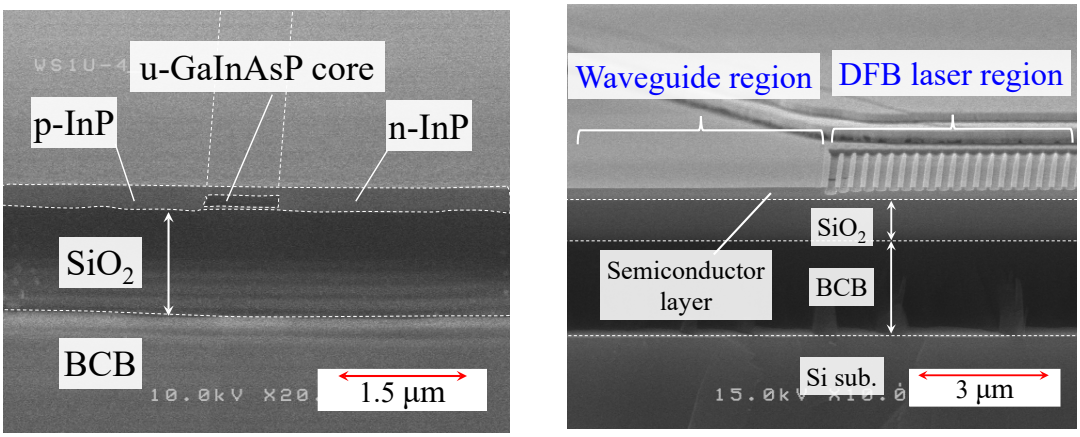


(a) (b)

**Figure 4.26** (a) SEM image of the cross section perpendicular to the stripe observed at the passive waveguide section. (b) SEM image of the cross section parallel to the stripe observed at the coupling section.

are indicated by characters of A and B. Figure 4.26(a) shows an SEM image of the cross section perpendicular to the stripe observed at the passive waveguide section. In spite of the fabrication process including a three-step regrowth process, an LCI buried heterostructure with a flat surface is obtained. Figure 4.26(b) shows an SEM image of the cross section parallel to the stripe observed at the coupling section. The semiconductor core layer is formed on a Si substrate intermediated by 2-μm-thick BCB and 1-μm-thick $SiO_2$ cladding layer.

## 4.4 Static characteristics of membrane DFB lasers

The fabricated membrane DFB lasers are characterized in terms of light output power and lasing spectrum. Low-threshold properties of membrane DFB lasers was experimentally confirmed. The measurement was performed for devices with uniform grating and $\lambda/4$-shifted grating. To confirm the reliability of membrane DFB laser, preliminary aging test was conducted. Different *p*-side electrode devices that have non-alloy Ti/Au or alloyed Au/Zn/Au electrodes were prepared for the aging test.

### 4.4.1 Uniform grating membrane DFB laser

Figure 4.27 shows the top-view of the measured membrane DFB laser structure. The measured bar consisted of, from the front, 370-μm-long passive waveguide, 50-μm-long DFB laser, 500-μm-long passive waveguide, 50-μm-long DFB laser and 370-μm-long passive waveguide. The total bar length is 1340 μm. The front facet is formed at a passive waveguide section. The rear side is connected to another DFB laser for absorbing the rear side optical output. The DFB laser has a stripe width of 0.8 μm. The grating period $\Lambda$ is 298 nm. Figure 4.28 shows the light–current (*L–I*) and voltage–current (*V–I*) characteristics of the membrane DFB laser under room-temperature (RT) continuous-wave (CW) conditions. A threshold current $I_{th}$ of 0.23 mA and an external differential quantum efficiency $\eta_d$ of 5% (front facet) were obtained. To the best of our knowledge, this value of the threshold current is a record low among the DFB lasers reported under RT-CW conditions. The threshold current density, $J_{th}$, was 575 A/cm$^2$ (115 A/cm$^2$/well). The maximum output power from the front waveguide was 32 μW at the injection current of 1.3 mA. This low-threshold current lasing was achieved thanks to the introduction of a strongly index-coupled grating structure with a short cavity for decreasing the active region volume. The differential resistance was approximately 3.6 kΩ at a bias current of 1.0 mA. This large differential resistance is attributed to the poor contact of *p*-side Ti/Au electrode. It can be seen that the *I-L* is fluctuated near the saturation region of light output

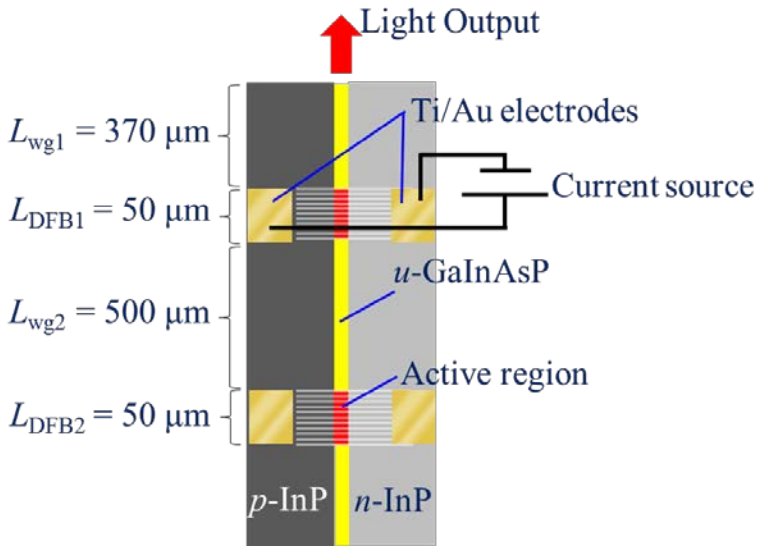


**Figure 4.27** Top-view of the measured membrane DFB laser structure. The front facet is formed at a passive waveguide section. The rear side is connected to another device.

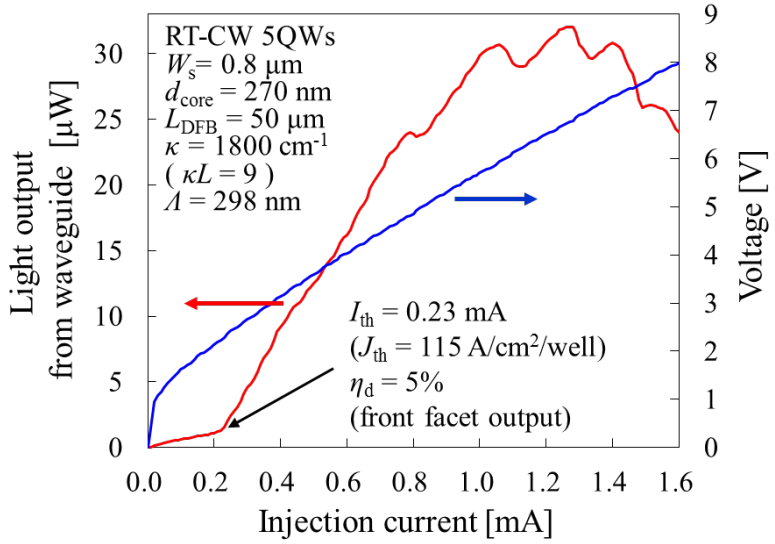


**Figure 4.28** Light-output and voltage–current characteristics of the membrane DFB laser with uniform grating.

power. This is because the reflection from the front facet or rear DFB region affects the stable operation of the DFB laser, which can be avoided by forming the facet at the active region. The obtained threshold current of 0.23 mA is lower than that of 0.39 mA for previous record device without integrated waveguides [1]. In addition, the one-sixth length cavity comparing with previous works was realized. Figure 4.29 shows the *L–I* characteristics for various heat sink temperatures under CW condition. The heat sink

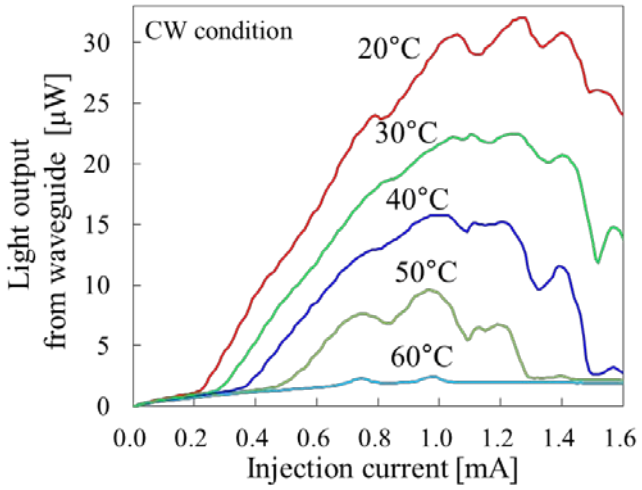


**Figure 4.29** Light-output characteristics of the membrane DFB laser with uniform grating for various operating temperatures under CW condition.

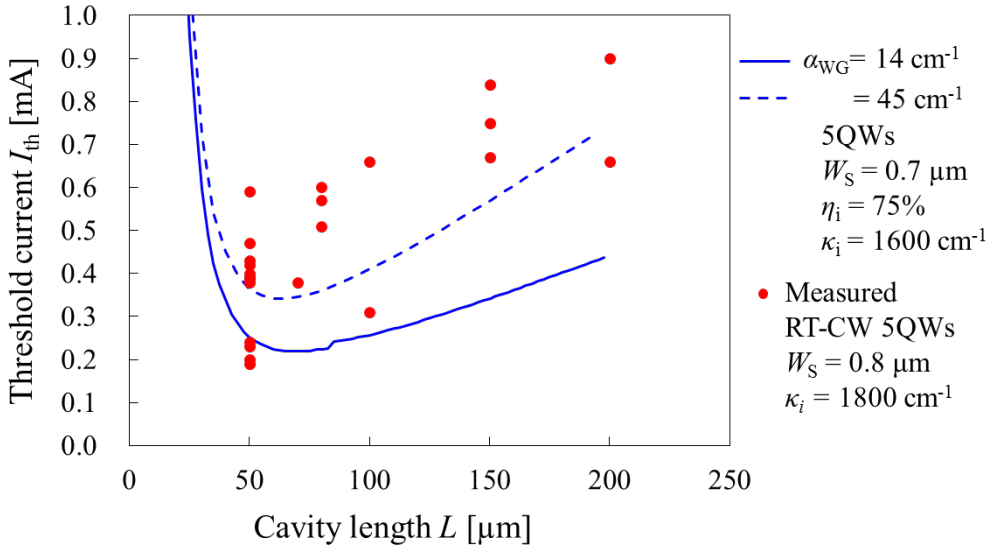


**Figure 4.30** Plots of obtained threshold current of membrane DFB laser with uniform grating.

temperature is controlled by thermos electric cooler (TEC). Lasing operation was obtained up to 50°C. Generally, the temperature of LSI rises up to 90°C, thus the laser is required to operate in temperature same as that of on a LSI. The deviation between the lasing wavelength and material gain induced by temperature change restricts the maximum operating temperature. To improve the temperature characteristics, Bragg wavelength detuning should be introduced to the grating period design so as to match the lasing wavelength and material gain in high temperature condition. Figure 4.30 shows the

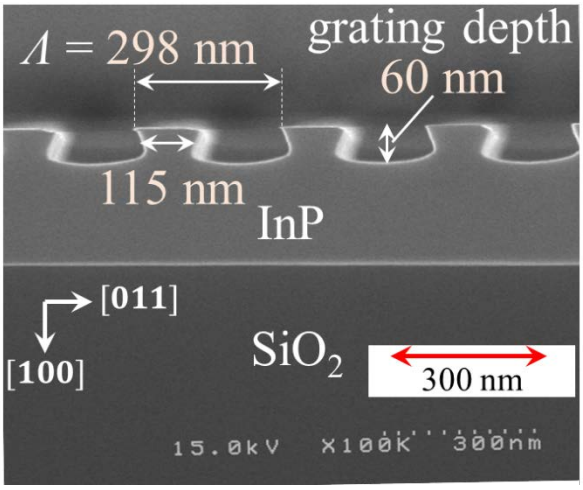


(a)

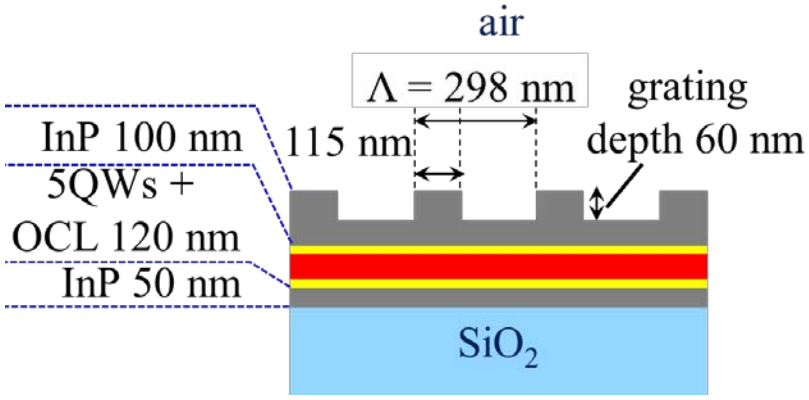


(b)

**Figure 4.31** (a) SEM image of the surface grating observed at the InP side cladding region beside the active-region stripe. (b) Calculation model to estimate the refractive index coupling coefficient of the surface grating structure approximated by a square shape.

plots of obtained threshold current of membrane DFB laser with uniform grating as a function of cavity length. The blue lines are theoretical curves showing for different waveguide loss of experimentally obtained value of 42 $cm^{-1}$[2] and ideal value of 14 $cm^{-1}$. From the obtained plots, as the cavity length becomes shorter, the threshold current tends to decrease. The plots are appeared close to the theoretical curve using the experimentally obtained waveguide loss of 42 $cm^{-1}$. Figure 4.31(a) shows a cross sectional SEM image of the surface grating observed at InP side cladding region. The fine structure formed by wet etching was confirmed. The grating depth was observed to be

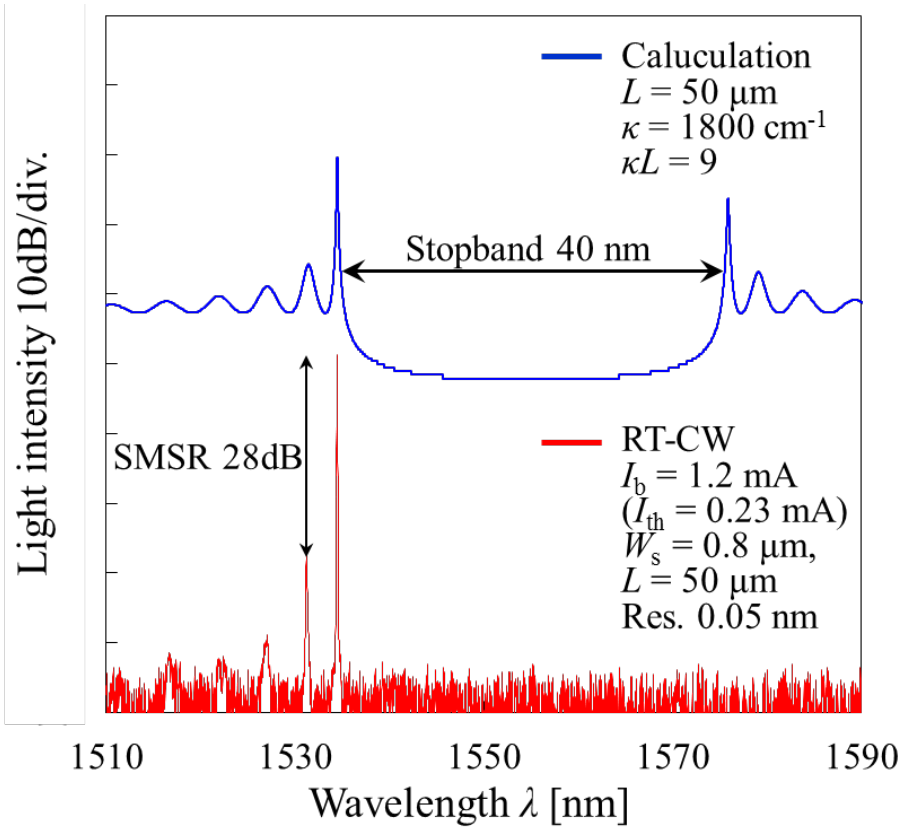


**Figure 4.32** Lasing spectrum of the membrane DFB laser with uniform grating with cavity length of 50 μm and stripe width of 0.8 μm. The red and blue lines indicate the measured spectrum at a bias current of 1.2 mA and the calculated spectrum with a refractive-index coupling coefficient of 1800 $cm^{-1}$, respectively.

approximately 60 nm. The length of m-region is approximately 115 nm. Therefore, the grating has duty ratio of 0.39. For simplicity, we estimate the index-coupling coefficient $\kappa_i$ by approximating the grating shape as a square shape, as seen in Figure 4.31(b). The $\kappa_i$ is calculated to be 1800 $cm^{-1}$ using a grating depth of 60 nm and grating duty of 0.39. This large $\kappa_i$ is sufficient value to realize a very short-cavity DFB laser with a strong cavity confinement. Figure 4.32 shows the lasing spectrum of the membrane DFB laser with uniform grating at a bias current of 1.2 mA. In this figure, the red and blue lines indicate the measured spectrum at a bias current of 1.2 mA and the calculated spectrum below threshold for an index-coupling coefficient $\kappa_i$ of 1800 $cm^{-1}$, respectively. A lasing wavelength of 1534 nm and a sub-mode suppression ratio (SMSR) of 28 dB were obtained at this bias current. The stopband width was estimated to be 40 nm from the

calculation even though it was not clearly observed in the measured spectrum. Resonant modes at the longer wavelength side of the stopband were very weak because this stopband width was wider than the gain spectrum of the multiple quantum wells. The equivalent refractive index obtained from Bragg wavelength of 1551 nm was 2.6 which was in good agreement with the value calculated by FDM analysis of the obtained structure.

### 4.4.2 λ/4-shifted grating membrane DFB laser

Membrane DFB lasers with λ/4-shifted grating were characterized. Figure 4.33 shows the SEM image of top view of surface grating with λ/4 phase shift. The phase shift region was successfully introduced in a periodical grating at the center of the DFB cavity. Figure 4.34 shows the light-output of the membrane DFB laser with λ/4-shifted grating for the cavity length of 30 μm, 100 μm and 150 μm. These device has the stripe width of 0.7 μm. It was confirmed that the threshold current decreased as the cavity length becomes shorter. In addition, lasing action was obtained as short as a cavity length of 30 μm. This is the shortest cavity length among the DFB type lasers. However, the slope efficiency of the spontaneous emission decreased and the threshold current density was significantly higher than that of the device with long cavity length. Figure 4.35 shows the plots of obtained threshold current of membrane DFB laser with λ/4-shifted grating versus cavity length. The blue line shows calculation using $\eta_i$ of 75 % and waveguide loss of 14 $cm^{-1}$. The dashed lines of green and orange color show the calculation using low $\eta_i$ of 35 % and high waveguide loss of 45 $cm^{-1}$, respectively. The obtained threshold currents are close to the theoretical blue lines which assuming good internal parameters. Figure 4.36

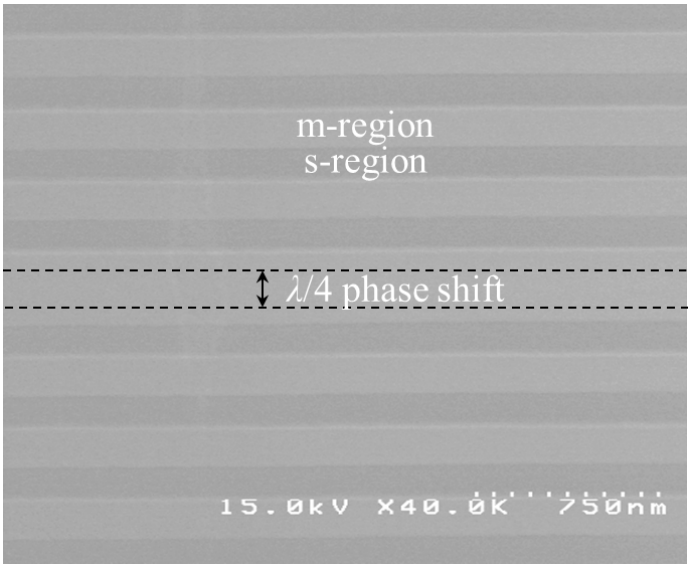


**Figure 4.33** SEM image of top view of surface grating with λ/4 phase shift.

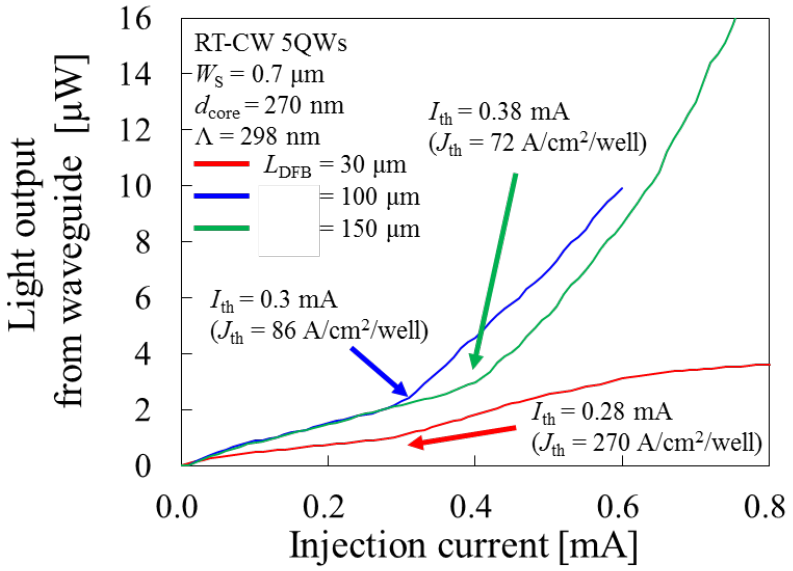


**Figure 4.34** Light-output of the membrane DFB laser with λ/4-shifted grating for different cavity length.

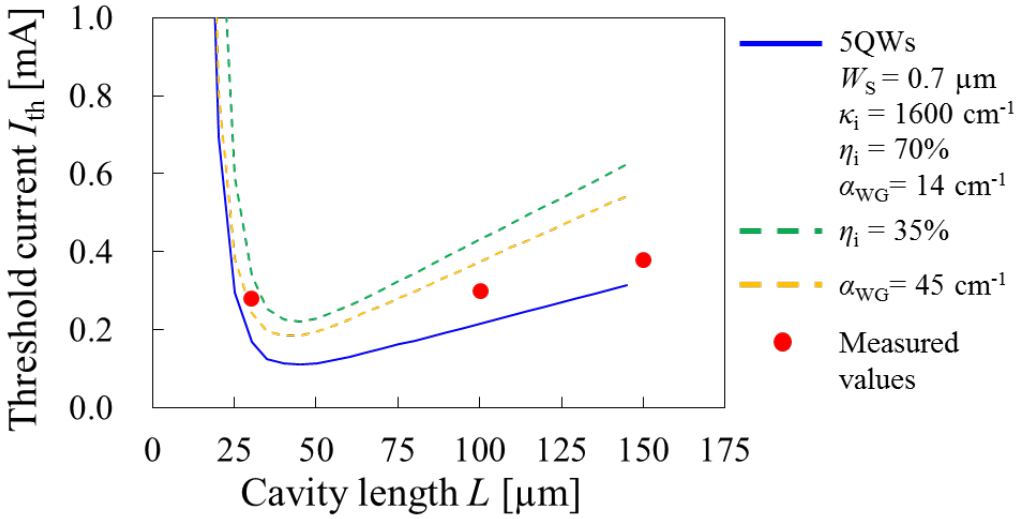


**Figure 4.35** Plots of obtained threshold current of membrane DFB laser with λ/4-shifted grating versus cavity length.

shows plots of external differential quantum efficiency as a function of the cavity length. The theoretical curves uses same parameters as calculation in Figure 4.35. For the cavity length of 100 μm and 150 μm, the fabricate devices show higher $\eta_d$ than theoretical lines. This is because these devices are seem to not operate in fundamental mode due to its long

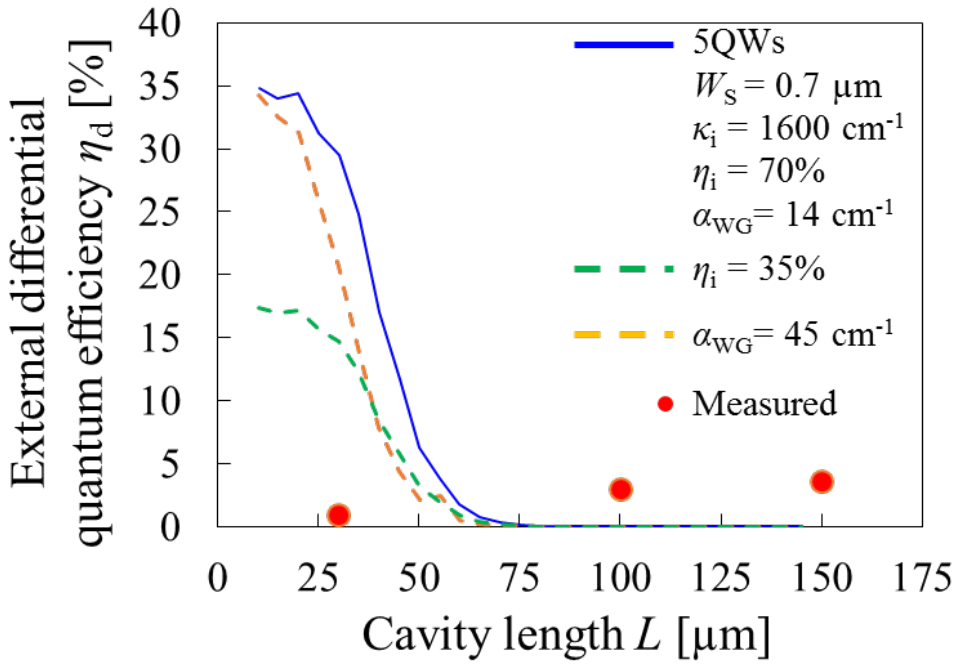


**Figure 4.36** Plots of obtained external differential quantum efficiency of membrane DFB laser with $\lambda/4$-shifted grating versus cavity length.

cavity length. For the cavity length of 30 μm, the obtained $\eta_d$ is significant lower than the expected value from the calculations. This small $\eta_d$ cannot be explained by low $\eta_i$ or high waveguide loss. It is considered that the $\eta_i$ drops due to the leakage current being dominant for the short cavity device and this cause the low $\eta_d$. Figure 4.37 shows the lasing spectra of $\lambda/4$-shifted membrane DFB laser for the cavity length of (a) 100 μm and (b) 30 μm. Although the resonance mode inside the stopband was appeared by a $\lambda/4$ phase shift, the multi-mode lasing was observed. The stopband width of 35 nm corresponds to the index coupling coefficient of 1600 cm$^{-1}$. The introduction of $\lambda/4$ phase shift into the long cavity degrades the single-mode oscillation and induce the lasing of ordinary DFB modes. In Figure 4.37(b) showing lasing spectrum of the device with cavity length of 30 μm, single mode

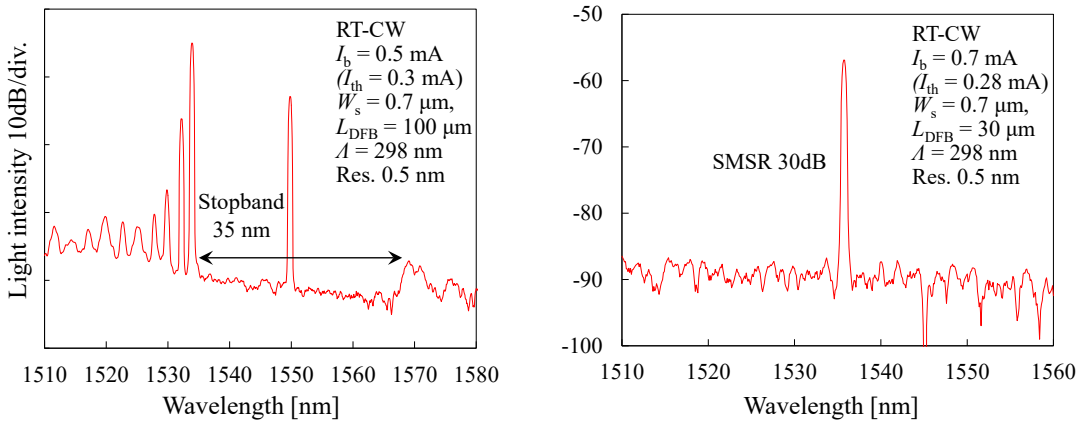


(a) (b)

**Figure 4.37** Lasing spectrum of the membrane DFB laser with $\lambda/4$-shifted grating with cavity length of (a) 100 μm and (b) 30 μm.

operation at the wavelength of 1535.6 nm was confirmed. The SMSR was more than 30dB at a bias current of 0.7 mA. The stopband could not be observed due to the small optical output power. As a conclusion, by introducing the $\lambda/4$ phase shift in a grating design of membrane DFB laser, very short cavity device with 30-μm-long cavity is operated with single mode oscillation. However, single mode property of long cavity device was degraded.

### 4.4.3 Reliability of membrane DFB lasers

While the fundamental characteristics of the membrane DFB laser were confirmed in the previous section, its reliability was not investigated, so far. The fabrication process through 3-steps regrowth by OMVPE and adhesive BCB bonding have the possibility to degrade the reliability of the laser. In this subsection, the results of an aging test of membrane DFB lasers bonded on a Si substrate measured at room temperature (20 °C) are described.

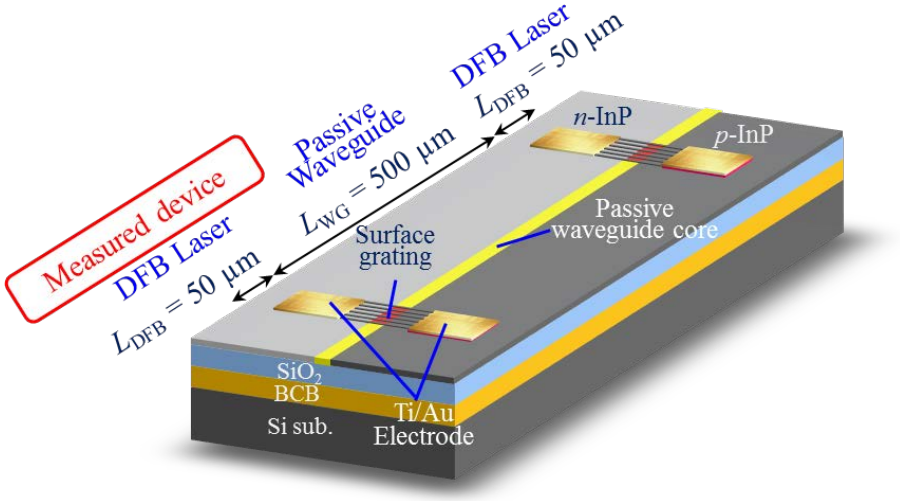


(a)

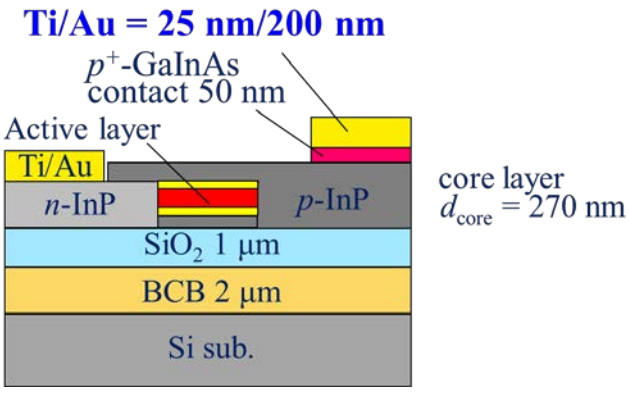


(b)

**Figure 4.38** (a) Bird view of membrane DFB laser with Ti/Au electrode on p-side (b) Cross sectional view.

Figure 4.38 shows a bird view and cross sectional image of the membrane DFB laser with Ti/Au electrode on p-side. The electrode metal for both n-and p-InP side contacts is Ti/Au = 25 nm/200 nm deposited by electron beam evaporation. It was found that the poor electrical characteristics (such as in Figure 4.28) of the device using this type of electrode were attributed to the unintentional *n*-type doping spike at the regrowth interface owing to surface contamination, as explained later. For this reason, an alloyed Au/Zn/Au electrode is introduced in order to obtain good electrical characteristics at the *p*-side by using an alloying layer which induce the counter doping by Zn diffusion as shown in

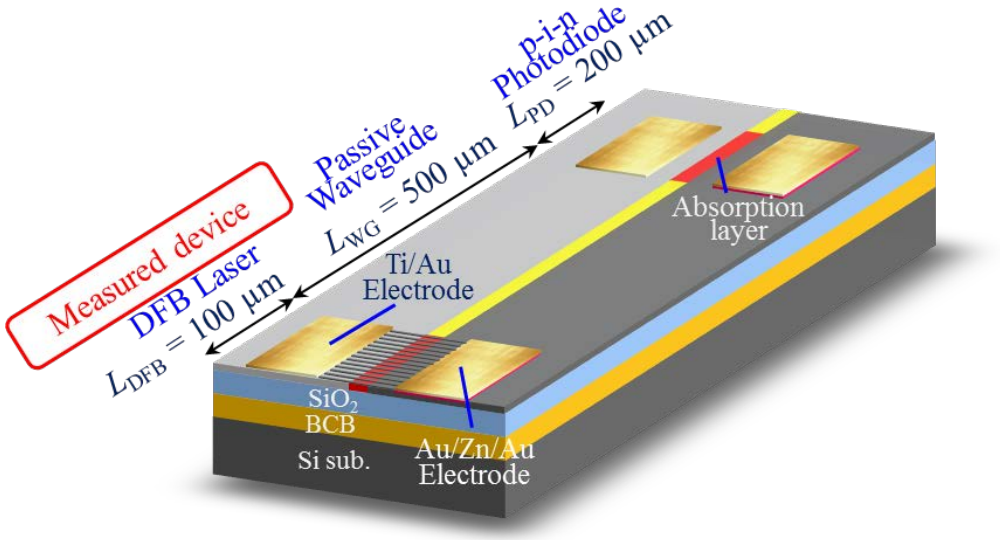


(a)

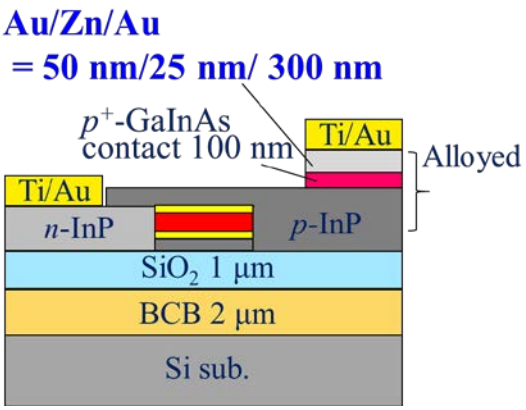


(b)

**Figure 4.39** (a) Bird view of membrane DFB laser with Au/Zn/Au electrode on p-side (b) Cross sectional view.

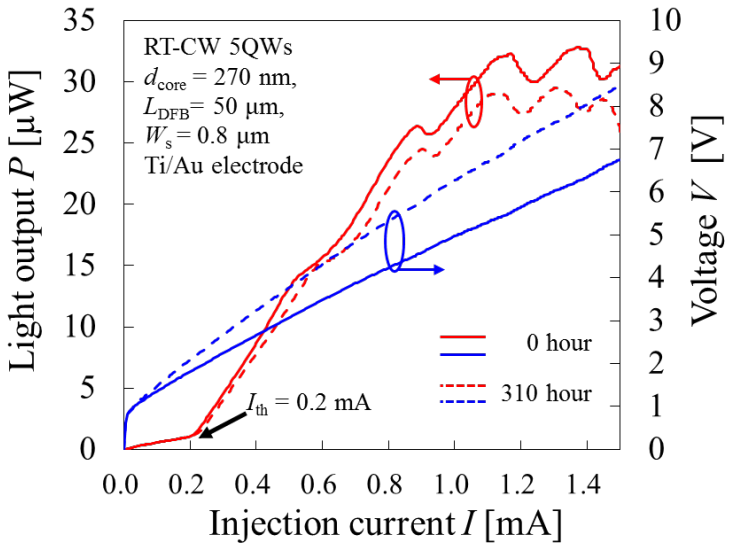


**Figure 4.40** Light output and voltage characteristics before and after 310 hours aging test of Ti/Au electrode device.

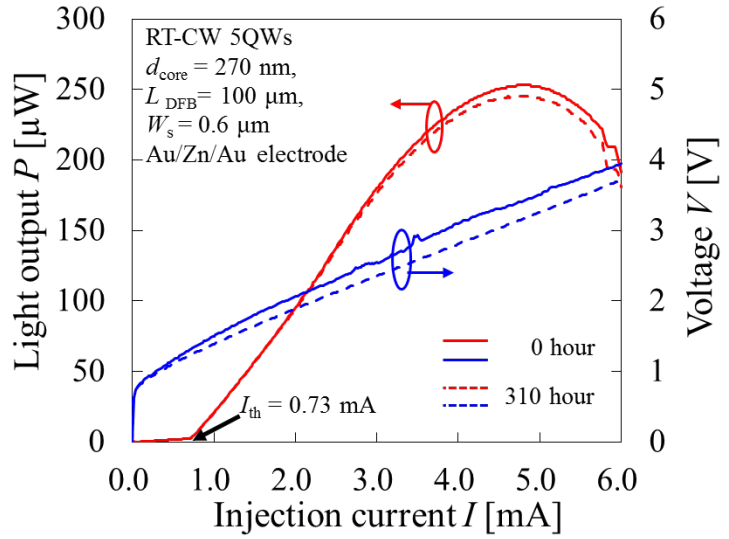


**Figure 4.41** Light output and voltage characteristics before and after 310 hours aging test of Au/Zn/Au electrode device.

Figure 4.39. Thermal evaporation is used to deposit Au/Zn/Au = 50 nm/25 nm/300 nm. The deposited metal is annealed in ambient $N_2$ by rapid thermal annealing at 350°C for 1 minute. The aging test was performed for the two devices with the Ti/Au and Au/Zn/Au *p*-side electrodes under CW conditions at 20°C. The laser chips were directly mounted on a heat sink in ambient air. The temperature of the heat sink was controlled by a thermo-electric cooler. The bias current was injected by contacting the electrodes using needle

probes. The measurement was conducted under constant current conditions. The Ti/Au electrode device has cavity length $L_{DFB}$ of 50 μm, passive waveguides for output at both sides and the threshold current $I_{th}$ of 0.2 mA. The Au/Zn/Au electrode device has a cavity length $L_{DFB}$ of 100 μm, one output of passive waveguide and the other side cleaved facet and threshold current $I_{th}$ of 0.73 mA. The Ti/Au and Au/Zn/Au electrode devices were biased with the current densities $J_{th}$ of 2.5 kA/cm$^2$ (1.0 mA) and 5.0 kA/cm$^2$ (3.0 mA), respectively. The bias current density was chosen to as high a current as possible without thermal roll-off of output power occurring. Figure 4.40 and Figure 4.41 show *L-I* and *I-V* curves of Ti/Au and Au/Zn/Au electrode devices, respectively, where solid lines indicate those before the aging test and dashed lines indicate those after 310 hour aging test. As can be seen, the threshold currents of both devices were not degraded. As for the Ti/Au device, the drive voltage was increased and the external differential quantum efficiency was decreased from 5.4% to 4.8% after the aging. The Au/Zn/Au device showed a slight decrease of voltage and no degradation of the

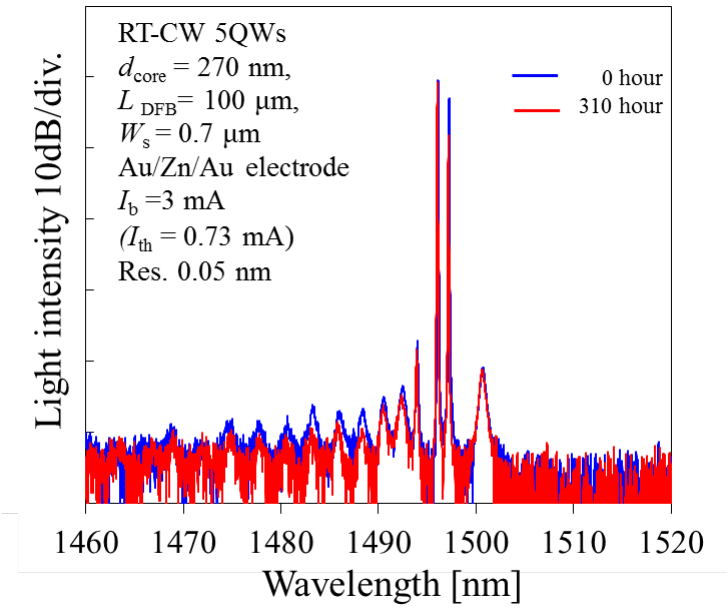


**Figure 4.42** Lasing spectra of Au/Zn/Au electrode device before and after 310 hours aging test.

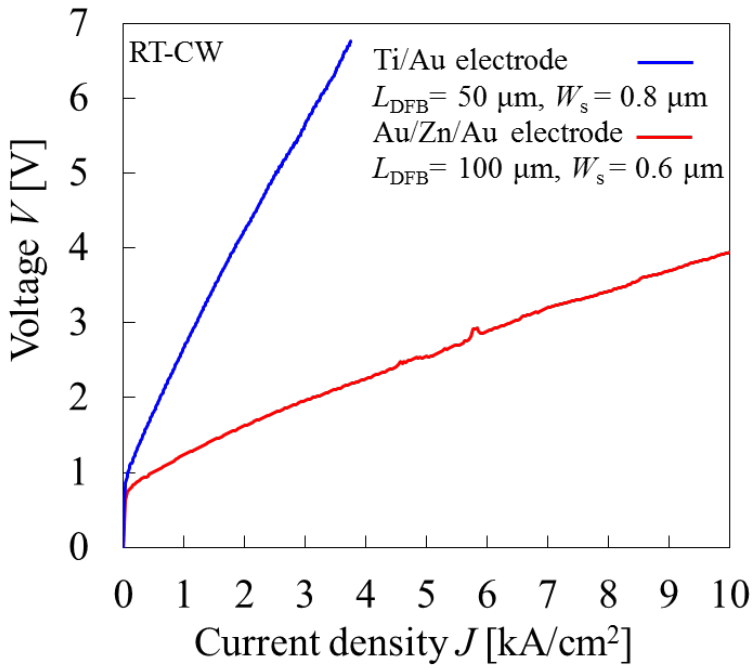


**Figure 4.43** Comparison of current versus voltage characteristics between the devices with different p-side electrode metals.

external differential quantum efficiency. In addition, the output power did not change up to the thermal roll-off region. The detailed transition of characteristics with aging time are described later. Figure 4.42 shows the lasing spectra of Au/Zn/Au electrode device before and after 310 hours aging test. There was no mode hopping before and after the aging test. The slight wavelength shift was attributed to the difference of heat dissipation to the heat sink.

Figure 4.43 shows a comparison of *J*-*V* characteristics between the devices with two different *p*-side electrodes. Current density was chosen as the x-axis because these devices had different cavity lengths. The differential resistance of the Au/Zn/Au electrode device was approximately one-fifth of that of the Ti/Au electrode device. In addition, the specific contact resistance of the Au/Zn/Au electrode device was measured to be $3.2 \times 10^{-6}$ Ω·cm$^2$ from transmission line model (TLM) measurements, while it was $5.4 \times 10^{-3}$ Ω·cm$^2$ for the Ti/Au electrode device. Secondary ion mass spectrometry (SIMS) performed on the

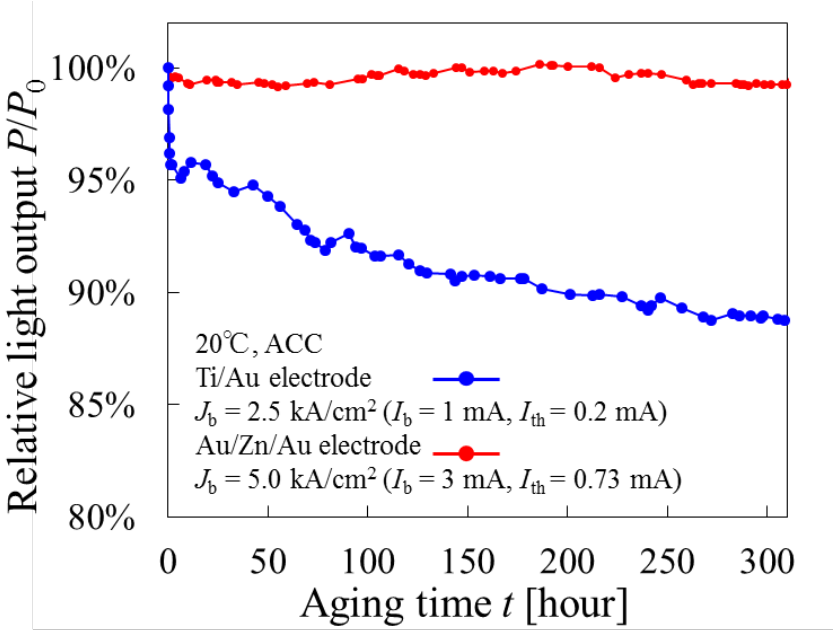


**Figure 4.44** Aging characteristics of the light output normalized by initial values.

substrate after *p*-InP regrowth shows Si atoms, which acted as *n*-type dopant, at the interface between the contact $p^{++}$-GaInAs layer and regrown *p*-InP [3]. The sources of the Si atoms were considered to be surface treatment before regrowth or contamination in the OMVPE reactor [4]. The *I-V* characteristics of the Au/Zn/Au electrode device were improved by the diffusion effect of the semiconductor and metal species during the annealing process [5]. Figure 4.44 shows the relative light output power normalized by the initial output power of the two DFB lasers during the aging test. This aging time is sufficient to observe the rapid degradation of lasers [6-8]. The light output of the Ti/Au electrode device decreased to 89% of the initial value after 310 hours. The degradation of the light output *P* can be approximated by the following relationship [9],

$$P = P_o \exp(-\frac{t}{T}) \tag{4.3}$$

where $P_0$ is the initial value of the light output, *t* is the aging time, and *T* is a fitting

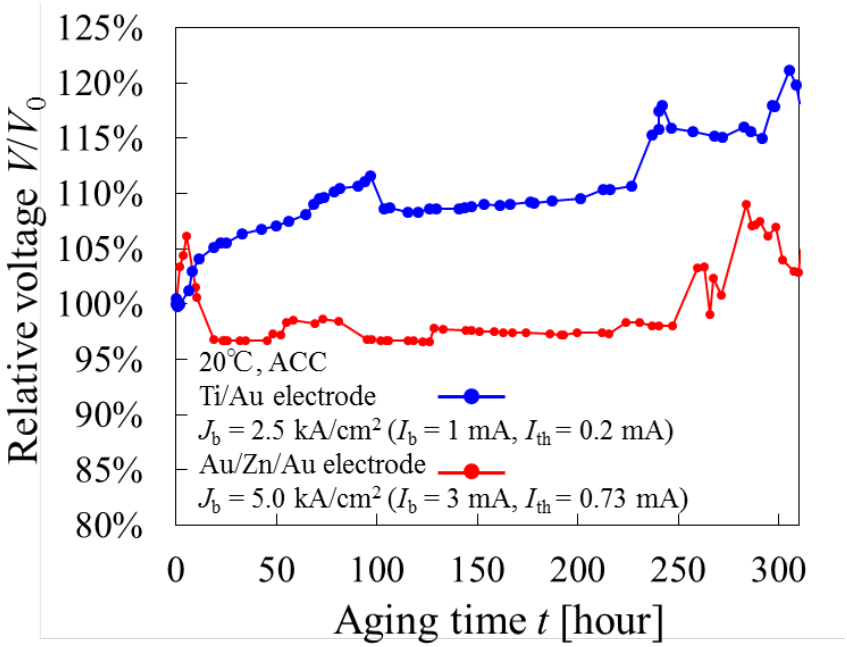


**Figure 4.45** Aging characteristics of the voltage normalized by initial values.

constant. The fitting results gave an estimation of $T$ for the Ti/Au device of 3310 hours. By contrast, the Au/Zn/Au electrode device showed no significant degradation in light output up to 310 hours, even though higher bias current density than the Ti/Au electrode device was injected. The fluctuation in light output was within 1% during the measurement. The time constant $T$ for the Au/Zn/Au electrode device could not be defined because degradation was not observed. Figure 4.45 shows the relative voltage normalized by the initial voltage of the two DFB lasers during the aging test. The voltage of the Ti/Au electrode device increased to 120% of the initial value. The voltage of the Au/Zn/Au electrode device showed constant value in the range from 23 to 247 hour. The voltage variation after 247 hour seems to be originated from the instability of needle probe contact. It is well known that Au/Zn/Au electrodes cause faster degradation of contacts than Ti/Au electrodes owing to Au diffusion into the semiconductor [10]. However, the membrane structure has lateral current injection structure, which gives a different diffusion profile compared with conventional vertical injection type lasers. This has a major impact on the reliability of the membrane DFB laser in this experiment. In

conclusion of this subsection, preliminary reliability of membrane DFB laser bonded on a Si substrate was measured. The device with alloyed Au/Zn/Au *p*-side electrode had better voltage characteristics than the device with non-alloyed Ti/Au p-side electrode device, and showed reliable operation up to 310 hours. The membrane DFB laser fabricated by multi-regrowth and BCB bonding showed no tendency of degradation of threshold current during the aging test.

## 4.5 Dynamic characteristics of membrane DFB laser

The modulation characteristics of membrane DFB lasers are investigated. In section 4.5.1, to measure the intrinsic modulation capability of membrane DFB laser, relative-intensity-noise (RIN) measurement is performed to measure the relaxation oscillation frequency $f_r$. Small signal modulation measured the frequency response characteristics and 3dB bandwidth of the membrane DFB laser. From the fitting curves, the slope of the $f_r$ as a function of bias current so-called modulation efficiency is obtained. In section 4.5.3, large signal modulation of membrane DFB laser is performed. The eye diagrams and bit-error-rate characteristics are measured.

### 4.5.1 Relative intensity noise (RIN) measurement

Relative Intensity Noise (RIN) is noise component contained in continuous-wave laser output. RIN is used as an evaluation index of the noise characteristic of the optical signal itself. Since the peak frequency of the RIN spectrum is corresponds to the relaxation oscillation frequency $f_r$, we can estimate the slope efficiency of the relaxation oscillation frequency as a function of square root of the bias current above the threshold ($I_b$-$I_{th}$). Using this method, intrinsic modulation bandwidth of the laser can be estimated without being affected by the electrical bandwidth limitation. Frequency dependence of RIN can be derived by solving rate equation (4.4) (4.5) including Langevin noise by small signal analysis.

$$\frac{dS}{dt} = \left(\xi v_g g(N,S)\right)S + \frac{\xi R_{sp}}{V_a} + F_S(t) \tag{4.4}$$

$$\frac{dN}{dt} = \frac{I}{qV_a} - \frac{n}{\tau_s} - v_g g(N,S)S + F_N(t) \tag{4.5}$$

Solving this equations, RIN($f$) is expressed as equation (4.6) [11].The $f_r$ is obtained by fitting coefficients of $A$, $B$, $\omega_0$ and $\Gamma_0$ in equation (4.7) to the measured spectrum.

$$RIN(f) = \frac{2\xi R_{sp}}{SV_a} \frac{\omega^2 + \Gamma_n^2 + \left(v_g g_n S + \frac{1}{V_a}\frac{dR_{sp}}{dN}\right)^2 \left(1 + \frac{\xi N}{R_{sp}\tau_s S}\right) - 2\Gamma_n \left(v_g g_N S + \frac{1}{V_a}\frac{dR_{sp}}{dN}\right)}{(\omega^2 - \omega_0^2)^2 + \omega^2\Gamma_0^2} \quad (4.6)$$

$$= \frac{A + B\omega^2}{(\omega^2 - \omega_0^2)^2 + \omega^2\Gamma_0^2} \quad (4.7)$$

where, $S$ is photon density, N is carrier density, $F_s(t)$, $F_n(t)$ are Langevin noises, $g(N, S)$ is optical gain, $R_{sp}$ is spontaneous emission coupling factor, $I$ is injection current, $V_a$ is active region volume, $\xi$ is optical confinement factor, $\tau_s$ is carrier life time, $\tau_{ph}$ is photon life time and $v_g$ is group velocity.

$$\Gamma_s = \frac{\Gamma R_{sp}}{SV} - \Gamma v_g g_s S \quad (4.8)$$

$$\Gamma_N = v_g g_n S + \frac{d}{dN}\left(\frac{N}{\tau_s}\right) \quad (4.9)$$

To measure the RIN, average photocurrent and included noise power should be specified.

$$\text{RIN} = \frac{<\Delta P^2>}{<P^2>} \quad (4.10)$$

$$= \frac{<\text{Noise of average optical power density}>^2}{<\text{Average optical power density}>^2} \quad (4.11)$$

$$= \frac{<\text{Noise current density}>^2}{<\text{Average photocurrent}>^2}\,[\text{dB/Hz}] \quad (4.12)$$

However, direct measurement of the laser intensity noise is inhibited by measurement system noise. Figure 4.46 shows the principle of RIN measurement system. The system has three noise sources of laser intensity noise $I_{laser}$, shot noise $I_q$ and thermal noise $I_{thermal}$. The shot noise is generated at p-i-n PD and proportional to the photocurrent. The thermal noise comes from the low-noise amplifier (LNA) and RF spectrum analyzer. The measurement procedure is as follow;

(1) Measuring thermal noise spectrum by RF spectrum analyzer without laser light input.

(2) Measuring shot noise from average photocurrent of p-i-n PD by digital multimeter with laser light input.

(3) Measuring the noise spectrum of the laser by spectrum analyzer and obtaining total system noise including all noise factors.

(4) Calculating the laser intensity noise $I_{laser}$ using following relation;

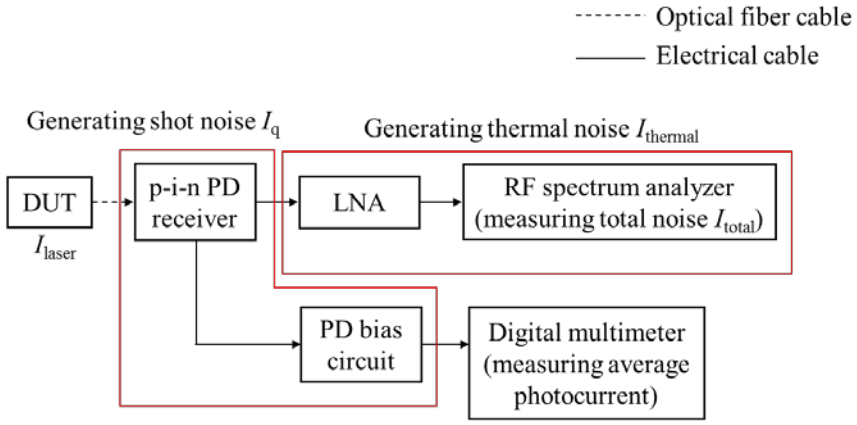


**Figure 4.46** Measurement principle of laser RIN spectrum.

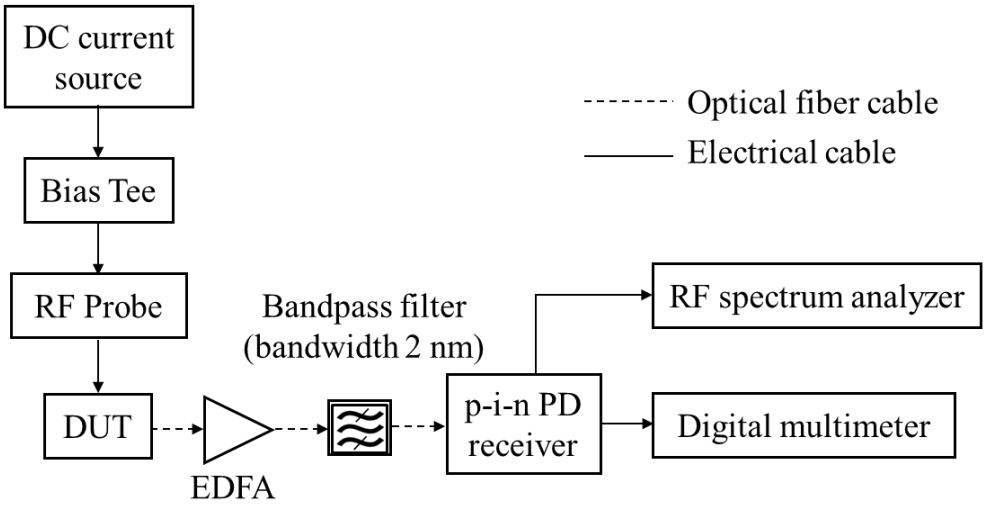


**Figure 4.47** Measurement setup for RIN measurement.

$$I_{laser} = \frac{I_{\text{total}} - I_{\text{thermal}}}{\text{gain}} - I_{\text{shot}} \tag{4.13}$$

Figure 4.47 shows the measurement setup for RIN measurement. The continuous current was injected to the device-under-test (DUT) via a 20-GHz high-speed GS probe. The optical output signal from the DUT was collected via a spherical-lensed single-mode fiber. The collected optical signal was amplified using an erbium-doped fiber amplifier (EDFA) with noise figure of approximately 4dB to obtain receivable optical power by the p-i-n photoreceiver. Bandpass filter with bandwidth of 2 nm was inserted to eliminate the amplified spontaneous emission (ASE). The DC component of detected power was

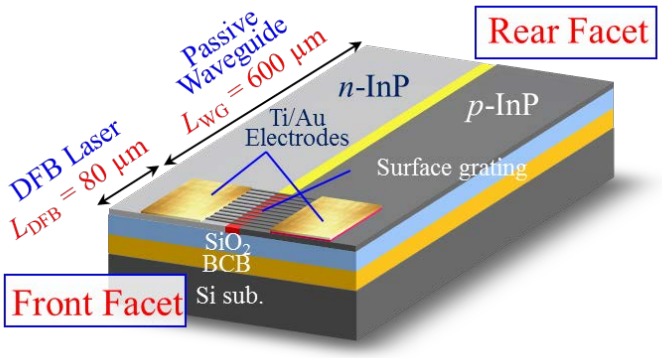


**Figure 4.48** Measured device structure of membrane DFB laser.

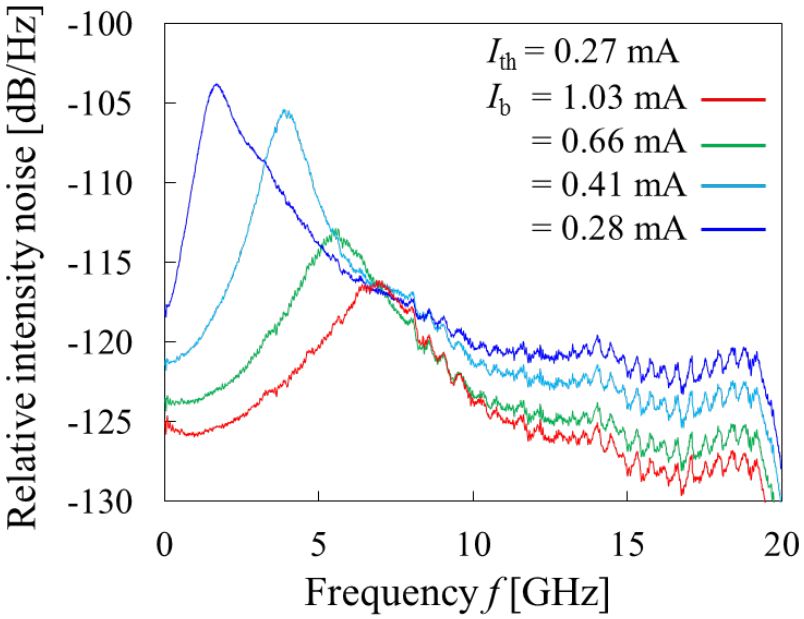


**Figure 4.49** RIN spectra of membrane DFB laser for various bias current conditions.

measured by the digital multimeter. The RF component of detected signal was analyzed by RF spectrum analyzer. Figure 4.48 shows the schematic of measured membrane DFB laser. The device has cavity length of 80 μm with a cleaved facet at the front side of the active region. The stripe width of the active region is 0.7 μm. The both side of electrodes are Ti/Au electrode. The threshold current $I_{th}$ is 0.27 mA. Figure 4.49 shows RIN spectra for various bias currents measured at room temperature. It was observed that the peak frequency shifted as increasing bias current. The RIN peak intensity at a bias current of

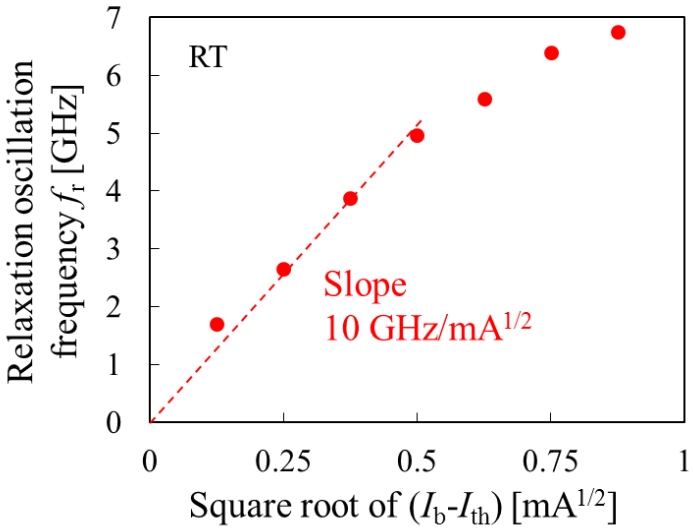


**Figure 4.50** Plots of relaxation oscillation frequency versus square root of bias current obtained from RIN measurement.

1.03 mA was 116 dB/Hz. Typically, RIN intensity below 140 dB/Hz is required to achieve good signal quality transmission. Although this measurement setup including the ASE noise from the EDFA, to suppress the RIN intensity, higher bias current and prevent back reflection from the waveguide facet are needed. Figure 4.50 shows the plots of relaxation oscillation frequency $f_r$ as a function of the square root of the bias current above the threshold. From linear fitting of measured plots, the slope of the relaxation oscillation frequency of 10 GHz/mA$^{1/2}$ is obtained. This modulation efficiency of $f_r$ is significant high value compared with typical DFB lasers thanks to the small active volume of 1.68 μm$^3$. The derailed comparison will be given a next subsection 4.5.2.

### 4.5.2 Small signal modulation

Small-signal modulation of a membrane DFB laser was performed using vector-network analyzer (VNA). The VNA is an instrument that measures the frequency response of the transmission and reflection amplitude and the phase in a high frequency electrical network. S-parameters of the device or circuit are identified for each frequency. The frequency response $S_{21}$ of semiconductor laser can be measured by directly modulating


**Figure 4.51** Vector Network Analyzer(Anritsu 37397C,40 MHz-65 GHz).

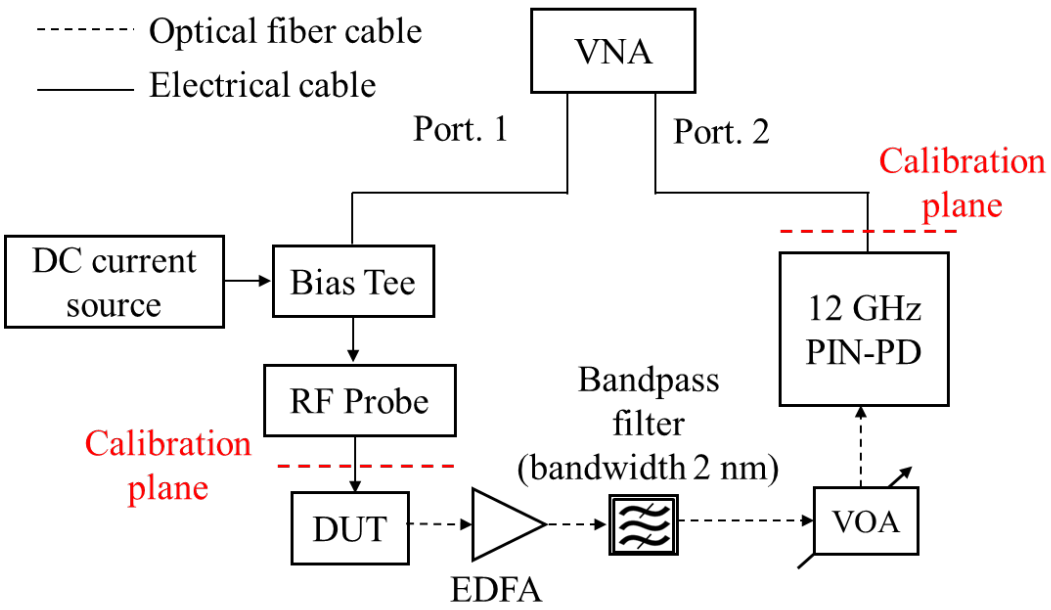


**Figure 4.52** Measurement setup for small-signal modulation.

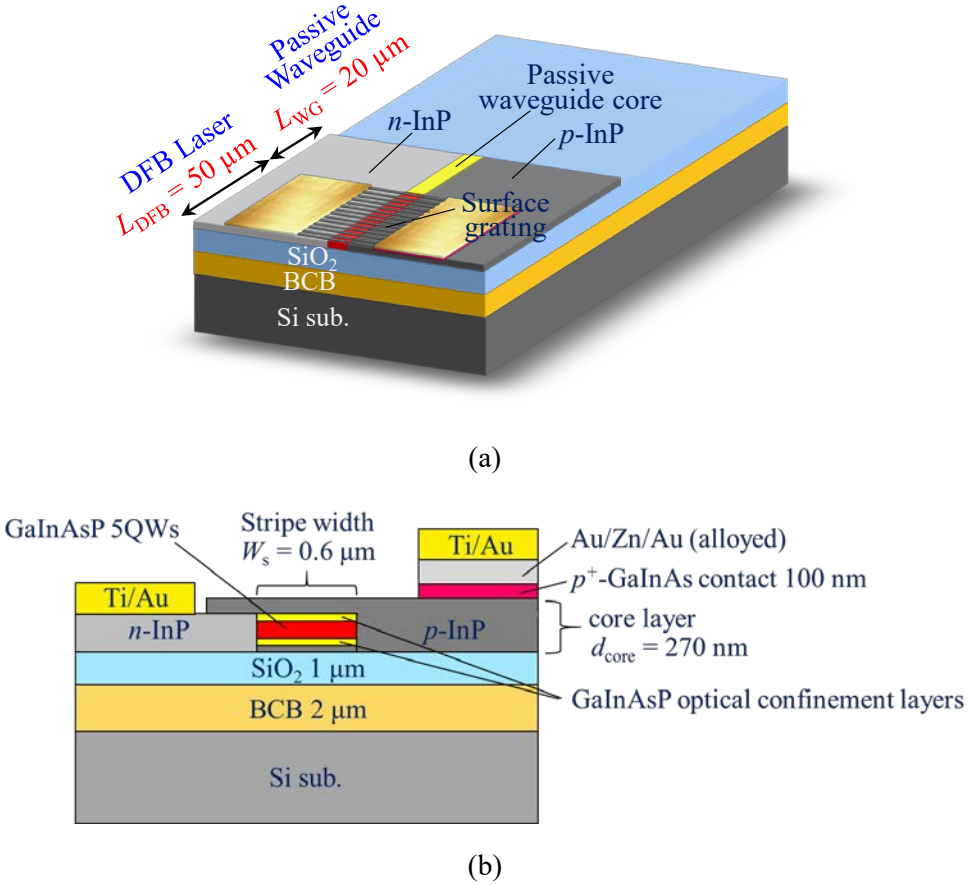


**Figure 4.53** Device structure of membrane DFB laser for small-signal modulation.

the laser with test signal from VNA. Figure 4.51 shows the Anritsu 37397C VNA used in this measurement. The microwave frequency from 40 MHz to 65 GHz is available. The measurement setup for small-signal measurement is depicted in Figure 4.52. Ports 1 of the VNA is connected to bias-tee. A DC current source is supplied to a bias-tee. A DC-coupled modulation signal is applied to the DFB laser via a 100-μm-pitch ground-signal (GS) RF probe (Cascade Microtech ACP40). The modulated optical signals are transmitted via optical fibers. The optical signal is amplified by an EDFA (Alnair Labs Corp., LNA-220) to compensate the small output power of the DUT. The ASE light is filtered by bandpass filter with bandwidth of 2 nm (Santec, OTF-350). A 12-GHz-bandwidth p-i-n PD (Discovery Semiconductors, Inc., DSC50S-69-FC/UPC-K-2) converts the optical signal to the electrical signal. The RF component of the detected

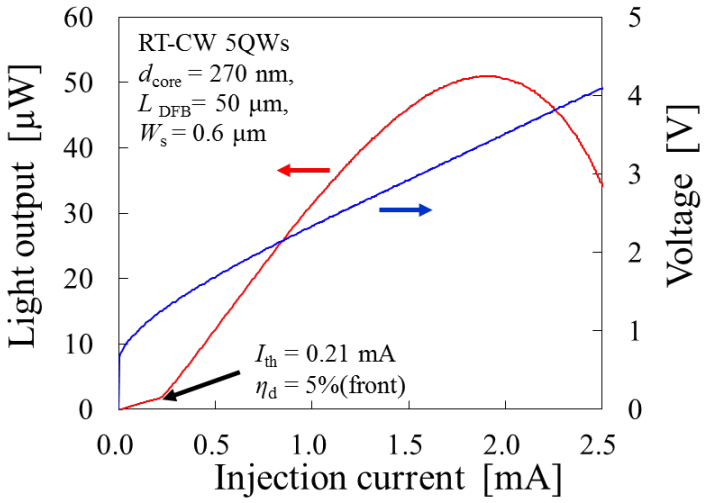


**Figure 4.54** Light output and voltage versus injection current characteristics of the membrane DFB laser for small-signal modulation.

signal is input to Port 2 of the VNA. The DUT chip is put on a heat sink, that temperature is controlled at 20 °C. Full 1-2 port calibration is performed before measuring the device, whose calibration plane is indicated by red dashed lines in Figure 4.52. Therefore, the contribution of measurement system is excluded from the results.

A schematic illustration showing the structure of the fabricated membrane DFB laser is presented in Figure 4.53(a). The cavity length of the DFB laser is 50 μm. The device has a 20-μm-long passive waveguide on the rear side, which is prepared to integrate a photodiode. The front side facet was cleaved and the rear side facet was formed by mechanically removing the bonded semiconductor layer. The both facets have no optical coatings. The period of the surface grating formed on the active region is $\Lambda$ = 295 nm. Figure 4.53(b) shows a cross-section of the active region. The stripe width of the active layer is 0.6 μm. This device has alloyed Au/Zn/Au of 25/50/300 nm thickness as *p*-side electrode to improve the *p*-side contact characteristics. Advance to the modulation measurement, the static characteristics of the membrane DFB laser are measured under room-temperature (20 °C) CW conditions. Figure 4.54 shows light output and the voltage versus injection current characteristics. The threshold current $I_{th}$ was 0.21 mA, and the threshold current density $J_{th}$ was 140 A/cm$^2$/well. The external differential quantum efficiency $\eta_d$ was 5% (front facet). The operating voltage was reduced to approximately

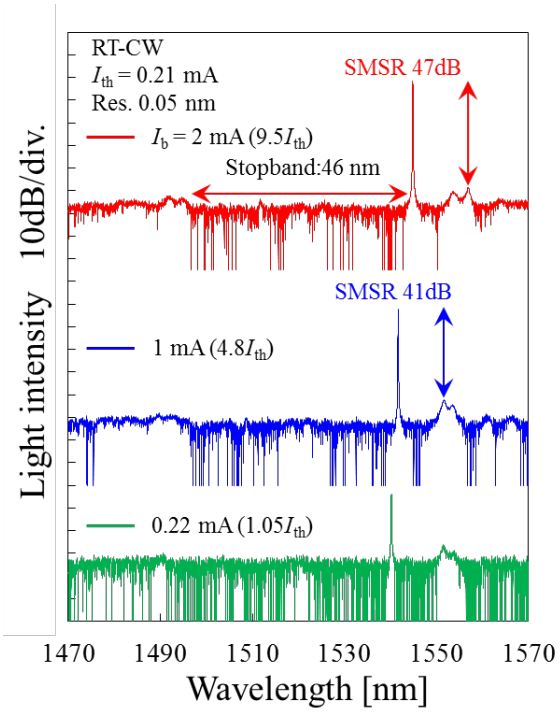


**Figure 4.55** Lasing spectra of the membrane DFB laser for small-signal modulation measured for three different bias current conditions.

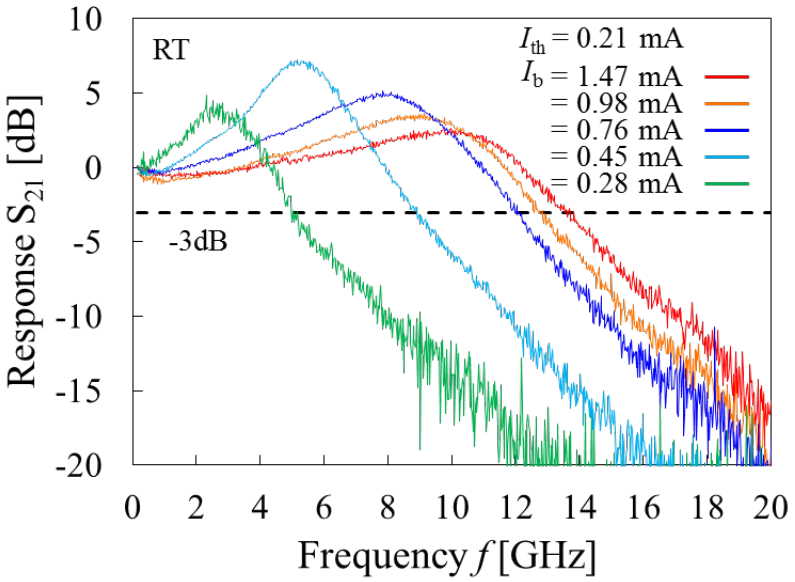


**Figure 4.56** Small signal modulation responses of $S_{21}$ measured for various bias current conditions.

half of that for the same device length with Ti/Au electrode as shown in Figure 4.28. Figure 4.55 shows lasing spectra measured for different bias currents. Stable single-mode operation was observed for a bias current up to 2 mA, after which the light output showed

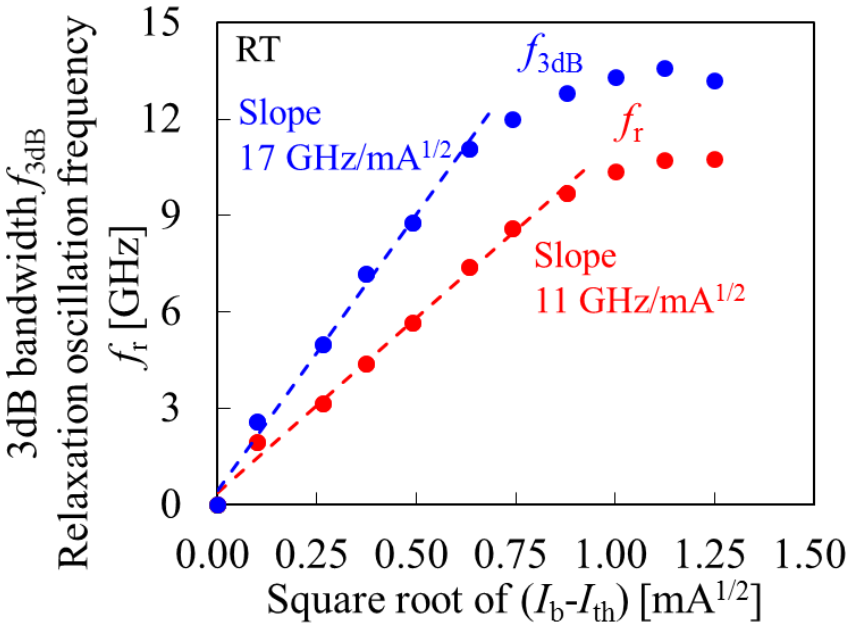


**Figure 4.57** Plots of relaxation oscillation frequency $f_r$ and 3dB bandwidth $f_{3dB}$ versus square root of bias current above threshold.

a thermal roll-off. The lasing wavelength was 1542 nm at bias current of 1.0 mA. The values of SMSR were 41 dB and 47 dB at bias currents of 1.0 mA and 2.0 mA, respectively. From the lasing spectrum at the bias current of 2 mA, a stopband width was determined by measuring the wavelength span where a level of the spontaneous emission intensity was much lower than the noise level of the spectrum analyzer (Ando (currently Yokogawa), AQ6317B). Based on the theory of emission spectrum of the DFB laser [12], the obtained stopband width of 46 nm corresponded to an index-coupling coefficient of 2100 cm$^{-1}$. The mode span of the spectrum was different from that of calculated spectrum. It can be attributed to facet phase of front and rear facets because both facets had no AR coatings.

The small-signal responses ($S_{21}$) of the membrane DFB laser measured at various injection currents from 0.28 to 1.47 mA are shown in Figure 4.56. Because the 3dB bandwidth of 12.8 GHz was obtained at 0.98-mA bias current, 10 Gbit/s operation was considered to be possible with a bias current below 1.0 mA. The maximum 3-dB bandwidth of 13.6 GHz was obtained at a bias current of 1.47 mA. The $f_r$ of the laser was obtained by fitting the measured response curve to theoretical three-pole transfer function

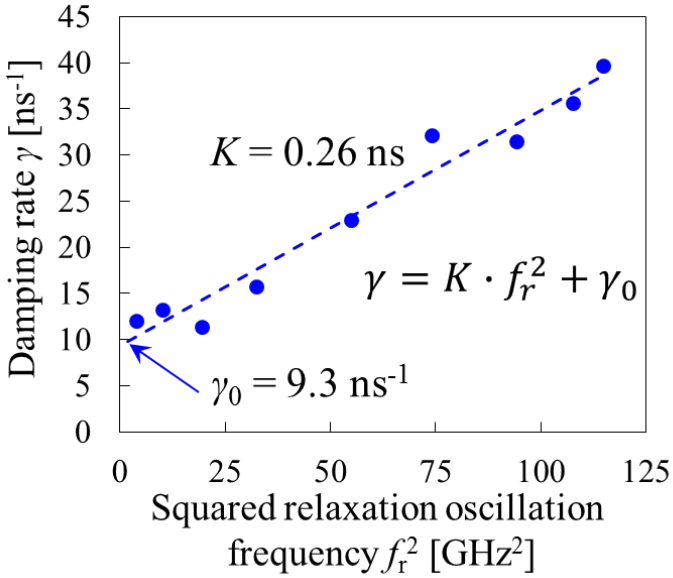


**Figure 4.58** Damping factor as a function of the squared relaxation oscillation frequency.

as follows;

$$|M(f)|^2 = \frac{1}{1+(2\pi f\tau)^2}\frac{f_r^4}{(f^2-f_r^2)+(\frac{f\gamma}{2\pi})^2} \tag{4.14}$$

where $\tau$ is the delay constant including the contributions of carrier transmit time, carrier capture time at the quantum wells and *RC* bandwidth. Figure 4.57 shows relaxation oscillation frequency $f_r$ and 3-dB bandwidth $f_{3dB}$ as a function of the square root of bias current above the threshold. The modulation efficiencies for $f_r$ and $f_{3dB}$ are 11 GHz/mA$^{1/2}$ and 17 GHz/mA$^{1/2}$, respectively. The damping rate was also extracted from the small-signal responses. Figure 4.58 shows the plots of damping rate versus squared relaxation oscillation frequency. The *K*-factor and intrinsic damping offset $\gamma_0$ were obtained from the linear fitting of the plots as following equation;

$$\gamma = K \cdot f_r^2 + \gamma_0 \tag{4.15}$$

As a result from Figure 4.58, the *K*-factor and offset $\gamma_0$ were 0.26 ns and 9.3 ns$^{-1}$, respectively. The maximum intrinsic bandwidth, $f_{3dB,\,max}$ is given by [13, 14];

$$f_{3dB,max} = \frac{2\sqrt{2}\pi}{K} \tag{4.16}$$

The obtained *K*-factor corresponds to an intrinsic maximum bandwidth, neglecting the

self-heating and parasitic cutoff, of 34 GHz. The relaxation oscillation frequency of the device shown in Figure 4.57 seems to be saturated by heating. This can be solved by reducing the electrical resistance as well as thinning BCB layer thickness to reduce thermal resistance. Reducing resistance and parasitic capacitance is also important to increase total bandwidth. The modulation efficiency of $f_r$ was also extracted from the device with different active volume. Table 4.11 shows the structural differences of measured devices. The device with $V_a$ of 1.68 μm$^3$ had a Ti/Au *p*-side electrode and 2.0 μm-thick BCB layer. The device with $V_a$ of 0.90 μm$^3$ had a Au/Zn/Au *p*-side electrode and 2.0 μm-thick BCB layer. The device with $V_a$ of 0.77 μm$^3$ had a Au/Zn/Au *p*-side electrode and 0.5 μm-thick BCB layer. These differences affect the self-heating properties of the laser. Therefore the structural differences only affect the maximum value of $f_r$, and the modulation efficiency does not depends on these difference. Figure 4.59 shows the comparison of modulation efficiency of $f_r$ for devices with three different active volume of 1.68 μm$^3$, 0.90 μm$^3$ and 0.77 μm$^3$. According to the section 2.3.2, modulation efficiency is proportional to inverse of square root of cavity volume, which was assumed to be as same as active volume in this structure, $1/(V_a)^{1/2}$. Table 4.12 summarizes the active volume, ratio of active volume normalized by 1.68 μm$^3$, modulation efficiency and ratio of modulation efficiency normalized by 9.9 GHz/mA$^{1/2}$ for three devices. It was confirmed that the modulation efficiency increased as the active volume decreased as expected from the fundamental relation. However the obtained modulation efficiencies were lower than expected from the ratio of active volume. This is because the modulation efficiency depends on not only the active volume but also the threshold current density. The most right column of Table 4.12 shows threshold current density for each device. Increased threshold current density weaken the effect of scaling of modulation efficiency. Suppressed threshold current density for small active volume structure will lead to further enhancement of modulation efficiency.

**Table 4.11** Structural difference of measured devices.

| Active volume | *p*-side electrode | BCB thickness |
|---|---|---|
| $V_a$ = 1.68 μm$^3$ | Ti/Au | 2.0 μm |
| $V_a$ = 0.90 μm$^3$ | Au/Zn/Au | 2.0 μm |
| $V_a$ = 0.77 μm$^3$ | Au/Zn/Au | 0.5 μm |

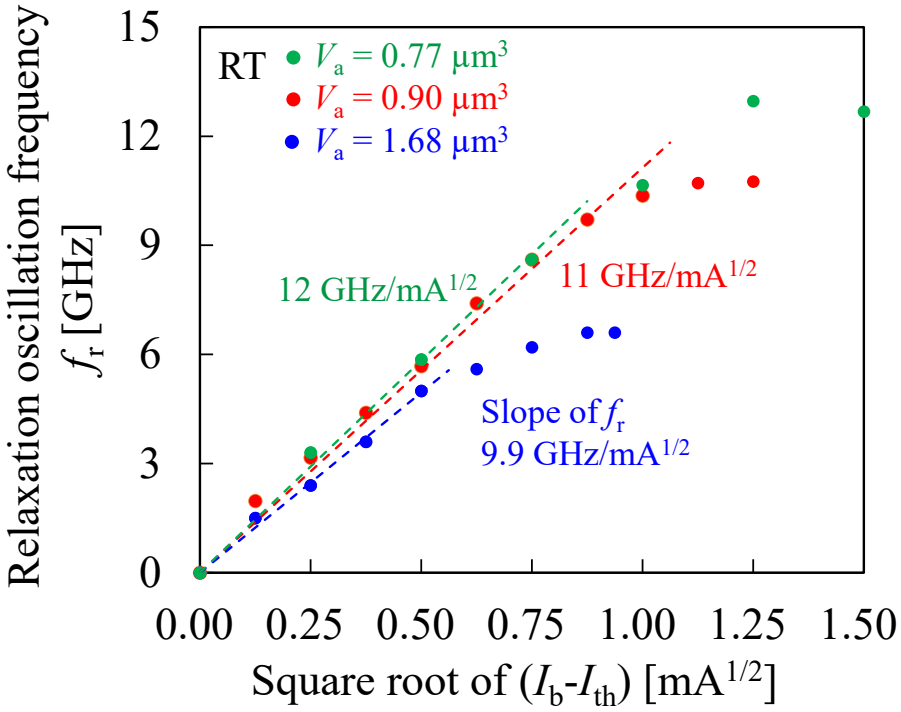


**Figure 4.59** Comparison of modulation efficiency of $f_r$ for devices with three different active volume of 1.68 μm$^3$, 0.90 μm$^3$ and 0.77 μm$^3$.

**Table 4.12** Ratio of active volume $V_a$ and modulation efficiency

| Active volume | Ratio of $1/V_a^{1/2}$ ( (1.68 μm$^3$ / $V_a$ )$^{1/2}$) | Modulation efficiency | Ratio of modulation efficiency ( modulation efficiency / 9.9 GHz/mA$^{1/2}$ ) | Threshold current density for 5QW |
|---|---|---|---|---|
| $V_a$ = 1.68 μm$^3$ | 1.00 | 9.9 GHz/mA$^{1/2}$ | 1.00 | 480 A/cm$^2$ |
| $V_a$ = 0.90 μm$^3$ | 1.36 | 11 GHz/mA$^{1/2}$ | 1.11 | 700 A/cm$^2$ |
| $V_a$ = 0.77 μm$^3$ | 1.47 | 12 GHz/mA$^{1/2}$ | 1.20 | 820 A/cm$^2$ |

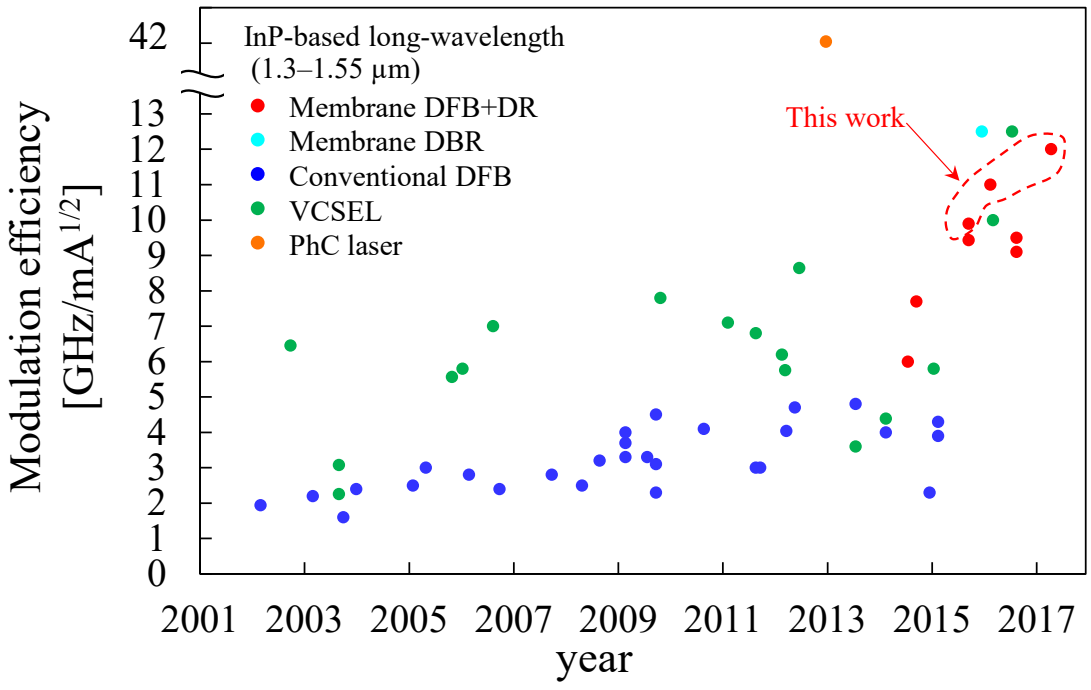


**Figure 4.60** Trend of the modulation efficiency of InP-based long wavelength (1.3–1.55 μm) DFB lasers, DBR lasers, DR lasers, VCSELs and PhC laser. Full-reference used in this graph is available in appendix inserted at end of this chapter.

obtained modulation efficiencies of $f_r$ are compared with that of various lasers, such as InP-based long-wavelength ($\lambda$ = 1.3–1.55 μm) conventional type DFB and DR lasers, membrane DFB, DBR and DR lasers, VCSELs and PhC laser as shown in Figure 4.60. The list of full-reference used in this graph is available in appendix 4-1 inserted at end of this chapter. The conventional DFB lasers demonstrated maximum modulation efficiencies for GaInAsP-based and AlGaInAs-based active layer devices of 3.0 GHz/mA$^{1/2}$ [15] and 4.8 GHz/mA$^{1/2}$ [16], respectively. many efforts have been paid to enhance modulation efficiency of DFB lasers mainly by optimizing quantum well structures including well number, width, strain and doping. In contrast, VCSELs demonstrated high modulation efficiency owing to their small-active volume and strong confinement DBRs cavity [17]. For membrane lasers, higher efficiencies than conventional DFB lasers have been reported [18-22]. The modulation efficiency of 9.9, 11 and 12 GHz/mA$^{1/2}$ obtained in this work is the significantly high values ever reported

to date for DFB lasers to the best of our knowledge. This is attributed to the small active volume ($V_a$ = 0.77–1.68 μm$^3$) of membrane DFB laser. We note that a much higher value of 42.4 GHz/mA$^{1/2}$ was reported for a PhC laser using a very small active volume 2.5 × 0.3 × 0.018 μm (0.0135 μm$^3$, assuming a 6-nm-thick quantum well) [23]. However, it becomes more difficult to obtain sufficient light output power for a communication with such significantly small active volume.

### 4.5.3 Eye diagrams and bit-error-rate (BER) measurement

The large signal modulation of membrane DFB laser is performed. The electrical modulating signals are generated by a pulse-pattern generator (Anritsu Signal Quality Analyzers MP1800A implementing MU181020B, and MU182021A). The bit-error-rate (BER) characteristics are measured by an error detector (Anritsu Signal Quality Analyzers MP1800A implementing MU181040B, and MU182041A). Figure 4.61 shows the appearance of these instruments. The clock signal is generated by analog-signal generator (Agilent, E8257D PSG Analog Signal Generator, 100 kHz to 67 GHz).


**Figure 4.61** MP1800A Signal Quality Analyzers implementing MU181020B, MU182021A, MU181040B, and MU182041A.

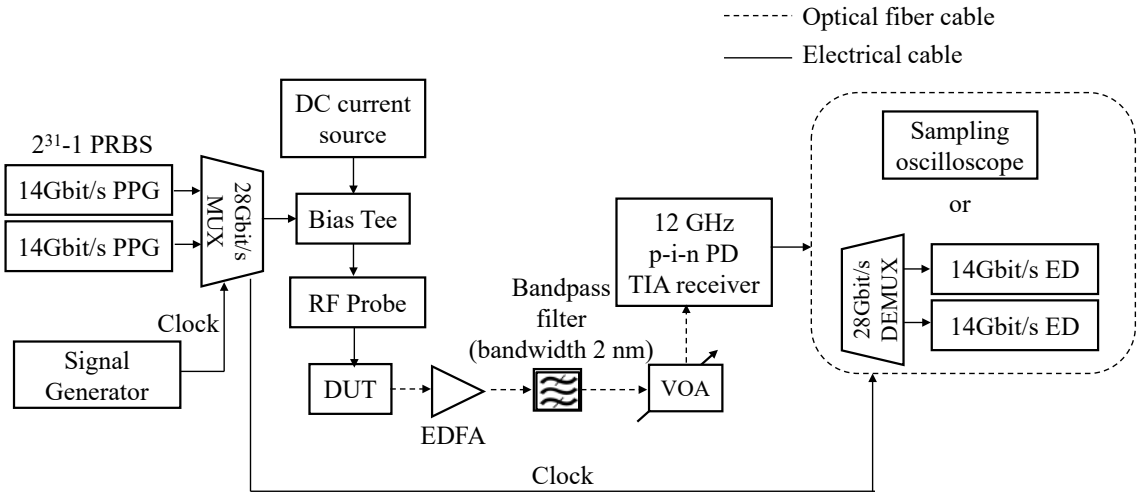


**Figure 4.62** Measurement setup for large signal modulation of membrane DFB laser.

Figure 4.62 shows the measurement setup for large signal modulation of membrane DFB lasers. Pseudo-random-bit-sequence (PRBS) signals are generated by two 14 Gbit/s PPGs and 28 Gbit/s multiplexer. Electrical modulation signals are applied to the DFB laser via a bias-tee and a GS probe. The optical signal of the DFB laser is collected by spherical lensed fiber. The optical signal is amplified by EDFA; then bandpass filter eliminates the ASE light. The optical power in a fiber is monitored and controlled by variable optical attenuator (VOA). The optical signal is converted to electrical signal by 12-GHz-bandwidth p-i-n PD-TIA photoreceiver (New Focus, 1544-B). The signals are recorded by a sampling oscilloscope (Agilent 86109B) to construct an eye diagram. For the BER measurement, the signals are analyzed with an error detector consists of two 14 Gbit/s error-detector and 28 Gbit/s demultiplexer.

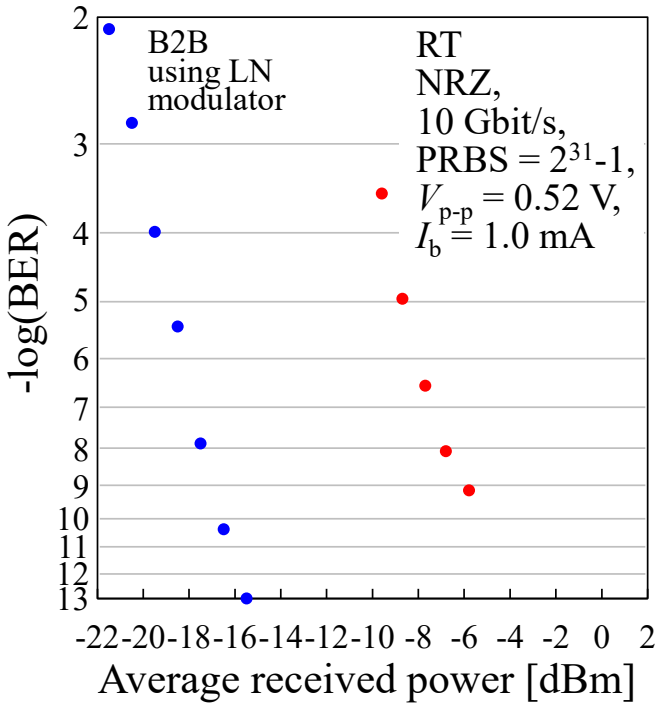


**Figure 4.63** 10 Gbit/s BER characteristics of membrane DFB laser at bias current of 1.0 mA. The blue plots shows sensitivity curve of used PD-TIA photoreciever measured by external light source and LN modulator.

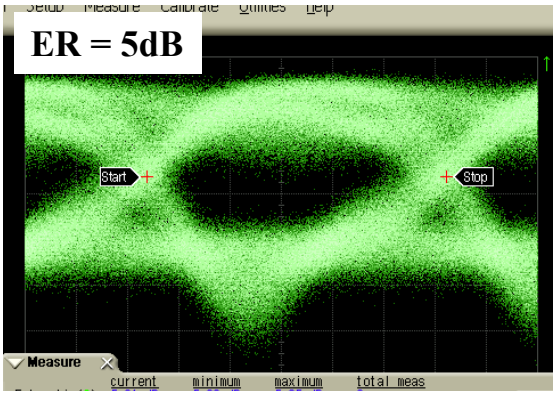


**Figure 4.64** Eye diagram of membrane DFB laser biased at 1.0 mA for 10 Gbit/s of NRZ signal using a $2^{31}$-1 pattern.

The measured device is same one as shown in Figure 4.53. The measured membrane DFB laser has the cavity length of 50 μm and the threshold current of 0.21 mA. A data signal of non-return-to-zero (NRZ) with a PRBS having a word length of $2^{31}$-1 was transmitted. First, the modulation characteristics under the condition with low-bias current of 1.0 mA

was measured. Figure 4.63 shows the BER characteristics of the membrane DFB laser at a data rate of 10 Gbit/s as a function of the averaged received optical power. The blue plots shows the sensitivity curve of used PD-TIA photoreciever measured by external light source and LN modulator (COVEGA, Mach-40$^{TM}$005). The modulation voltage swing to the laser was set to 0.52 $V_{pp}$. The BER of less than $1\times10^{-9}$ was achieved at an averaged received power of -5.8 dBm. The difference from the sensitivity curve of the photoreciever is attributed to the use of EDFA, which degrade the SN ratio of the signal. The BER characteristic is improved if sufficient light output power is obtained without using an EDFA. Figure 4.64 shows the 10 Gbit/s eye diagram measured under the same modulation conditions. The eye opening was confirmed with an extinction ratio (ER) of 5dB. To the best of our knowledge, this bias current was the lowest value used for 10 Gbit/s large-signal direct modulation of DFB laser, which was attributed to the low-threshold current and high-modulation efficiency characteristics of the membrane DFB structure. Although an error-floor appears in the BER curve, the linearity of the BER curve and eye opening are expected be improved if the external differential quantum efficiency is improved to the same value as that of a conventional DFB laser. Next, the energy cost of this experiments is calculated. The driving voltage of the laser is 2.3 V as seen in Figure 4.54 at the bias current of 1.0 mA. The energy cost per bit for data transmission can be calculated by the product of bias current and voltage divided by the data rate as following relation;

$$\text{Energy cost} = \frac{I_{\text{b}} V_{\text{b}}}{\text{Data} - \text{rate}} \tag{4.17}$$

According to this relationship, the energy cost in this modulation is calculated to be 230 fJ/bit. This energy cost is small in comparison to a conventional DFB laser, but still high value to the target of 100 fJ/bit. This is caused by a relatively high driving voltage of 2.3 V because of the differential resistance of 1.2 kΩ. It is expected that the differential resistance can be reduced to 200 Ω by reducing the distance between the p-side electrode and the active stripe, thereby resulting in a driving voltage of approximately 1 V at 1.0 mA

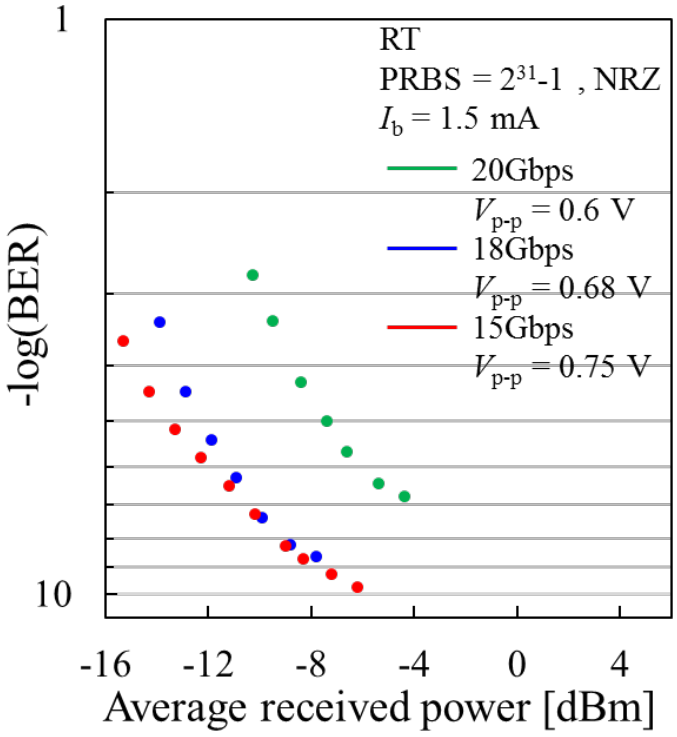


**Figure 4.65** BER characteristics of membrane DFB laser at bias current of 1.5 mA for various data-rate signals.

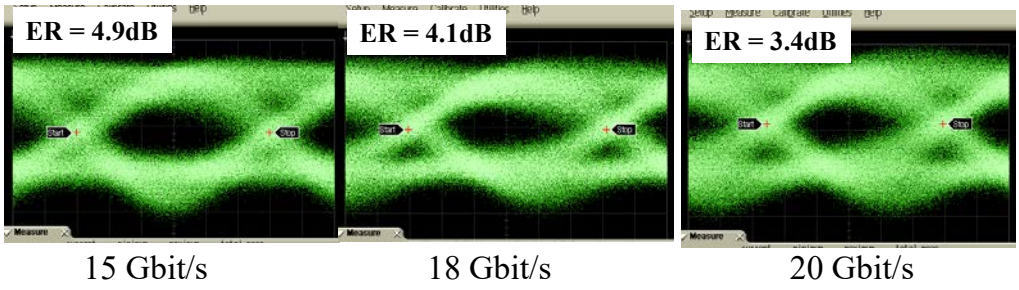


**Figure 4.66** Eye diagrams of membrane DFB laser biased at 1.5 mA for 10 Gbit/s, 15 Gbit/s and 20 Gbit/s of NRZ PRBS = $2^{31}$-1 pattern signal.

bias current.

Subsequently, large-signal modulation characteristics of the same device was investigated by applying higher bias current. Figure 4.65 shows the BER characteristics of membrane DFB laser at the bias current of 1.5 mA measured for data-rate of 15 Gbit/s, 18 Gbit/s and 20 Gbit/s. The bit-error in the order of $10^{-9}$ was obtained up to 18 Gbit/s operation. Figure 4.66 shows the eye diagrams of membrane DFB laser biased at 1.5 mA

for 10 Gbit/s, 15 Gbit/s and 20 Gbit/s of NRZ signal using a PRBS of $2^{31}$-1 pattern. The values of extinction ratio of these eye were 4.9dB, 4.1dB and 3.4 dB for 10 Gbit/s, 15 Gbit/s and 20 Gbit/s signals, respectively. In 20 Gbit/s operation, degradation of extinction ratio caused the poor BER characteristics. For the higher data-rate modulation, further bandwidth improvement as well as more output power are required.

## 4.6 Conclusion

This chapter described the fabrication and characterization of membrane DFB lasers with BJB integrated waveguide. Grating formation process is established so as to obtain smooth etched profiles. Membrane DFB lasers on a Si substrate with a short cavity and strong index-coupling coefficient was fabricated. A record-low threshold current of 0.23 mA was obtained under RT-CW condition. Preliminary reliability test of membrane DFB laser bonded on a Si substrate was investigated. The device with a p-side Au/Zn/Au electrode had better voltage characteristics than the device with a Ti/Au p-side electrode device. The device with Au/Zn/Au electrode showed reliable operation up to 310 hours. As a modulation characteristics, 3dB bandwidth of 12.8 GHz at a bias current of 0.98 mA, and a modulation efficiency of 11 GHz/mA$^{1/2}$ were obtained. Large-signal direct modulation at 10 Gbit/s was performed using an NRZ signal with PRBS = $2^{31}$-1, and a BER less than $1\times10^{-9}$ was achieved with bias current of 1.0 mA. The energy cost for this modulation was calculated to be 230 fJ/bit.

# References

[1] Y. Atsuji, K. Doi, T. Hiratani, D. Inoue, J. Lee, Y. Atsumi, *et al.*, "Low-threshold-current operation of membrane distributed-feedback laser with surface grating bonded on Si substrate," *Japanese Journal of Applied Physics,* vol. 54, p. 080301, 2015.

[2] D. Inoue, J. Lee, K. Doi, T. Hiratani, Y. Atsuji, T. Amemiya, *et al.*, "Room-temperature continuous-wave operation of GaInAsP/InP lateral-current-injection membrane laser bonded on Si substrate," *Applied Physics Express,* vol. 7, p. 072701, 2014.

[3] T. Hiratani, "Study of Membrane Distributed-Reflector Lasers for On-Chip Optical Interconnection," Ph. D., Department of Electrical and Electronic Engineering, Tokyo Institute of Technology, 2017.

[4] D. Knight, G. Kelly, J. Hu, S. Watkins, and M. Thewalt, "Characterization of interfacial dopant layer for high-purity InP grown by MOCVD," *Journal of crystal growth,* vol. 182, pp. 23-29, 1997.

[5] 山口章, 唐内一郎, 奥田寛, 山林直之, and 柴田雅裕, "リン化インジウム (p 型) オーミックコンタクトの界面微細構造," *分析化学* vol. 40, pp. 741-747, 1991.

[6] K. Endo, S. Matsumoto, H. Kawano, I. Sakuma, and T. Kamejima, "Rapid degradation of InGaAsP/InP double heterostructure lasers due to< 110> dark line defect formation," *Applied Physics Letters,* vol. 40, pp. 921-923, 1982.

[7] E. Omura, H. Uesugi, T. Kimura, Y. Kawama, and H. Namizaki, "Low threshold current 1.3 mu m GaInAsP lasers grown on GaAs substrates," *Electronics Letters,* vol. 25, pp. 1718-1719, 1989.

[8] T. Yamada, M. Tachikawa, T. Sasaki, H. Mori, Y. Kadota, and M. Yamamoto, "Stable CW operation of 1.3 mu m double-heterostructure laser heteroepitaxially grown on Si," *Electronics Letters,* vol. 31, pp. 455-457, 1995.

[9] O. Ueda, *Reliability and degradation of III-V optical devices*: Artech House Publishers, 1996.

[10] M. Fukuda, "Laser and LED reliability update," *Journal of Lightwave Technology,* vol. 6, pp. 1488-1495, 1988.

[11] M. Tatham, I. Lealman, C. P. Seltzer, L. Westbrook, and D. Cooper, "Resonance frequency, damping, and differential gain in 1.5 mu m multiple quantum-well lasers," *IEEE journal of quantum electronics,* vol. 28, pp. 408-414, 1992.

[12] T. Makino and J. Glinski, "Transfer matrix analysis of the amplified spontaneous emission of DFB semiconductor laser amplifiers," *IEEE journal of quantum electronics,* vol. 24, pp. 1507-1518, 1988.

[13] R. Tucker, "High-speed modulation of semiconductor lasers," *Journal of Lightwave Technology,* vol. 3, pp. 1180-1192, 1985.

[14] R. Olshansky, P. Hill, V. Lanzisera, and W. Powazinik, "Frequency response of 1.3 μm InGaAsP high speed semiconductor lasers," *IEEE Journal of Quantum Electronics,* vol. 23, pp. 1410-1418, 1987.

[15] S. Lee, D. Takahashi, T. Shindo, K. Shinno, T. Amemiya, N. Nishiyama, *et al.*, "Low-Power-Consumption High-Eye-Margin 10-Gb/s Operation by GaInAsP/InP Distributed Reflector Lasers With Wirelike Active Regions," *IEEE Photonics Technology Letters,* vol. 23, pp. 1349-1351, 2011.

[16] W. Kobayashi, T. Ito, T. Yamanaka, T. Fujisawa, Y. Shibata, T. Kurosaki, *et al.*, "50-Gb/s direct modulation of a 1.3-μm InGaAlAs-based DFB laser with a ridge waveguide structure," *IEEE Journal of Selected Topics in Quantum Electronics,* vol. 19, pp. 1500908-1500908, 2013.

[17] S. Spiga, W. Soenen, A. Andrejew, D. M. Schoke, X. Yin, J. Bauwelinck, *et al.*, "Single-Mode High-Speed 1.5-μm VCSELs," *Journal of Lightwave Technology,* vol. 35, pp. 727-733, 2017.

[18] S. Matsuo, T. Fujii, K. Hasebe, K. Takeda, T. Sato, and T. Kakitsuka, "40-Gbit/s direct modulation of

membrane buried heterostructure DFB laser on $SiO_2$/Si substrate," in *Semiconductor Laser Conference (ISLC), 2014 International*, 2014, pp. 30-31.

[19] S. Matsuo, T. Fujii, K. Hasebe, K. Takeda, T. Sato, and T. Kakitsuka, "Directly Modulated DFB Laser on $SiO_2$/Si Substrate for Datacenter Networks," *Journal of Lightwave Technology,* vol. 33, pp. 1217-1222, 2015.

[20] H. Nishi, T. Fujii, K. Takeda, K. Hasebe, T. Kakitsuka, T. Tsuchizawa*, et al.*, "Membrane distributed-reflector laser integrated with SiOx-based spot-size converter on Si platform," in *Optical Communication (ECOC), 2015 European Conference on*, 2015, pp. 1-3.

[21] T. Fujii, K. Takeda, E. Kanno, K. Hasebe, H. Nishi, R. Nakao*, et al.*, "Low operating-energy directly modulated membrane distributed-reflector lasers on Si," in *ECOC 2016; 42nd European Conference on Optical Communication; Proceedings of*, 2016, pp. 1-3.

[22] E. Kanno, K. Takeda, T. Fujii, K. Hasebe, H. Nishi, T. Yamamoto*, et al.*, "Membrane distributed-reflector lasers with 20-μm-long DFB section and front/rear DBRs on Si substrates," in *Semiconductor Laser Conference (ISLC), 2016 International*, 2016, pp. 1-2.

[23] S. Matsuo, T. Sato, K. Takeda, A. Shinya, K. Nazaki, H. Taniyama*, et al.*, "Ultra-low Operating Energy Electrically Driven Photonic Crystal Lasers," *IEEE Journal of Selected Topics in Quantum Electronics,* vol. 19, pp. 4900311-4900311, 2013.

# Appendix 4-1

# Full reference used in Figure 4.60

| year | Material | wavelength [μm ] | Institute | Modulation efficiency[GHz/mA$^{1/2}$]. | Ref. |
|---|---|---|---|---|---|
| DFB, DBR and DR lasers | | | | | |
| March , 2002 | GaInAsP | 1.3 | Alcater | 1.9 | [1] |
| March , 2003 | AlGaInAs | 1.3 | NEC | 2.2 | [2] |
| October , 2003 | AlGaInAs | 1.3 | Oki | 1.6 | [3] |
| January , 2004 | AlGaInAs | 1.3 | Hitachi | 2.4 | [4] |
| February , 2005 | AlGaInAs | 1.3 | NEC | 2.5 | [5] |
| May , 2005 | AlGaInAs | 1.3 | Opnext | 3.0 | [6] |
| March , 2006 | AlGaInAs | 1.3 | Hitachi | 2.8 | [7] |
| October , 2006 | AlGaInAs | 1.3 | Fujitsu | 2.4 | [8] |
| October , 2007 | AlGaInAs | 1.3 | Hitachi | 2.8 | [9] |
| May , 2008 | AlGaInAs | 1.3 | Fujitsu | 2.5 | [10] |
| September , 2008 | AlGaInAs | 1.3 | Fujitsu | 3.2 | [11] |
| March , 2009 | AlGaInAs | 1.3 | Finisar | 3.7 | [12] |
| March , 2009 | AlGaInAs | 1.3 | Fujitsu | 4.0 | [13] |
| March , 2009 | AlGaInAs | 1.3 | avago | 3.3 | [14] |
| August , 2009 | AlGaInAs | 1.3 | NTT | 3.3 | [15] |
| October , 2009 | AlGaInAs | 1.55 | Fujitsu | 4.5 | [16] |
| October , 2009 | AlGaInAs | 1.3 | SEI | 3.1 | [17] |
| October , 2009 | GaInAsP | 1.55 | TIT | 2.3 | [18] |
| September , 2010 | AlGaInAs | 1.3 | Mitsubishi | 4.1 | [19] |
| September , 2011 | GaInAsP | 1.55 | TIT | 3.0 | [20] |
| October , 2011 | AlGaInAs | 1.3 | Hitachi | 3.0 | [21] |
| April , 2012 | AlGaInAs | 1.3 | Fujitsu | 4.04 | [22] |

| | | | | | |
|---|---|---|---|---|---|
| June , 2012 | AlGaInAs | 1.3 | NTT | 4.7 | [23] |
| August , 2013 | AlGaInAs | 1.3 | NTT | 4.8 | [24] |
| March , 2014 | AlGaInAs | 1.3 | Oclaro | 40 | [25] |
| August , 2014 | GaInAsP | 1.55 | NTT | 6.0 | [26] |
| October , 2014 | GaInAsP | 155 | NTT | 7.7 | [27] |
| January , 2015 | GaInAsP | 1.3 | NTT | 2.3 | [28] |
| March , 2015 | AlGaInAs | 1.3 | Hitachi | 4.3 | [29] |
| March 1, 2015 | AlGaInAs | 1.3 | Mitsubishi | 3.9 | [30] |
| October , 2015 | GaInAsP | 1.55 | NTT | 9.43 | [31] |
| October , 2015 | GaInAsP | 1.55 | Titech | 9.9 | [32] |
| June , 2016 | GaInAsP | 1.55 | Titech | 11 | [33] |
| June , 2016 | GaInAsP | 1.55 | NTT | 12.5 | [34] |
| September , 2016 | GaInAsP | 1.55 | NTT | 9.1 | [35] |
| September , 2016 | GaInAsP | 1.55 | NTT | 9.5 | [36] |
| May , 2017 | GaInAsP | 1.55 | Titech | 12 | [37] |
| VCSELs | | | | | |
| October , 2001 | GaInAsP | 1.55 | UCSB | 2.6 | [38] |
| September , 2002 | AlGaInAs | 1.55 | TU München | 6.5 | [39] |
| September , 2003 | GaInAsP | 1.3 | Agilent | 3.1 | [40] |
| September , 2003 | GaInAsP | 1.55 | Agilent | 2.3 | [40] |
| November, 2005 | AlGaInAs | 1.3 | Corning | 5.57 | [41] |
| January , 2006 | AlGaInAs | 1.55 | TU München | 5.8 | [42] |
| August , 2006 | AlGaInAs | 1.55 | TU München | 7.0 | [43] |
| November , 2009 | AlGaInAs | 1.55 | TU München | 7.8 | [44] |
| September , 2011 | AlGaInAs | 1.55 | TU München | 6.8 | [45] |
| February , 2011 | AlGaInAs | 1.55 | TU München | 7.1 | [46] |
| March , 2012 | AlGaInAs | 1.55 | TU München | 6.2 | [47] |
| March , 2012 | AlGaInAs | 1.55 | TU München | 5.8 | [48] |

| | | | | | |
|---|---|---|---|---|---|
| July , 2012 | AlGaInAs | 1.3 | TU München | 8.6 | [49] |
| August , 2013 | AlGaInAs | 1.55 | U.C. Barkley | 3.6 | [50] |
| March , 2014 | AlGaInAs | 1.3 | Vertilas GmbH | 4.4 | [51] |
| January , 2015 | AlGaInAs | 1.55 | U.C. Barkley | 5.8 | [52] |
| March , 2016 | AlGaInAs | 1.55 | TU München | 10 | [53] |
| August , 2016 | AlGaInAs | 1.55 | TU München | 12.5 | [54] |
| PhC laser | | | | | |
| February , 2013 | AlGaInAs | 1.55 | NTT | 42.4 | [55] |

[1] O. Gauthier-Lafaye, V. Colson, J. Py, B. Thedrez, and J.-L. Gentner, "High temperature 10 Gbit/s directly modulated 1.3/spl mu/m DFB lasers using InAsP/InGaAsP materials," *Electronics Letters,* vol. 38, pp. 275-277, 2002.

[2] Y. Muroya, T. Okuda, R. Kobayashi, K. Tsuruoka, Y. Ohsawa, T. Koui, T. Tsukuda, T. Nakamura, A. Ito, and J. Shimizu, "100ºC, 10-Gb/s Direct Modulation with a Low Operation Current of 1.3-μm AlGaInAs Buried Heterostructure DFB Laser Diodes," in *Optical Fiber Communication Conference*, 2003, p. FG6.

[3] K. Takemasa, T. Sugiyama, and Y. Yatagai, "Development of the 10Gbit/s 1.3 μm AlGaInAs DFB Laser," *OKI Technical Review,* vol. 70, p. 196, 2003.

[4] K. Nakahara, T. Tsuchiya, T. Kitatani, K. Shinoda, T. Kikawa, F. Hamano, S. Fujisaki, T. Taniguchi, E. Nomoto, and M. Sawada, "12.5-Gb/s direct Modulation up to 115°C in 1.3-μm InGaAlAs-MQW RWG DFB lasers with notch-free grating structure," *Journal of lightwave technology,* vol. 22, pp. 159-165, 2004.

[5] T. Nakamura, T. Okuda, R. Kobayashi, Y. Muroya, K. Tsuruoka, Y. Ohsawa, T. Tsukuda, and S. Ishikawa, "1.3-μm AlGaInAs strain compensated MQW-buried-heterostructure lasers for uncooled 10-Gb/s operation," *IEEE Journal of selected topics in quantum electronics,* vol. 11, pp. 141-148, 2005.

[6] K. Uomi, M. Mukaikubo, H. Yamamoto, K. Nakahara, K. Motoda, K. Okamoto, Y. Sakuma, H. Singh, R. Washino, and M. Aoki, "10Gbit/s InGaAlAs uncooled directly modulated MQW-DFB lasers for SONET and Ethernet applications," in *Indium Phosphide and Related Materials, 2005. International Conference on*, 2005, pp. 637-642.

[7] K. Nakahara, T. Tsuchiya, T. Kitatani, K. Shinoda, T. Taniguchi, T. Kikawa, M. Aoki, and M. Mukaikubo, "High extinction ratio operation at 40-Gb/s direct modulation in 1.3-μm InGaAlAs-MQW RWG DFB lasers," in *Optical Fiber Communication Conference, 2006 and the 2006 National Fiber Optic Engineers Conference. OFC 2006*, 2006, p. 3.

[8] K. Takada, M. Matsuda, S. Okumura, M. Ekawa, and T. Yamamoto, "Low-Drive-Current 10-Gb/s Operation of AlGaInAs Buried-Heterostructure $\lambda$/4-Shifted DFB Lasers," in *Optical Communications, 2006. ECOC 2006. European Conference on*, 2006, pp. 1-2.

[9] K. Nakahara, T. Tsuchiya, T. Kitatani, K. Shinoda, T. Taniguchi, T. Kikawa, M. Aoki, and M. Mukaikubo, "40-Gb/s direct modulation with high extinction ratio operation of 1.3-μm InGaAlAs multiquantum well ridge waveguide distributed feedback lasers," *IEEE Photonics Technology Letters,* vol. 19, pp. 1436-1438, 2007.

[10] K. Otsubo, M. Matsuda, K. Takada, S. Okumura, M. Ekawa, H. Tanaka, S. Ide, K. Mori, and T. Yamamoto, "Uncooled 25 Gbit/s direct modulation of semi-insulating buried-heterostructure 1.3 μm AlGaInAs quantum-well DFB lasers," *Electronics Letters,* vol. 44, pp. 631-633, 2008.

[11] K. Otsubo, M. Matsuda, K. Takada, S. Okumura, M. Ekawa, and T. Yamamoto, "40-Gb/s direct modulation of 1.3-μm semi-insulating buried-heterostructure AlGaInAs MQW DFB lasers," in *Semiconductor Laser Conference, 2008. ISLC 2008. IEEE 21st International*, 2008, pp. 19-20.

[12] A. K. Verma, M. Steib, Y. L. Ha, and T. Sudo, "25Gbps 1.3μ m DFB Laser for 10-25km Transmission in 100GBE Systems," in *Optical Fiber Communication Conference*, 2009, p. OThT2.

[13] K. Otsubo, M. Matsuda, S. Okumura, A. Uetake, M. Ekawa, and T. Yamamoto, "Low-driving-current high-speed direct modulation up to 40 Gb/s using 1.3-μm semi-insulating buried-heterostructure AlGaInAs-MQW distributed reflector (DR) lasers," in *Optical Fiber Communication Conference*, 2009, pp. 1-3.

[14] R. Paoletti, M. Agresti, D. Bertone, C. Bruschi, S. Codato, C. Coriasso, R. Defranceschi, P. Dellacasa, M. Diloreto, and R. Fang, "Uncooled 20 Gb/s direct modulation of high yield, highly reliable 1300 nm InGaAlAs ridge DFB lasers," in *Optical Fiber Communication Conference*, 2009, p. OThT1.

[15] T. Tadokoro, T. Yamanaka, F. Kano, H. Oohashi, Y. Kondo, and K. Kishi, "Operation of a 25-Gb/s Direct Modulation Ridge Waveguide MQW-DFB Laser up to 85°C," *IEEE Photonics Technology Letters,* vol. 21, pp. 1154-1156, 2009.

[16] A. Uetake, K. Otsubo, M. Matsuda, S. Okumura, M. Ekawa, and T. Yamamoto, "40-Gbps direct modulation of 1.55-μm AlGaInAs semi-insulating buried-heterostructure distributed reflector lasers up to 85° C," in *LEOS Annual Meeting Conference Proceedings, 2009. LEOS'09. IEEE*, 2009, pp. 839-840.

[17] H. Yagi, Y. Onishi, K. Koyama, Y. Tsuji, H. Ichikawa, H. Yoshinaga, N. Kaida, T. Nomaguchi, K. Hiratsuka, and K. Uesaka, "1.3 μm wavelength AlGaInAs/InP ridge-waveguide lasers utilizing benzocyclobutene planarization process," *SEI Technical Review,* vol. 69, p. 93, 2009.

[18] T. Shindo, S. Lee, D. Takahashi, N. Tajima, N. Nishiyama, and S. Arai, "Low-threshold and high-efficiency operation of distributed reflector laser with wirelike active regions," *IEEE Photonics Technology Letters,* vol. 21, pp. 1414-1416, 2009.

[19] G. Sakaino, T. Takiguchi, H. Sakuma, C. Watatani, T. Nagira, D. Suzuki, T. Aoyagi, and T. Ishikawa, "25.8 Gbps direct modulation of BH AlGaInAs DFB lasers with p-InP substrate for low driving current," in *Semiconductor Laser Conference (ISLC), 2010 22nd IEEE International*, 2010, pp. 197-198.

[20] S. Lee, D. Takahashi, T. Shindo, K. Shinno, T. Amemiya, N. Nishiyama, and S. Arai, "Low-Power-Consumption High-Eye-Margin 10-Gb/s Operation by GaInAsP/InP Distributed Reflector Lasers With Wirelike Active Regions," *IEEE Photonics Technology Letters,* vol. 23, pp. 1349-1351, 2011.

[21] T. Fukamachi, K. Adachi, K. Shinoda, T. Kitatani, S. Tanaka, M. Aoki, and S. Tsuji, "Wide temperature range operation of 25-Gb/s 1.3-μm InGaAlAs directly modulated lasers," *IEEE Journal of Selected Topics in Quantum Electronics,* vol. 17, pp. 1138-1145, 2011.

[22] M. Matsuda, T. Simoyama, A. Uetake, S. Okumura, M. Ekawa, and T. Yamamoto, "Uncooled, low-driving-current 25.8 Gbit/s direct modulation using 1.3 μm AlGaInAs MQW distributed-reflector lasers," *Electronics letters,* vol. 48, pp. 450-452, 2012.

[23] T. Tadokoro, W. Kobayashi, T. Fujisawa, T. Yamanaka, and F. Kano, "43 Gb/s 1.3 μm DFB Laser for 40 km Transmission," *Journal of Lightwave Technology,* vol. 30, pp. 2520-2524, 2012.

[24] W. Kobayashi, T. Ito, T. Yamanaka, T. Fujisawa, Y. Shibata, T. Kurosaki, M. Kohtoku, T. Tadokoro, and H. Sanjoh, "50-Gb/s direct modulation of a 1.3-μm InGaAlAs-based DFB laser with a ridge waveguide structure," *IEEE Journal of Selected Topics in Quantum Electronics,* vol. 19, p. 1500908, 2013.

[25] T. Fukamachi, A. Nakamura, Y. Sakuma, S. Hayakawa, R. Washino, M. Mukaikubo, K. Okamoto, T. Nakajima, K. Motoda, and K. Naoe, "Uncooled clear-eye-opening operation (25 to 95° C) of 25.8/28-Gbps

1.3-μm InGaAlAs-MQW directly modulated DFB lasers," in *Optical Fiber Communication Conference*, 2014, p. Th3A. 7.

[26] S. Matsuo, T. Fujii, K. Hasebe, K. Takeda, T. Sato, and T. Kakitsuka, "40-Gbit/s direct modulation of membrane buried heterostructure DFB laser on $SiO_2$/Si substrate," in *Semiconductor Laser Conference (ISLC), 2014 International*, 2014, pp. 30-31.

[27] S. Matsuo, T. Fujii, K. Hasebe, K. Takeda, T. Sato, and T. Kakitsuka, "Ultralow operating energy of directly modulated DFB laser on $SiO_2$/Si substrate," in *Optical Communication (ECOC), 2014 European Conference on*, 2014, pp. 1-3.

[28] S. Kanazawa, T. Ito, T. Sato, R. Iga, W. Kobayashi, K. Takahata, H. Sanjoh, and H. Ishii, "Flip-chip mounted 25.8-Gb/s directly modulated InGaAsP DFB laser with Ru-doped semi-insulating buried heterostructure," *IEICE Electronics Express,* vol. 12, pp. 20141028-20141028, 2015.

[29] N. Nakamura, M. Shimada, G. Sakaino, T. Nagira, H. Yamaguchi, Y. Okunuki, A. Sugitatsu, and M. Takemi, "25.8 Gbps direct modulation AlGaInAs DFB lasers of low power consumption and wide temperature range operation for data center," in *Optical Fiber Communications Conference and Exhibition (OFC), 2015*, 2015, pp. 1-3.

[30] T. Nakajima, T. Fukamachi, M. Akashi, A. Nakamura, Y. Sakuma, S. Hayakawa, R. Washino, M. Mukaikubo, K. Okamoto, and K. Motoda, "25.8 Gbps Error Free Transmission over 10 km at Wavelengths from 1271 to 1331nm by Uncooled (25 to 85 °C) Directly Modulated DFB Lasers for 100G-CWDM4," in *Optical Fiber Communication Conference*, 2015, p. Th1G. 6.

[31] H. Nishi, T. Fujii, K. Takeda, K. Hasebe, T. Kakitsuka, T. Tsuchizawa, T. Yamamoto, K. Yamada, and S. Matsuo, "Membrane distributed-reflector laser integrated with SiOx-based spot-size converter on Si platform," in *Optical Communication (ECOC), 2015 European Conference on*, 2015, pp. 1-3.

[32] D. Inoue, T. Hiratani, K. Fukuda, T. Tomiyasu, T. Amemiya, N. Nishiyama, and S. Arai, "High-modulation efficiency operation of GaInAsP/InP membrane distributed feedback laser on Si substrate," *Optics express,* vol. 23, pp. 29024-29031, 2015.

[33] D. Inoue, T. Hiratani, K. Fukuda, T. Tomiyasu, T. Amemiya, N. Nishiyama, and S. Arai, "10 Gbps operation of membrane DFB laser on silicon with record high modulation efficiency," in *Compound Semiconductor Week (CSW)[Includes 28th International Conference on Indium Phosphide & Related Materials (IPRM) & 43rd International Symposium on Compound Semiconductors (ISCS),*, 2016, pp. 1-2.

[34] K. Takeda, E. Kanno, T. Fujii, K. Hasebe, T. Yamamoto, T. Kakitsuka, and S. Matsuo, "Continuous-wave operation of ultra-short cavity distributed bragg reflector lasers on Si substrates," in *Compound Semiconductor Week (CSW)[Includes 28th International Conference on Indium Phosphide & Related Materials (IPRM) & 43rd International Symposium on Compound Semiconductors (ISCS), 2016*, 2016, pp. 1-2.

[35] T. Fujii, K. Takeda, E. Kanno, K. Hasebe, H. Nishi, R. Nakao, T. Yamamoto, T. Kakitsuka, and S. Matsuo, "Low operating-energy directly modulated membrane distributed-reflector lasers on Si," in *ECOC 2016; 42nd European Conference on Optical Communication; Proceedings of*, 2016, pp. 1-3.

[36] E. Kanno, K. Takeda, T. Fujii, K. Hasebe, H. Nishi, T. Yamamoto, T. Kakitsuka, and S. Matsuo, "Membrane distributed-reflector lasers with 20-μm-long DFB section and front/rear DBRs on Si substrates," in *Semiconductor Laser Conference (ISLC), 2016 International*, 2016, pp. 1-2.

[37] T. Tomiyasu, T. Hiratani, D. Inoue, N. Nakamura, K. Fukuda, T. Uryu, T. Amemiya, N. Nishiyama, and S. Arai, "High Efficiency and High-speed Modulation Characteristics of Membrane Distributed-Reflector Laser on Si," in *Compound Semiconductor Week (CSW)[Includes 29th International Conference on Indium Phosphide & Related Materials (IPRM) & 44th International Symposium on Compound Semiconductors (ISCS), 2017*, 2017, pp. 1-2.

[38] K. Black, E. Bjorlin, J. Piprek, E. Hu, and J. Bowers, "Small-signal frequency response of long-wavelength vertical-cavity lasers," *IEEE Photonics Technology Letters,* vol. 13, pp. 1049-1051, 2001.

[39] M. Ortsiefer, R. Shau, F. Mederer, R. Michalzik, J. Rosskopf, G. Bohm, F. Kohler, C. Lauer, M. Maute, and M.-C. Amann, "High-speed modulation up to 10 Gbit/s with 1.55 μm wavelength InGaAlAs VCSELs," *Electronics Letters,* vol. 38, pp. 1180-1181, 2002.

[40] C.-K. Lin, D. P. Bour, J. Zhu, W. H. Perez, M. H. Leary, A. Tandon, S. W. Corzine, and M. R. Tan, "High temperature continuous-wave operation of 1.3-and 1.55-μm VCSELs with InP/air-gap DBRs," *IEEE Journal of selected topics in quantum electronics,* vol. 9, pp. 1415-1421, 2003.

[41] N. Nishiyama, C. Caneau, and C. Zah, "InP-based vertical cavity surface emitting lasers for 10G applications," in *Asia-Pacific Optical Communications*, 2005, pp. 602001-602001-9.

[42] W. Hofmann, N. Zhu, M. Ortsiefer, G. Bohm, J. Rosskopf, L. Chao, S. Zhang, M. Maute, and M.-C. Amann, "10-Gb/s data transmission using BCB passivated 1.55-μm InGaAlAs-InP VCSELs," *IEEE photonics technology letters,* vol. 18, pp. 424-426, 2006.

[43] W. Hofmann, N. Zhu, M. Ortsiefer, G. Böhm, Y. Liu, and M. Amann, "High speed (> 11 GHz) modulation of BCB-passivated 1.55 lm InGaAlAs-InP VCSELs," *Electronics Letters,* vol. 42, p. 1, 2006.

[44] M. Muller, W. Hofmann, G. Bohm, and M.-C. Amann, "Short-cavity long-wavelength VCSELs with modulation bandwidths in excess of 15 GHz," *IEEE Photonics Technology Letters,* vol. 21, pp. 1615-1617, 2009.

[45] M. Muller, W. Hofmann, T. Grundl, M. Horn, P. Wolf, R. D. Nagel, E. Ronneberg, G. Bohm, D. Bimberg, and M.-C. Amann, "1550-nm high-speed short-cavity VCSELs," *IEEE Journal of selected topics in Quantum Electronics,* vol. 17, pp. 1158-1166, 2011.

[46] W. Hofmann, M. Müller, P. Wolf, A. Mutig, T. Gründl, G. Böhm, D. Bimberg, and M.-C. Amann, "40 Gbit/s modulation of 1550 nm VCSEL," *Electronics Letters,* vol. 47, pp. 270-271, 2011.

[47] M.-C. Amann, E. Wong, and M. Mueller, "Energy-efficient high-speed short-cavity VCSELs," in *Optical Fiber Communication Conference and Exposition (OFC/NFOEC), 2012 and the National Fiber Optic Engineers Conference*, 2012, pp. 1-3.

[48] B. Kögel, M. Ortsiefer, and A. Daly, "Report on 1.55 μm BTJ-VCSEL with> 25 Gb/s modulation speed at room-temperature."

[49] M. Müller, C. Grasse, and M. C. Amann, "InP-based 1.3 μm and 1.55 μm short-cavity VCSELs suitable for telecom-and datacom-applications," in *Transparent Optical Networks (ICTON), 2012 14th International Conference on*, 2012, pp. 1-4.

[50] Y. Rao, W. Yang, C. Chase, M. C. Huang, D. P. Worland, S. Khaleghi, M. R. Chitgarha, M. Ziyadi, A. E. Willner, and C. J. Chang-Hasnain, "Long-wavelength VCSEL using high-contrast grating," *IEEE Journal of Selected Topics in Quantum Electronics,* vol. 19, p. 1701311, 2013.

[51] M. Ortsiefer, B. Kögel, J. Rosskopf, and C. Neumeyr, "Long wavelength high speed VCSELs for long haul and data centers," in *Optical Fiber Communication Conference*, 2014, p. W4C. 2.

[52] J. Ferrara, W. Yang, L. Zhu, P. Qiao, and C. J. Chang-Hasnain, "Heterogeneously integrated long-wavelength VCSEL using silicon high contrast grating on an SOI substrate," *Optics express,* vol. 23, pp. 2512-2523, 2015.

[53] S. Spiga, D. Schoke, A. Andrejew, M. Müller, G. Boehm, and M.-C. Amann, "Single-mode 1.5-μm VCSELs with 22-GHz small-signal bandwidth," in *Optical Fiber Communication Conference*, 2016, p. Tu3D. 4.

[54] S. Spiga, W. Soenen, A. Andrejew, D. M. Schoke, X. Yin, J. Bauwelinck, G. Boehm, and M.-C. Amann, "Single-Mode High-Speed 1.5-μm VCSELs," *Journal of Lightwave Technology,* vol. 35, pp. 727-733, 2017.

[55] S. Matsuo, T. Sato, K. Takeda, A. Shinya, K. Nozaki, H. Taniyama, M. Notomi, K. Hasebe, and T. Kakitsuka, "Ultralow operating energy electrically driven photonic crystal lasers," *IEEE Journal of Selected Topics in Quantum Electronics,* vol. 19, p. 4900311, 2013.

# Chapter 5
# Integration of membrane DFB laser and p-i-n photodiode

5.1 Introduction 255
5.2 Device structure and fabrication 257
5.2.1 Device structure 257
5.2.2 Fabrication process 259
5.3 Electrical isolation between the integrated devices 262
5.3.1 Isolation process 264
5.3.2 Measurement of isolation resistance 266
5.3.3 Isolation effect on the photocurrent characteristics 270
5.4 Integrated membrane DFB laser and p-i-n photodiode with isolated structure 272
5.4.1 Lasing characteristics of integrated laser 275
5.4.2 Static optical transmission characteristics 277
5.4.3 Dynamic optical transmission characteristics 281
5.5 Conclusion 289
References

## 5.1 Introduction

This chapter describes the integration of membrane DFB lasers and p-i-n photodiodes (PDs) the by BJB structure. The fabrication method and characteristics of the membrane BJB structure were explained in the chapter 3. The integration of membrane DFB lasers and passive waveguides was realized in the chapter 4. For the on-chip optical link device using the membrane structure, integration of a laser, a waveguide and detector is an essential step. The fabricated device in this chapter consists of a membrane DFB laser, BJB passive waveguide and a lateral junction p-i-n PD which are

key components to construct optical link. Section 5.2 describes the device structure and the fabrication process. Section 5.3 describes the electrical isolation process of the integrated device. A sufficient isolation is needed to independently drive each component device. Section 5.4 describes the characterization of integrated membrane optical link device consisting of a DFB laser and a p-i-n PD. First, fundamental characteristics of the integrated DFB laser is shown. Static optical transmission characteristics is measured by using a semiconductor parameter analyzer. Signal transmission characteristics are also measured for small-signal and large signal modulations.

## 5.2 Device structure and fabrication

### 5.2.1 Device structure

The structure of the membrane optical link is explained. Figure 5.1 shows the schematic structure of a membrane optical link using a DFB laser and a p-i-n photodiode (PD) integrated by the BJB structure. The semiconductor core layer and $SiO_2$ cladding layer are bonded on a Si substrate by BCB adhesive layer. The membrane DFB laser and lateral junction p-i-n PD are connected by a straight BJB integrated waveguide. The active layer of the DFB laser is strain compensated GaInAsP five-quantum wells. The absorption layer of p-i-n PD is same as the active layer of the DFB laser. The surface grating is formed on only DFB laser region. The unnecessary *n*- and *p*-InP regions for the device operation are removed to enhance the electrical isolation between the indivisual devices. The $SiO_2$ cladding layer is exposed on the region where InP is removed. Figure 5.2 shows the cross sectional image of a membrane optical link along with the light propagation direction. Figure 5.3 shows the

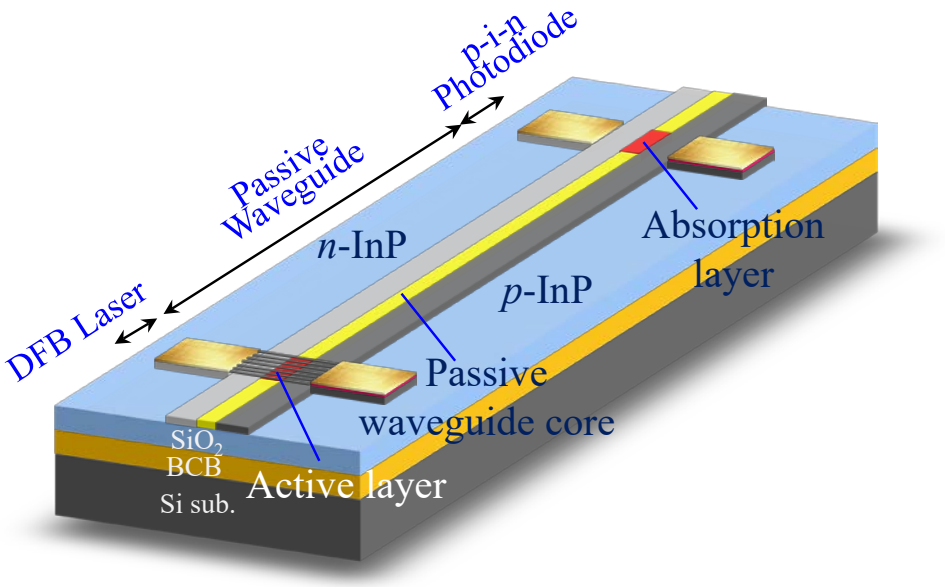


**Figure 5.1** Schematic structure of membrane optical link using DFB laser and p-i-n PD.

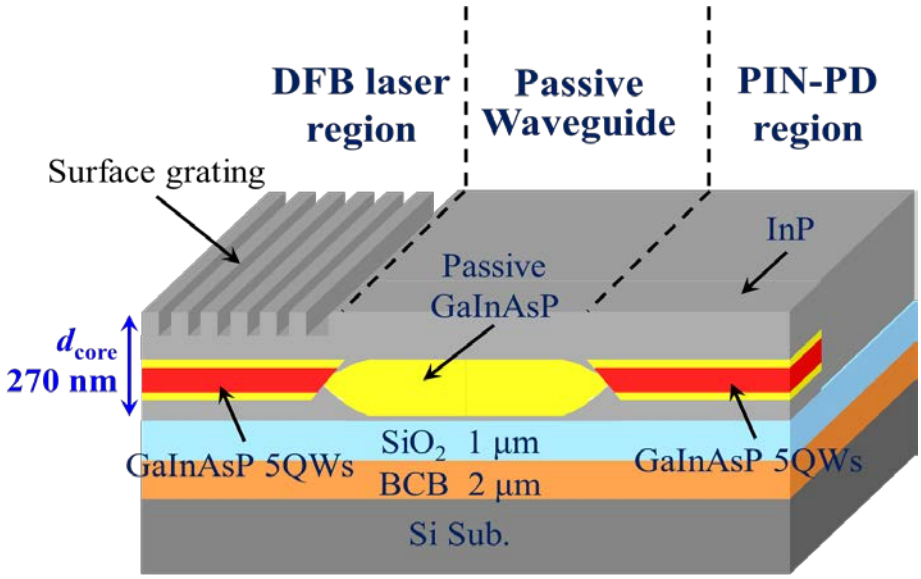


**Figure 5.2** Cross sectional image of membrane optical link in light propagation direction.

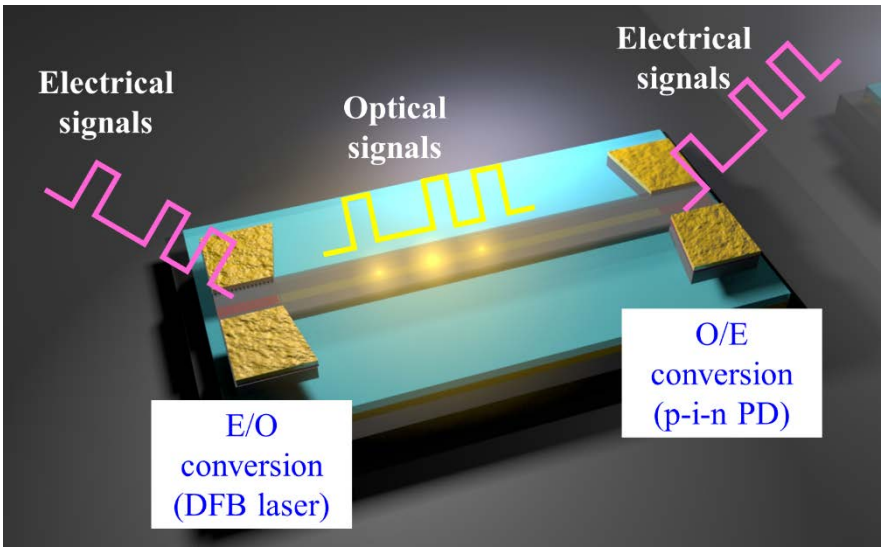


**Figure 5.3** Explanation for the function of membrane optical link.

explanation for the function of membrane optical link. The input electrical signal drives the DFB laser. The signal is converted from electrical domain to optical domain in the laser, then propagating through the passive waveguide. The optical signal is again converted to electrical signal by the p-i-n PD. This membrane optical link can perform the fundamental function as an optical interconnection. Although there is no specific reason to form a cleavage facet for the purpose of operation as an optical link, the facet is needed to be formed when the laser characteristics is directly measured.

### 5.2.2 Fabrication process

The fabrication process of membrane optical link is described. Figure 5.4 shows the initial wafer structure used for the fabrication. The detailed design of MQWs active layer is as same as that described in Table 4.12. The top InP and GaInAs cap layers are introduced for the protection of the surface before starting the process. The core layer of 270 nm is formed in a final structure. The whole fabrication process flow is shown in Figure 5.5 and Figure 5.6. The process steps from (1) to (12) are the same as the fabrication process of membrane DFB laser with integrated BJB waveguide already described in the section 4.3.4. The different procedures are steps (13) and (14).

(13) Grating formation

The grating is formed on only the surface of DFB laser region. Surface of absorption region of p-i-n PD has no pattering.

(14) Electrical isolation

A stripe-shaped photoresist (AZ5218) for protecting both an active and a passive waveguide region is formed by photolithography. The unnecessary InP regions are then removed by chemical solution of $H_2O_2$ : HCl : $CH_3COOH$ = 1 : 2 : 20 at 20°C for 5 sec, to enhance the electrical isolation between the devices.

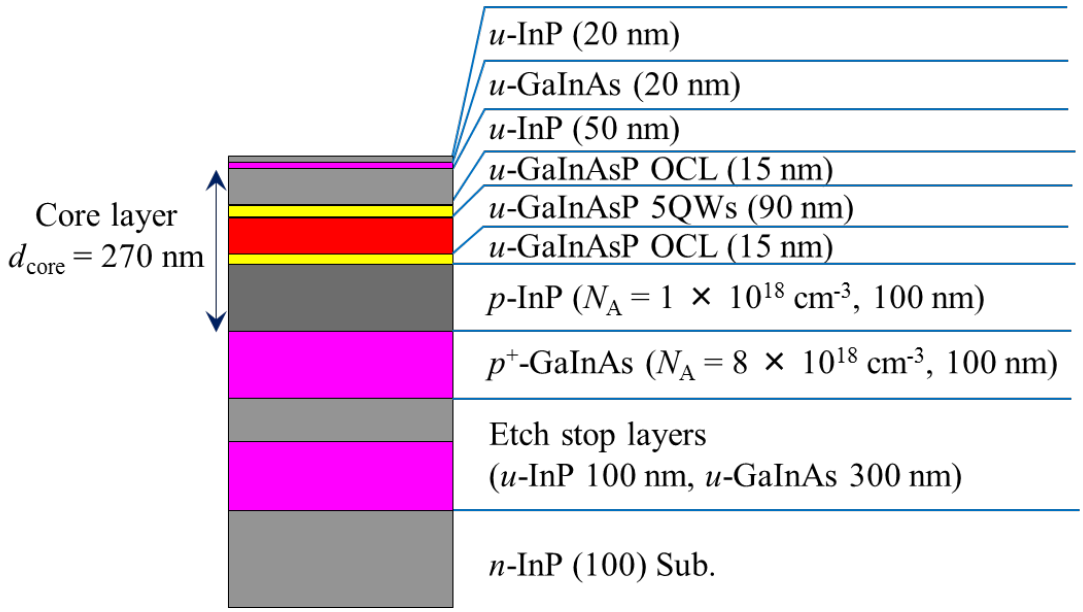


**Figure 5.4** Initial wafer structure for fabrication of membrane optical link.

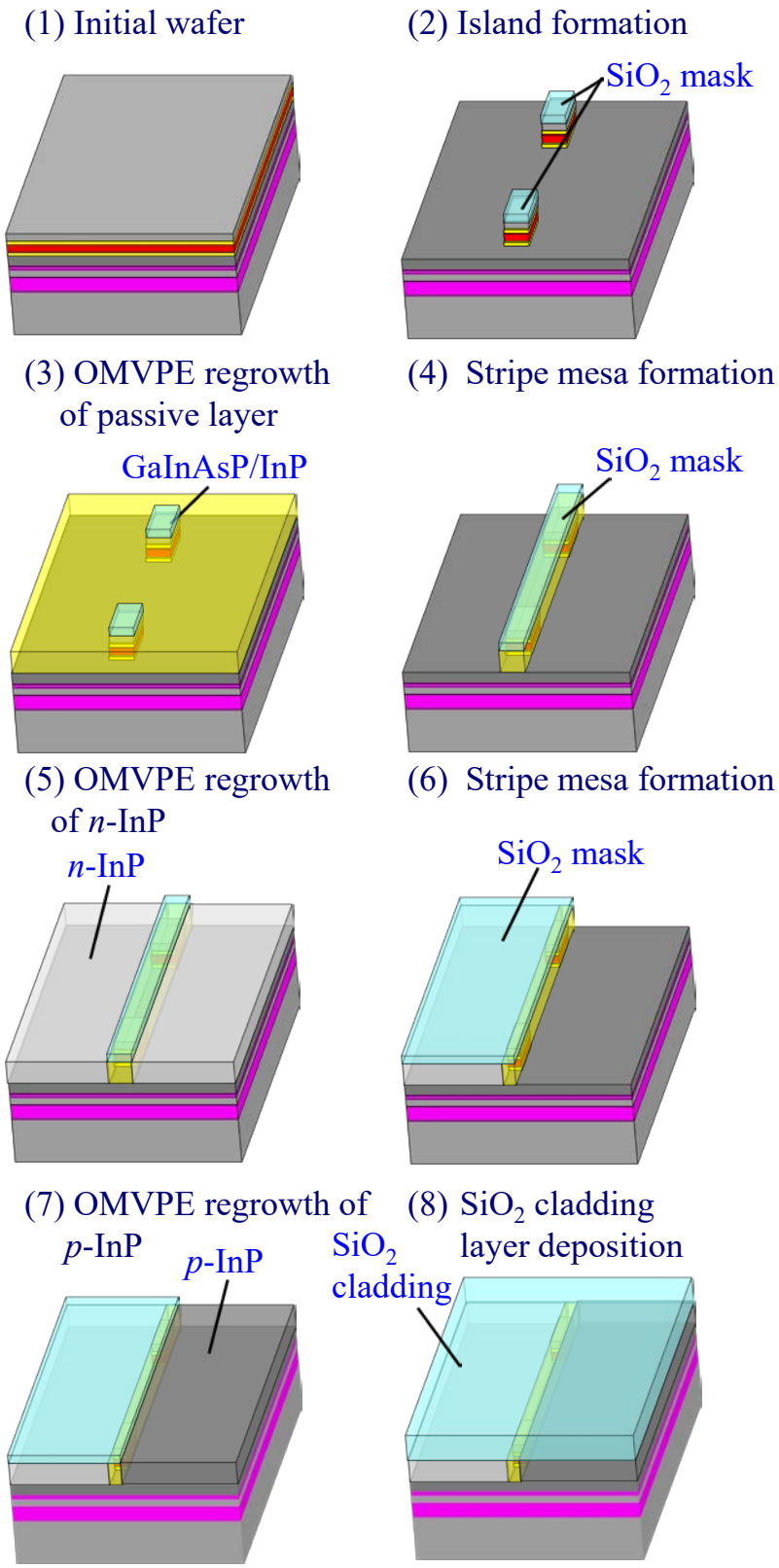


**Figure 5.5** Fabrication procedure of membrane DFB laser (initial wafer ~ $SiO_2$ cladding layer deposition).

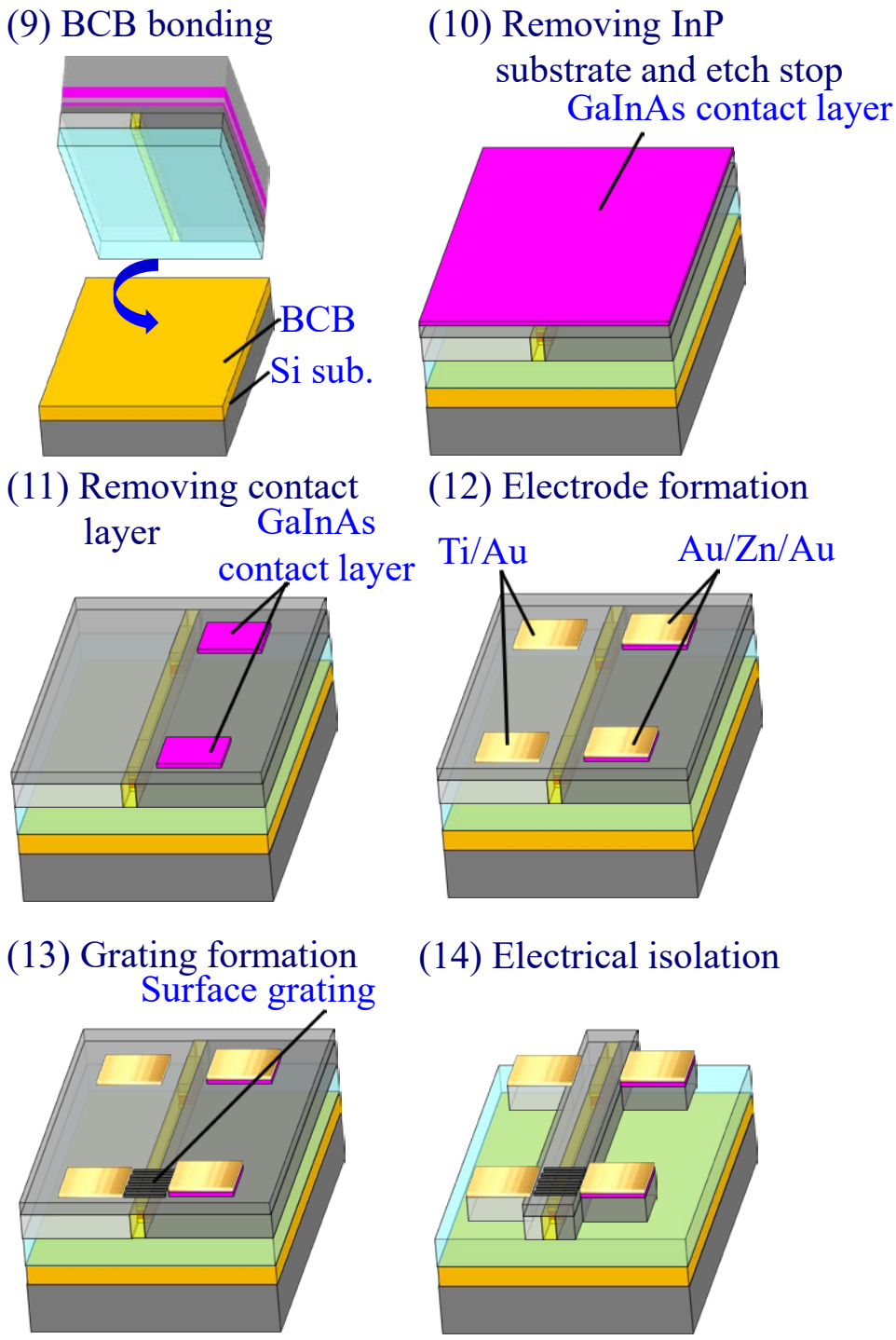


**Figure 5.6** Fabrication procedure of membrane DFB laser (BCB bonding ~ electrical isolation).

## 5.3 Electrical isolation between the integrated devices

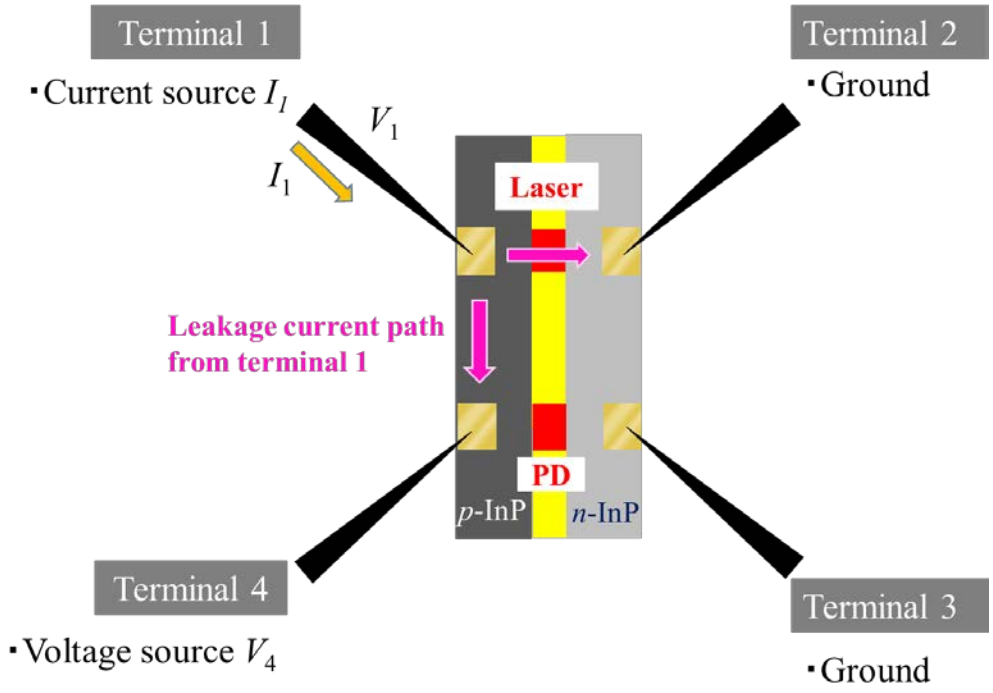


**Figure 5.7** Terminal configuration in measurement of optical link device.

The electrical isolation resistance between the DFB laser and the p-i-n PD is important to ensure independent device driving and to suppress high frequency crosstalk in the integrated structure. The electrical isolation resistance $R_{iso}$ between the *p*-side electrodes of the DFB laser and the p-i-n PD has major impact of the measurement. Figure 5.7 shows the terminal configuration in measurement of the optical link device. The terminal 1 has a function as a current source for injecting current into the laser and is connected to the *p*-side electrode of the DFB laser. Terminals 2 and 3 are set to ground and connected to *n*-side electrodes of the DFB laser and p-i-n PD. Terminal 4 has a function as a voltage source for biasing the p-i-n PD and connected to the *p*-side electrode of the p-i-n PD. The polarity of these terminals is defined as current flow from the instrument to the device is positive direction. Given that the *n*-electrodes will be set to common ground during the optical transmission measurement, the isolation resistance between the *n*-side electrodes becomes not a serious problem. There is a leakage current path between the p-side

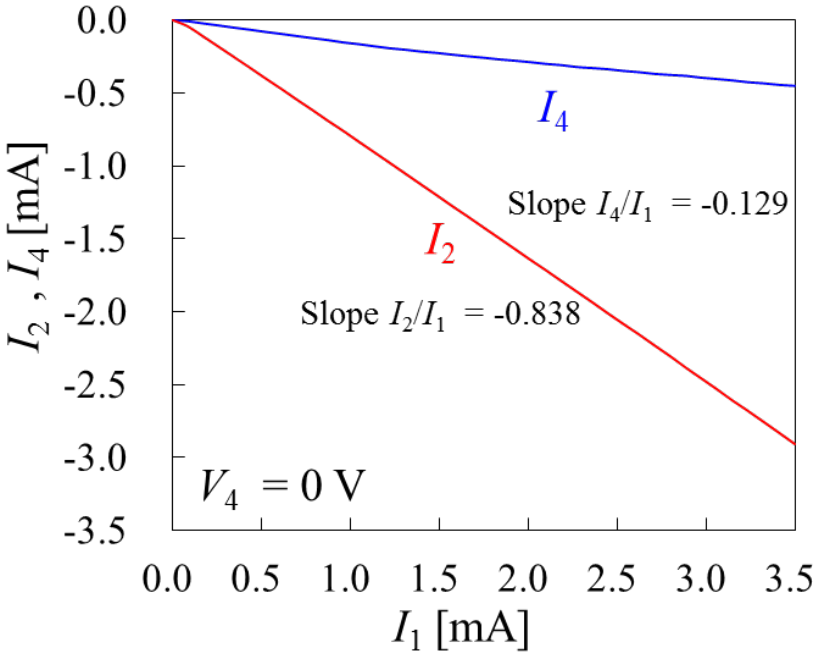


**Figure 5.8** Current flow division of $I_1$ to $I_2$ and $I_4$.

electrodes, because voltage difference is occurred when the DFB laser and the p-i-n PD are biased forward current and reverse voltage, respectively. To confirm the current amount of leakage current, current flow from the terminal 1 to the other terminals were measured. The measured device has no isolation structure and isolation resistance between the p-side electrodes was 25k Ω. Figure 5.8 shows current $I_1$ versus currents $I_2$ and $I_4$ characteristics. When the devices are ideally isolated, current $-I_2$ is equal to the $I_1$ and the slope $I_2/I_1$ becomes -1. However, the obtained results indicated the presence of leakage current. Estimating from the slope of $I_4/I_1$ = -0.129, 12.9% of driving current for the DFB laser is leaked to the terminal 4. This leakage current problem should be solved before measuring the integrated device.

### 5.3.1 Isolation process

The current blocking structure is needed to enhance the electrical isolation. Figure 5.9 shows the schematic illustration of top view of the isolation process. First, the DFB laser, passive waveguide and p-i-n PD region are protected by stripe shape photoresist. The uncovered InP region is etched by wet chemical solution of $H_2O_2$ : HCl : $CH_3COOH$ = 1 : 2 : 20 at 20°C. This chemical solution provide fast and uniform etching result for InP. Then, after removing the resist and cleaning the surface by $O_2$ plasma reactor, the electrically isolated structure is formed. Figure 5.10 shows the optical microscope images of the processed substrate (a) before isolation process with stripe shape resist, and (b) after isolation process. It can be seen that the InP at uncovered region is completely removed. The electrodes are not left from the substrate after the wet etching process. Figure 5.11 shows the enlarged image of the DFB laser region after isolation process. The remaining semiconductor stripe region has width of 14 μm. If the width of core stripe is 1 μm, and *n*- and *p*-InP side cladding have same width, the possible current leakage path becomes 6.5-μm-wide *p*-InP side cladding region.

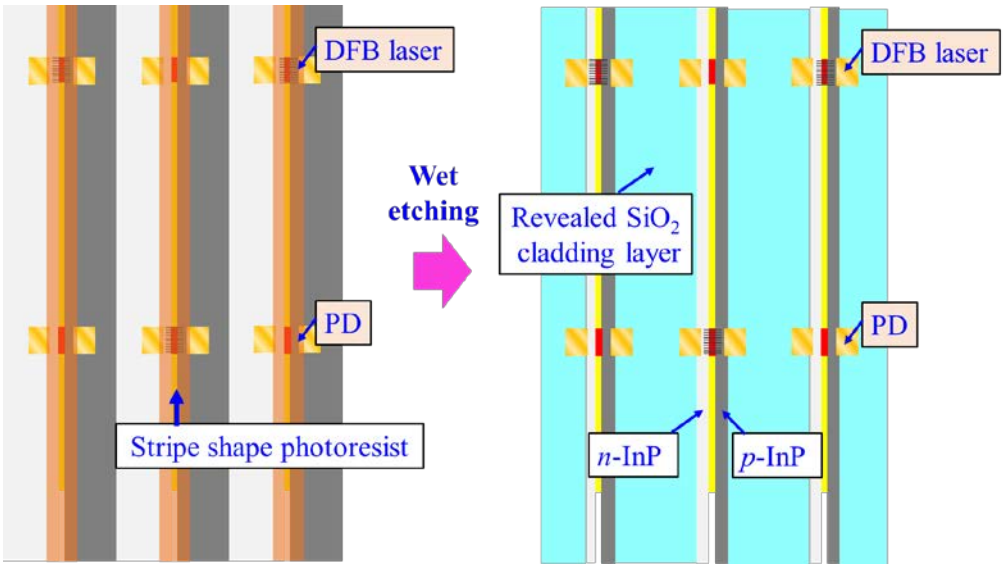


**Figure 5.9** Schematic illustration of top view of the isolation process.


(a) (b)

**Figure 5.10** Optical microscope images during the isolation process (a) with stripe shape resist. (b) Completed structure.

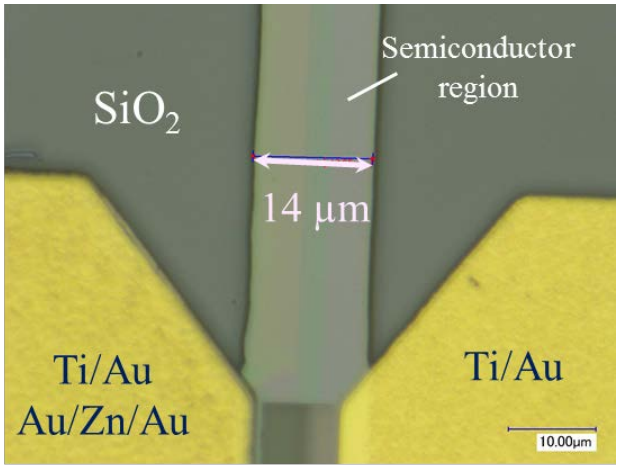


**Figure 5.11** Enlarged image of the device after isolation.

### 5.3.2 Measurement of isolation resistance

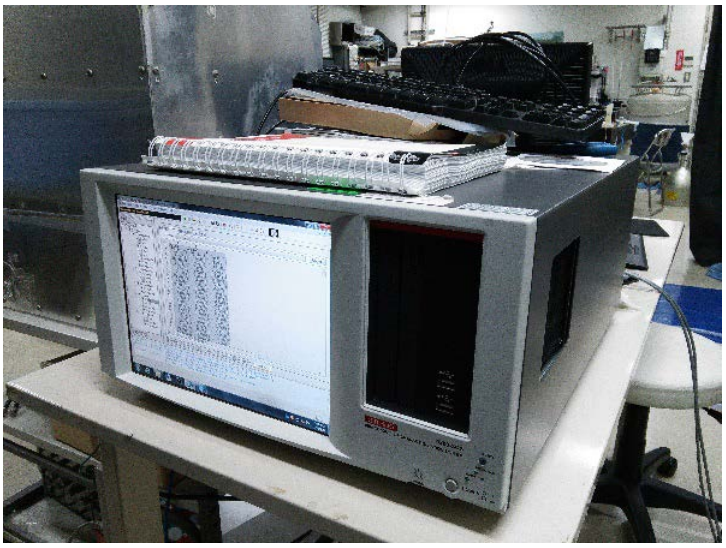

**Figure 5.12** Semiconductor parameter analyzer (Keithley, 4200-SCS)

In this subsection, isolation characteristics before and after isolating process were measured. To perform 4-terminal measurement, a semiconductor parameter analyzer was used. Figure 5.12 shows the appearance of semiconductor parameter analyzer (Keythley, 4200-SCS). This equipment provide *C*-*V* measurement, transistor evaluation and 2–4 terminal measurement. The function of 4-terminal can be arbitrary changed. Source-measure-unit (SMU) has current measurement range from 1.05 pA to 105 mA. When the measurement range is 1.05pA, the minimum current resolution becomes 50 aA. The terminal configuration for optical link measurement is shown in Figure 5.7. In the measurement of isolation resistance, 2-terminal configuration was used. Figure 5.13 shows the voltage-current characteristics between the *p*-side electrodes measured for before and after isolation process. Figure 5.13(a) shows measured position in a device. Figure 5.13(b) shows graph of *I*-*V* curves. The isolation resistance of *p*-side was increased from 40k Ω to 380k Ω by isolation process. Considering the condition for optical link operation, the terminal 1 has voltage of 1–2 V for the laser driving and the terminal 4 has voltage of -1–-3 V for bias of p-i-n PD. The possible voltage difference $V_{14}$ between the terminal 1 and 4 is in the range from 2–5 V. When the isolation resistance is only 40k Ω,

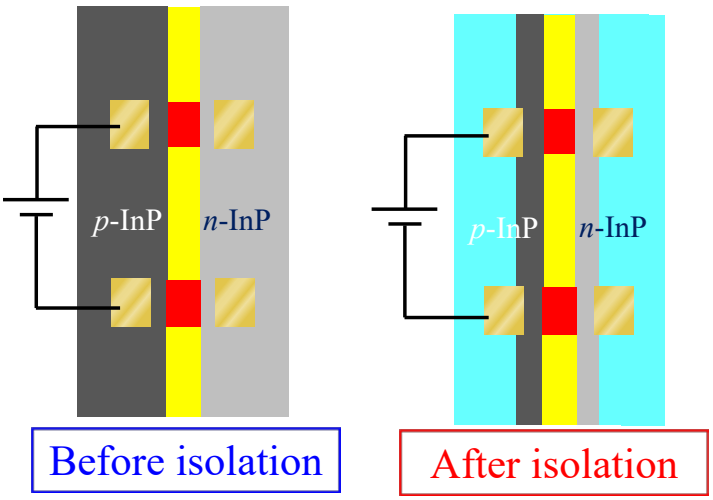


(a)

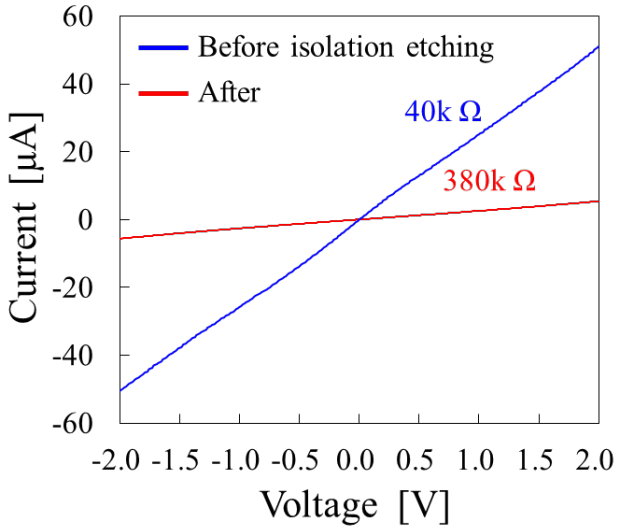


(b)

**Figure 5.13** Measurement of *p*-side isolation resistance before and after isolation process. (a) Measured position in a device. (b) The voltage-current characteristics between the *p*-side electrodes measured for before and after isolation process

the leakage current up to 125 μA is estimated. This current is on the order of greater than or equal to the photocurrent, and obscuring the generated photocurrent. After isolation process, the isolation resistance of 380k Ω results in leakage current less than or around 10 μA. In this case, the photocurrent can be distinguished from measured total current. Figure 5.14 shows the measurement of *n*-side isolation resistance before and after

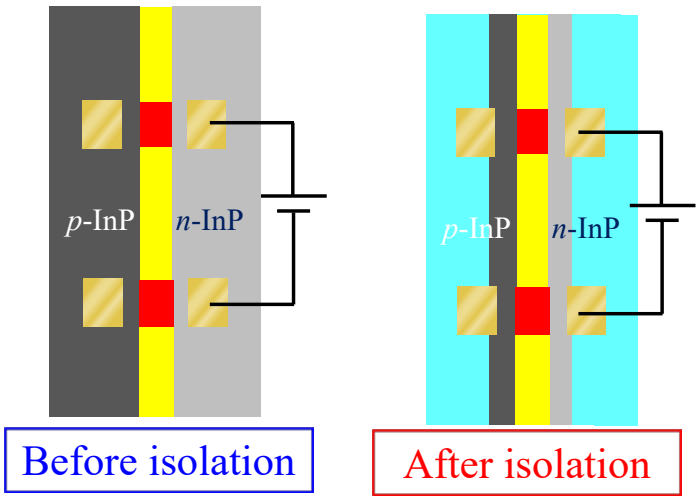


(a)

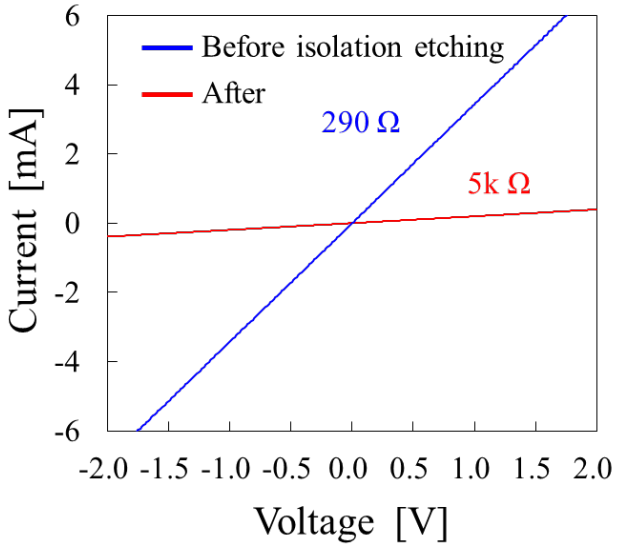


(b)

**Figure 5.14** Measurement of n-side isolation resistance before and after isolation process. (a) Measured position in a device. (b) The voltage-current characteristics between the n-side electrodes measured for before and after isolation process

isolation process. As well as *p*-side characteristics, isolation of n-side electrodes is also enhanced one-order of magnitude. Table 5.1 summarizes the characteristics change for *p*-side isolation by isolation process. In order to confirm that the isolation process does not degrade the electrical characteristics of the laser, the diode characteristics of the laser before and after

**Table 5.1** Isolation characteristics in *p*-side electrodes

| | $R_{iso\text{-}p}$ | Possible leakage current ($V_{14}$ = 5V) |
|---|---|---|
| Before | 40k Ω | 125 μA |
| After | 380k Ω | 13 μA |

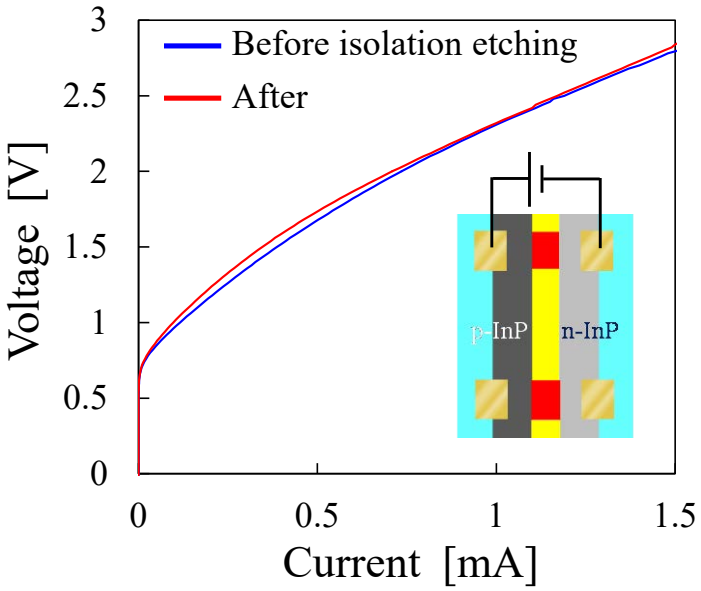


**Figure 5.15** *I-V* characteristics of the laser before and after isolation process.

isolation process were measured. Figure 5.15 shows the *I-V* characteristics of the DFB laser before and after isolation process. There was a little different between two *I-V* curves. The turn-on voltage of 0.8 V was unchanged, and it was confirmed that no leakage path was formed in the current path of the laser. As a results, the sufficient isolation enhancement was obtained by introduced process. In addition, this process does not change the other electrical characteristics of the devices.

### 5.3.3 Isolation effect on the photocurrent characteristics

The photocurrent characteristics of integrated p-i-n PD was measured. Figure 5.16(a) shows the illustration of measurement method. By injecting the current into the laser, p-i-n PD output the detected photocurrent. Therefore, the laser injection current versus photocurrent characteristics corresponds to the light output-current curves of the laser.

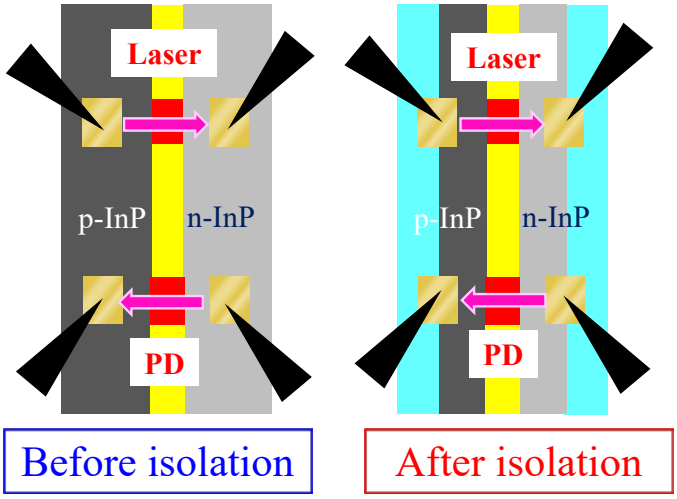


(a)

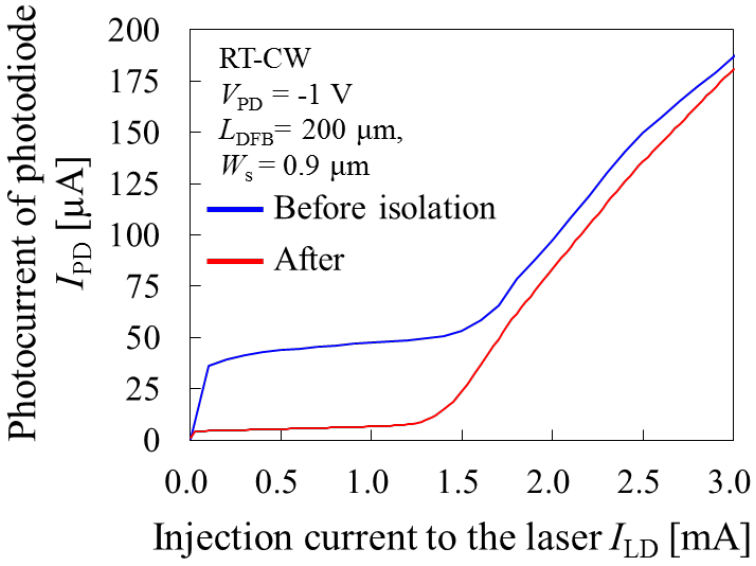


(b)

**Figure 5.16** (a) Illustration of measurement. (b) Laser injection current versus photocurrent characteristics before and after isolation process.

Figure 5.16(b) shows the laser injection current versus photocurrent characteristics before and after isolation process. The measurements were performed for the same device at room-temperature (RT) continuous-wave condition. The bias voltage of p-i-n PD was -1 V. The blue line (before isolation) showed abrupt rising up at laser current of 0 mA. This is caused by insufficient isolation resistance in p-side region. The leakage current due to the voltage difference of 1.8 V (PD bias voltage of -1 V and laser turn-on voltage of 0.8 V) was flown. In the red line (after isolation), small rise up of 5 μA was observed. Rapid increase of photocurrent was observed above the threshold of the integrated laser.

## 5.4 Integrated membrane DFB laser and p-i-n photodiode with isolated structure

The measurement results of a membrane optical link consisting of an integrated DFB laser and a p-i-n PD are shown in this section. Figure 5.17(a) shows an optical microscopy image of the fabricated membrane optical link to be characterized in this section. The DFB laser and the p-i-n PD have lengths of 80 and 200 μm, respectively. The stripe width $W_s$ of the DFB laser and the p-i-n PD is a same value of 0.9 μm. The *p*-side electrode of both devices consisted of alloyed Au/Zn/Au electrode. Because the passive waveguide has a side cladding layer of approximately 3-μm-wide InP, an optical confiment in lateral direction is realized by not an air but a InP cladding layer. The grating design is uniform

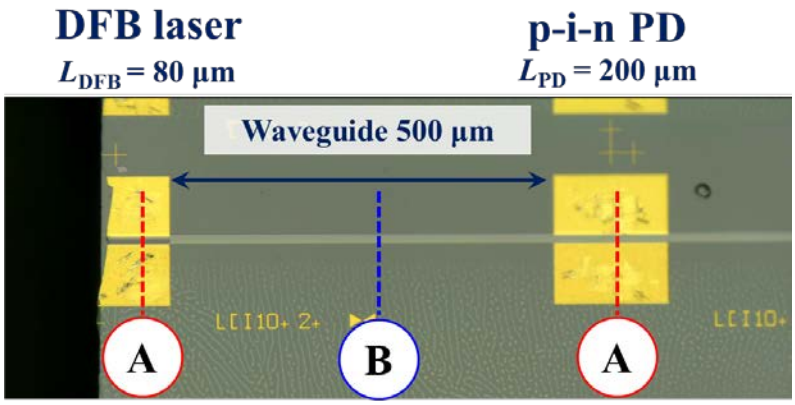


(a)

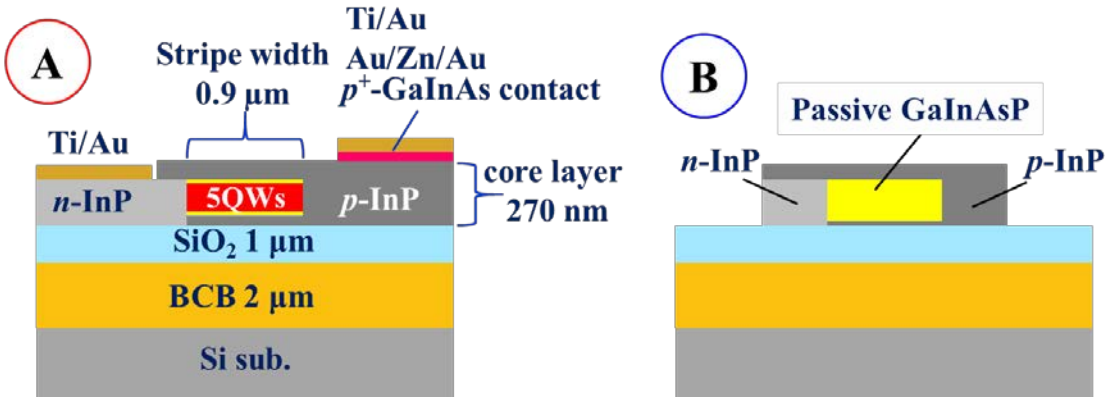


(b)

**Figure 5.17** (a) Optical microscopy image of the optical link using a membrane DFB laser and a p-i-n PD. (b) Schematic of cross section at active and passive waveguide regions.

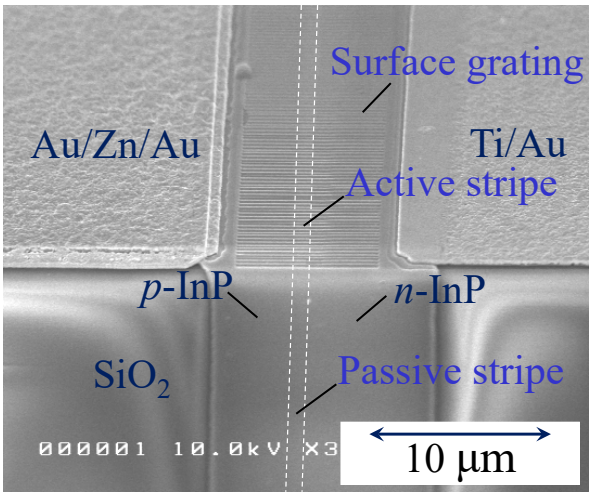


**Figure 5.18** Scanning electron microscopy image of a joint region of the DFB laser and the passive waveguide.

first order grating with the period of 295 nm and the duty ratio of 0.43. The absorption layer of the *p*-i-n PD is as same as that of the active region of the DFB laser. These devices are connected by a 500-μm-long passive waveguide. Figure 5.17(b) shows the cross-sections at the active and passive regions. The coupling efficiency between the active and passive section was calculated to be more than 98% in the chapter 3. The propagation loss of the passive waveguide was measured to be more than 8 dB/cm by using the Fabry-Perot resonance method performed for the waveguide with both cleaved facets. According to the propagation loss of 8 dB/cm and the length of 500 μm, the propagation loss for a 500-μm-long waveguide is at least 0.4dB. The output of the DFB laser on the opposite side to the p-i-n PD was cleaved, for measuring the lasing characteristics. Figure 5.18 shows the scanning electron microscopy image of a joint region of the DFB laser and the passive waveguide. As shown in the image, the surface grating pattern was successfully formed on the InP cap layer. The electrical isolation resistance $R_{iso}$ between the *p*-side electrodes of this device was measured, as shown in Figure 5.19(a). Figure 5.19(b) shows the obtained current–voltage characteristics. The isolation resistance $R_{iso}$ between the *p*-side electrodes was measured to be approximately 479k Ω within the measured voltage range. The leakage current was therefore expected to be less than 10 μA in a device operation, which implied that sufficient electrical isolation was obtained

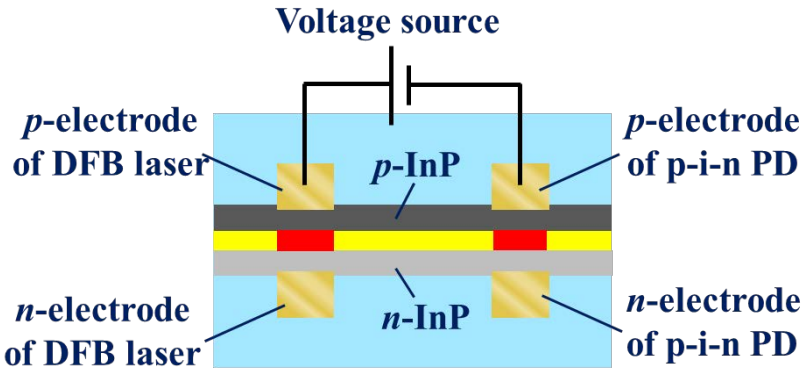


(a)

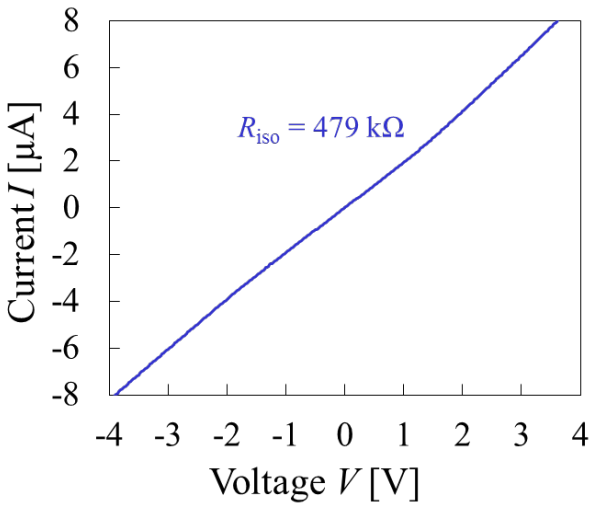


(b)

**Figure 5.19** Electrical isolation measurement. (a) Schematic of the measuring configuration. (b) Current–voltage characteristics.

in the fabricated structure.

### 5.4.1 Lasing characteristics of integrated laser

Prior to evaluate the fabricated optical link, the static characteristics of the integrated membrane DFB laser were measured. The DFB laser was characterized by measuring the light output from the cleaved facet formed on the side opposite to the p-i-n PD. The light output was detected by a commercial GaInAs p-i-n PD (G8370-10, Hamamatsu Photonics). Figure 5.20 shows *I-L*, *I-V* characteristics. The obtained threshold current $I_{th}$ was 0.48 mA, and the corresponding threshold current density $J_{th}$ was 667 A/cm$^2$ for the 5QW active layer. The external differential quantum efficiency $\eta_d$ was 2.5 % (facet output). It should be noted that even though the output efficiency from the facet was small, the facet output was not used in the optical transmission measurement to be shown later. Figure 5.21 shows the lasing spectrum measured at a bias current of 2.5 mA. The lasing wavelength was 1525 nm and the sub-mode suppression-ratio was 34dB. The stopband widthwas 43 nm, corresponding

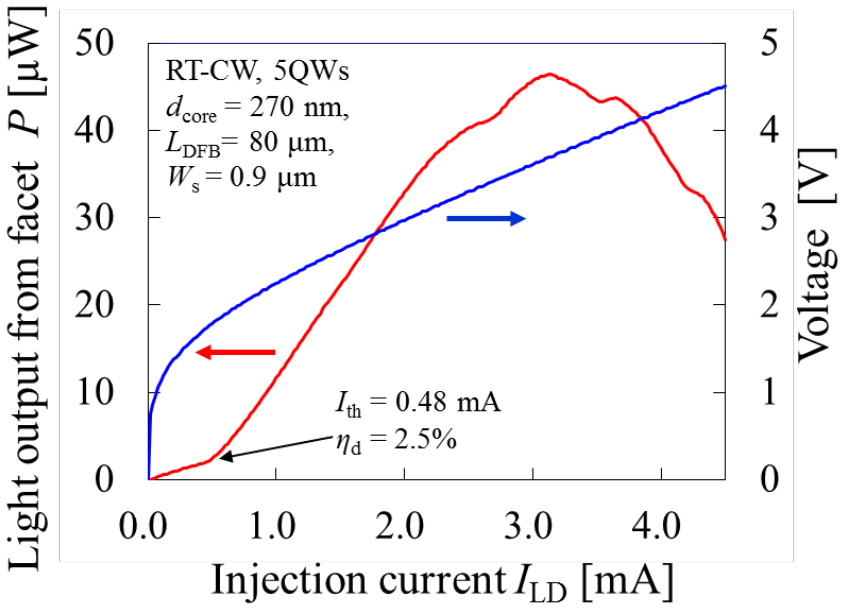


**Figure 5.20** Light output versus current characteristics of the membrane DFB laser integrated in an optical link.

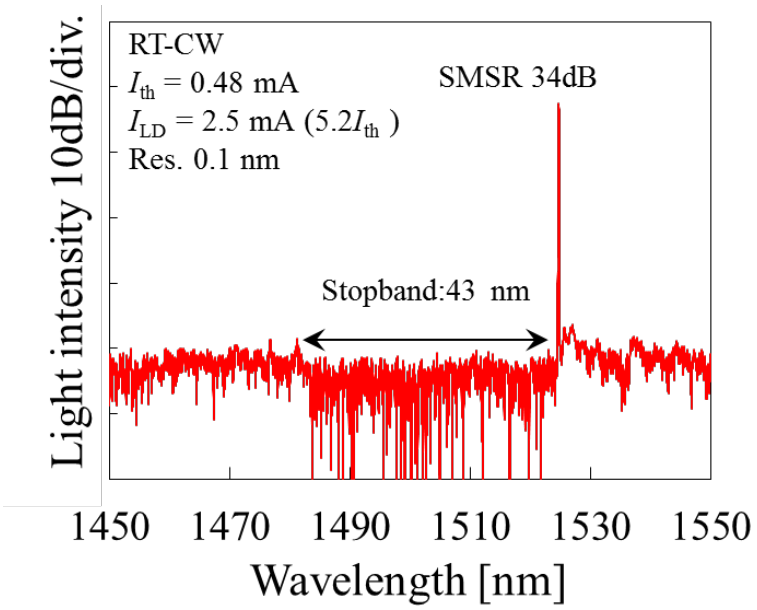


**Figure 5.21** Lasing spectrum of the integrated DFB laser at a bias current of 2.5 mA.

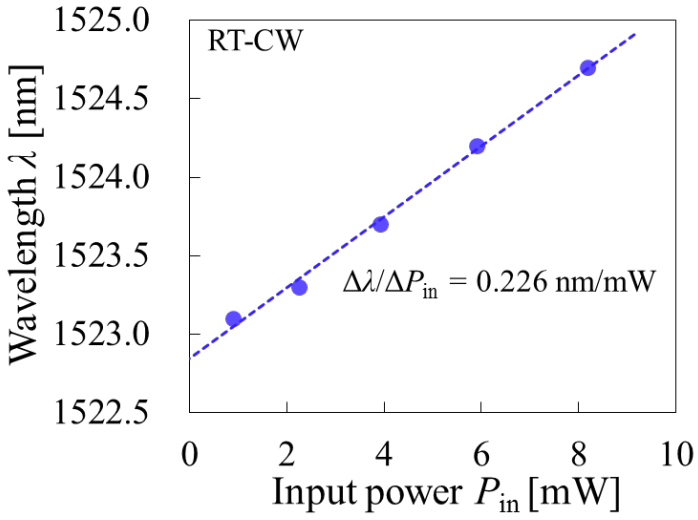


**Figure 5.22** Input power versus lasing wavelength characteristics.

to an index-coupling coefficient of 2000 $cm^{-1}$. The same values of stopband width were observed for the different devices on a same chip. The slight difference of Bragg wavelength was observed between the devices, which was attributed to the variation of stripe width or non-uniformity of regrowth thickness. Figure 5.22 shows input power versus lasing wavelength characteristics. The slope $\Delta\lambda/\Delta P_{in}$ was 0.226 nm/mW. By

approximating the input power as the dissipated power, and using wavelength shift due to the temperature of $\Delta\lambda/\Delta T$ = 0.01 nm, the thermal resistance of the DFB laser was calculated to be 2260 K/W.

### 5.4.2 Static optical transmission characteristics

The membrane optical link was statically characterized, by measuring the optical transmission properties between the DFB laser and the p-i-n PD. The light output of the DFB laser into the passive waveguide section was detected by the integrated p-i-n PD. The obtained photocurrent of the p-i-n PD, $I_{PD}$, as a function of the current injected into the DFB laser, $I_{LD}$ is shown in Figure 5.23. The light output from the cleaved facet (the same curve shown in Figure 5.20) is also shown, for comparison. The threshold current of the DFB laser observed from the photocurrent characteristic was 0.48 mA, which was the same value measured using the external p-i-n PD. The slope of $I_{LD}$-$I_{PD}$ characteristics was 68.4 μA/mA. The $\eta_d$ for the p-i-n PD side output can be calculated by assuming the

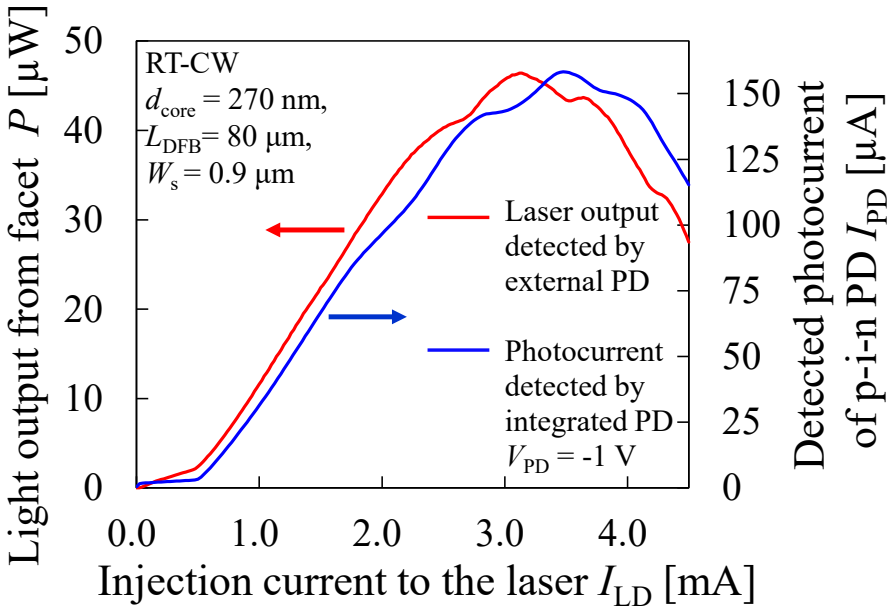


**Figure 5.23** Photocurrent of the integrated p-i-n PD and light output power of the laser (measured by the external PD) as functions of the laser injection current.

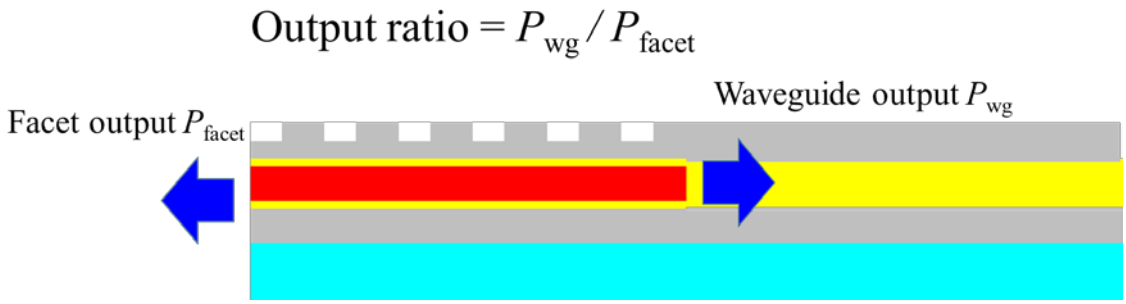


**Figure 5.24** Definition of the output ratio of the DFB laser.

**Table 5.2** Isolation characteristics in *p*-side electrodes

| Laser bias current $I_{LD}$ | Facet output $P_{facet}$ | Photocurrent $I_{ph}$ | Waveguide output $P_{wg}$ calculated from $I_{ph}$ | Output ratio $P_{wg}/P_{facet}$ |
|---|---|---|---|---|
| 1.0 mA | 11.6 μW | 31.5 μA | 25.2 μW | 2.2 |
| 1.5 mA | 22.4 μW | 66.7 μA | 53.4 μW | 2.4 |
| 2.0 mA | 32.5 μW | 96.7 μA | 77.4 μW | 2.4 |
| 2.5 mA | 40.3 μW | 126 μA | 101 μW | 2.5 |

internal quantum efficiency of p-i-n PD of 100% and incorporating the propagation loss of 500-μm-long waveguide of 0.4dB. The $\eta_d$ of the DFB laser was calculated to be 7.5% from the slope of the photocurrent by assuming the p-i-n PD responsivity of 1.25 A/W. The asymmetry in output power of the DFB laser is analyzed. Figure 5.24 shows the definition of an output ratio of the DFB laser in this time. Given that the photocurrent values of $I_{PD}$ at each laser bias current $I_{LD}$, the output power of the DFB laser into the integrated waveguide $P_{wg}$ was estimated as shown in Table 5.2. The waveguide output power was calculated using following relation;

$$P_{wg} = \frac{I_{ph}}{1.25\ \mathrm{A/W}} \tag{5.1}$$

The output ratio was in the range from 2.2–2.5 at each bias current. As one of the reasons for this asymmetry in the output ratio, the facet phase of the grating was considered.

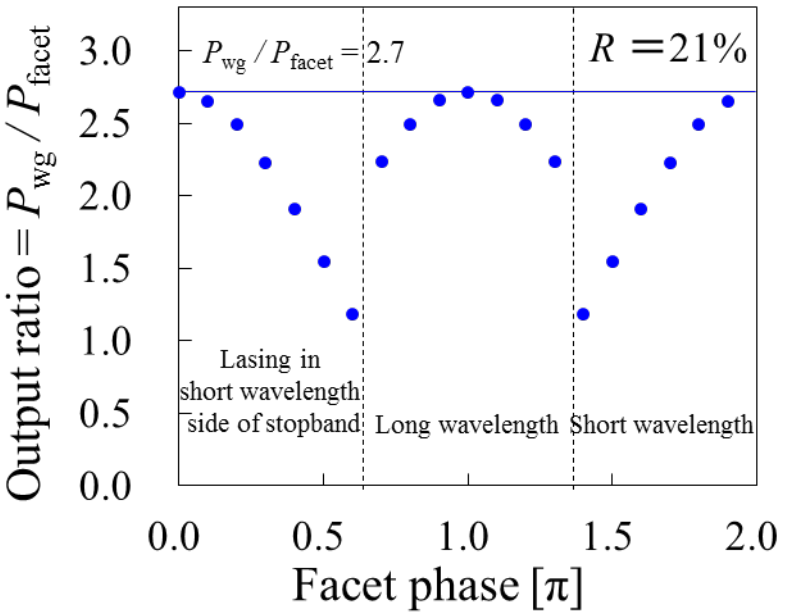


**Figure 5.25** Output ratio between the facet and waveguide output power as a function of facet phase. The facet reflectivity of 21% was used.

Figure 5.25 shows the output ratio between the facet and waveguide output power. The facet reflectivity of 21% was used in this calculation. It can be seen from the graph that the maximum output ratio of 2.7 is possible. The facet phase is consistent for the explanation of obtained output asymmetry.

Figure 5.26 shows the current–voltage characteristics of the integrated p-i-n PD for various laser bias currents, from 0 to 2.5 mA. To avoid a leakage current between the DFB laser and the p-i-n PD, only the curve at a laser current of 0 mA was obtained with opened electrode pads at the DFB laser. As shown, the p-i-n PD dark current was 0.2 μA at a bias voltage of -1 V. The dark current normalized by the absorption area was 0.1 A/cm$^2$. This unremarkable dark current density was due either to surface leakage or leakage at the waveguide region. The absorption of p-i-n PD did not reach the saturation region, as can be seen from the fact that the p-i-n PD current in reverse bias conditions was almost independent of the bias voltage.

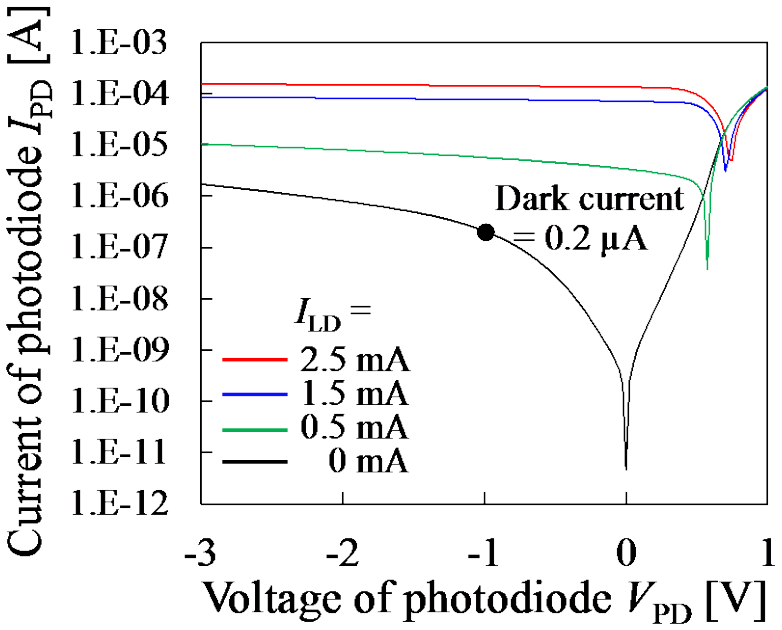


**Figure 5.26** Current–voltage characteristics of the integrated p-i-n PD, for various injection currents in the DFB laser.

### 5.4.3 Dynamic optical transmission characteristics

The small-signal frequency response $S_{21}$ of the full-optical link was measured with a vector network analyzer (VNA; Anritsu, 37397C). The setup for small-signal measurement is depicted in Figure 5.27. The ports 1 and 2 of the VNA were connected to bias-

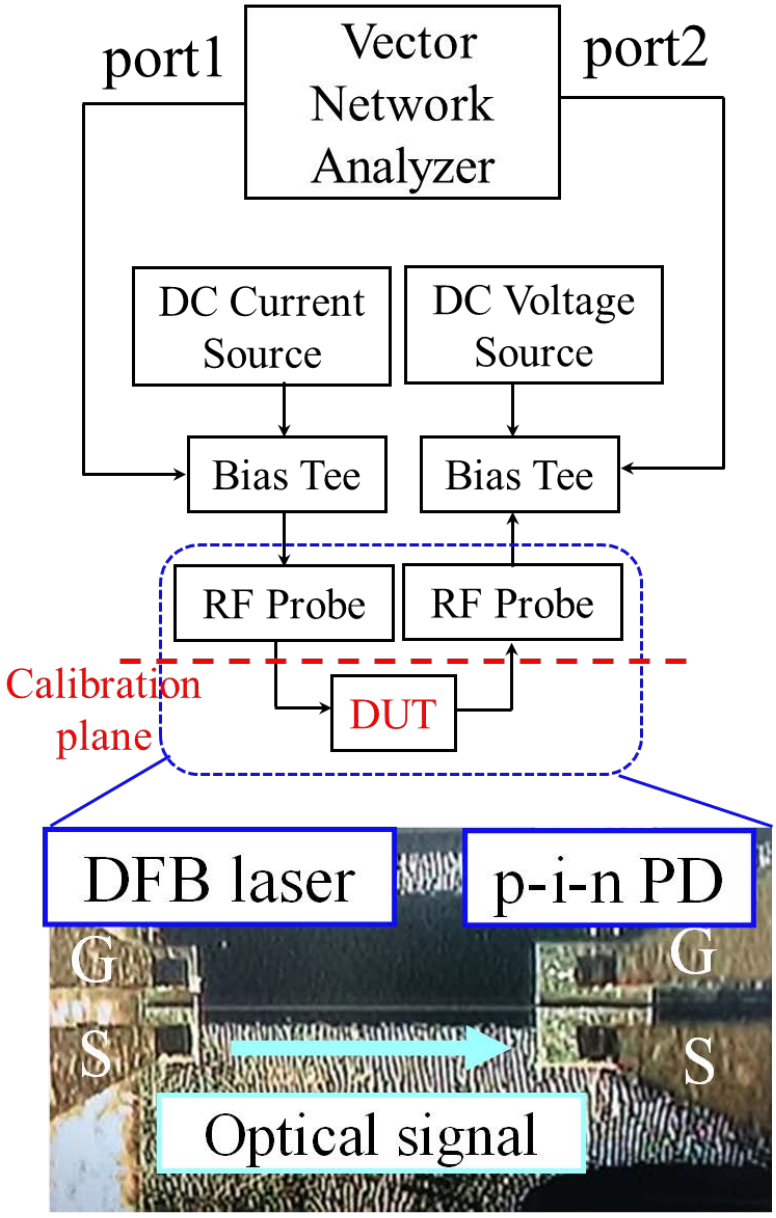


**Figure 5.27** Setup used to measure the small-signal response of the optical link. The left side image shows the block diagram of the measurement setup. The right side image shows an optical microscopy image of the device under test.

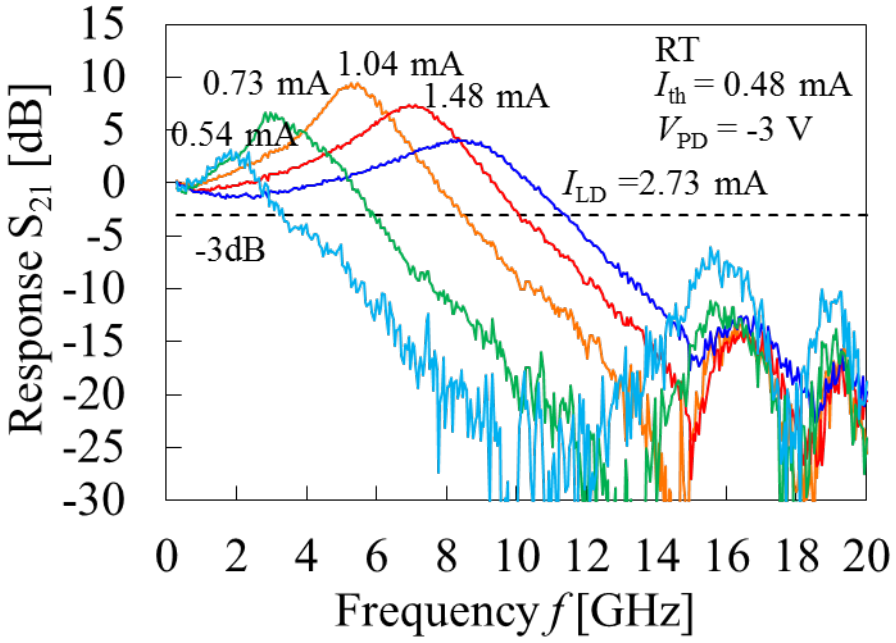


**Figure 5.28** Small-signal response of the fabricated optical link. (a) Bias current dependence measured at a -3 V PD bias voltage.

tees. A DC source was supplied to each bias-tee. A DC-coupled modulation signal was applied to the DFB laser via a 100-μm-pitch ground-signal (GS) RF probe (Cascade Microtech ACP40). The modulated optical signals were then transmitted via the optical link. The p-i-n PD electrical output was received by a signal-ground probe. The RF component of the detected signal was separated by a bias-tee, and input to Port 2 of the VNA. The measured device chip was put on a heat sink, whose temperature was controlled at 20 °C. In advance of measuring the device, a calibration up to the RF probe tips was performed with an impedance standard substrate (Cascade Microtech, 103-726, GS/SG, up to 67 GHz, pitch : 100 μm–250 μm). Therefore, the contribution of measurement system was excluded from the results.

Figure 5.28 shows the small-signal frequency response (40 MHz to 20 GHz) of the optical link for various bias currents, with a fixed p-i-n PD bias voltage of -3 V. A clear relaxation oscillation behavior was observed. In addition, the peak frequency increased with the increase in the DFB laser bias current. Therefore, these responses were not

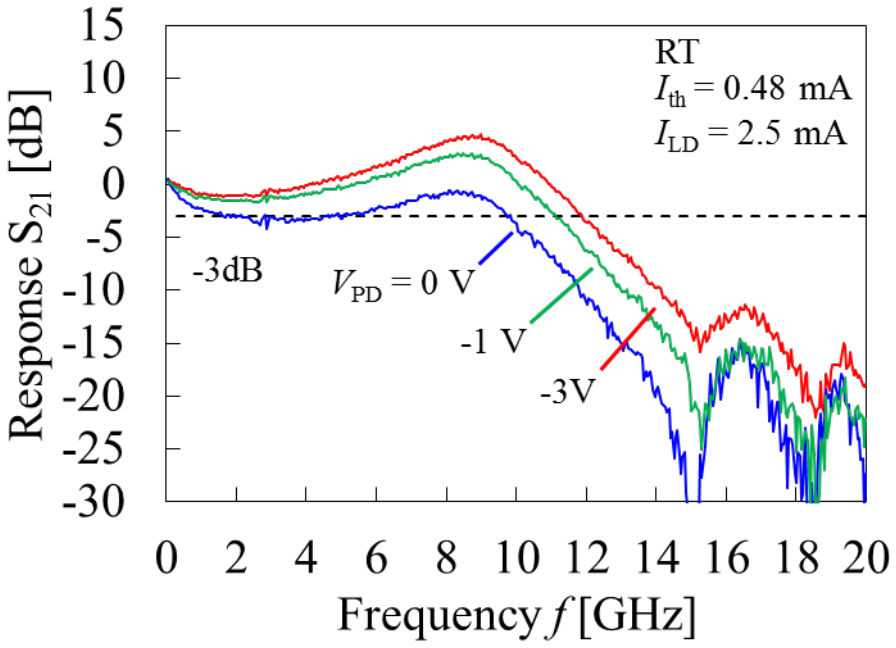


**Figure 5.29** Small-signal response of the fabricated optical link. Bias voltage dependence measured at a 2.5 mA DFB laser bias current.

electrical crosstalk between probes, but indeed the transmitted optical signal. The 3-dB bandwidth of the optical link was 11.3 GHz at a DFB laser bias current of 2.73 mA. Figure 5.29 shows the small-signal response for various p-i-n PD bias voltages, for a fixed DFB laser current of 2.5 mA. Increasing the bias voltage enhanced the 3-dB bandwidth, because the electrical field assisted in charge carrier extraction. The maximum bandwidth was obtained at a bias voltage of -3 V. We also determined the modulation efficiency of the integrated membrane DFB laser from the small-signal frequency response of the optical link.

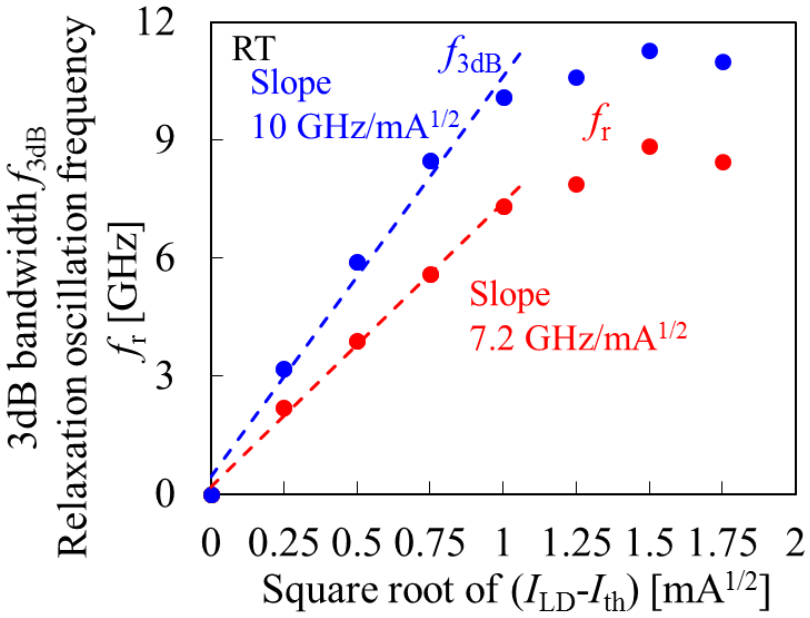


**Figure 5.30** Relaxation oscillation frequency $f_r$ and 3-dB bandwidth $f_{3dB}$ as a function of the square root of the bias current above threshold.

Figure 5.30 shows the 3 dB bandwidth $f_{3dB}$ and the relaxation oscillation frequency $f_r$ as functions of the square root of the bias current above threshold. Because the measurements were performed using on-chip p-i-n PD, $f_{3dB}$ represents bandwidth of the optical link. Modulation efficiencies of 10.8 GHz/mA$^{1/2}$ and 7.6 GHz/mA$^{1/2}$ were obtained for $f_{3dB}$ and $f_r$, respectively; the latter was smaller than that of the DFB laser described in the chapter 4 (9.9–12 GHz/mA$^{1/2}$) . However, the active volume of this DFB laser was 2.16 μm$^3$, which was larger than that of previous ones (1.68–0.77 μm$^3$). Given that the modulation efficiency is proportional to the square root of the active volume, the value of 7.6 GHz/mA$^{1/2}$ for an active volume of 2.16 μm$^3$ is in good agreement with the previous result. In measured small signal responses, there were bias-current independent peaks near the 16 and 19 GHz frequencies. To confirm the origin of these peaks, Figure 5.31 shows the frequency response of $S_{21}$ and $S_{12}$. The response $S_{21}$ (from the laser to the PD) contains the contribution from both optical signal and electrical cross talk signal. In contrast, the response $S_{12}$ (from the PD to the laser) contains the contribution from only electrical signal directly propagating the device. The $S_{12}$ had peaks near the 16 and 19 GHz frequencies, which implied these peaks were due to the electrical signal. Although

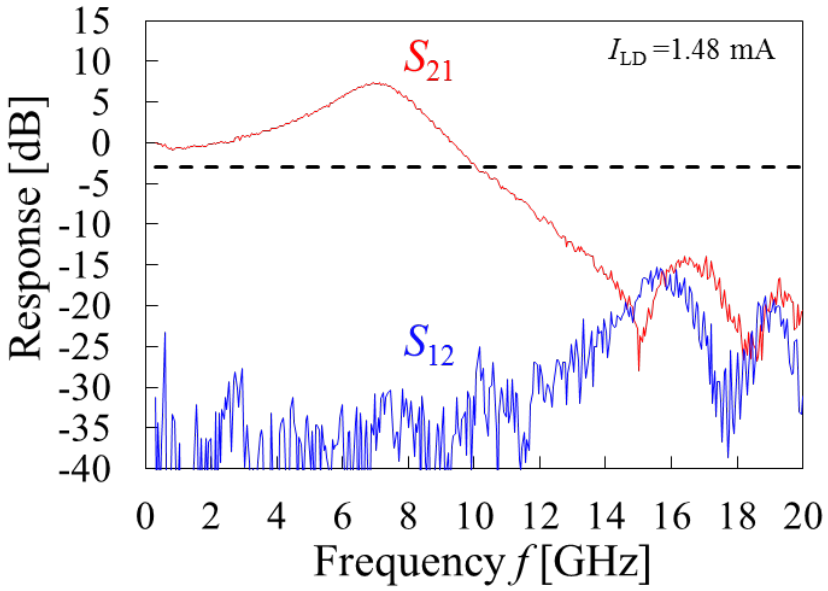


**Figure 5.31** Frequency responses of $S_{21}$ and $S_{12}$.

these peaks were due to the electrical signal being transmitted between the RF probes, it was believed that the peaks had little effect on the modulation measurement, because the response magnitude was small compared with that of the optical signal.

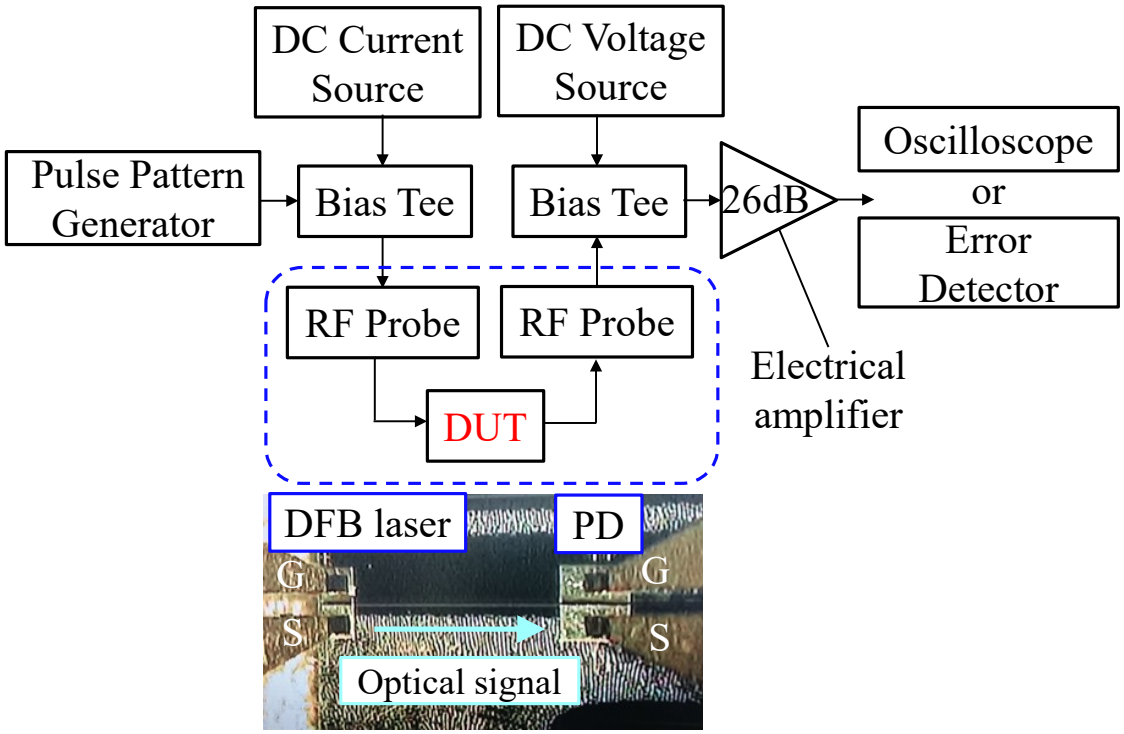


**Figure 5.32** Measurement setup for evaluation of large-signal transmission through the optical link.

Data transmission via the membrane optical link was performed by large-signal direct modulation of the DFB laser. Figure 5.32 shows an experimental setup for data-transmission measurements. The electrical modulating signals were generated by a pulse-pattern generator (Anritsu MP1800A implementing MU181020B, and MU182021A). Electrical signals were sent to the DFB laser via a bias-tee and a GS probe. The optical signal from the DFB laser was transmitted through the passive waveguide, and detected by the p-i-n PD. The electrical output signal of the p-i-n PD was amplified by a 38 GHz electrical amplifier with a 26-dB gain (SHF Communication Technologies, SHF806E). The signals were recorded with a sampling oscilloscope (Agilent, 86109B) or analyzed with an error detector (Anritsu, MP1800A implementing MU181040B, and MU182041A). In this measurement setup, AC components of the p-i-n PD output signals were separated from the signals at a bias-tee. Therefore, an extinction ratio of transmitted signal was not obtained. The input electrical signal to the DFB laser was a non-return-to-zero (NRZ) pseudorandom binary sequence (PRBS) of $2^{31}$-1 signals, with a voltage swing of 0.75 $V_{pp}$. Figure 5.33 shows transmitted 10 Gbit/s eye diagrams at a 2.5 mA DFB laser

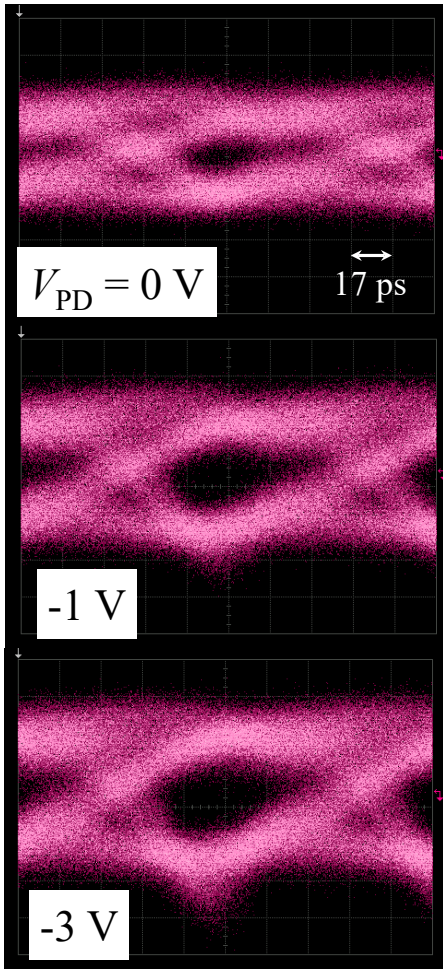


**Figure 5.33** 10 Gbit/s eye diagrams transmitted through the optical-link for various p-i-n PD bias voltages (0 to -3V). The DFB laser was biased at 2.5 mA, and driven by an NRZ, PRBS ($2^{31}$-1 signals) electrical modulating signal with a voltage swing of 0.75 $V_{pp}$.

bias current, recorded for various p-i-n PD bias voltages. As the bias voltage of the p-i-n PD increased, larger eye openings were observed, which was consistent with the results of the small-signal measurements as shown in Figure 5.29. Figure 5.34(a) shows the measured bit-error-rate (BER) versus the data-rate and the energy consumption in the laser at each data-rate. All plots were obtained in the same operating conditions (except for the data-rate). A BER in the order of $10^{-7}$ was obtained up to a data rate of 10 Gbit/s. An energy consumption of the laser at 10 Gbit/s was 825 fJ/bit. Above 10 Gbit/s, the BER rapidly degraded. The

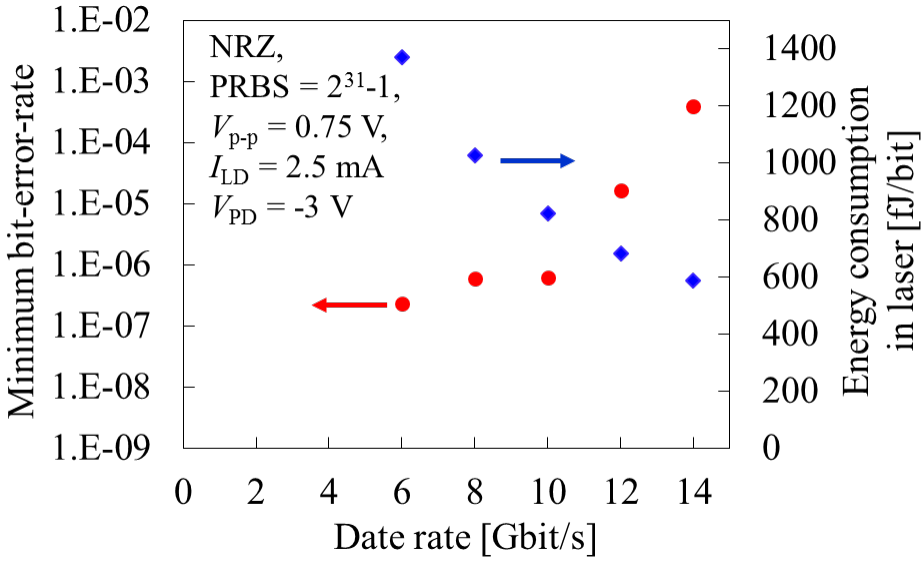


(a)

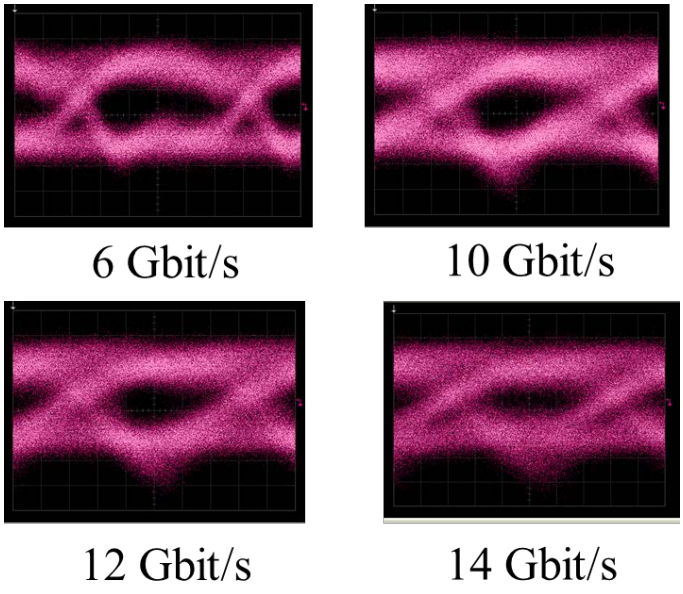


(b)

**Figure 5.34** (a) Bit-error-rate characteristics and energy consumption in the laser of NRZ signal transmission through the membrane optical link; with the laser bias current of 2.5 mA, and the p-i-n PD bias voltage of -3 V. (b) Eye diagrams for various data rates.

eye diagrams corresponding to the measured BER plots are shown in Figure 5.34(b); as shown, the eye diagrams for 12 and 14 Gbit/s were more closed because of signal distortion.

## 5.5 Conclusion

This chapter described the integrated membrane optical link consisting of DFB laser, passive waveguide and p-i-n PD. In section 5.2, the device structure and fabrication process of optical link device were explained. The electrical isolation process is introduced for the fabrication. Section 5.3 described the electrical isolation characteristics of the membrane optical link. The additional isolation process was successfully performed. The introduced process enhance the isolation resistance between the *p*-side electrodes to one-order of magnitude. The expected leakage current was less than 10 μA in device operation condition. From the laser current versus photocurrent characteristics, significant suppression of leakage current was confirmed. Section 5.4 described the static and dynamic characteristics of the fabricated membrane optical link device. The integrated DFB laser showed a threshold current of 0.48 mA, with a sub-mode suppression ratio of 34 dB at a bias current of 2.5 mA. The detection of the transmitted light output of the DFB laser by integrated p-i-n PD was confirmed from static measurements of the optical link. The dynamic characteristics of the membrane optical link were measured for both small-signal and large-signal modulations. For a DFB laser bias current of 2.73 mA and a p-i-n PD bias voltage of -3V, the 3 dB bandwidth of the optical link was 11.3 GHz. Data-transmission with NRZ PRBS of $2^{31}$-1 signals was performed. 10 Gbit/s transmission with a BER of $6\times10^{-7}$ was achieved at a DFB laser bias current of 2.5 mA.

# Chapter 6

# Future prospects of membrane optical link

6.1 Introduction 290
6.2 Integration of low-loss waveguide 291
6.2.1 Properties of membrane rib-waveguide 292
6.2.2 Preliminary experimental results 294
6.3 Integration of membrane distributed-reflector laser 297
6.4 Conclusion 302
References

## 6.1 Introduction

This chapter describes future prospects expected from the achievements in this research. Low-threshold and high-speed direct modulation of membrane DFB lasers were realized in the chapter 4. A fundamental integrated optical link device using membrane-based DFB laser and p-i-n PD was fabricated in the chapter 5. As a further approach, an extending the connection length of the optical link and enhancing the efficiency of membrane DFB laser are essential to exhibit the capability of membrane optical link as an on-chip interconnection. The section 6.2 describes the low-loss InP waveguide for the integration with membrane DFB laser and p-i-n PD. The current device has a waveguide with highly doped InP cladding layers. To realize low-loss waveguide having around 1 dB/cm waveguide loss, the doped cladding layers should be removed. The fundamental mode characterizes and fabrication results are described. In section 6.3, membrane distributed-reflector (DR) lasers are described. The uniform grating DFB laser has the

equal output power for two output ports. The DR laser structure, which consists of integrated DFB laser and DBR, enhances the single directional output power.

## 6.2 Integration of low-loss waveguide

The origins of waveguide loss are the absorption of material, radiation and scattering loss. The former two factor can be avoid by choosing material and waveguide design. However, scattering loss strongly depends on fabrication process as well as the waveguide structure. For the high density integration of an optical circuits, strongly confined waveguide can be bend by the radius of less than 10 μm. In strongly confined waveguide, however, optical field interact with the roughness of the core and results in high waveguide loss. As the report for the low waveguide loss of silicon photonics waveguide, the loss was 0.27 dB/cm using the shallow-rib structure as shown in Figure 6.1 [1]. In the shallow-rib structure, scattering loss is significantly small because the small fraction of the electric field distribution overlapped on a sidewall. However, since such weak confinement waveguide has the minimum bending radius around several tens μm. A deeply etched waveguide should be introduced in bending section. Here, consideration of low-loss rib waveguide into a membrane optical link will be presented.

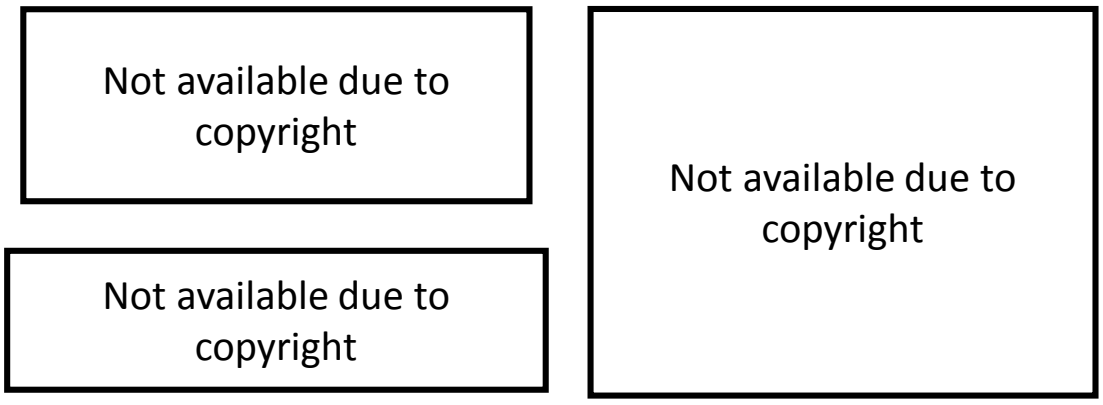


**Figure 6.1** (a) Mode-profile and cross sectional SEM image of silicon shallow rib-waveguide. (b) Plots for insertion loss versus waveguide length [1].

### 6.2.1 Properties of membrane rib-waveguide

Figure 6.2 shows the comparison of the waveguide structure for conventional buried structure and shallow rib structure. The passive waveguide in chapter 4 and 5 has highly doped InP side cladding layers, which causes the high propagation loss due to the absorption by free-carrier and intervalence absorption. The rib-waveguide in this chapter consists of only undoped InP and $SiO_2$ cladding layer. It is expected that this structure avoids both absorption loss and scattering at sidewall by roughness. The optical confinement is realized by equivalent refractive index different created by slightly etching the surface InP. The characteristic comparison is shown in Table 6.1. The GaInAsP/InP buried waveguide has extremly low coupling loss but propagation loss is relatively high. This waveguide is preferred to be used in short distance connection or integrated DBR. The undoped InP rib waveguide has low propagation loss despite of higher coupling loss. This waveguide structure is suited to long distance connection. Figure 6.3 shows the schematic structure of membrane optical link utilizing the undoped InP rib waveguide. The undoped InP layer can be formed by the same BJB regrowth method as GaInAsP layer described in chapter 3. The optical confinement structure in a passive waveguide is obtained by slight etching of surface layer. Figure 6.4 shows the optical mode profile of TE-0th mode in the rib waveguide. The rib height is 70 nm in this calculation. The waveguide width of 0.8 μm satisfies the single mode condition. It can be confirmed that the only small portion of the optical field is overlapped on the sidewall.

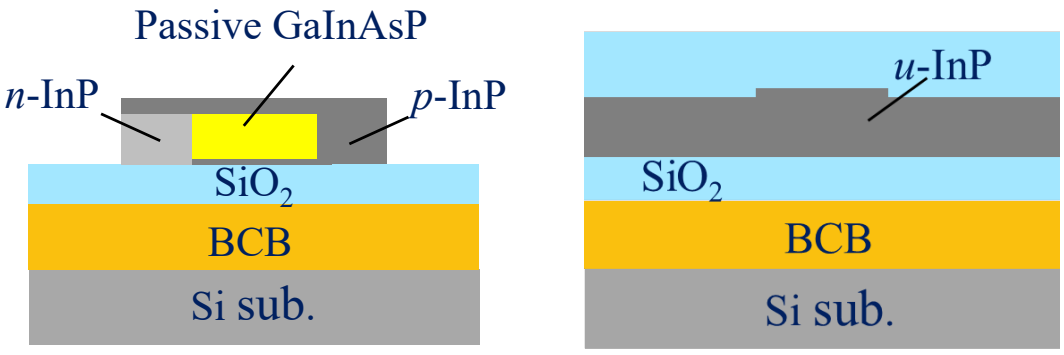


(a) (b)

**Figure 6.2** Comparison of waveguide structure (a) buried structure waveguide (b) shallow rib waveguide.

**Table 6.1** Characteristic comparison of two waveguide structures

| | Propagation loss | Coupling loss | Application |
|---|---|---|---|
| Figure 6.2(a) GaInAsP/InP | High (~10 dB/cm) | Extremely Low (<0.09dB) | Integrated DBR, short distance connection |
| Figure 6.2(b) Undoped InP | Low (<1 dB/cm possible) | Low (~0.5dB) | Long distance connection |

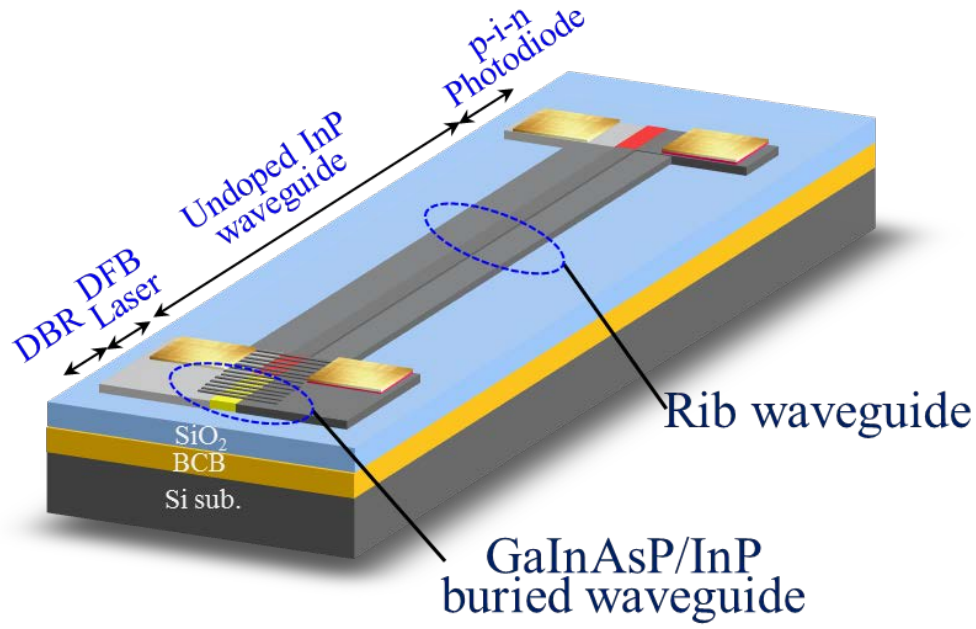


**Figure 6.3** Schematic structure of membrane optical link with undoped InP rib waveguide.

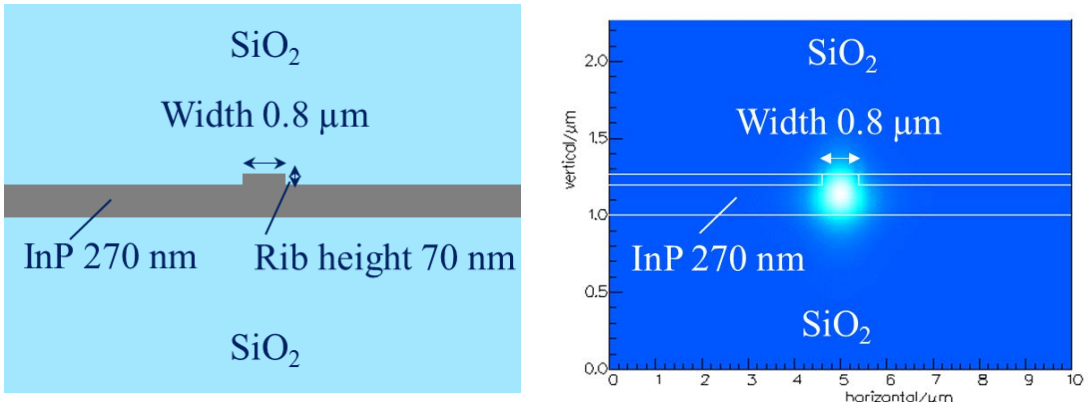


(a) (b)

**Figure 6.4** Schematic structure of membrane optical link using DFB laser and p-i-n photodiode.

### 6.2.2 Preliminary experimental results

The initial wafer consists of etch stop layers and 270-nm-thick undoped InP layer. The the whole fabrication process flow of undoped InP membrane rib-waveguide (Figure 6.5) is described as follows;

(1) Wafer bonding and formation of undoped InP layer

The process is performed by the procedure given in section 4.3.2.

(2) $SiO_2$ mask deposition

The 50-nm-thick $SiO_2$ layer is deposited by PECVD.

(4) ZEP resist coating

As an EB lithography resist, 700-nm-thick ZEP 520 is spin coated.

(5) $SiO_2$ etching

The resists patterns are transferred onto $SiO_2$ layer by using $CF_4/SF_6$ ICP-RIE.

(6) Removing resist

The ZEP 520 is removed by resist remover (ZDMAC) and $O_2$ plasma reactor.

(7) InP etching

The InP layer is etched by wet chemical solution of $HCl:H_2SO_4:H_2O_2$ = 1:1:8 at 20°C. This etchant has etching rate of approximately 1 nm/sec.

(8) $SiO_2$ cladding layer deposition

A 1-μm-thick $SiO_2$ cladding layer is deposited onto the substrate by PECVD.

The processed substrate is cleaved so as to form the output facets because a measurement is performed by butt-coupling the spherical lensed fiber to the facets.

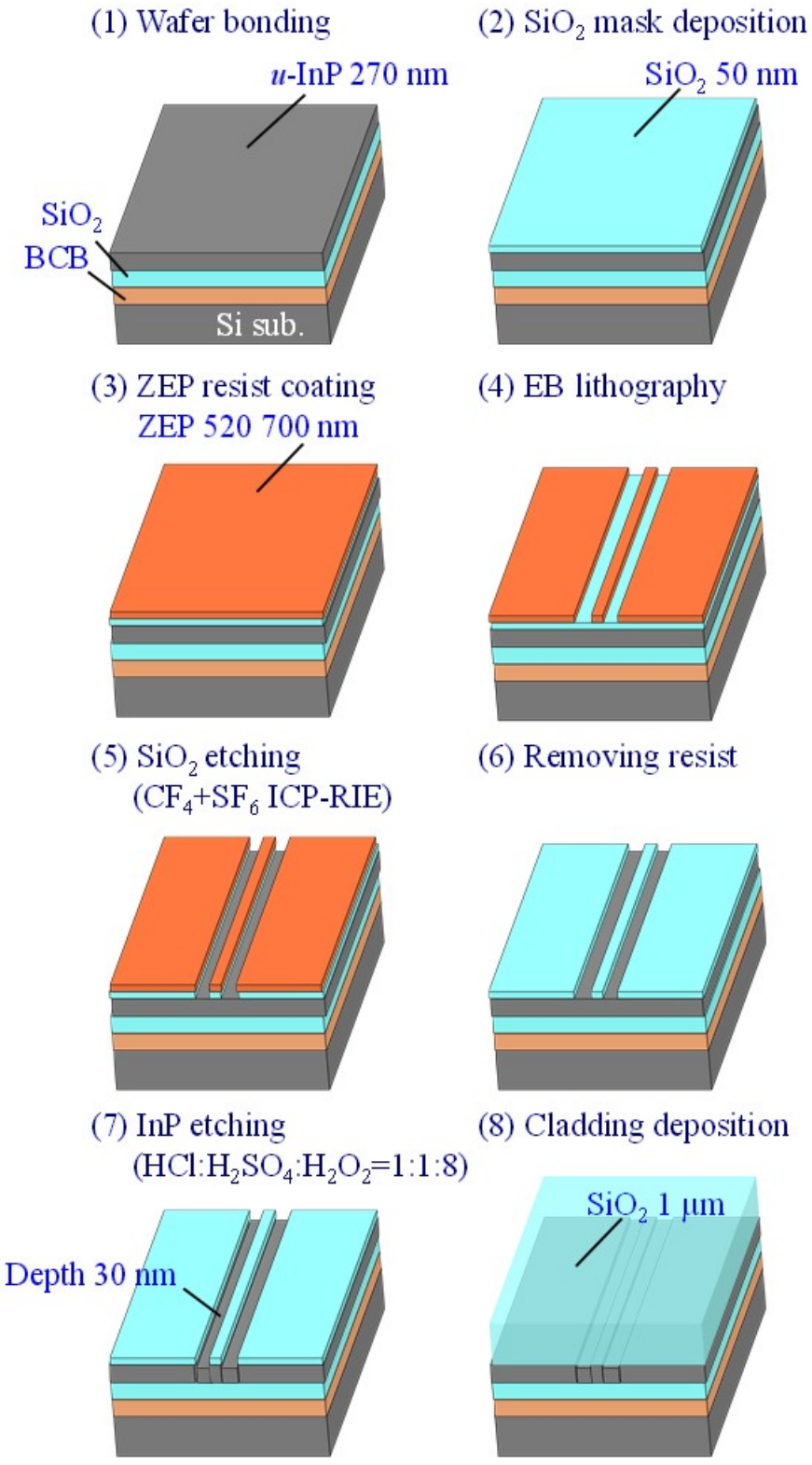


**Figure 6.5** The whole fabrication process flow of undoped InP membrane rib-waveguide.

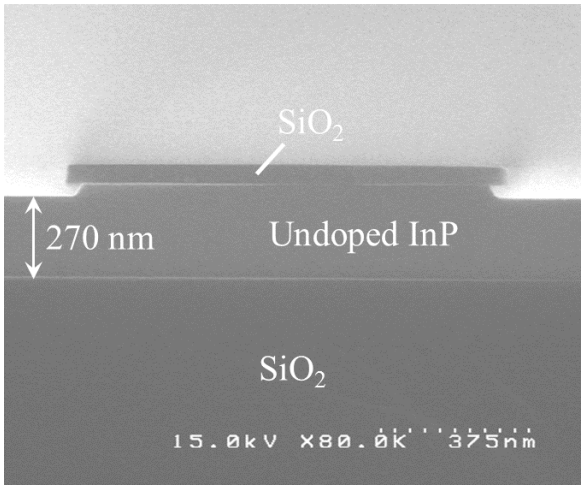


**Figure 6.6** SEM image of cross sectional view of the InP membrane rib waveguide.

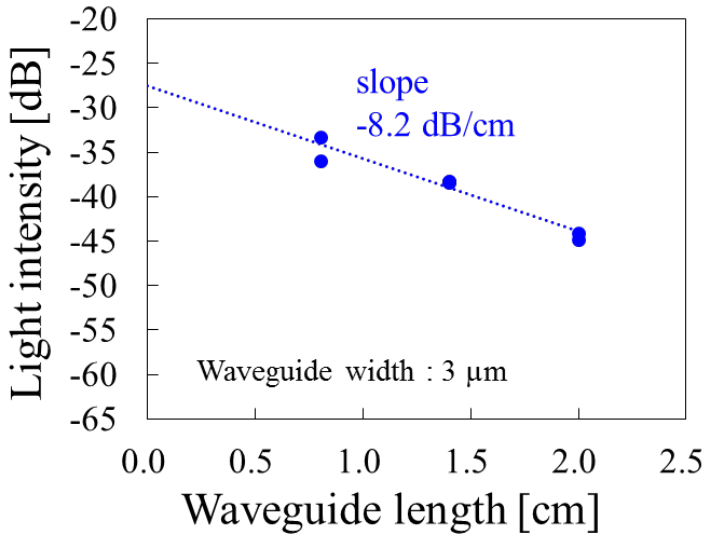


**Figure 6.7** Light transmission intensity versus waveguide length characteristics.

Figure 6.6 shows the SEM image of cross sectional view of the InP membrane rib waveguide after InP wet etching process. The top $SiO_2$ mask was to be removed next process. The smoothly etched surface was confirmed. The rib height was precisely controlled thanks to the low etching rate of used chemical solution 1 nm/sec. To characterize the propagation loss of the waveguide, the devices with three different waveguide length of 0.8, 1.4 and 2 cm were prepared. Figure 6.7 shows the light transmission intensity versus waveguide length characteristics. From the slope of the linear fitting for these plots, the propagation loss was measured to be 8.2 dB/cm. This propagation loss is very high value expected for the weak confiment rib-waveguide.

Although the reason is not specified yet, it seems that the surface of the InP may has the problem such as having residual absorption layer. If the remaining problem is solved, a propagation loss of approximately 1 dB/cm can be expected as demonstrated in a silicon rib-waveguide.

## 6.3 Integration of membrane distributed-reflector laser

The distributed-reflector laser is the DFB laser integrated with DBR at the one or both output. Single directional output is obtained without any optical coating technique. Figure 6.8 shows the schematic structure of membrane DR laser. The DFB region is the same structure as the device in chapter4. The DBR is formed on a one side of passive waveguide. The integrated DRB modifies the standing-wave profile in the cavity, then optical power strongly output only from one side.

Recently, our group realize the highly efficient membrane DR lasers. I briefly introduce these works.

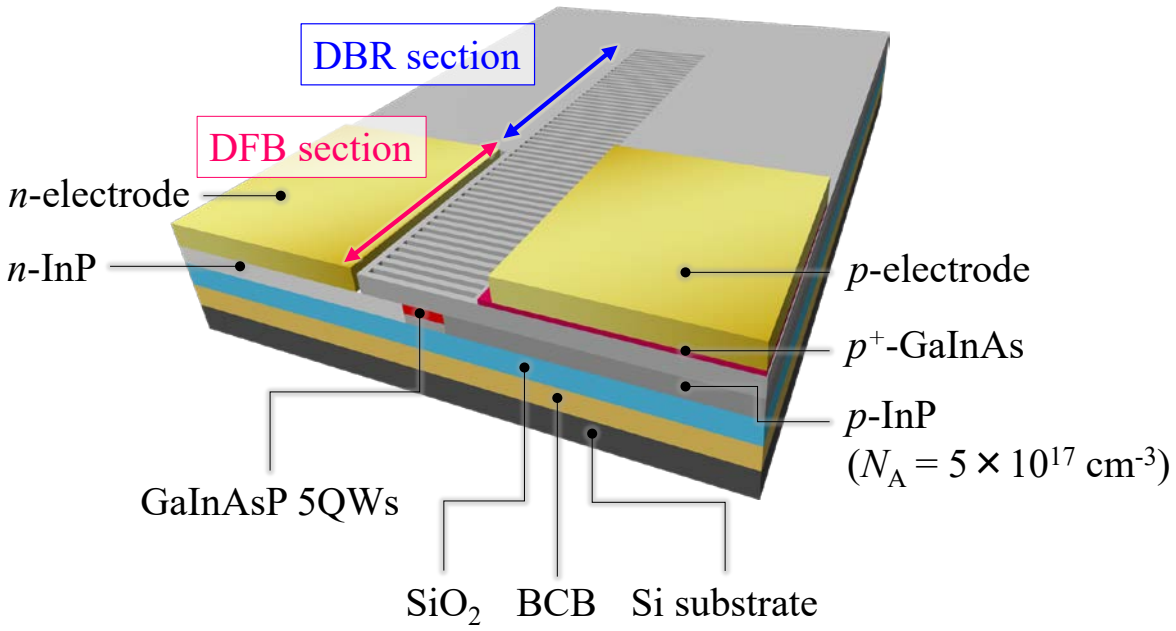


**Figure 6.8** Schematic structure of membrane DR laser.

**Membrane DR laser with reduced doping concentration of side *p*-InP [2]**

The current membrane laser has waveguide loss of 42 $cm^{-1}$ [3]. This loss was reduced to be 22 $cm^{-1}$ by changing the doping concentration of *p*-InP from $4 \times 10^{18}$ $cm^{-1}$ to $5 \times 10^{17}$ $cm^{-1}$[4]. By incorporating the reduced doping design, the membrane DR laser with low-doped ($5 \times 10^{17}$ $cm^{-1}$) *p*-InP showed higher external differential quantum efficiency. Figure 6.9 shows the light output and voltage characteristics of the membrane DR laser with reduced *p*-doping concentration. The length of DFB and DBR region are 32 μm and 50 μm, respectively. The periods of both the DFB and DBR gratings are same value of 298 nm. The index coupling coefficient was 1800 $cm^{-1}$, measured from the stopband width in emission spectrum. The BCB adhesive layer of this device was 0.5 μm reduced from 2 μm to improve the thermal impedance characteristics. The threshold current $I_{th}$ was 0.21 mA, corresponding to a threshold current density, $J_{th}$, of 820 A/$cm^2$. The external differential quantum efficiency, $\eta_{df}$, was 32% for the front-side output. In addition to the high $\eta_d$, the maximum power conversion efficiency of 12 % was obtained.

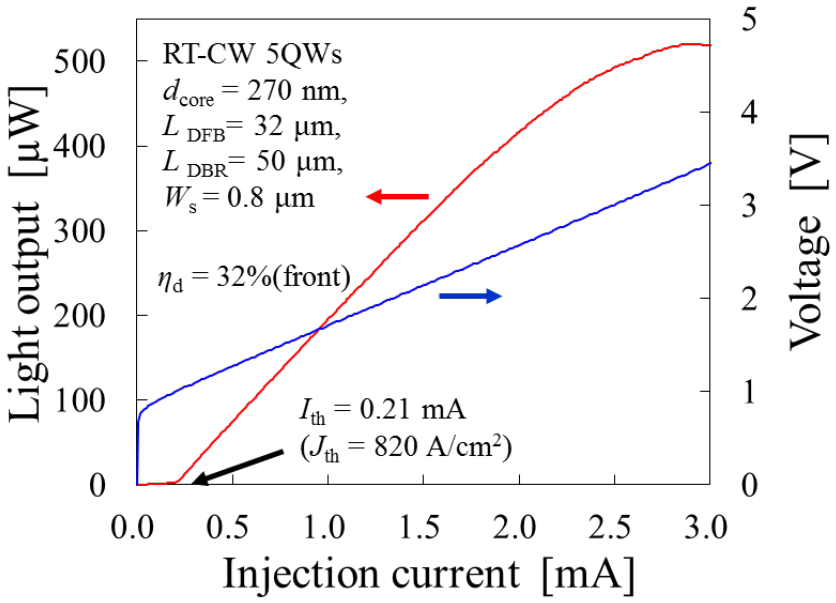


**Figure 6.9** Light output and voltage characteristics of the membrane DR laser with reduced doping concentration of *p*-InP.

**Membrane DR laser with reduced index coupling coefficient $\kappa$**

Deep surface grating is required to obtained strong index coupling coefficient. However, there is concerns for deeply etched grating cause scattering loss in a cavity. The membrane DR laser with shallow grating depth of 25 nm was fabricated. According to Figure. 2.8, the 25-nm-depth grating corresponds to the index coupling coefficient of 800 $cm^{-1}$. Figure 6.10 shows the light output and voltage characteristics of the membrane DR laser with reduced index coupling coefficient. The threshold current $I_{th}$ was 0.44 mA, corresponding to threshold current density $J_{th}$ of 1570 $A/cm^2$. The external differential quantum efficiency from front facet $\eta_{df}$ was 36%. The maximum power conversion efficiency was 14.6%. In this work, the high efficiency operation was realized experimental demonstration. It is valuable to analytically clarify the relation between the grating depth and scattering loss in future work.

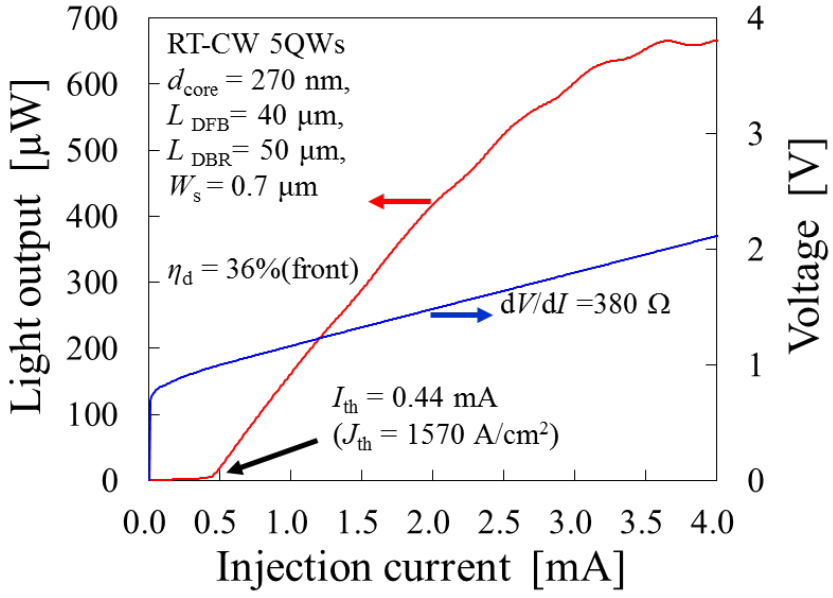


**Figure 6.10** Light output and voltage characteristics of the membrane DR laser with reduced index coupling coefficient.

**Direct modulation of membrane DR laser**

The modulation characteristics were also evaluated. Figure 6.11 shows the large-signal modulation measurement setup for membrane DR laser. Comparing setup shown in

Figure 4.62 the total system bandwidth was improved to perform better modulation measurement. Arbitrary waveform generator (AWG; Keysight, M8196A) was used as signal source. The AWG can compensate attenuation and group-delay in RF components by using feed-forward-equalization (FFE). Before measuring the device, $S_{21}$ characteristics of the connection cables from AWG to the device were measured and input to the AWG. As another improved point, the length of RF cable connecting photoreciever and error-detector was shorten from 1 m to 0.3 m. Figure 6.12 shows the 20 Gbit/s eye diagram of membrane DR laser biased at 1.06 mA using NRZ and PRBS pattern of $2^{11}$-1.

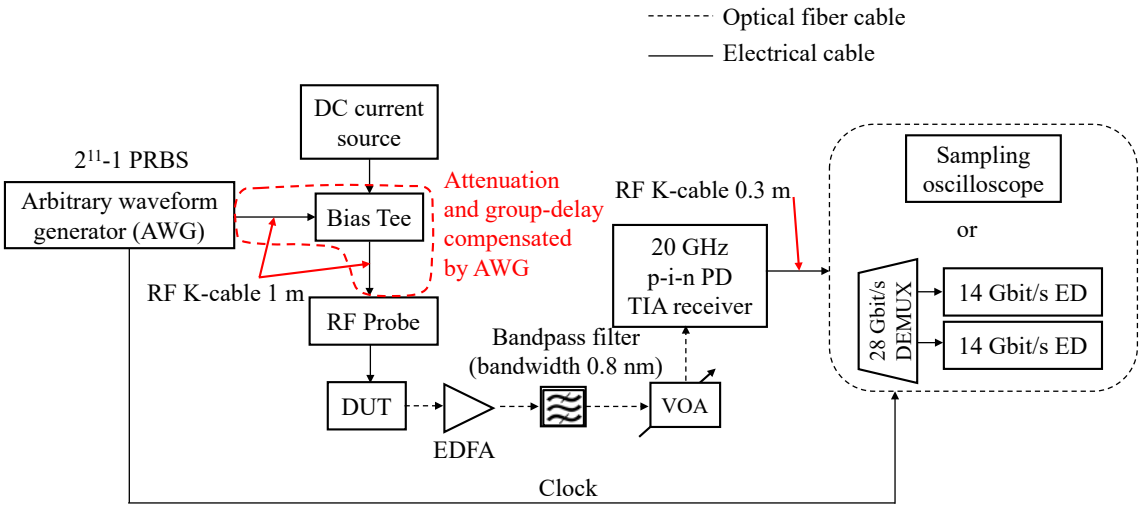


**Figure 6.11** Measurement setup for large-signal modulation of membrane DR laser.

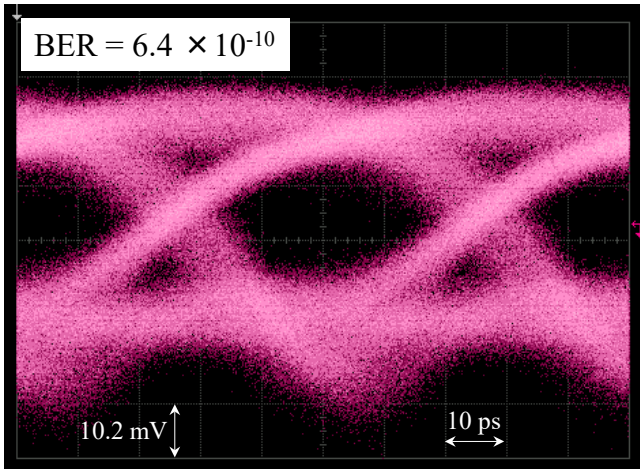


**Figure 6.12** Eye diagram of membrane DR laser biased at 1.06 mA for 20 Gbit/s NRZ signal using a $2^{11}$-1 pattern.

The minimum bit-error-rate (BER) was $6.4\times10^{-10}$. The energy cost per bit for this data transmission can be calculated by the product of the bias current and the voltage divided by the data rate as same as calculated in section 4.5.3.

$$\text{Energy cost} = \frac{I_\text{b}V_\text{b}}{\text{Data}-\text{rate}} \tag{6.1}$$

$$= \frac{1.06\ \text{mA} \times 1.76\ \text{V}}{20\ \text{Gbit/s}} \tag{6.2}$$

$$= 93\ \text{fJ/bit} \tag{6.3}$$

The obtained energy cost was 93 fJ/bit. This value was lower than the target energy cost of 100 fJ/bit. And the lowest energy cost among the DFB or DR laser was successfully achieved to the best of our knowledge [5]. Further energy cost reduction can be achieved by improving following points.

**BER measurement system**

When BER measurement was performed without using EDFA, data-transmission with 2dB penalty to the sensitivity curve of used photoreciever was obtained. For the device which can emit sufficient light output power, improvement of BER characteristics is expected by eliminating EDFA from measurement system.

**Active region volume $V_\text{a}$**

The reason for the bias current used for modulation could not be reduced further is the relaxation oscillation and the relative intensity noise. Reduction of active volume results in increment of current density at a same bias current. The modulation characteristic at low bias current will be improved by a stronger damping and flat frequency response characteristics obtained by increasing bias current density.

**Differential resistance $R_\text{diff}$**

In order to reduce the operating voltage, it is necessary to reduce the differential resistance with maintaining low-threshold current operation. The differential resistance increases as a cavity length shortened. By decreasing the active layer volume with a long cavity length by reducing the stripe width or the number of quantum wells, it is considered possible to avoid increasing the differential resistance for short cavity length device.

## 6.4 Conclusion

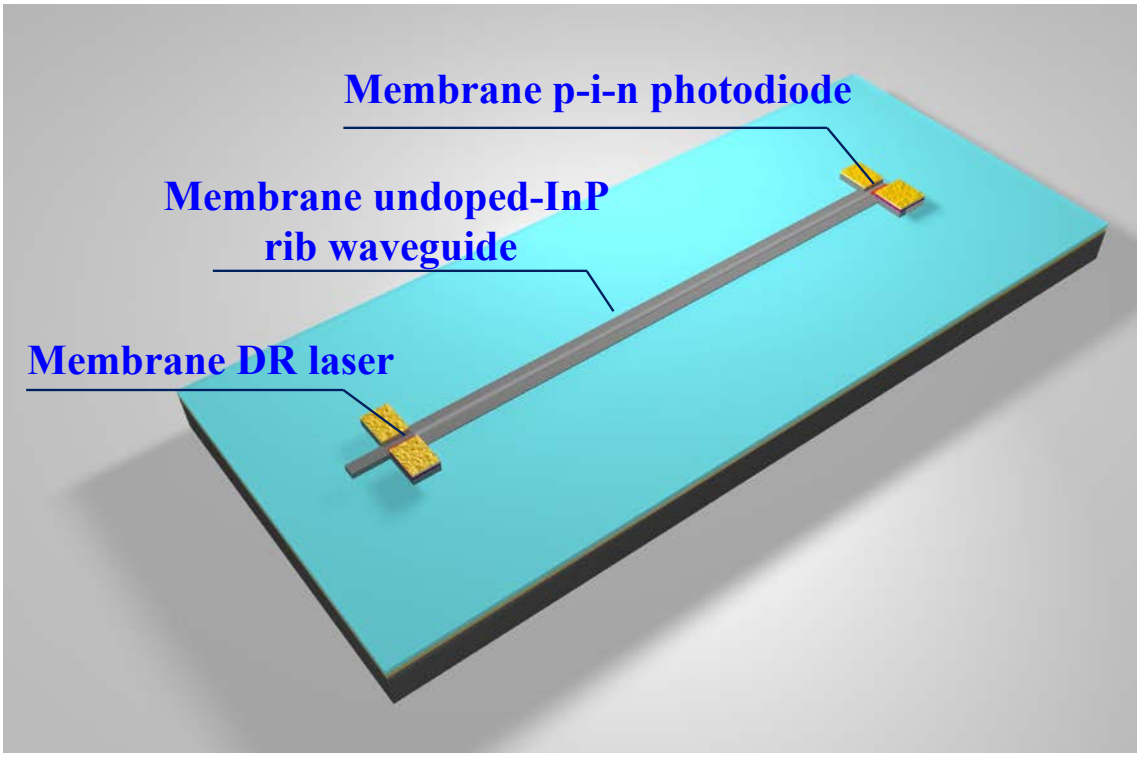


**Figure 6.13** Membrane optical link incorporating the low-loss undoped-InP rib waveguide and membrane DR laser.

This chapter discussed future prospects of membrane optical link. To extend the connection length of the link, a waveguide structure to achieve low propagation loss was presented. The shallow rib-structure avoid the optical field overlapped on side wall of the waveguide. As a preliminary experimental results, optical transmission through the undoped InP membrane rib-waveguide was confirmed. For the high efficiency operation of a membrane laser, our group fabricated membrane DR lasers, which consists of DFB section and integrated DBR. The membrane DR laser with reduced doping concentration of *p*-InP side cladding showed an external differential quantum efficiency $\eta_{df}$ and power conversion efficiency $\eta_{PC}$ of 32% and 12%, respectively. By adopting shallow grating depth of approximately 25 nm, the membrane DR laser with relatively small refractive index coupling coefficient of 800 $cm^{-1}$ was realized. This device showed also high $\eta_{df}$ and $\eta_{PC}$ of 36% and 14.6%, respectively. Prior to the further cavity design, the relation between the grating depth and scattering loss should be clarified by analytical way. By

combining these two approaches of reduced doping concentration and shallow grating structure, higher efficiency can be expected for the membrane lasers. As a result of direct modulation of membrane DR laser, the energy cost of 93 fJ/bit was obtained at a bias current of 1.06 mA for 20 Gbit/s NRZ signal. Figure 6.13 shows membrane optical link incorporating low-loss waveguide and DR structure. Ultra-low energy consumption operation as an on-chip optical interconnection will be realized this structure.

# References

[1] P. Dong, W. Qian, S. Liao, H. Liang, C.-C. Kung, N.-N. Feng, R. Shafiiha, J. Fong, D. Feng, and A. V. Krishnamoorthy, "Low loss shallow-ridge silicon waveguides," *Optics express,* vol. 18, pp. 14474-14479, 2010.

[2] T. Tomiyasu, T. Hiratani, D. Inoue, N. Nakamura, K. Fukuda, T. Uryu, T. Amemiya, N. Nishiyama, and S. Arai, "High-differential quantum efficiency operation of GaInAsP/InP membrane distributed-reflector laser on Si," *Applied Physics Express,* vol. 10, p. 062702, 2017.

[3] D. Inoue, J. Lee, K. Doi, T. Hiratani, Y. Atsuji, T. Amemiya, N. Nishiyama, and S. Arai, "Room-temperature continuous-wave operation of GaInAsP/InP lateral-current-injection membrane laser bonded on Si substrate," *Applied Physics Express,* vol. 7, p. 072701, 2014.

[4] T. Tomiyasu, T. Hiratani, D. Inoue, N. Nakamura, T. Amemiya, N. Nishiyama, and S. Arai, "Waveguide loss reduction of lateral-current-injection type GaInAsP/InP membrane Fabry–Pérot laser," *Japanese Journal of Applied Physics,* vol. 56, p. 050311, 2017.

[5] T. Fujii, K. Takeda, E. Kanno, K. Hasebe, H. Nishi, R. Nakao, T. Yamamoto, T. Kakitsuka, and S. Matsuo, "Low operating-energy directly modulated membrane distributed-reflector lasers on Si," in *ECOC 2016; 42nd European Conference on Optical Communication; Proceedings of*, 2016, pp. 1-3.

# Chapter 7
# Conclusion

The main objective of this thesis is to realize the integration and high speed operation of membrane optical devices. An on-chip optical interconnection has possibility to surpass the performance of state-of-art on-chip electrical wirings. For this purpose, ultra-low power consumption and highly efficient optical devices as well as integrated structure are essential property. The membrane DFB laser is the key device for the membrane optical interconnection because the total energy consumption significantly depending on the directly modulated light source. Our group has achieved successful room-temperature continuous-wave operation of lateral-current-injection membrane Fabry-Perot laser. However, there were still problems to be solved to demonstrate the advantage of membrane optical devices. First one is that the integration method of membrane optical devices need to be developed. Second one is that the low-threshold and high-speed properties are not achieved in an experimental way.

The realization of the integrated structure for the membrane devices and high performance integrated membrane laser is needed. Therefore, in order to investigate the characteristics of integrated membrane optical devices following issues were studied and demonstrated in this thesis.

**[Object 1]** To establish design and fabrication of integration structure for membrane optical devices.

(a) Calculation of coupling efficiency and back reflection

(b) Fabrication of membrane butt-jointed built-in (BJB) structure

**[Object 2]** To realized low-threshold and high-speed direct modulation of membrane DFB laser

(a) Investigation of fabrication process

(b) Characterization of static and dynamic properties

**[Object 3]** To realize data-transmission through optical link using membrane DFB laser.

(a) Investigation of electrical isolation process

(b) Characterization of static and dynamic properties

The summaries of each chapter are described as follows;

In chapter 1, the role of on-chip optical interconnection in a LSI was mentioned. According to the history of performance improvements of microprocessors, the power dissipation for interconnection became a serious problem. To overcome this problem, power reduction techniques such as novel circuit design and newly on-chip electrical wiring have been developed. However, the electrical wiring is intrinsically difficult to operate with high-speed and low-energy consumption for a long distant interconnection. On-chip optical interconnection is thought as a candidate for breakthrough technology in the field of on-chip wiring. Ultra-low power consumption semiconductor laser is a key device to realize this. Our group proposed membrane DFB laser for a directly modulated light source of on-chip optical interconnection. The properties of DFB type cavity will provide desired characteristics of low-energy consumption and high efficiency. After brief introduction of our research history, the problems still remaining were clarified and the objectives of this thesis were given.

Chapter 2 described the theoretical analysis of performances of membrane optical devices and their integration properties. The link loss in on-chip interconnection decides the required output power of a light source. The link loss can be divided into the coupling loss and propagation loss. The amount of coupling loss is independent on wiring length. Therefore, in a structure in which has low coupling efficiency, the increase in required power is caused even in a short interconnect length. In contrast, the propagation loss is

exponentially increased as the wiring length becomes long. In this sense, small propagation loss is essential factor for the waveguide. For the order of cm-long interconnect, a propagation loss of approximately 1 dB/cm is strongly desired. If a propagation loss of 1 dB/cm and a coupling loss of 0.1dB/coupling as an example of efficient optical link are obtained, the output power required for a light source for the wiring length of 2 cm becomes 83 μW.

Threshold current and modulation efficiency of membrane DFB laser were calculated. The relation between the surface grating depth and the refractive index coupling coefficient was shown. The 60-nm-depth grating created a coupling coefficient of 2000 $cm^{-1}$. For the membrane DFB laser with a uniform grating with a coupling coefficient of 2000 $cm^{-1}$, the minimum threshold current of 0.17 mA was obtained at a cavity length of 60 μm. By introducing a $\lambda/4$-shifted into the center of the cavity, the minimum threshold current became 0.08 mA at a cavity length of 35 μm. The modulation efficiency, which has a significant meaning to achieve high speed operation with low bias current, was also theoretically investigated. It was considered that the design to obtain the 3dB bandwidth of 7.7 GHz necessary for 10 Gbit/s operation at bias current of 1 mA for 100 fJ/bit energy consumption. At this situation, the modulation efficiency must be at least 5 $GHz/mA^{1/2}$ and for the 20 Gbit/s operation, 10 $GHz/mA^{1/2}$ is needed. From the relationship between the modulation efficiency and the active volume, the modulation efficiency of more than 5 $GHz/mA^{1/2}$ and 10 $GHz/mA^{1/2}$ are obtained for the active layer volume of less than 2.25 $\mu m^3$ and 0.56 $\mu m^3$, respectively. When the cavity length was 35 μm with the threshold current and the modulation efficiency of 0.24 mA and 8.7 $GHz/mA^{1/2}$, the bias current required for 10 Gbit/s operation was as low as 0.57 mA. This bias current corresponded to a value that can realize an energy cost of 57 fJ/bit when assuming a data-rate of 10 Gbit/s and a driving voltage of 1 V. By using the possible extreme design to realize ultra-low energy consumption, the bias current required for 10 Gbit/s operation was calculated to be 0.38 mA, which was not determined by the value of $f_r$ but a required optical output power. The prospect for realizing the 38 fJ/bit energy consumption operation in a membrane DFB laser was obtained. As a conclusion of this chapter, the need for high

efficient link structure and laser performance with respect to the threshold current and modulation efficiency were mentioned.

As the answers for the objective 1, chapter 3 described calculation and experimental results of a membrane BJB structure for the integration of membrane optical devices. First, monolithic photonic integration methods were introduced. In a membrane structure, BJB integration structure fabricated through butt-joint regrowth was thought to be most compatible approach. The membrane BJB structure was numerically investigated from the view point of coupling loss and back reflection ratio. The numerical calculations based on the finite difference method (FDM) and eigenmode expansion (EME) method were performed. As a result, low-coupling loss of 0.09dB (2%) and small back reflection of below -42dB can be simultaneously achieved in the growth thickness deviation in the range of ±20 nm. This fact was thanks to the mode matching between the active and passive waveguide region. The experimental investigation for the membrane BJB structure was conducted. The undercut etching condition with a depth of 165 nm and a mesa angle of 50° resulted in a good growth structure. The regrown GaInAsP layer was evaluated by micro photoluminescence measurement. There was no distinguished degradation in pholuminescence intensity around the active region confirmed by mapping measurement. The emission wavelength of regrown layer was same as that of grown on a bulk InP substrate. The full-width at half-maximum (FWHM) of the regrown layer was 58 meV, which was comparable to the typical FWHM of GaInAsP at room-temperature. As a conclusion of this chapter, the efficient coupling characteristics of membrane BJB structure was realized for numerical and experimental approaches.

As the answers for the objective 2, chapter 4 described the development of fabrication process and characterization of membrane DFB laser integrated with BJB passive waveguide. Surface grating formed by $CH_4/H_2$ RIE had rough surface. It was afraid that the increment of non-radiative recombination at damaged surface. By adopting wet chemical solution of HCl : $CH_3COOH$ : $H_2O_2$ : $H_2O$, the grating formation process

was improved to obtain smooth etched profiles. Subsequently, membrane DFB laser was fabricated using the obtained fabrication process of a BJB structure and a surface grating. First, the static characteristics of the fabricated devices were measured. The device with the cavity length of 50 μm showed a record low-threshold current of 0.23 mA under RT-CW condition. Preliminary reliability test of membrane DFB laser was performed. The device with a *p*-side alloyed Au/Zn/Au electrode had better voltage characteristics than the device with a *p*-side non-alloyed Ti/Au electrode device. The device with Au/Zn/Au electrode showed reliable operation up to 310 hours. The dynamic characteristics of membrane DFB lasers were investigated. From the small-signal modulation measurements, 3dB bandwidth of 12.8 GHz was obtained at the bias current of 0.98 mA. This result indicated that the membrane DFB laser had a capability to operate higher than 10Gbit/s at below 1 mA bias current. The highest modulation efficiency of $f_r$ was 12 GHz/mA$^{1/2}$, which was a record value among the DFB laser. Large-signal direct modulation at 10 Gbit/s was performed using a non-return-to-zero (NRZ) signal with pseudo-random-bit-sequence (PRBS) of $2^{31}$-1. The minimum bit-error-rate (BER) less than $1\times10^{-9}$ was achieved at a bias current of 1mA. The energy cost for this modulation was calculated to be 230 fJ/bit. The low-threshold and high-speed characteristics of membrane DFB laser was successfully realized.

As the answers for the objective 3, chapter 5 described the experimental results of integrated membrane optical link consisting of a DFB laser, a passive waveguide and a p-i-n PD. For the operation of integrated device as an optical link, sufficient electrical isolation between each integrated device was needed. The introduced isolating process resulted in successful enhancement of isolation resistance. The static and dynamic characteristics of the fabricated membrane integrated optical link device were evaluated. The DFB laser integrated in the optical link showed the threshold current of 0.48 mA. The integrated p-i-n PD successfully detected the transmitted light output from the DFB laser. The dynamic characteristics of the membrane optical link were measured. From the small-signal modulation measurement, the 3dB bandwidth of the optical link was 11.3

GHz at a DFB laser bias current of 2.73 mA and a p-i-n PD bias voltage of -3 V, which was sufficient bandwidth for a 10 Gbit/s data-transmission. Next, Large-signal data-transmission experiment using NRZ, PRBS of $2^{31}$-1 signals was performed. 10 Gbit/s transmission through the optical link was achieved with the BER of $6\times10^{-7}$ at a DFB laser bias current of 2.5 mA and a p-i-n PD bias voltage of -3 V. The high speed data-transmission though the membrane optical link was realized in this chapter.

Chapter 6 discussed brief future prospects of membrane optical link. As a low-propagation loss waveguide for the membrane optical link, InP membrane rib waveguide was considered. For the higher efficiency operation of a membrane laser, our group fabricated membrane distributed-reflector (DR) lasers. By adopting different two approaches that the low-doped *p*-InP side cladding structure or shallow grating depth structure, the external differential quantum efficiencies of 32% and 36% were realized, respectively. For the direct modulation results of membrane DR laser, a 93 fJ/bit 20 Gbit/s operation was obtained at the bias current of 1.06 mA. If these low-loss waveguide and high efficiency membrane DR laser are incorporated into a membrane optical link, I believe an ultra-low energy consumption on-chip optical wiring will be realized.

Through this thesis, the design and device structure of low-threshold and high-speed membrane integrated DFB laser were established. High-speed direct modulation at low-bias current of membrane integrated DFB laser was experimentally performed. The preliminary optical link structure using membrane DFB laser realized the data-transmission through the membrane optical link. The obtained results showed that optical link platform using a membrane laser and related membrane optical devices are attractive candidates for on-chip optical interconnections.

## Publication list

### Journal papers

[1] **D. Inoue**, J. Lee, K. Doi, T. Hiratani, Y. Atsuji, T. Amemiya, N. Nishiyama, and S. Arai, "Room-temperature continuous-wave operation of GaInAsP/InP lateral-current-injection membrane laser bonded on Si substrate," *Applied Physics Express,* vol. 7, p. 072701, 2014.

[2] **D. Inoue**, J. Lee, T. Hiratani, Y. Atsuji, T. Amemiya, N. Nishiyama, and S. Arai, "Sub-milliampere threshold operation of butt-jointed built-in membrane DFB laser bonded on Si substrate," *Optics express,* vol. 23, pp. 7771-7778, 2015.

[3] **D. Inoue**, T. Hiratani, Y. Atsuji, T. Tomiyasu, T. Amemiya, N. Nishiyama, and S. Arai, "Monolithic integration of membrane-based butt-jointed built-in DFB lasers and pin photodiodes bonded on Si substrate," *IEEE Journal of Selected Topics in Quantum Electronics,* vol. 21, pp. 392-398, 2015.

[4] **D. Inoue,** T. Hiratani, K. Fukuda, T. Tomiyasu, T. Amemiya, N. Nishiyama, and S. Arai, "High-modulation efficiency operation of GaInAsP/InP membrane distributed feedback laser on Si substrate," *Optics express,* vol. 23, pp. 29024-29031, 2015.

[5] **D. Inoue**, T. Hiratani, K. Fukuda, T. Tomiyasu, T. Amemiya, N. Nishiyama, and S. Arai, "Low-bias current 10 Gbit/s direct modulation of GaInAsP/InP membrane DFB laser on silicon," *Optics Express,* vol. 24, pp. 18571-18579, 2016.

[6] **D. Inoue**, T. Hiratani, K. Fukuda, T. Tomiyasu, G. Zhichen, T. Amemiya, N. Nishiyama, and S. Arai, "Integrated Optical Link on Si Substrate Using Membrane Distributed-Feedback Laser and p-i-n Photodiode," *IEEE Journal of Selected Topics in Quantum Electronics, ,* vol. 23, p. 3700208, 2017.

[7] T. Hiratani, K. Doi, J. Lee, **D. Inoue**, T. Amemiya, N. Nishiyama, and S. Arai, "Thermal properties of lateral-current-injection semiconductor membrane Fabry–Perot laser under continuous-wave operation," *Japanese Journal of Applied Physics,* vol. 54, p. 042701, 2015.

[8] Y. Atsuji, K. Doi, T. Hiratani, **D. Inoue**, J. Lee, Y. Atsumi, T. Amemiya, N. Nishiyama, and S. Arai, "Low-threshold-current operation of membrane distributed-feedback laser with surface grating bonded on Si substrate," *Japanese Journal of Applied Physics,* vol. 54, p. 080301, 2015.

[9] T. Hiratani, T. Shindo, K. Doi, Y. Atsuji, **D. Inoue**, T. Amemiya, N. Nishiyama, and S. Arai, "Energy cost analysis of membrane distributed-reflector lasers for on-chip optical interconnects," *IEEE Journal of Selected Topics in Quantum*

*Electronics,* vol. 21, pp. 299-308, 2015.

[10] N. Nishiyama, S. Arai, T. Hiratani, **D. Inoue**, and T. Amemiya, "Low Threshold and High Speed Operation of 1.55-μm-Band Lasers by InP-Based Membrane Structure," *The Review of Laser Engineering,* vol. 44, pp. 508–513, 2016.

[11] T. Hiratani, **D. Inoue**, T. Tomiyasu, Y. Atsuji, K. Fukuda, T. Amemiya, N. Nishiyama, and S. Arai, "Room-temperature continuous-wave operation of membrane distributed-reflector laser," *Applied Physics Express,* vol. 8, p. 112701, 2015.

[12] K. Fukuda, **D. Inoue**, T. Hiratani, T. Amemiya, N. Nishiyama, and S. Arai, "Preliminary reliability test of lateral-current-injection GaInAsP/InP membrane distributed feedback laser on Si substrate fabricated by adhesive wafer bonding," *Japanese Journal of Applied Physics,* vol. 56, p. 028002, 2017.

[13] T. Hiratani, **D. Inoue**, T. Tomiyasu, K. Fukuda, T. Amemiya, N. Nishiyama, and S. Arai, "90° C continuous-wave operation of GaInAsP/InP membrane distributed-reflector laser on Si substrate," *Applied Physics Express,* vol. 10, p. 032702, 2017.

[14] T. Tomiyasu, T. Hiratani, **D. Inoue**, N. Nakamura, T. Amemiya, N. Nishiyama, and S. Arai, "Waveguide loss reduction of lateral-current-injection type GaInAsP/InP membrane Fabry–Pérot laser," *Japanese Journal of Applied Physics,* vol. 56, p. 050311, 2017.

[15] T. Tomiyasu, T. Hiratani, **D. Inoue**, N. Nakamura, K. Fukuda, T. Uryu, T. Amemiya, N. Nishiyama, and S. Arai, "High-differential quantum efficiency operation of GaInAsP/InP membrane distributed-reflector laser on Si," *Applied Physics Express,* vol. 10, p. 062702, 2017.

[16] T. Hiratani, **D. Inoue**, T. Tomiyasu, K. Fukuda, T. Amemiya, N. Nishiyama, and S. Arai, "High Efficiency Operation of Membrane Distributed-Reflector Lasers on Silicon Substrate," *IEEE Journal of Selected Topics in Quantum Electronics, ,* vol. 23, p. 3700108, 2017.

[17] T. Amemiya, T. Kanazawa, T. Hiratani, **D. Inoue**, Z. Gu, S. Yakasaki, T. Urakami, and S. Arai, "Organic membrane photonic integrated circuits (OMPICs)," *Optics Express,* vol. 25, pp. 18537-18552, 2017.

**International conference**

[1] **D. Inoue**, J. Lee, T. Shindo, M. Futami, K. Doi, T. Amemiya, N. Nishiyama, and S. Arai, "Butt-joint built-in (BJB) structure for membrane photonic integration," *Compound Semiconductor Week 2013, 25th International Conference on Indium Phosphide and Related Materials (IPRM2013)*, Kobe, Japan, TuD3-6, May. 2013.

[2] **D. Inoue**, J. Lee, T. Hiratani, Y. Atsuji, T. Amemiya, N. Nishiyama, and S. Arai, "GaInAsP/InP lateral-current-injection membrane DFB laser integrated with GaInAsP waveguides on Si substrate," *The 24th IEEE International Semiconductor Laser Conference (ISLC 2014)*, Mallorca, Spain, MB.03, Sep. 2014.

[3] **D. Inoue**, T. Hiratani, Y. Atsuji, T. Tomiyasu, T. Amemiya, N. Nishiyama, and S. Arai, "Integration of membrane-based DFB laser and PIN photodiode on Si substrate toward on-chip interconnection," *The IEEE Optical Interconnects Conference 2015 (OI Conference 2015)*, San Diego, US, WB7, Apr. 2015.

[4] **D. Inoue**, T. Hiratani, T. Tomiyasu, K. Fukuda, T. Amemiya, N. Nishiyama, and S. Arai, "Monolithic integration of low threshold-current membrane DFB laser and low dark-current PIN photodiode," *The International Nano-Optoelectronics Workshop 2015 (iNOW2015)*, Tokyo, Japan, ThP13, Aug. 2015.

[5] **D. Inoue**, T. Hiratani, K. Fukuda, T. Tomiyasu, T. Amemiya, N. Nishiyama, and S. Arai, "High modulation efficiency of sub-milliampere threshold GaInAsP/InP membrane DFB laser," *The 2015 IEEE Photonics Conference, 28th Annual Conference of the IEEE Photonics Society (IPC2015)*, Virginia, US, WE2.5, Oct. 2015.

[6] **D. Inoue**, T. Hiratani, K. Fukuda, T. Tomiyasu, T. Amemiya, N. Nishiyama, and S. Arai, "10 Gbps operation of membrane DFB laser on silicon with record high modulation efficiency," *Compound Semiconductor Week 2016, The 28th International Conference on Indium Phosphide and Related Materials (IPRM2016)*, Toyama, Japan, ThD1-3, June. 2016.

[7] **D. Inoue**, T. Hiratani, K. Fukuda, T. Tomiyasu, T. Amemiya, N. Nishiyama, and S. Arai, "Impedance analysis of high-speed lateral-current-injection membrane DFB laser on silicon," *The 25th International Semiconductor Laser Conference (ISLC2016)*, Kobe, Japan, ThB3, Sep. 2016.

[8] **D. Inoue**, T. Hiratani, K. Fukuda, Z. Gu, T. Tomiyasu, T. Amemiya, N. Nishiyama, and S. Arai, "10 Gbit/s data transmission through optical link by using membrane DFB laser and PIN-PD," *The 2016 IEEE Photonics Conference, 29th Annual Conference of the IEEE Photonics Society (IPC2016)*, Hawaii, US, WC1.4, Oct. 2016.

[9] **D. Inoue**, T. Hiratani, K. Fukuda, T. Tomiyasu, T. Amemiya, N. Nishiyama, and S. Arai, "Temperature dependence of threshold current of GaInAsP/InP membrane lasers

with Bragg wavelength detuning," *Compound Semiconductor Week 2017, The 29th International Conference on Indium Phosphide and Related Materials (IPRM2017)*, Berlin, Germany, C7.2, May 2017.

[10] K. Doi, T. Shindo, M. Futami, J. Lee, T. Hiratani, **D. Inoue**, S. Yang, T. Amemiya, N. Nishiyama, and S. Arai, "Room-temperature continuous-wave operation of lateral current injection membrane laser," *Compound Semiconductor Week 2013, The 25th International Conference on Indium Phosphide and Related Materials (IPRM2013)*, Kobe, Japan, WeD2-3, May. 2013.

[11] J. Lee, K. Doi, T. Hiratani, **D. Inoue**, T. Amemiya, N. Nishiyama, and S. Arai, "$SiO_2$ thickness dependence of bandgap wavelength shift in quantum-well intermixing for photonic integration," *Compound Semiconductor Week 2014, The 26th International Conference on Indium Phosphide and Related Materials (IPRM2014)*, Montpellier, France, P28, May. 2014.

[12] Y. Atsuji, K. Doi, J. Lee, Y. Atsumi, T. Hiratani, **D. Inoue**, T. Amemiya, N. Nishiyama, and S. Arai, "Low-threshold-current operation of lateral current injection membrane distributed-feedback laser bonded on Si," *Compound Semiconductor Week 2014, The 26th International Conference on Indium Phosphide and Related Materials (IPRM2014)*, Montpellier, France, We-D2-2, May. 2014.

[13] T. Hiratani, Y. Atsuji, J. Lee, **D. Inoue**, T. Amemiya, N. Nishiyama, and S. Arai, "Electrode position dependence of energy cost in lateral-current-injection membrane distributed reflector laser," *The 24th IEEE International Semiconductor Laser Conference (ISLC 2014)*, Mallorca, Spain,, TuP.04, Sep. 2014.

[14] T. Hiratani, **D. Inoue**, T. Tomiyasu, Y. Atsuji, K. Fukuda, T. Amemiya, N. Nishiyama, and S. Arai. "Semiconductor membrane distributed-reflector (DR) laser," *Compound Semiconductor Week 2015, The 27th International Conference on Indium Phosphide and Related Materials (IPRM2015)*, We1O6.1, June 2015.

[15] T. Amemiya, T. Hiratani, **D. Inoue**, T. Tomiyasu, K. Fukuda, N. Nishiyama, and S. Arai, (Invited) "Membrane photonic integration on Si platform," *The 20th Opto Electronics and Communications Conference (OECC 2015)*, Shanghai, China, JThC.21, July 2015.

[16] T. Tomiyasu, **D. Inoue**, T. Hiratani, Y. Atsuji, T. Amemiya, N. Nishiyama, and S. Arai, "Room-temperature continuous-wave operation of $\lambda$/4-shifted membrane distributed feedback lasers," *The 11th Conference on Lasers and Electro-Optics Pacific Rim (CLEO-PR 2015)*, Busan, Korea, 28J2-2, Aug. 2015.

[17] S. Arai, N. Nishiyama, T. Amemiya, T. Hiratani, and **D. Inoue**, "Integrated membrane-based DFB and DR," *Photonic West 2016, SPIE*, San Francisco, US, 9767-30, Feb. 2016.

[18] S. Arai, N. Nishiyama, T. Amemiya, T. Hiratani, and **D. Inoue**, "GaInAsP/InP

membrane lasers," *Conference on Lasers and Electro-Optics 2016 (CLEO 2016)*, San Jose, US, SF2L.3, June 2016.

[19] S. Arai, N. Nishiyama, T. Amemiya, T. Hiratani, and **D. Inoue**, "Membrane distributed-reflector lasers," *Optoelectronics and Communications Conference 2016 (OECC2016),* Niigata, Japan, WD3-1, July 2016.

[20] T. Hiratani, **D. Inoue**, T. Tomiyasu, K. Fukuda, T. Amemiya, N. Nishiyama, and S. Arai, "High asymmetric light output characteristics of membrane distributed-reflector laser on Si substrate," *The 25th International Semiconductor Laser Conference (ISLC2016)*, Kobe, Japan, ThB3, Sep. 2016.

[21] T. Amemiya, T. Kanazawa, T. Hiratani, **D. Inoue**, Z. Gu, S. Yamasaki, T. Urakami and S. Arai, "Organic Membrane Photonic Waveguide with Metal Grating Couplers," *The Conference on Lasers and Electro-Optics 2017 (CLEO 2017)*, San Jose, US, SF2I.7, May. 2017.

[22] T. Tomiyasu, T. Hiratani, **D. Inoue**, N. Nakamura, T. Amemiya, N. Nishiyama, and S. Arai, "High Efficiency and High-speed Modulation Characteristics of Membrane Distributed-Reflector Laser on Si," *Compound Semiconductor Week 2017, The 29th International Conference on Indium Phosphide and Related Materials (IPRM2017)*, Berlin, Germany, D5.7, May 2017.

[23] T. Tomiyasu, T. Hiratani, **D. Inoue**, N. Nakamura, T. Amemiya, N. Nishiyama, and S. Arai, "Waveguide loss reduction of GaInAsP/InP membrane lasers by reduction of doping concentration of p-InP cladding layer," *Compound Semiconductor Week 2017, The 29th International Conference on Indium Phosphide and Related Materials (IPRM2017)*, Berlin, Germany, C6.3, May 2017.

**Meeting report and symposia**

1. **D. Inoue**, J. Lee, T. Shindo, M. Futami, K. Doi, T. Amemiya, N. Nishiyama, and S. Arai, "GaInAsP Butt-Joint Regrowth for Membrane Photonic Integration by OMVPE," *IEICE Technical meeting on optoelectronics (OPE)*, Shizuoka, Japan, 2-9, Apr. 2013.
2. **D. Inoue**, J. Lee, K. Doi, T. Amemiya, N. Nishiyama, and S. Arai, "GaInAsP Butt-Joint Regrowth by OMVPE toward InP-based Membrane Photonic Integration on Si Substrate," *IEICE The 20th Technical meeting on silicon photonics*, Tokyo, Japan, SIPH2013-P11, Oct. 2013.
3. **D. Inoue**, J. Lee, T. Hiratani, Y. Atsuji, T. Amemiya, N. Nishiyama and S. Arai, "Integrated waveguide type membrane DFB lasers by BCB bonding on Si substrate," *IEICE Technical meeting on laser and quantum electronics (LQE)*, Hokkaido, *IEICE Technical Report*, Vol. 114, No. 187, pp. 17-22, Aug. 2014.

4. **D. Inoue**, J. Lee, T. Hiratani, Y. Atsuji, T. Amemiya, N. Nishiyama, and S. Arai, "Low-threshold current operation of GaInAsP/InP membrane DFB laser with butt-jointed built-in waveguide bonded on Si substrate," *The 4th International Symposium on Photonics and Electronics Convergence (ISPEC2014)*, Tokyo, Japan, P-6, Nov. 2014.

5. **D. Inoue**, T. Hiratani, K. Fukuda, T. Tomiyasu, T. Amemiya, N. Nishiyama, and S. Arai, "Direct modulation properties of GaInAsP/InP membrane DFB laser on Si," *The 5th International Symposium on Photonics and Electronics Convergence (ISPEC2015)*, Tokyo, Japan, P-5, Dec. 2015.

6. **D. Inoue**, T. Hiratani, K. Fukuda, Z. Gu, T. Tomiyasu, T. Amemiya, N. Nishiyama, and S. Arai, "Monolithically integrated 10 Gbit/s optical link on Si using membrane DFB laser and pin-photodiode," *The 6th International Symposium on Photonics and Electronics Convergence (ISPEC2016)*, Tokyo, Japan, P-18, Dec. 2016.

7. T. Hiratani, **D. Inoue**, T. Tomiyasu, Y. Atsuji, K. Fukuda, T. Amemiya, N. Nishiyama and S. Arai, "Room-temperature continuous-wave operation of current-injection-type semiconductor membrane distributed-reflector laser," *IEICE Technical meeting on laser and quantum electronics (LQE)*, Ishikawa, *IEICE technical report*, Vol. 115, No. 46, pp. 1-6, May. 2015.

8. T. Tomiyasu, T. Hiratani, **D. Inoue**, K. Fukuda, T. Uryu, T. Amemiya, N. Nishiyama and S. Arai, "Investigation on the High Efficiency Operation of Semiconductor Membrane Distributed-Reflector Laser," *IEICE Technical meeting on laser and quantum electronics (LQE)*, Miyazaki, *IEICE Technical Report*, vol. 116, no. 275, pp. 1-6, Oct. 2016.

9. T. Tomiyasu, T. Hiratani, **D. Inoue**, K. Fukuda, T. Uryu, T. Amemiya, N. Nishiyama and S. Arai, "Light Output Properties of Membrane DBR Laser bonded on Si substrate," *3rd Workshop on IEICE Integrated Photonic Devices and their Applications*, Shizuoka, P11, Mar. 2016.

**Domestic conference**

1. **D. Inoue**, J. Lee, T. Shindo, M. Futami, K. Doi, T. Amemiya, N. Nishiyama, and S. Arai, "GaInAsP Butt-Joint Regrowth for Membrane Photonic Integration by OMVPE," The 60th Spring Meeting, 2013; The Japan Society of Applied Physics, Kanagawa, 29p-B4-6, Mar. 2013.

2. **D. Inoue**, J. Lee, K. Doi, T. Hiratani, Y. Atsuji, T. Amemiya, N. Nishiyama and S. Arai, "Lateral Current Injection Type GaInAsP/InP Membrane Laser on Si Substrate," The 61st Spring Meeting, 2014; The Japan Society of Applied Physics, Kanagawa, 18p-F9-10, Mar. 2014.

3. **D. Inoue**, J. Lee, T. Hiratani, Y. Atsuji, T. Amemiya, N. Nishiyama and S. Arai,

"GaInAsP/InP Membrane Distributed-Feedback Laser Integrated with Waveguides on Si Substrate," The 2014 IEICE Society Conference, Tokushima, C-4-14, Sep. 2014.

4. **D. Inoue**, T. Hiratani, T. Tomiyasu, Y. Atsuji, T. Amemiya, N. Nishiyama and S. Arai, "Room-temperature Continuous-wave Operation of $\lambda$/4-shifted GaInAsP/InP Membrane DFB Lasers," The 2015 IEICE General Conference, Shiga, C-4-5, Mar. 2015.

5. **D. Inoue**, T. Hiratani, T. Tomiyasu, Y. Atsuji, T. Amemiya, N. Nishiyama and S. Arai, "Monolithic Integration of $\lambda$/4-shifted DFB Laser and PIN-PD by Membrane BJB Structure," The 2015 IEICE General Conference, Shiga, C-4-13, Mar. 2015.

6. **D. Inoue**, T. Hiratani, K. Fukuda, T. Tomiyasu, T. Amemiya, N. Nishiyama and S. Arai, "Direct Modulation Response of GaInAsP/InP Membrane DFB Laser on Si substrate," The 76th Autumn Meeting, 2014; The Japan Society of Applied Physics, Nagoya, 13a-2S-8, Sep. 2015.

7. **D. Inoue**, T. Hiratani, K. Fukuda, T. Tomiyasu, T. Amemiya, N. Nishiyama and S. Arai, "High Modulation Efficiency Operation of GaInAsP/InP Membrane DFB Laser on Si Substrate, The 63th Spring Meeting, 2016; The Japan Society of Applied Physics, Tokyo, 20p-S321-8, Mar. 2016.

8. **D. Inoue**, T. Hiratani, K. Fukuda, Z. Gu, T. Tomiyasu, T. Amemiya, N. Nishiyama and S. Arai, "10 Gbit/s Optical Link Using Membrane DFB Laser Integrated with PIN-Photodiode," The 2016 IEICE Society Conference, Hokkaido, C-4-11, Sep. 2016.

9. K. Doi, T. Shindo, M. Futami, J. Lee, Y. Yamahara, T. Hiratani, **D. Inoue**, S. yang, T. Amemiya, N. Nishiyama and S. Arai, "Room-temperature CW Operation of GaInAsP/InP Semiconductor Membrane Laser," The 60th Spring Meeting, 2016; The Japan Society of Applied Physics, Kanagawa, 29p-B4-5, Mar. 2013.

10. T. Hiratani, Y. Atsuji, J. Lee, K. Doi, **D. Inoue**, T. Amemiya, N. Nishiyama and S. Arai, "Energy Cost Dependence on Electrode Position in Lateral-Current-Injection (LCI) Semiconductor Membrane Distributed Reflector Lasers," The 2014 IEICE General Conference, Niigata, C-4-32, Mar. 2014.

11. J. Lee, K. Doi, T. Hiratani, **D. Inoue**, T. Amemiya, N. Nishiyama and S. Arai, "Bandgap Wavelength Change in Quantum Well Intermixing by Introducing $SiO_2$ Protection Layer," The 61st Spring Meeting, 2016; The Japan Society of Applied Physics, Kanagawa, 20p-F8-8, Mar. 2014.

12. Y. Atsuji, K. Doi, J. Lee, Y. Atsumi, T. Hiratani, **D. Inoue**, T. Amemiya, N. Nishiyama and S. Arai, "Low-threshold-current Operation of GaInAsP/InP Membrane-DFB Laser," The 75th Autumn Meeting, 2014; The Japan Society of Applied Physics, Hokkaido, 18p-C6-11 , Sep. 2014.

13. T. Hiratani, **D. Inoue**, T. Tomiyasu, Y. Atsuji, T. Amemiya, N. Nishiyama and S. Arai,

"Room-temperature continuous-wave operation of semiconductor membrane distributed-reflector laser with butt-joint built-in structure," The 62nd Spring Meeting, 2016; The Japan Society of Applied Physics, Kanagawa, 12p-A17-10 , Mar. 2015.

14. Y. Atsuji, K. Fukuda, T. Hiratani, **D. Inoue**, T. Amemiya, N. Nishiyama and S. Arai, "Low voltage operation of GaInAsP/InP Membrane Laser," The 62nd Spring Meeting, 2016; The Japan Society of Applied Physics, Kanagawa, 12p-A17-11 , Mar. 2015.

15. K. Fukuda, **D. Inoue**, T. Hiratani, T. Amemiya, N. Nishiyama and S. Arai, "Initial Reliability of GaInAsP/InP Membrane DFB Laser on Si Substrate," The 63th Spring Meeting, 2016; The Japan Society of Applied Physics, Tokyo, 20p-S321-9, Mar. 2016.

16. Z. Gu, **D. Inoue**, T. Hiratani, T. Amemiya, N. Nishiyama and S. Arai, "Investigation ofmembrane photodiode with photonic crystal structure," The 63th Spring Meeting, 2016; The Japan Society of Applied Physics, Tokyo, 20a-S321-3, Mar. 2016.

17. T. Amemiya, T. Hiratani, **D. Inoue**, T. Tomiyasu, K. Fukuda, N. Nishiyama and S. Arai, ［Invited talk］ "Membrane Photonic Integration on Si Platform," The 2016 IEICE General Conference, Fukuoka, C-4-6, Mar. 2016.

18. T. Hiratani, **D. Inoue**, T. Tomiyasu, K. Fukuda, T. Uryu, T. Amemiya, N. Nishiyama and S. Arai, "Light output characteristics of membrane distributed Bragg reflector laser with surface grating," The 63rd Spring Meeting, 2016; The Japan Society of Applied Physics, Tokyo, 20p-S321-10, Mar. 2016.

19. T. Hiratani, **D. Inoue**, T. Tomiyasu, K. Fukuda, T. Amemiya, N. Nishiyama and S. Arai, "Realization of High Efficiency Operation of Membrane Distributed-Reflector Laser," The 2016 IEICE Society Conference, Hokkaido, C-4-21, Sep. 2016

20. T. Tomiyasu, T. Hiratani, **D. Inoue**, K. Fukuda, T. Amemiya, N. Nishiyama and S. Arai, "Investigation on the Waveguide Loss Reduction of Semiconductor Membrane Laser," The 2016 IEICE Society Conference, Hokkaido, C-4-20, Sep. 2016.

21. T. Uryu, **D. Inoue**, T. Hiratani, K. Fukuda, T. Tomiyasu, T. Amemiya, N. Nishiyama and S. Arai, "Bandwidth Analysis of Membrane DFB Laser by Impedance Measurements," The 2016 IEICE Society Conference, Hokkaido, C-4-12, Sep. 2016.

22. Z. Gu, **D. Inoue**, T. Hiratani, T. Amemiya, N. Nishiyama and S. Arai, "Investigation of bandwidth of membrane photodetector using slow light effect," The 77th Autumn Meeting, 2014; The Japan Society of Applied Physics, Niigata, 15a-P6-5, Sep. 2016.

23. T. Amemiya, T. Kanazawa, T. Hiratani, **D. Inoue**, Z. Gu, T. Urakami and S. Arai, "Organic Membrane Photonic Integrated Circuit (OMPIC): Analysis of Each Device," The 77th Autumn Meeting, 2014; The Japan Society of Applied Physics, Niigata, 15p-B8-10, Sep. 2016.

24. K. Fukuda, **D. Inoue**, T. Hiratani, T. Tomiyasu, T. Uryu, T. Amemiya, N. Nishiyama and S. Arai, "Temperature Dependence of Threshold Current of GaInAsP/InP

Membrane DFB Lasers by Bragg Wavelength Detuning," The 64rd Spring Meeting, 2017; The Japan Society of Applied Physics, Kanagawa, 15p-422-12, Mar. 2017.

25. N. Nakamura, T. Tomiyasu, T. Hiratani, **D. Inoue**, T. Amemiya, N. Nishiyama and S. Arai, "GaInAsP/InP Membrane DR Lasers with Low Differential Resistance," The 64rd Spring Meeting, 2017; The Japan Society of Applied Physics, Kanagawa, 15p-422-13, Mar. 2017.

26. T. Hiratani, **D. Inoue**, T. Tomiyasu, K. Fukuda, T. Amemiya, N. Nishiyama and S. Arai, "Temperature dependences of membrane distributed-reflector laser on silicon substrate," The 64rd Spring Meeting, 2017; The Japan Society of Applied Physics, Kanagawa, 16p-F204-5, Mar. 2017.

27. T. Tomiyasu, T. Hiratani, **D. Inoue**, N. Nakamura, T. Amemiya, N. Nishiyama and S. Arai, "Waveguide Loss Reduction of Semiconductor Membrane Laser for High Efficiency Operation," The 2017 IEICE General Conference, Fukuoka, Aichi, C-4-9, Mar. 2017.

**Awards**

1. “Honorable Mention, Best Student Poster Award” from The International Nano-Optoelectronics Workshop 2015 (iNOW2015), Aug. 2015.

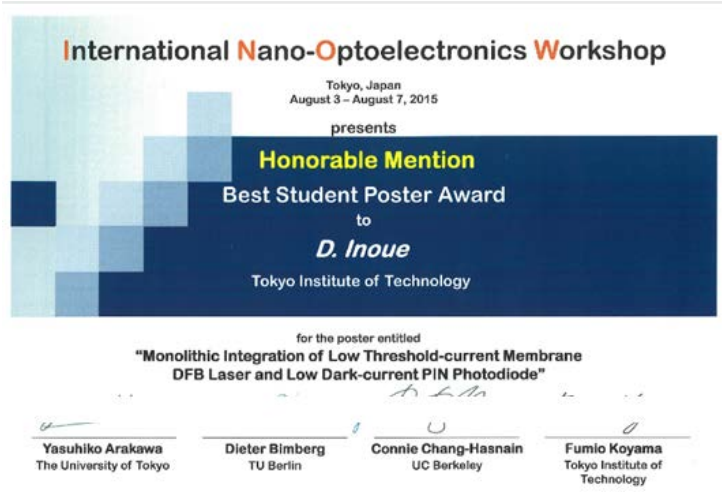


2. “The CSW2016 Best Student Paper Award” from The 28th International Conference on Indium Phosphide and Related Materials (IPRM2016), June 2016.

3. “Best Oral Presentation 賞” from The 39th International Symposium on Optical communication 2016, Aug. 2016.

賞 状

Best Oral Presentation 賞

井 上 大 輔 殿

あなたは第39回光通信研究会において 教員投票の結果 最も優れた口頭発表と認められました
よって記念品を贈呈し ここにこれを賞します
2016年8月10日

光通信研究会
代表 末松 安晴

# Acknowledgement

First, I would like to express my deepest gratitude to Professor Shigehisa Arai for his supervision. His knowledge of laser fundamentals and device fabrication supremely helps the progress of my research. I also thanks his continuous encouragement and discussion as well as supporting for daily laboratory life.

My co-advisor, associate Professor Nobuhiko Nishiyama, was willing to offer his expert OMVPE growth and high-speed measurement of semiconductor laser. He has always taken the time discuss with students to find and offer the ideas.

This thesis would not be possible without the technical advice by Assistant Professor Tomohiro Amemiya. He has deep knowledge over the field of politics, economics, stocks and photonics. Always He spent his time for students in our laboratory.

The author would like to show my greatest appreciation Professor Tetsuya Mizumoto, Professor Yasuyuki Miyamoto, Associate Professor Yuya Shoji, Dr. Takaaki Kakitsuka (NTT), for guidance and numerous discussions on this study.

The author would like to acknowledge Professor Emeritus Yasuharu Suematsu, Professor Emeritus Kenichi Iga, Professor Emeritus Kohroh Kobayashi, Professor Fumio Koyama, Professor Masahiro Asada, Professor Hiroyuki Uenohara, Associate professor Masahiro Watanabe, Associate Professor Tomoyuki Miyamoto, Associate Professor Safumi Suzuki, Assistant Professor Toru Kanazawa and Assistant Professor Masanori Nakahama for their encouraging and constructive discussions.

The author wishes to acknowledge Professor Minoru Yamada of Malaysia-japan International Institute of Technology, Professor Toshihiko Baba of Yokohama National University, Professor Hideo Kawanishi of Kogakuin University, Professor Katsumi Kishino of Sophia University, Professor Yasuo Kokubun of Yokohama National University, Professor Katsuyuki Utaka of Waseda University, Professor Kazuhiko Shimomura of Sophia University, Professor Toru Honda of Kogakuin University, Professor Michihiko Suhara of Tokyo Metropolitan University, Professor Takashi Suemasu of Tsukuba University, Associate Professor Takeo Maruyama, Associate

Professor Masakazu Arai of Miyazaki University, Associate Professor Yoshiaki Nishijima of Yokohama National University and the members of the summer seminar on optical communications for helpful advice and fruitful discussions.

The author would like to thank Dr. Hajime Shoji, Dr. Hideki Yagi, Mr. Koji Ebihara, Mr. Yoshifumi Nishimoto, Mr. Munetaka Kurokawa, and Mr. Kenichi Nakayama (Sumitomo Electric.) for helpful support on job searching.

The author would like to thank to Specially Appointed Assistant Professor Xiaodong Gu, Mr. Shunya Inoue and Mr. Minoru Saito.

The author expresses his sincere thanks to Technical Staff Shigeo Tamura for his experimental help on this study.

The author would like to sincerely thank to Mr. Junichi Suzuki and Mr. Zhichin Gu for fruitful discussion from beginning of this study.

The author would like to thank Dr. Tadashi Okumura (Hitachi), Dr. Mizuki Shirao (Mitsubishi Electric), Dr. Yuki Atsumi (AIST), Dr. Joonhyun Kang (KIST), Assistant Professor Yusuke Hayashi (Mie University) for helpful discussions.

The author deeply appreciates the continuous help and support for membrane photonic integrated circuits members, Dr. Takahiko Shindo (NTT), Ms. Jieun Lee, Mr. Mitsuaki Futami (Mitsubishi Electric), Mr. Yoshiaki Yamahara (JX Metal), Mr. Kyohei Doi (MUFG), Dr. Takuo Hiratani(Sumitomo Electric.), Mr. Shu yang, Mr. Yuki Atsuji (Softbank), Mr. Tatsuya Matou(Sony), Mr. Takahiro Tomiyasu (Furukawa Electric.), Mr. Kai Fukuda (FANUC), Mr. Tatsuya Uryu (Sandisk), Ms. Nagisa Nakamura, Mr. Takamasa Yoshida, Mr. Jo Tei and Mr. Kensyo Oguri.

The author would like to sincerely thank to group members, Mr. Takuma Kitamoto (P and G), Mr. Noriaki Sato (Sony), Mr. Daisuke Take (NTT East), Mr. Keita Fukuda (Denso), Mr. Seiji Myoga (Nikon), Mr. Eijun Murai (FANUC), Mr. Masashi Yukinari (Murata), Mr. Takumi Yoshida (Casio Computer Co.), Mr. Naotaro Shimizu, Mr. Yuki Hashimoto (Fujitsu), Mr. Hiroki Taniguchi (NTT), Mr. Shovon MD Tanvir Hasam (DeNA), Mr. Yuki Kuno (Santec), Mr. Takaski Kaneko (RICHO), Mr. Akio Yasui (Softbank), Mr. Naoya Hojo (Furukawa Electric), Mr. Shotaro Tadano (Softbank), Mr.

Kazuto Ito (Sony), Mr. Satoshi Inoue (NTT East), Mr. Satoshi Yamasaki (Murata), Mr. Kentaro Yamanaka (RICHO), Ms. Kumi Nagasaka (Murata), Mr. Shoichi Yoshitomi, Ms. Min Yulim, Mr. Moataz Eissa, Mr. Yusei Goto, Mr. Fumihito Tashibana, Mr. Liu Bai, Mr. Keisuke Masuda, Mr. Hibiki Kagami, Mr. Nao Fujimoto and Mr, Takuya Mitarai.

The author thanks all of his colleagues in Prof. Asada's group, Prof. Miyamoto's group, Assoc. Prof. Watanabe's group and Assoc. Prof. Suzuki's group for private advice as well as technical advice.

The author appreciates the kindness and help of the secretaries, Ms. Kyoko Kasukawa, Ms. Emi Takada, Ms. Asako Suzuki, Ms. Keiko Yashima, Ms. Hitomi Matsumura and Ms. Chikako Yoshida (COI office).

The author deeply thanks his family for their continuous support and encouragements.

This research was also financially supported by Grants-in-Aid for Scientific Research from the Ministry of Education, Culture, Sports, Science and Technology, Japan. The author was especially supported by Japan Society for the Promotion of Science (JSPS) for Research Fellowship for Young Scientists.